Long-term observation of
Arabidopsis thaliana root growth under
close-to-natural conditions using
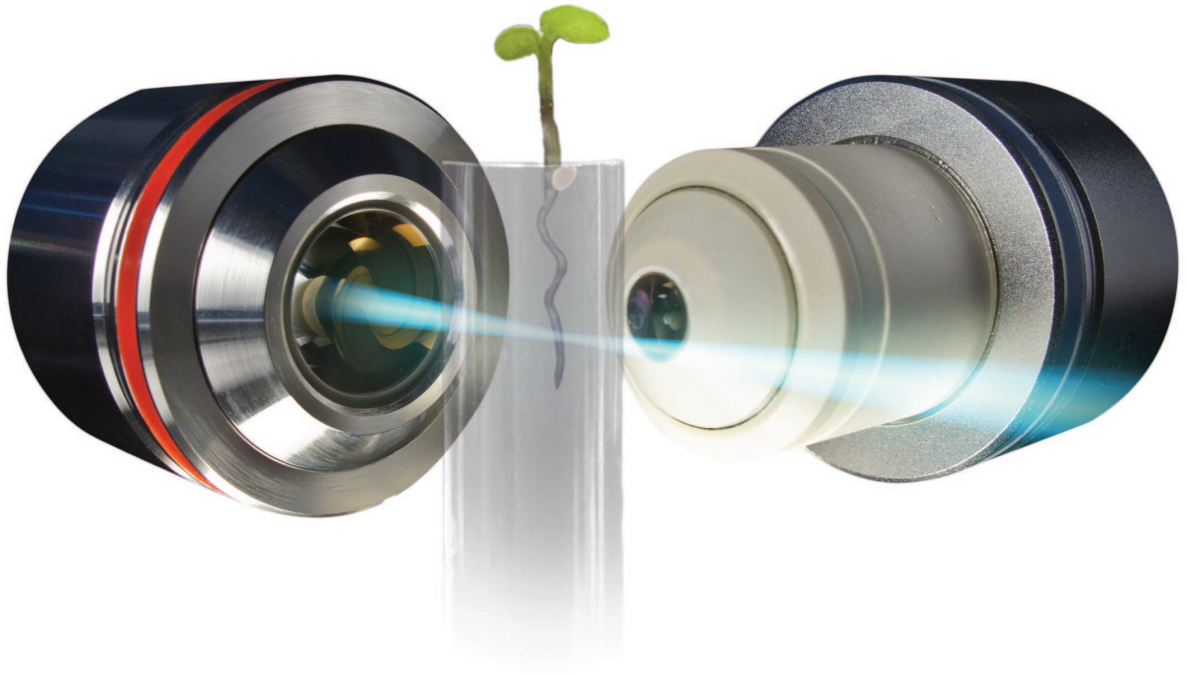# Light Sheet-based Fluorescence Microscopy

vom Fachbereich Biowissenschaften der
Johann Wolfgang Goethe-Universität als Dissertation angenommen.

Dekanin: Prof. Dr. Meike Piepenbring

Erster Gutachter: Prof. Dr. Ernst H. K. Stelzer
Zweiter Gutachter: Prof. Dr. Enrico Schleiff

Datum der Disputation: 17. April 2015

Contents

Zusammenfassung

Es ist faszinierend wie sich aus Genen, Proteinen und Zellen im gegenseitigen Zusammenspiel Gewebe, Organe und Organismen bilden. Um die Entwicklung eines Organs verstehen zu können, müssen subzelluläre Vorgänge im Zusammenhang des gesamten, dreidimensionalen Gewebes gesehen werden. Ferner können kurze Zeiträume entscheidend für die vergleichsweise langsame Entwicklung eines Organs sein. Die Mikroskopie erlaubt es, Wachstum und Differenzierungsprozesse auf zellulärer Ebene zu beobachten und ist deshalb in der Entwicklungsbiologie eine wichtige Methode. Das Dilemma der Lichtmikroskopie, insbesondere der Fluoreszenzmikroskopie, besteht darin, dass Moleküle mit Licht angeregt werden müssen. Diese Lichtenergie kann einen Einfluss auf die Molekülstruktur nehmen und zu toxischen Effekten in der Zelle führen. Dennoch, die moderne Fluoreszenzmikroskopie ermöglicht die gezielte Untersuchung der Expression, Lokalisation und Interaktion von Proteinen in Echtzeit. Die Lichtscheiben-Fluoreszenzmikroskopie (LSFM) erlaubt es, aufgrund einer um mehrere Größenordnungen geringeren Anregungsenergie, die Probe nahezu ohne phototoxische Effekte untersuchen zu können. LSFM hat sich daher in den vergangenen zehn Jahren als ausgezeichnete Methode in der Entwicklungsbiologie etabliert. Bisher konnte die Embryogenese des Zebrafisches *Danio rerio*, der Fruchtfliege *Drosophila melanogaster* oder des Rotbraunen Reismehlkäfers *Tribolium castaneum* über Tage hinweg aufgenommen und auf zellulärer Ebene analysiert werden.

Die Motivation dieser Arbeit war es, neue Erkenntnisse in Wachstums- und Entwicklungsprozessen von Pflanzenorganen zu gewinnen. Hierfür mussten Verfahren für Langzeitaufnahmen einer sich entwickelnden Pflanze etabliert werden. Ziel der Arbeit war es, mit Hilfe der Lichtscheiben-Fluoreszenzmikroskopie Wachstum auf zellulärer Ebene aufzunehmen und quantitativ zu analysieren, um damit zu einem besseren Verständnis der Pflanzenentwicklung beizutragen. Viele Erkenntnisse über die Mechanismen der Pflanzenentwicklung sind in den letzten Jahren mit Hilfe der Fluoreszenzmikroskopie veröffentlicht worden, aber derartige Untersuchungen beschränkten sich auf wenige Zellen und kurze Zeiträume. Langzeitaufnahmen mit hoher räumlich-zeitlicher Auflö-

sung existieren bisher nicht. In dieser Arbeit wurde die Entwicklung von Pflanzenor-
ganen über Tage hinweg aufgenommen und quantitativ analysiert. Als Modellpflanze
wurde *Arabidopsis thaliana* verwendet, weil sie eine der meist untersuchten Modellpflanze
ist, und zahlreiche transgene Pflanzenlinien zur Verfügung stehen. Zudem besteht die
Wurzel von Arabidopsis aus nur wenigen Zellschichten und ist deshalb vergleichsweise
transparent, somit für die Lichtmikroskopie geeignet. Aufnahmen von Reis *Oryza sativa*
haben gezeigt, dass sich die Methode auch für andere Modellpflanzen eignet. In Ara-
bidopsis wurden Gravitropismus, Tag-Nacht-Rhythmen, Organmorphogenese, sowie Dy-
namiken des Zytoskeletts und endosomaler Kompartimente untersucht. Die Ergebnisse
der Untersuchungen wurden in Zusammenarbeit mit Prof. Jozef Šamaj (Palacký Univer-
sity, Olomouc, Czech Republic), Prof. Niko Geldner (University of Lausanne, Switzer-
land), Prof. Malcom Bennett (University of Nottingham, UK) und Dr. Jürgen Kleine-
Vehn (Universität für Bodenkultur Wien, Österreich) durchgeführt und erfolgreich veröf-
fentlicht. Das Hauptthema dieser Arbeit behandelt die Entwicklung von Seitenwurzeln
und wurde in enger Zusammenarbeit mit Dr. Alexis Maizel (Universität Heidelberg, Ger-
many) durchgeführt. In seinem Labor wurden transgene Reporter-Pflanzen entwickelt,
die mit bis zu drei Fluorophor-gekoppelten Proteinen die Verfolgung der Seitenwurze-
lentstehung von der ersten Zellteilung an ermöglichen.

Pflanzen sind den Reizen ihrer Umwelt, wie Licht, Temperatur, Nährstoffe, Wasser,
Erdanziehung, mechanischen Reizen oder Bakterien und Pilzen ausgesetzt. Sie reagieren
schnell auf Veränderungen in ihrer Umwelt, weshalb das Beobachten des Pflanzenwach-
stums eine besondere Herausforderung darstellt. Um die beobachtete Pflanze in ihrer
Physiologie nicht zu beeinträchtigen, müssen die Umweltbedingungen in der Mikroskop-
kammer optimiert sein. Darüber hinaus können kontrollierte Umweltbedingungen mod-
uliert werden, um die daraufhin erfolgenden Reaktionen der Pflanze zu analysieren. Eine
Besonderheit des Mikroskops ist, dass die Objektive auf der Seite liegen. Diese Anord-
nung bietet neue Möglichkeiten die Probe zu positionieren und erlaubt es die Pflanze
in der Mikroskopkammer aufrecht, also in ihrer natürlichen Position wachsen zu lassen.
Um die Pflanze stabil in ihrer Position zu halten, wurden in dieser Arbeit verschiedene
Probenhalter und Präparationsmethoden entwickelt. Dabei befanden sich die Wurzeln
in einer Flüssigkeit, wohingegen die Blätter an der Luft blieben. Das Detektionsob-
jektiv befindet sich im Wasser der Mikroskopkammer, d.h. die mikroskopischen Auf-
nahmen fanden Unterwasser statt. Durch die aufrechte Position der Pflanze kann die
Wachstumsdynamik relativ zur Erdanziehung untersucht werden. Seitenwurzeln erster
Ordnung von Arabidopsis wachsen grundsätzlich in einem festgelegten Winkel relativ

zur Erdanziehung. Aufnahmen einer herauswachsenden Seitenwurzel ermöglichten eine Quantifizierung der Dynamik der Zellstreckung bei der Etablierung dieses Winkels.

Die Probe wurde im Mikroskop von unten fixiert, so dass die Pflanze von oben frei zugänglich für die Beleuchtung der Blätter war. Die Beleuchtung in der Mikroskopkammer wurde mit Hilfe einer Blende vor jeder Aufnahme aus- bzw. nach der Aufnahme wieder eingeschaltet. Über eine Zeitschaltuhr wurde die Tageslänge kontrolliert gesteuert. Die Pflanze erfuhr also standardisierte Bedingungen in der Mikroskopkammer, die es ermöglichten, Langzeitaufnahmen von Haupt- und Seitenwurzelwachstum zu erstellen. Die Aufnahmen zeigten ein mit dem Tag-Nacht-Rhythmus periodisch oszillierendes Wachstum. Auch die Fluoreszenzintensität der überexprimierten Proteine stieg tagsüber an, was auf eine erhöhte Aktivität der Pflanze am Tage schließen lässt. Die Beleuchtung des Wurzelsystems hat einen erheblichen Einfluss auf das Wurzelwachstum (Phototropismus). Um die Beleuchtungssituation in der Mikroskopkammer weiter zu optimieren, wurde das Wurzelsystem in der Mikroskopkammer abgedunkelt, so dass das auf die Wurzel einfallende Licht auf 42 % reduziert werden konnte. Neben den Tag-Nacht Untersuchungen und Beobachtungen des Gravitropismus von Seitenwurzeln wurde die Anwendbarkeit der Methode auf verschiedene biologische Fragestellungen hin geprüft. Es wurden unterschiedliche Organe (Wurzelspitze, Seitenwurzel oder Blätter) in verschiedenen zeitlichen Größenordnungen, von Sekunden bis Tage, untersucht. Aufnahmen der oberirdischen Pflanzenteile demonstrierten die optische Qualität der Aufnahme solcher Gewebe. Hierbei beeinflussten Kutikula und Luft zwischen den Zellen die Bildqualität in tiefer liegenden Zellschichten deutlich. Oberirdische Pflanzenorgane sind zudem photosynthetisch aktive Gewebe und bedürfen eines Gasaustausches. Da die Probe in Wasser aufgenommen wurde, war es nicht möglich, diese Gewebe über lange Zeit aufzunehmen, ohne dass sich Stressreaktionen in der Pflanze zeigten.

LSFM zeichnet sich durch ein hohes Signal-zu-Rausch Verhältnis aus und der Einsatz von modernen Kameras erlaubt eine hohe Bildwiederholungsrate. Diese Eigenschaften eignen sich, um intrazelluläre dynamische Prozesse zu beobachten, wie Aufnahmen und Analysen von Endosomenbewegungen oder sich rasch verändernden Strukturen des Zytoskeletts zeigen. Das Mikroskop lässt sich im Hinblick auf Aufnahmegeschwindigkeit und Bildqualität mit anderen modernen Verfahren der Fluoreszenzmikroskopie, wie der Spinning-Disc-Mikroskopie, vergleichen. Die Spinning-Disc-Mikroskopie verwendet ebenso wie die LSFM schnelle Kameras, jedoch ist die axiale Auflösung vergleichsweise niedriger. Der entscheidende Vorteil der Lichtscheibenmikroskopie liegt aber in der reduzierten Belastung der Probe durch intensives Laserlicht. Das Resultat der

Wurzelhaarwachstumsanalyse ist ein Paradebeispiel dafür, welche Möglichkeiten die Lichtscheiben-Fluoreszenzmikroskopie bietet. Die komplette Wurzelspitze wurde mit 40-facher Vergrößerung alle zwei Minuten über einen Zeitraum von zehn Stunden aufgenommen. Zu jedem Zeitpunkt wurde ein Bildstapel von 388 Bildern aufgezeichnet, das entspricht 2.145 Megapixel (Voxelabmessungen x/y/z = $0.16\,\mu m/0.16\,\mu m/0.645\,\mu m$). Insgesamt umfasst diese Aufnahme 1,17 Terabyte Daten, was eine große Herausforderung in der Bildanalyse darstellt. In diesem Datensatz konnten in der Wurzelspitze dutzende wachsende Zellplatten vermessen werden. Durch die lange Aufnahmedauer konnte im späteren Verlauf der Aufnahme das Herauswachsen von Wurzelhaaren verfolgt, und eine erhöhte Fluoreszenzintensität in der Wurzelhaarspitze mit der Wachstumsgeschwindigkeit korreliert werden. Die Ergebnisse gaben einen Hinweis darauf, dass die mit GFP-RabA1d markierten Endosomen an den Wachstumsprozessen von Wurzelhaaren und an der Bildung der Zellplatte beteiligt sind. Derartige Untersuchungen waren bislang mit herkömmlichen Mikroskopietechnologien nicht möglich.

Aufgrund der vielversprechenden Ergebnisse bei den Untersuchungen des Wurzelsystems von Arabidopsis, entwickelte sich die Forschungsperspektive, die Organentwicklung am Beispiel der Seitenwurzelentstehung zu untersuchen. Die Aufnahme einer entstehenden Seitenwurzel stellt hohe Anforderungen an ein mikroskopisches Verfahren. Weil erstens, der Prozess der Seitenwurzelentstehung im Inneren der Hauptwurzel stattfindet und sich die Qualität der Aufnahme durch die lichtstreuende Wirkung des darüber liegenden Gewebes verringert. Zweitens, die Pflanze den Beobachtungszeitraum von etwa 48 Stunden im Mikroskop wohlbehalten überdauern muss. Und drittens, die benötigte räumliche und zeitliche Auflösung mit phototoxischen Effekte einhergehen kann, die zumindest in herkömmlichen Fluoreszenzmikroskopen zu einem Wachstumsstopp führen. Alle bisherigen Untersuchungen mit herkömmlichen Fluoreszenzmikroskopen zur Seitenwurzelentstehung konnten nur an einzelnen Zellen und nur für kurze Zeitabschnitte durchgeführt werden. Jetzt ist es möglich, die Entstehung und Morphogenese des komplexen Organs der Seitenwurzel in einer bislang noch nicht dagewesenen zeitlichen und räumlichen Auflösung zu beobachten. Erste Aufnahmen wurden auf Formveränderungen des wachsenden Organs und dessen Dynamik auf zellulärer Ebene untersucht. Noch vor der ersten Zellteilung konnte z.B. ein Anschwellen der Perizykelzellen gemessen werden. Weitere Untersuchungen der Formentwicklung zeigten ein rasches Wachstum des Seitenwurzelprimordiums nach dem spontanen "Aufbrechen" der darüberliegenden Gewebe. Diese Beobachtung gibt Hinweise darauf, dass das Primordium Druck auf das umliegende Gewebe ausübt, und deren mechanische Eigenschaften das Wachstum des

Primordiums beeinflussen. Die Verfolgung aller an der Seitenwurzelbildung beteiligten Zellteilungen sollte Aufschluss über etwaige Zellteilungsmuster und deren Einfluss auf die Formveränderung geben. Bei der Verfolgung der Zellteilung ist es hilfreich die Metaphase zu erfassen, denn in diesem Moment sind die Chromosomen dicht gepackt, und das Fluoreszenzsignal des an Histon2B gekoppelten Fluoreszenzproteins konzentriert sich. Dadurch wird eine Erkennung von Zellteilungen erleichtert. Um diesen wichtigen Moment zu erfassen, war es notwendig die Zellen alle 5 Minuten aufzunehmen. Die Verkürzung des Aufnahmeintervalls von ursprünglich 15 Minuten auf 5 Minuten bedeutete auch, dass die Zellen mehr Anregungsenergie ausgesetzt waren, was in den ersten Versuchen zu einem Wachstumsstopp führte. Nur wenn die Laserintensität auf ein Minimum reduziert wurde, konnte der Prozess vollständig beobachtet werden. Die Konsequenz für die geringe Anregungsenergie war ein verringertes Signal-zu-Rausch-Verhältnis und Zellkerne konnten fast nicht mehr vom Hintergrundrauschen unterschieden werden. Erst der Einsatz des Kamera-Binnings (das Licht von vier Pixeln wird gesammelt und in einem Pixel summiert) erhöhte den Kontrast, so dass alle Zellkerne lokalisiert werden konnten. Darüber hinaus ist im Binning-Modus die Auslesegeschwindigkeit erhöht und erlaubt eine höhere Bildwiederholungsrate. Ein einzelner Zeitpunkt konnte so schneller ($40\,s$ statt $90\,s$) aufgenommen werden, so dass sich die Beleuchtungszeit der Blätter verlängerte und die Bedingungen für die Pflanze verbessert wurden.

Die Entstehung von Seitenwurzeln wurde von der ersten Zellteilung bis zum Herauswachsen der Seitenwurzel aus der Hauptwurzel erfasst. Die Fluoreszenz von Zellkernmarkern (UBQ10::H2B-RFP) und der Plasmamembran (UBQ10::YFP-PIP1;4) wurden alle 5 Minuten über einen Zeitraum von über 64 Stunden aufgenommen, so dass alle an der Entstehung beteiligten Zellen erkannt und verfolgt werden konnten. Um die Seitenwurzelenstehung zu stimulieren wurden die sieben Tage alten Pflanzen 6-9 Stunden vor der Aufnahme um 90° gedreht. Um sicher zu stellen, dass die Aufnahme noch vor der ersten Zellteilung startete, besitzt die Pflanze noch einen dritten Fluorezenzmarker, der noch vor der ersten Zellteilung in den Perizykelzellen exprimiert wird (GATA23::NLS-GUS-GFP). Insgesamt wurden sechs Datensätze aufgezeichnet, sodass die Ergebnisse statistisch relevant wurden. Die Positionen und Zellteilungen aller beteiligten Zellen wurden manuell erfasst und mit der Hilfe von Alexander Schmitz und Jens Fangerau konnten die Daten auf ihre Eigenschaften hin analysiert werden. Eine Seitenwurzel entstand aus anfänglich 8-15 Gründerzellen (Durchschnitt 11 ± 2), welche in 5-8 Zellreihen angeordnet waren. Für einen direkten Vergleich der Seitenwurzeln wurden die Datensätze anhand ihrer Zellzahl aufeinander synchronisiert. Die Gestalt der Primordia

und die Wachstumskurven zeigten große Ähnlichkeiten. Eine Klassifizierung der Zellteilungen aufgrund ihrer räumlichen Ausrichtung ermöglichte eine Analyse, zu welchem Zeitpunkt neue Reihen oder Schichten entstehen. Die Schichten z.B. entstanden in jedem Datensatz bei etwa gleichem Entwicklungsstand. Zudem entsprach die zeitliche Abfolge der Schichtbildung dem Modell von Malamy und Benfey von 1997.

Neben diesen Gemeinsamkeiten zeigte sich im Vergleich der Datensätze eine große Variabilität in der zellulären Zusammensetzung. Anhand der räumlichen Anordnung der Zellen am Anfang konnte nicht erkannt werden, wo exakt das zukünftige Zentrum der Seitenwurzel liegen wird. Es ist bekannt, dass die Endodermis die Initiierung und Entwicklung eines Primordiums beeinflusst. Auch anhand der Position der Endodermiszellen konnte kein Zentrum abgeleitet werden. Einzelne Zellen und Zellreihen trugen unterschiedlich zur Gesamtzellzahl bei. Die Entwicklung der Reihen konnte in einer Radialansicht des Membrankanals über das Herauswachsen der Seitenwurzel hinaus verfolgt werden und zeigte, dass sich die Zellen an der Basis des Primordiums strecken und die Spitze herausdrücken. Bei genauerer Analyse der Zellteilungen zeigte sich, dass der zweite Zellzyklus 50 % asymmetrische Zellteilungen aufwies. Im Vergleich dazu wiesen der 3. und 4. Zellzyklus nur jeweils 20 % asymmetrische Zellteilungen auf. Des Weiteren erfolgte nach dem zweiten Zellzyklus die Zellteilungsrichtung immer senkrecht zur vorherigen. Die ersten zwei Zellteilungszyklen schienen daher einer besonderen Kontrolle zu unterliegen und könnten bei der Positionierung des Primordiums eine größere Bedeutung haben. Wenn die Orientierung von asymmetrischen Zellteilungen gestört wird, wie es bei der aurora Doppelmutante *aur1-2 aur2-2* der Fall ist, war das Herauswachsen des Primordiums verzögert. Zudem wurde die Morphologie des Organs eher von mechanischen Eigenschaften der umliegenden Schichten bestimmt. Diese Ergebnisse gaben Hinweise darauf, dass sowohl eine präzise Kontrolle von asymmetrischen Zellteilungen als auch die mechanischen Eigenschaften der umliegenden Gewebe entscheidend für die Morphologie des Primordiums sind. Trotz des anfänglichen Defekts der asymmetrischen Zellteilungen schafften es die Zellen, ein funktionstüchtiges Organ aufzubauen, was ein flexibles Zellteilungsmuster voraussetzt. Die Zellteilungen erfolgen also nicht nach einem stereotypischen Muster, sondern verhalten sich eher adaptiv. Zusammenfassend weisen die Ergebnisse darauf hin, dass neben einem stereotypen Muster von Zellteilungen zu festen Entwicklungsstadien, ebenso eine dynamisch angepasste Steuerung der Zellteilungen existiert. Beide Eigenschaften ermöglichen es dem entstehenden Organ sich trotz unterschiedlicher Zell-Topologie und mechanischer Gegebenheiten des umgebenden Gewebes flexibel und dennoch kontrolliert zu entwickeln.

Die Ergebnisse dieser Arbeit zeigen wie mit Hilfe der Lichtscheiben-Fluoreszenzmikroskopie und natur-ähnlichen Bedingungen in der Mikroskopkammer, das Pflanzenwachstum über Tage hinweg mit hoher räumlich-zeitlichen Auflösung beobachtet und analysiert werden kann. Mit dieser Methode können Umwelteinflüsse wie Temperaturänderungen, Nährstoffmangel, Überflutung/Trockenheit oder Salzstress und die Reaktionen der Pflanze auf Änderungen dieser Parameter auf zellulärer Ebene untersucht werden. Tag-Nacht-Rhythmen, Gravitropismus und Phototropismus können über lange Zeiträume aufgenommen und analysiert werden. Dabei ist es möglich, Differenzierungsprozesse einzelner Zellen in ihrem dreidimensionalen Gewebeverband zu analysieren und so die Entstehung von Organen detailliert zu erforschen. Derartige Untersuchungen waren bis heute nicht realisierbar und ermöglichen ungeahnte neue Erkenntnisse in der Forschung der Pflanzenentwicklung.

Summary

In the interest of understanding the development of a multicellular organism, subcellular events must be seen in the context of the entire three-dimensional tissue. In addition, events that occur within a short period of time can be of great importance for the relatively long developmental process of the organ. Thus, in order to understand morphogenesis, it is required to capture subcellular events in a larger spatio-temporal scale context, which has been up to now a technical challenge. In developmental biology, light microscopy has always been an important tool, which allows to observe growth and differentiation events in real time. The dilemma of light microscopy, in particular fluorescence microscopy, is that molecules receive high light intensities. This energy might change the conformation of molecules, which can have signaling or toxic effects. Nevertheless, advanced fluorescence microscopy with high-resolution and live-cell imaging capabilities allows to monitor gene expression, localization and interaction of specific proteins within a cell. In Light Sheet-based Fluorescence Microscopy (LSFM), the energy required for a single recording is reduced by several orders of magnitude compared to other fluorescence microscopy techniques such as wide-field, confocal and even, to a certain extent, multiphoton fluorescence microscopy. During the last ten years, LSFM has emerged as a preferred tool to capture all cells during embryogenesis of the zebrafish *Danio rerio*, the fruit fly *Drosophila melanogaster* or recently the red flour beetle *Tribolium castaneum* for a period of several days. The motivation of this work was gain new insights in developmental related processes of plant organs. The aim of this work was to establish a protocol for imaging plant growth over a long period of time using LSFM and perform comprehensive analyses at the cellular level. The Thale Cress *Arabidopsis thaliana* was used as a model organism in most of the experiments. In addition, recordings of rice *Oryza sativa* showed that other plants can be monitored as well.

Plants have to cope with a variety of environmental conditions, like light, temperature, nutrients, water, gravity, mechanical stimuli, or bacteria and fungi. They quickly adopt to environmental changes, which is a major technical challenge for long term observations. In order to keep the physiology of the plant in good conditions, the environmental

conditions inside the microscope chamber had to be brought under control. The microscope setup is characterized by a horizontal arrangement of the objective lenses and allows to grow the plant in its natural, upright position. While the leaves remain in the air, the root system is perfused with a liquid medium. An illumination system kept the plant in a photosynthetic active state and mimicked the natural day / night cycle. To prevent light from reaching the root system, the root system was covered. Thus, only the leaves were exposed to light. The sample preparation methods and the standardized conditions at a physiological level allowed to study gravity response, day-night rhythms, organ shape development as well as the intracellular dynamic events of the cytoskeleton and endosomal compartments in an unprecedented manner. Several of these projects were successfully published in collaborations with Prof. Jozef Šamaj (Palacký University Olomouc, Czech Republic), Prof. Niko Geldner (University of Lausanne, Switzerland), Prof. Malcom Bennett (University of Nottingham, UK) and Dr. Jürgen Kleine-Vehn (University of Natural Resources and Life Sciences, Austria). The main part of my work focused on the formation of lateral roots in *Arabidopsis thaliana* and was conducted in close collaboration with Dr. Alexis Maizel (University of Heidelberg, Germany). Previously, most experiments that describe lateral root formation have been performed on a small number of cells and for short periods of time. Capturing the complete process of lateral roots is an ambitious goal, because first, the primordium of a lateral root is located deep inside the primary root and imaging quality is impaired due to scattering of the overlaying tissue. Second, the process takes about 48 h, i.e. the plant has to be kept healthy for the whole period. Third, the amount of excitation light required for the spatio-temporal might have phototoxic effects that lead to a stop of growth at least in conventional microscopic techniques. In Arabidopsis embryogenesis, the sequence of cell divisions is relatively invariant. However, whether lateral root organogenesis follows particular cell division patterns has been unknown. The complete process of lateral root formation was captured from the first cell division until after the emergence from the main root. Images of a nuclei marker and a plasmamembrane marker were recorded every 5 min for a time period of up to 64 h. To stimulate lateral root formation, the seven days old plants were gravity-stimulated for 6-9 h by positioning them at a 90° angle. In order to locate the region of interest, the plant has an additional nuclear marker which is expressed in lateral root founder cells prior to their first division. This allowed to capture the complete process of lateral root formation in five specimens. The positions and cell divisions of all cells were tracked manually. In collaboration with Alexander Schmitz (Goethe University Frankfurt am Main, Germany) and Jens Fangerau (University of

Heidelberg, Germany), comprehensive analyses of the data were performed. A lateral root forms from initially 8-15 founder cells, arranged in a patch of 5-8 parallel files. For a direct comparison, the data sets were synchronized based on their number of cells. The overall shape and growth curves were consistent across the five data sets. In addition, the occurrence of new cell layers by periclinal divisions, as well as the sequence of layer generation was conserved and resembles the sequence suggested by Malamy and Benfey in 1997. Besides this stereotyped occurrence of periclinal divisions, radial divisions were found to appear stochastically, following no particular pattern. A large variability was also found in the contribution of founder cells and cell files to the final lateral root. The topology of the founder cells did not indicate which cell would contribute most to the primordium and become the future tip of the lateral root. The future center was also not prefigured by the spatial configuration of endodermis cells, which are known to be involved in initiation and development of the primordium. In all data sets, the central cell file that contributed most of the cells also forms the tip of the primordium. During emergence from the primary root, cells at the base of the primordium expanded and the tip of the primordium was displaced out of the primary root. Thus, flanking cell files contributed more and more to the volume while the central cell file left a thin cell file behind. The first four rounds of cell divisions were classified into asymmetric and symmetric divisions based on the cell geometry in respect to the mother cell. In the second cell cycle, 50 % of the cell divisions were asymmetric. In contrast, the third and fourth cell cycle showed 20 % asymmetric cell divisions only. Disrupting the orientation of asymmetric divisions using the aurora double mutant *aur1-2 aur2-2* showed an impaired morphology of the primordium which was rather influenced by mechanical properties of the surrounding tissue and the process of emergence was affected and delayed. Nevertheless, despite the initial uncontrolled direction of cell divisions, at later stages, more cell divisions appear normal and the matured lateral root showed a more or less regular development. In summary, the results suggest that a stereotyped pattern of cell divisions at particular developmental stages and a dynamically adapted control of cell divisions exist in parallel. Both properties allow a controlled but flexible development of the organ according to variations in cell topology and mechanical properties of the surrounding tissue. This work shows that LSFM, the sample preparation methods and controlled environmental conditions allow to capture and analyse the development of plants over several days at high resolution in an unprecedented manner.

1 Introduction

1.1 Plant root system architecture and plasticity

Plant root systems show complex spatial configurations among species (Fig 1.1). To secure a continuous water and nutrient uptake as well as a proper anchoring of the plant in the soil the topology of the root system is of crucial importance. In both monocots and dicots, an embryo-derived primary root first explores the soil. In monocots, several adventitious roots emerge from the basis of the stem (homorhizic root system). In dicots, the primary root grows downwards parallel to the vector of gravity and generates continuously lateral roots that grow sideways (plagiogravitropism). Lateral roots of higher order show no response to gravity, they grow agravitrop. The root perceives gravity in specialized cells in the root cap designated as stathocytes (Morita, 2010). The stathocytes contain statholits, starch-filled amyloplastic organelles, which follow the gravity within the cell and thereby indicate the orientation of the cell (Volkmann and Sievers, 1979). An asymmetrically distribution of auxin (Friml et al., 2002; Mullen et al., 2005; Rosquete et al., 2013) and cytokinin (Aloni et al., 2004) controls cell elongation and thereby the growth direction of a root.

Although the basic morphology of root systems is controlled by genetic factors, the root architecture is highly plastic and influenced by the availability of light, water and nutrients (Forde and Lorenzo, 2001; López-Bucio et al., 2003; Hodge, 2004; Malamy, 2005; Osmont et al., 2007; Gruber et al., 2013) as well as the presence of symbiotic or pathogenic microorganisms such as fungi and bacteria (Curl et al., 1986; Wang and Qiu, 2006; Hodge et al., 2009). Thus, even the morphology of the root system within a species shows a large variety reflecting local adaptations to biotic and abiotic factors (Fig 1.2).
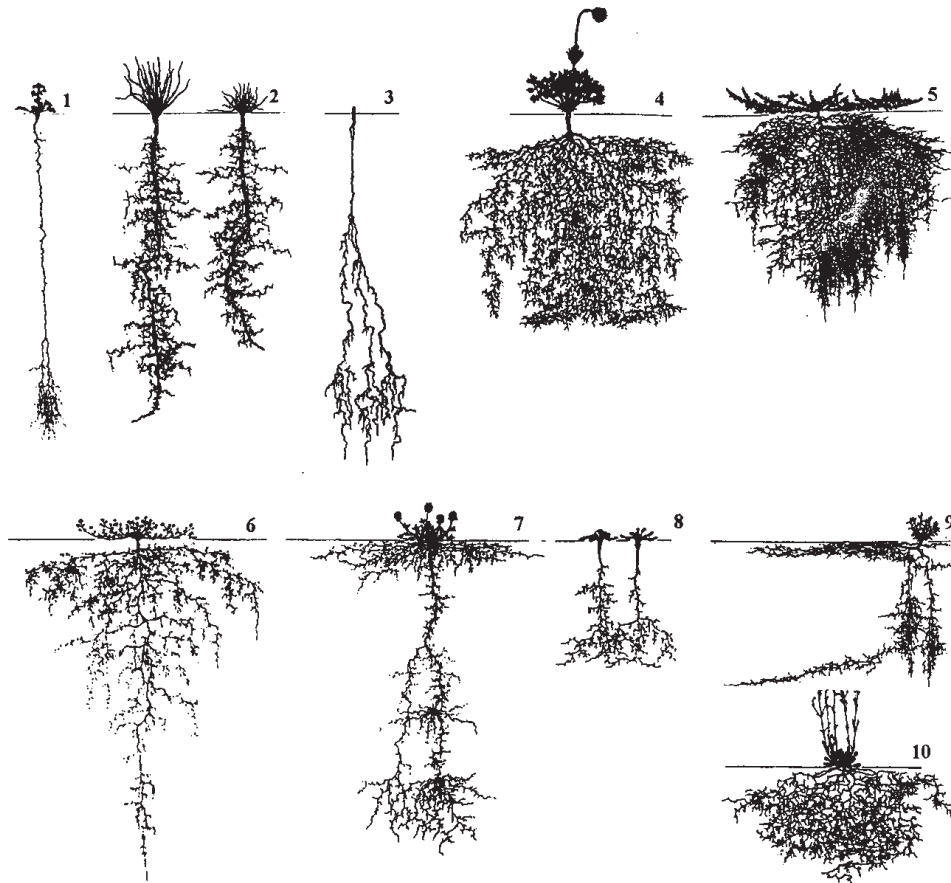
Figure 1.1: Diversity of root system architecture Diverse European dicotyledonous plants exemplifying the variation of root system architecture. 1, *Eryngium campestre*; 2, *Scorzonera villosa*; 3, *Chondrilla juncea*; 4, *Pulsatilla pratensis*; 5, *Genista germanica*; 6, *Trigonella balansae*; 7, *Trifolium trichocephalum*; 8, *Carum caucasicum*; 9, *Onosma arenarium*; 10, *Silene otites*. Figure from Kutschera and Lichtenegger (1992).
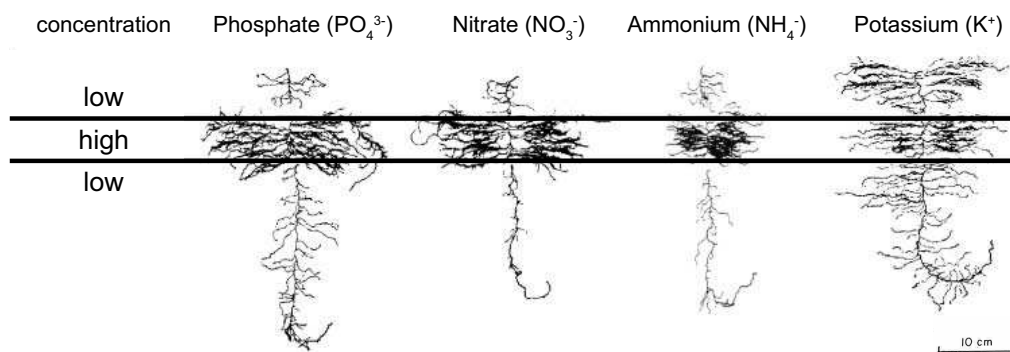
Figure 1.2: Variation of the root system of barley (Hordeum vulgare). Roots grown in solution culture with the middle root section exposed to a 100-fold higher concentration of phosphate, nitrate, ammonium or potassium ions compared to roots above or below (LHL). Controls were supplied with high concentration of nutrients in all zones (HHH). Abbreviations: H, high; L, low, referring to nutrient concentrations experienced by the top, middle and bottom sections of the root system. Figure modified from Drew (1975).

1.2 Arabidopsis root growth

Arabidopsis thaliana as model organism is widely used to study root growth using light microscopy, because of the transparency and the availability of transgenic lines. Prior to the seed germination the Arabidopsis embryo has already a root and leaves, called cotyledons. Once germinated, all organs that shape the plant derive post-embryonically from meristems which are located at the apical sides of the root and the shoot. In the center of the root apical meristem (RAM) a quiescent zone with a low cell division rate generates new cells arranged in cell files. These cells can divide several times anticlinal and thereby increase the number of cells within each cell file. Behind the meristematic zone, cells elongate and differentiate into concentric layers of tissue, i.e. the vasculature strand in the center of the root (comprised of phloem, xylem and procambium) is surrounded by one layer of pericycle-, cortex-, endodermis- and epidermis-cells (Dolan et al., 1993). Epidermis cells further differentiate into trichoblasts, cells that build root hairs, and atrichoblasts, cells that lack root hairs. The cell elongation pushes the root tip further into the soil (Fig 1.3), and the calyptra (root cap) protects the quiescent center against mechanical forces that arise. The root cap is furthermore involved in perceiving gravity (Morita, 2010).

Figure 1.3: Arabidopsis root tip growth. (A) Meristematic zone: Cells initially derive from the quiescent center (white triangle), but proliferate in the entire tip of the root. Elongation zone: Behind the root tip, cells elongate and begin to differentiate. Differentiation zone: Cells further differentiate into specific types of tissue, e.g. epidermis cells differentiate into trichoblast or atrichoblasts. Pericycle cells get primed for lateral root initiation already in the meristematic zone. (B) Time lapse recording of a primary root tip. Scale bar A and B: $100\,\mu m$. **Supplemental Movie-1.3**.

1.2.1 Auxin

Plant growth is regulated by several classes of phytohormones like auxins, abscisic acid, brassinosteroids, cytokinines, ethylene, gibberellines, jasmonates and strigolactones (Kamiya, 2010). Auxin (indol-3-acidic-acid - IAA) is one of the most prominent phytohormone because it is involved in many developmental processes like organogenesis, meristem patterning, cell elongation and all kinds of tropism (Friml, 2003; Benjamins and Scheres, 2008; Vanneste and Friml, 2009). A heterogeneous distribution of auxin in tissues and local accumulation of auxin in cells is responsible for differentiation and growth (Vieten et al., 2007). Local gradients of auxin originate from polar cell to cell transport mediated by a number of special auxin transporter including the efflux carriers (PIN-family) and influx carriers (AUX/LAX-family) (Friml, 2003; Zažímalová et al., 2010). There are eight PIN proteins characterized that are differently expressed in types of tissues and localized at the plasmamembrane (PIN1-4 and 7) and at the ER (PIN5,6 and 8) (Křeček et al., 2009; Zažímalová et al., 2010) creating an unique flux of auxin throughout the plant that controls development and growth (Teale et al., 2006). For the sake of keeping an overview the introduction of auxin signaling concentrates mostly on cellular growth processes.

Many of the auxin mediated growth processes rely on anisotropic cell elongation. There are two major effects of auxin, a rapid cytoplasmic response, and a long term response that activates gene expression. The rapid response is mediated by the auxin receptor ABP1 which is localized at the plasmamembrane and extracellular matrix (Sauer and Kleine-Vehn, 2011). ABP1 activates different responses that are not entirely understood on the molecular level. The activation of ATP-dependent proton pumps increase the H^+-ions concentration in the cell wall. This acidification activates expansins which causes a loosening of the cellulose fibrils (Cosgrove, 2000). In addition, the hyperpolarization of the plasmamembrane causes an influx of K^+- and Cl^--ions which results in an increased water uptake into the vacuole (Yamagami et al., 2004). The loose cell wall and the increased turgor lead to cell elongation. Furthermore, the cytoskeleton and clathrin-mediated endocytosis is modulated via the activation of ROPs (Robert et al., 2010; Xu et al., 2010). Xu et al. (2014) recently showed that this activation requires an auxin-dependent complex of a transmembrane kinase (TMK) and ABP1.

The second effect of auxin includes the expression of many genes (Abel and Theologis, 1996), e.g. genes encoding for cell wall material that allow to restore the cell wall stability and growth. Auxin binds TIR1 or the TIR1-related AFB proteins which are a subunit of the SCF complex localized in the nucleus (Kepinski and Leyser, 2005;

Dharmasiri et al., 2005a,b). In presence of auxin, this receptor-protein complex binds to the repressor protein AUX/IAA which in turn gets ubiquitinated and degrated by the proteasom (Zenser et al., 2001). As a consequence, the inhibition of the transcription factor ARF is reversed and auxin related genes are expressed. In Arabidopsis, there are six TIR1/AFB proteins, 29 genes coding for AUX/IAA repressors and 23 genes coding for ARF-transcription factors and the different combinations might operate specifically in types of tissues and developmental stages (Guilfoyle and Hagen, 2007; Calderón Villalobos et al., 2012; Wang and Estelle, 2014). Furthermore, ABP1 seems to modulate this signaling pathway but the molecular mechanism behind this is unkown (Tromas et al., 2013; Paque et al., 2014).

1.2.2 Root hair tip growth

Root hairs are tip-growing cells whose growth mechanism has many similarities to the tip-growth in other organisms such as fungal hyphae, algea rhizoids or plant pollen tubes (Yang, 1998; Palanivelu and Preuss, 2000; Schnepf, 2003; Rounds and Bezanilla, 2013). Root hairs show one of the fastest growth rates in plants and therefore they are good model for studying the principle regularities of cell growth. Root hairs are long tubular extensions of epidermis cells (trichoblasts) that are involved in the uptake of water and nutrients. The formation of root hairs starts with an acidification of the cell wall. Expansins are mainly involved in a pH-dependent cell wall loosening (Baluska et al., 2000; Cosgrove, 2000). During this initial phase an intense reorganization of the cytoskeleton can be observed (Baluska et al., 2000). In Arabidopsis, root hairs grow at a rate of $0.6 \text{-} 2.4 \, \mu m/min$ (Galway et al., 1997; Wymer et al., 1997). This rapid growth requires a continuous supply of plasmamembrane and cell wall material (Miller et al., 1997). The growing tip is rich of cytoplasm, full of Golgi vesicles but free of major organelles such as mitochondria, Golgi apparatus, or vacuole (Ryan et al., 2001; Carol and Dolan, 2002). The cellular organization of a typical tip-growing cell is shown in figure 1.4. During steady state growth, a Ca^{2+}-gradient towards the tip is essential for root hair growth (Bibikova et al., 1997; Wymer et al., 1997; Hepler, 2005). Variations in the Ca^{2+} concentration in the tip correlate with changes in the growth rates (Monshausen et al., 2008). It is thought that the Ca^{2+} affects growth through a modulation of the cytoskeleton and vesicular transport (Carol and Dolan, 2002; Monshausen et al., 2008). The small RabA-GTPases accumulate in the tip of growing root hairs and at the margin regions of the growing cell plate during cytokinesis (Asaoka et al., 2013). It has been shown that the RabA1d-GTPase is associated

with structures of the trans-Golgi network (Ovečka et al., 2010), and it is very likely that these endosomes are involved in the growth process. But a correlation between the growth rate and the presence of these endosomes in the tip has not been described so far.
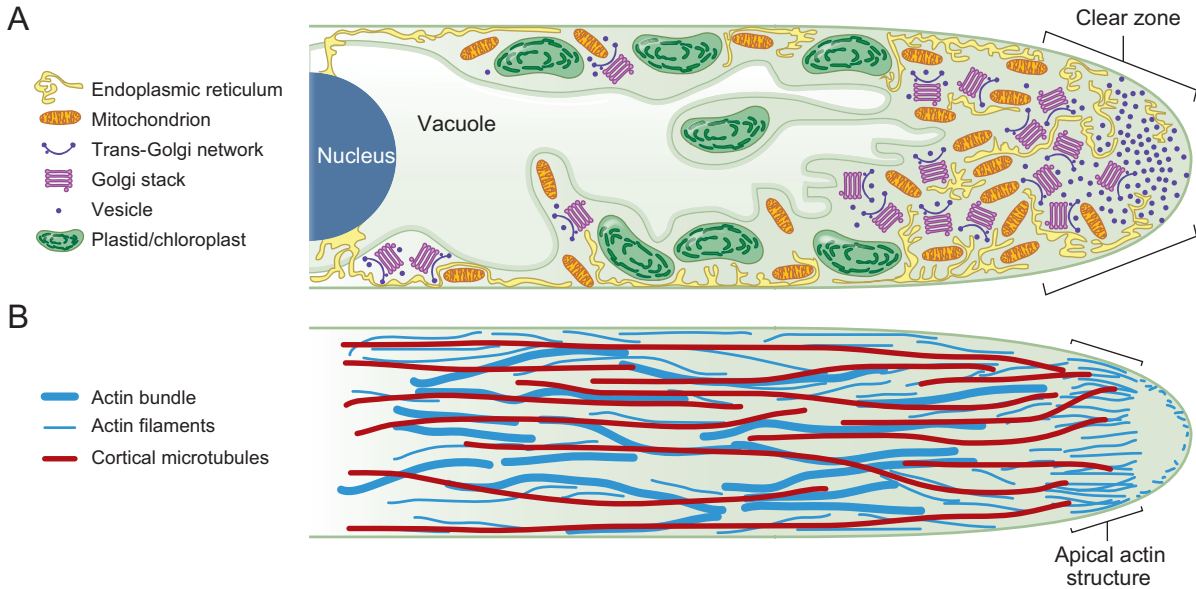

Figure 1.4: Cellular organization of typical tip-growing cells. (A) The organelle organization, with the clear zone at the apex (including Golgi stacks, vesicles, and endoplasmic reticulum) and sub-apical the vacuole and nucleus. Larger organelles, including plastids, are excluded from the clear zone but are otherwise distributed throughout the cell. (B) An idealized tip-growing cell, showing cortical microtubules as linear red structures. Actin bundles (thick blue lines) also appear as longitudinal structures. Actin filaments (thin blue lines) are distributed both cortical and throughout the cytosol, but most prominently appear as the apical actin structure, shown here as an actin fringe but appearing as a mesh or just a bright patch depending on the cell type. Figure from Rounds and Bezanilla (2013).

1.2.3 Lateral root development

The architecture of the root system depends mainly on the formation of lateral roots that emerge continuously from the primary root (Fig. 1.5). Cells in the primary root tip get primed regularly in order to form a lateral root primordium in response to peaks of auxin (Smet et al., 2007; De Rybel et al., 2010) and oscillating gene expression (Moreno-Risueno et al., 2010; Norman et al., 2014). In addition, environmental conditions as well as the curvature of the main root influences the initiation of lateral root formation (Laskowski, 2013). The curvature of the primary root results in differences in the auxin distribution on the outside as opposed inside the curve (Laskowski et al., 2008; Ditengou et al., 2008).
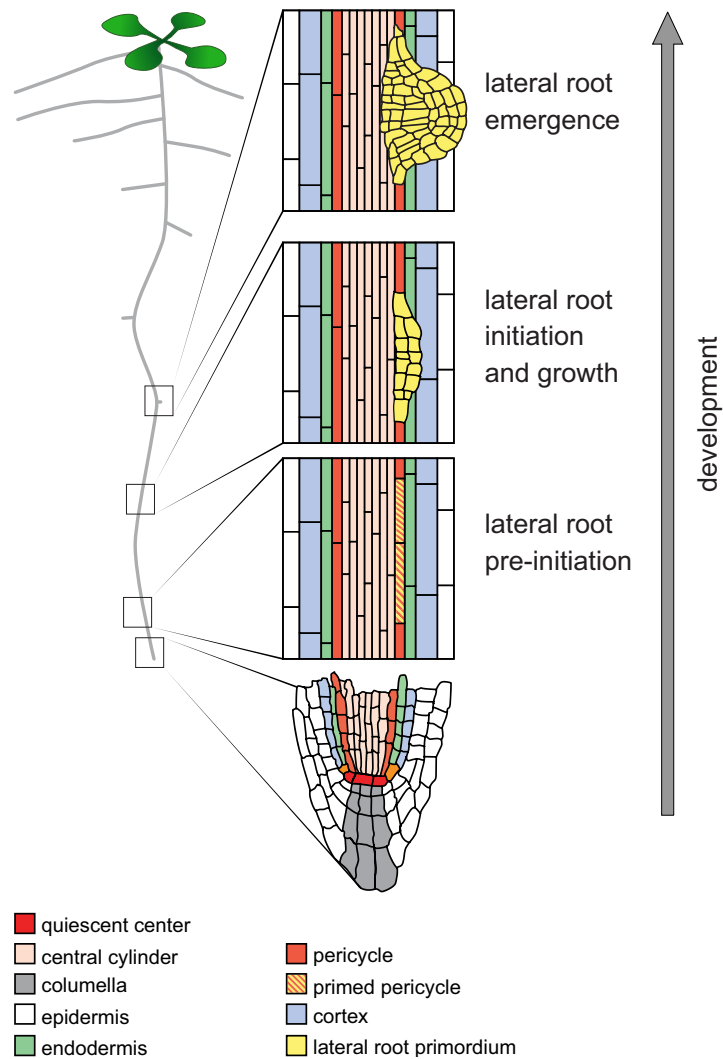
Figure 1.5: Lateral root development in Arabidopsis. Spatio-temporal organization of Arabidopsis lateral root formation. Pre-initiation occurs in the basal meristem. As the primary root grows, the primed pericycle divides transversal to form a unicellular primordium (initiation) that will further divide, creating a multilayered dome-shaped primordium (growth) which will emerge from the parental root (emergence). Figure modified from Dastidar et al. (2012).

This local increase in auxin can induce the formation of lateral roots on the outside of the curve (Casimiro et al., 2001; Dubrovsky et al., 2008). Auxin is involved in all stages of lateral root development, priming of founder cells (Smet et al., 2007), initiation (Dubrovsky et al., 2008), primordium growth and emergence (Benková et al., 2003; Swarup et al., 2008). Several molecular components of the auxin signaling pathways are identified but the detailed molecular mechanisms are not yet understood (Lavenus et al., 2013). The first cell division during lateral root formation occurs in the pericycle cells adjacent to the protoxylem (XPP, xylem pole pericycle cells) (Casimiro et al., 2003; Péret et al., 2009). XPPs divide continuously to form a lateral root primordium by

consecutive symmetric and asymmetric cell divisions (Smet et al., 2007; Parizot et al., 2008). A staging of lateral root development into seven stages according to the number of cell layers within the primordium was introduced by Malamy and Benfey (1997) (Fig. 1.6). Tissue specific expression markers allowed to assess the identity of cell types describing the lineage of each cell type. However, these results were performed in two-dimensional images of fixed and cleared samples and the exact sequence of divisions in the three dimensional context cannot be identified. In Arabidopsis embryogenesis the sequence of cell division patterns are relatively invariant (Scheres et al., 1994; Yoshida et al., 2014). Whether lateral root organogenesis follows particular cell division patterns is unknown.

During lateral root formation the primordium has to pass three overlaying cell layers (endodermis, cortex and epidermis). The endodermis is a water-tight epithelium that defines the inner vasculature from the outer tissues that are in contact with the soil. Signaling between pericycle and endodermis is required for lateral root initiation (Duan et al., 2013; Marhavý et al., 2013). For example, when auxin-signaling is blocked specifically in the endodermis, no first cell division in pericycle cells occurs (Vermeer et al., 2014). Vermeer et al. (2014) also showed that while the primordium grows the endodermis is actively thinning, creating a hole that allows the lateral root to emerge. In contrast to the thinning of endodermis cells, the cortex and epidermis cells maintain their volume throughout the emerging process. These cells facilitate lateral root emergence by loosening the connection between their well-attached cells. Auxin, coming from the lateral root primordium, is transported outside of the primordium via the PIN3 efflux carrier. Upon that, surrounding cells express LAX (like-AUX), an auxin influx carrier, which leads to an accumulation of auxin in cells directly overlaying the primordium (Swarup et al., 2008; Péret et al., 2013). In these cells, cell wall remodeling enzymes like expansins, pectate lyase, subtilisin-like protease, polygalacturonase, glycosyl hydrolase, or cutinase get expressed (Neuteboom et al., 1999; Swarup et al., 2008; Takahashi et al., 2010; Kumpf et al., 2013; Lee and Kim, 2013), apparently through IDA-HAE/HSL2 signaling (Kumpf et al., 2013). Péret et al. (2012) showed that auxin-dependent expression of aquaporins (water channels) controls the water transport during the formation process. Local differences in the expression can modify turgor pressure in the primordium compared to surrounding cells to influence growth and emergence. When auxin signaling is downregulated specifically in overlaying tissue, the primordium cannot emerge and the morphology of the primordium has a rather "flat"- than a typical "dome" shape (Lucas et al., 2013). Lucas et al. (2013) further showed that the shape of the

primordium is affected in the *aur1-2 aur2-2* double mutant, which has a defect in cell plate positioning in asymmetric cell divisions.

Taken together, a precise pattern of cell division as well as mechanical properties of the surrounding tissues play crucial roles during lateral root morphogenesis. In future, the study of gene expression and protein interaction must include the observation of mechanical interactions of the involved cells in order to understand the spatio-temporal organization of lateral root formation. Live imaging technologies are required that allow to monitor the development of the three dimensional organ at subcellular resolution with a high enough temporal resolution. At the same time the physiology of the plant must be preserved.
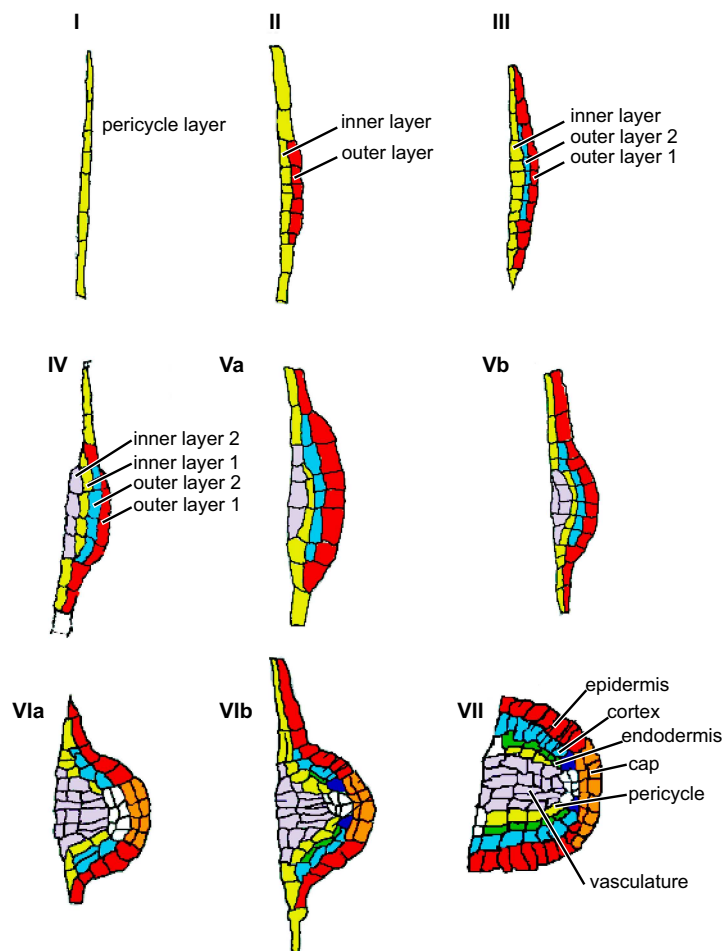

Figure 1.6: Model of lateral root development in Arabidopsis. Color coding shows the putative derivation of each tissue from Stage I through Stage VII, based on the information from the histological studies and marker lines. Note that by Stage VIb all the radial pattern elements of the primary root are present in the lateral root primordium. Figure from Malamy and Benfey (1997).

1.2.4 Cellular basis of plant morphogenesis

Pattern formation in plants involves the generation of specific cell types in a well-defined spatial context. In the absence of cell migration, due to cell walls, the shape of new organs relies on oriented cell divisions and polarized cell growth (De Smet and Beeckman, 2011).

Oriented cell division

The orientation of a cell division is established prior to mitosis via a cortical arrangement of the cytoskeleton called preprophase band (PPB, Fig. 1.7 B). Once the chromosomes are separated (metaphase), the cytokinesis is accomplished via the phragmoplast. The phragmoplast consists of cytoskeleton, membrane and vesicles that deliver new material to the growing cell plate. The cell plate grows from the center to the cortical regions predestined by the preprophase band. The orientation of a cell division can be described by their position relative to the organ surface. Anticlinal divisions build a cell plate perpendicular to the organ surface. In periucline divisions the cell plate is parallel to the organ surface. Radial divisions are anticlinal but longitudinal to the growth direction of the primary root (Fig. 1.8).

The majority of cells in a growing organ divide symmetric in which the plane of division in most cases follows the smallest area rule of the new cell wall (Errera, 1888; Besson and Dumais, 2011). In contrast, asymmetric cell divisions follow other rules to position the plane of divisions and the daughter cells can differ in size and function. Asymmetric cell divisions play important roles in plant development such as meristem maintenance, stomata development, embryogenesis or organogenesis (Petricka et al., 2009; De Smet and Beeckman, 2011). Cell polarity is required to recruit and orient the preprophase band (PPB) and the spindel apparatus. Actin is involved in the PPB formation as well as the migration of the nucleus to the future plane of division (Rasmussen et al., 2011). In Arabidopsis, the two α-Aurora kinases for example are required for a correct division plane orientation in asymmetric cell divisions and the double mutant *aur1-2 aur2-2* shows chaotic cell plate formations (Van Damme et al., 2011). Studying the orientation of cell divisions during the morphogenesis of a lateral root could shed light on the links between the individual cell fates in the context of the three dimensional tissue during differentiation associated events.
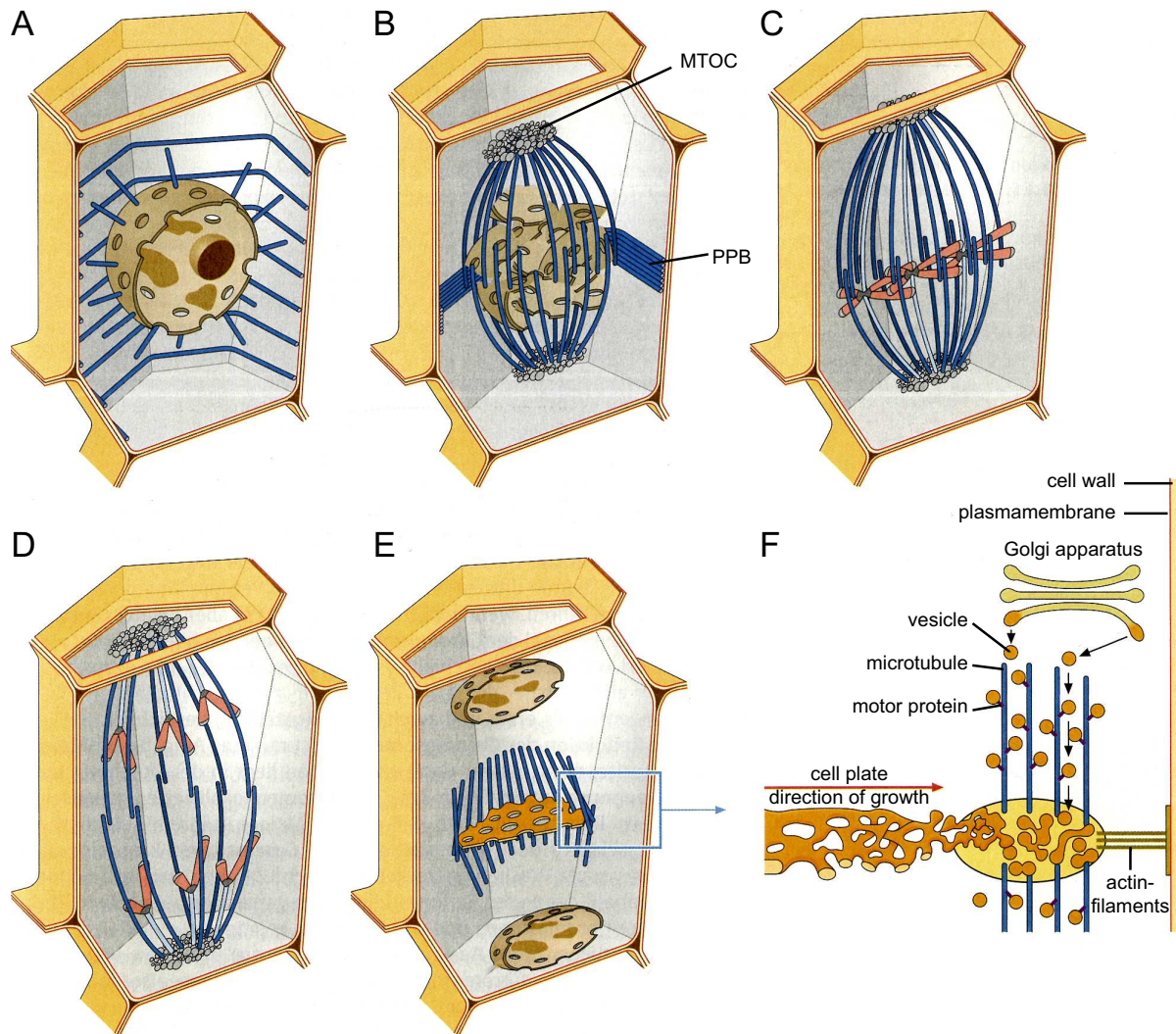
Figure 1.7: Organization of the microtubules during mitosis. (A) Interphase with nucleus. (B) Prophase, development of the preprophase band (PPB) and the microtubule-organizing center (MTOC). The nuclear envelope disintegrates. (C) Metaphase, complete spindle apparatus, chromosomes condense at the metaphase plate. (D) Anaphase, separation of the chromosomes. (E) Telophase, the phragmoplast forms and builts up the cell plate, nuclear envelope reassembles. Figure modified from Weiler and Nover (2008).

Figure 1.8: Orientation of anticlinal-, periclinal-, and radial- cell divisions. The nomenclature dependent on the orientation of the cell plate relative to the organ surface. Anticlinal divisions are perpendicular to the surface. Periclinal divisions are parallel to the organ surface. Radial divisions are anticlinal but longitudinal to the growth direction of the primary root.

Polarized cell growth

The shape of a plant cell is given by the cell wall and the internal turgor pressure that pushes against it. Cell growth can occur by controlling the plastici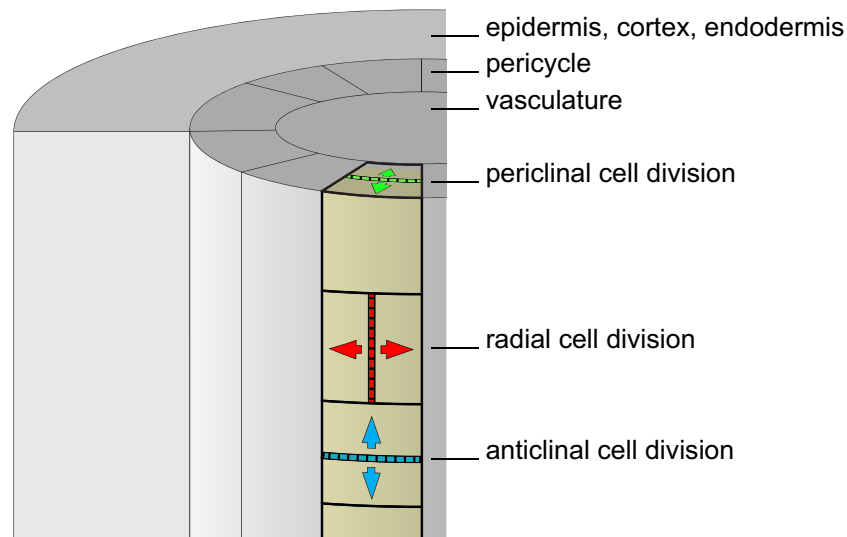ty of the rigid cell wall matrix by remodeling enzymes such as expansins, glycosyl hydrolase or pectate lyase. These enzymes lead to a loosening of the cell wall which allows the turgor to expand the cell (Cosgrove, 2005; Zonia and Munnik, 2007; Geitmann and Ortega, 2009). In order to direct cell expansion into a preferred direction (anisotropic growth) the rigid cellulose fibrils are oriented in a barrel like parallel arrangement. This restricts the growth in width but maintains a flexibility to grow in length (Baskin, 2005). Cellulose fibrils are synthesized by the membrane bound cellulose-synthase which is guided by cortical microtubules (Paredez et al., 2006). Thus, the orientation of cortical microtubules can indicate in which direction the cell tends to grow. Several studies showed that the orientation of microtubules is parallel to the main stress in the tissue, which helps to withstand the strains (Hamant et al., 2008; Corson et al., 2009; Uyttewaal et al., 2010). In conclusion, single cells can control their growth by remodeling the cell wall and by realigning their cellulose fibrils. In order to understand morphogenesis on a molecular level the regulation of genes and proteins must be seen in the context of the three dimensional tissue. Imaging methods are required to study the structure and dynamics at subcellular resolution over periods of time while the tissue develops.

1.3 Live imaging of plants

Live imaging microscopy is a common tool to study Arabidopsis development dynamics (Sappl and Heisler, 2013; Shaw and Ehrhardt, 2013; Sozzani et al., 2014). However, many developmental processes in plants require an observation time period of hours to days, such as lateral root formation (Malamy and Benfey, 1997) or organ regeneration (Sena et al., 2009). Live imaging is a trade-off between acquiring images with a high spatio-temporal resolution and preserving the physiological conditions of the specimen. High resolution and short recording intervals induce phototoxic effects and can finally lead to a stop of growth. Up to now, fluorescence microscopy experiments have been limited to relatively short observation periods. Most of the approaches, that can be found in literature, use confocal fluorescence microscopy and immobilize the plant between a cover slip and a block of agar (Laskowski et al., 2008; De Rybel et al., 2010) or put it back into the growth chamber between successive image acquisitions (Reddy et al., 2004; Heisler et al., 2005; Hamant et al., 2008; Heisler et al., 2010). In most cases the sample is positioned horizontal which induces a lot of changes since its growth is influenced by gravity (Swarup et al., 2005).

There are several microscopic techniques available that allow for three dimensional reconstruction. In wide field microscopy different post-processing deconvolution algorithms reassemble the sharp image of the focal plane. In confocal laser scanning microscopy (CLSM) a pinhole is used to block out of focus light such that only photons emitted from the focal plane reach the photo detector. But only a single point can be detected and scanning the region of interest point by point takes time. In spinning disc confocal microscopy hundreds of pinholes rotate in the optical path which allows the recording of the complete region of interest simultaneously. This enables the use of cameras and results in a very fast acquisition speed ($>25\,fps$). All mentioned techniques have in common that for the acquisition of each single plane the entire specimen is exposed to the excitation light. This energy change the conformation of molecules, which can have signaling or toxic effects. In summary, for long term investigations physiological conditions are required to ensure the specimen in an appropriate state and to avoid observing artifacts. At the same time it is crucial to reduce the energy for the imaging acquisition process to avoid photo-toxic effects.

1.3.1 Light Sheet-based Fluorescence Microscopy

Light Sheet-based Fluorescence Microscopy (LSFM) is one of the most valuable tools
in developmental biology (Huisken et al., 2004; Keller and Stelzer, 2008; Keller et al.,
2010; Höckendorf et al., 2012; Strobl and Stelzer, 2014). In contrast to a conventional
fluorescence microscope LSFM uses independent light paths for illumination and detec-
tion. The excitation lenses are arranged perpendicular relative to the detection lenses.
Either a laser scanning process or a cylindrical lens create a thin planar sheet of light
overlapping with the focal plane of the detection lens. This allows the use of modern
cameras that can record dozens of images per second. Optical sectioning as well as no
photo-bleaching and no photo-toxicity outside the detection focus are main advantages of
LSFM. Thereby, the required energy is reduced dramatically compared to conventional
fluorescence microscopy.
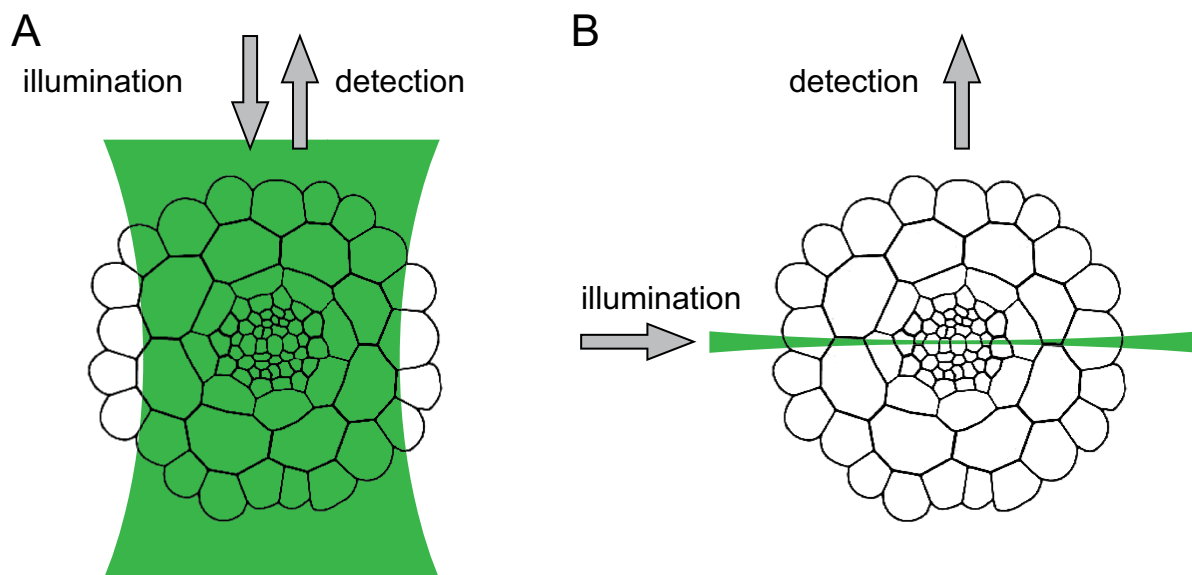
**Figure 1.9: Conventional microscopy versus Light Sheet-based Fluorescence Microscopy
(LSFM).** (A) In conventional microscopes the illumination and detection follows the same direction.
The entire sample is illuminated (B) In LSFM, the illumination and detection light paths are separated
and arranged in a perpendicular arrangement. Fluorophores are excited in a thin selective plane which
overlaps with the focal plane of the detection path. Optical sectioning and a low phototoxicity are main
advantages.

LSFM is particularly well suited for the imaging of plants over long periods of time.
So far, several studies analyzed the root system by means of LSFM (Maizel et al., 2011;
Sena et al., 2011) and showed lateral root shape dynamics during the formation process
(Lucas et al., 2013; Vermeer et al., 2014), oscillating root hair growth (Berson et al.,

2014), the lateral root response to gravity at the cellular level (Rosquete et al., 2013) or calcium dynamics in root cells (Costa et al., 2013). In addition, two book chapters describe Arabidopsis imaging with LSFM (Šamajová et al., 2012; Wangenheim et al., 2014). The Light-sheet microscopy in all mentioned publications were performed in our lab, with exception of Sena et al. (2011) and Costa et al. (2013). Nevertheless, the application of LSFM in plant-related research has only just started.

Taken together, in LSFM the low photo toxicity, the special sample preparation method, and the close-to-natural conditions allow imaging of long term processes such as organogenesis. At the same time, subcellular localization of specific proteins or the dynamic of vesicular traffic can be observed with high spatio-temporal resolution in combination with a large field of view.

2 Material and Methods

2.1 Model organisms *Arabidopsis thaliana* and *Oryza sativa*

Two organisms were used for microscopic observations. The model organism *Arabidopsis thaliana* was used because of the sequenced genome, ease of handling and the availability of transgenic lines. The root of Arabidopsis is very well suited for microscopic studies because of its transparency. The used Arabidopsis plant lines are listed in Tab. 2.1.

Oryza sativa was used because rice is one of the most widely used basic food and therefore an important organism for research. The deepwater rice L. ssp. indica, cultivar Pin Gaew 56 (PG56), was obtained from Dr. Bianka Steffens working in the group of Prof. Dr. Margret Sauter (Christian-Albrechts-Universität zu Kiel, Germany).

Table 2.1: Transgenic plants obtained from indicated laboratories.

constructs	cellular localization	reference
35S::SSU-GFP	plastids	Kim and Apel (2004)
35S::GFP-MAP4	microtubules	Marc et al. (1998)
UBQ10::YFP-RabF2a	late endosomes	Geldner et al. (2009)
35S::GFP-LTI6b	plasmamembrane	Maizel et al. (2011)
35S::H2B-RFP	nucleus, histones	
35S::GFP-RabA1d	early endosomes	Ovečka et al. (2010)
GATA23::GUS-GFP-NLS	lateral root founder cells	Lucas et al. (2013)
UBQ10::H2B-RFP	nucleus, histones	
GATA23::GUS-GFP-NLS	lateral root founder cells	cloned in the laboratory of
UBQ10::H2B-RFP	nucleus, histones	Alexis Maizel, University of Heidelberg
UBQ10::YFP-PIP1;4	plasmamembrane	
UBQ10::H2B-RFP	nucleus, histones	cloned in the laboratory of
PIN1::PIN1-GFP	plasmamembrane	Alexis Maizel, University of Heidelberg
UBQ10::H2B-RFP	nucleus, histones	cloned in the laboratory of
PIN1::PIN1-GFP	plasmamembrane	Alexis Maizel, University of Heidelberg
in aur1/2 mutant		
pin3 pin4 pin7 triple mutant		Rosquete et al. (2013)
PIN1::PIN1-GFP	plasmamembrane	Van Damme et al. (2011)
PIN1::PIN1-GFP	plasmamembrane	Van Damme et al. (2011)
in aur1/2 mutant		

2.1.1 Arabidopsis culturing

Seed sterilization

Arabidopsis seeds were surface sterilized with $1\,ml$ of sterilization solution ($10\,\%$ Sodiumhypochloride (NaClO), $0.1\,\%$ TritonX-100, in aqua dest.) in a microtube for $10\,min$ (shaker). Then, rinsed five times with sterile water.

Arabidopsis culturing in petri dishes

Murashige and Skoog-Medium (MS-medium) is a plant growth medium which is widely used in laboratories (Murashige and Skoog, 1962). $2.3\,g$ MS-Medium, $0.97\,g$ MES (2-(N-morpholino)-ethanesulfonic acid buffer) and $10\,g$ saccharose were diluted in $1\,l$ aqua dest. The pH was adjusted to 5.8 with potassium hydroxide (KOH). $1.5\,\%$ Phytagel was added to a bottle, filled with the medium, autoclaved and then poured into petri dishes. Single seeds were sowed side by side on 1/2 MS plates with at least $1\,cm$ space in between (this facilitated handling for future sample preparations). Plates were cultured vertically (slightly tilted) for $5\,\text{-}\,7$ days under long day conditions ($16\,h$ light, $8\,h$ darkness period with $120\,\text{-}\,140\,\mu mol/m^2/s$ amount of light, at $22\,°C$).

Arabidopsis culturing in transparent pots for root system architecture observation

Special transparent culture tubes were used to study the effect of light on the root system. The chambers were covered from the outside by an aluminum foil. The surface of the gel around the plant was covered by small sheets of black plastic foil. The plant pots were filled with $24\,ml$ 1/2-MS medium containing $0.3\,\%$ Phytagel. Two days old plants were transferred to the pots and cultured for at least two week under long day conditions ($16\,h$ bright light, $8\,h$ darkness period with $120\,\text{-}\,140\,\mu mol/m^2/s$ amount of light, at $22\,°C$). Note: The plants encounter conditions similar to those in the microscope chamber (roots in liquid, diameter of the chamber).

2.2 Sample preparation for microscopy imaging

Three different sample holders were developed to image the root system of Arabidopsis. For all three sample holders capillaries ($3\,mm$ in diameter, $30\,mm$ in height) and carbon rods ($0.28\,mm$ in diameter, $30\,mm$ in height), were cleaned in an ultrasound unit with

2 % Hellmanex III for 10 min, rinsed with water several times and then autoclaved. The various preparation methods with their advantages and disadvantages are described in the following sections.

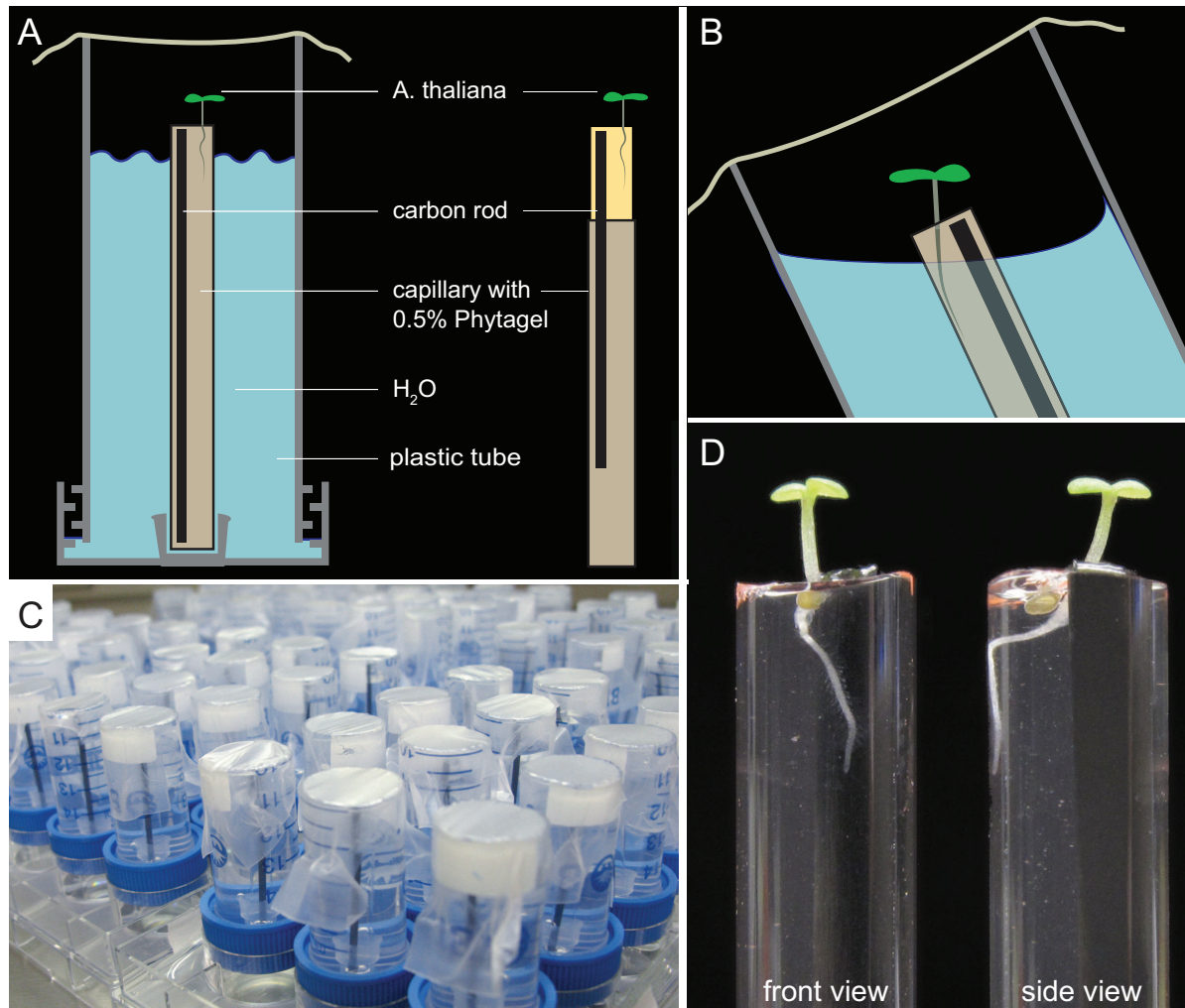## 2.2.1 Sample holder - root embedded in gel

Figure 2.1: Sample holder - Root embedded in gel. Seeds were sowed on capillaries filled with Phytagel (0.5 %, 1/2 MS-medium) and cultured in custom made chambers (15 ml Falcon tubes, A and C). The culturing chambers were tilted so that the root grew towards the glass (B and D). Before imaging the gel was extruded from the capillary rigified by an embedded carbon rod (A, right).

In this mounting technique Arabidopsis seeds were sowed directly on capillaries filled with a gel medium. This method is qualified for the observation of young seedlings or germinating seeds. The disadvantage is that Arabidopsis roots seem to grow very slowly into the capillary, maybe because of limited space inside the capillary. Furthermore,

imaging through a gel has an influence on the image quality due to light scattering. To overcome this the capillaries were tilted during the cultivation so that roots grew close to the surface of the gel.

In order to produce several medium filled capillaries at the same time, capillaries ($3\,mm$ in diameter, $30\,mm$ in height) were put into a tilted 96-well plate and equipped with a carbon rod ($0.28\,mm$ in diameter, $30\,mm$ in height). A serological pipette was used to fill the capillaries with 1/2 MS-medium containing $0.5\,\%$ Phytagel (Fig. 2.2). Once the gel solidified, the capillaries were put into chambers made of
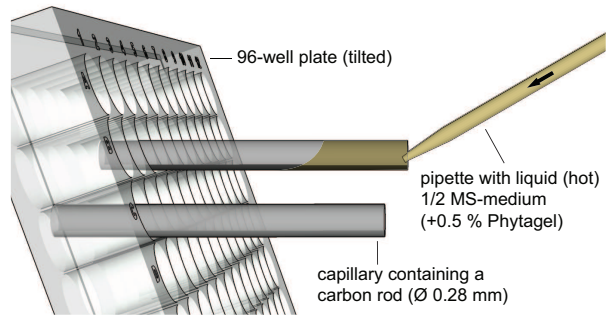

Figure 2.2: High-throughput capillary filling. Capillaries containing a carbon rod inside a tilted 96-well plate were filled with hot MS-medium containing $0.5\,\%$ Phytagel using a serological pipette.

$15\,ml$ Falcon tubes. Therefore, the tubes were cut at $4\,cm$ below the thread. $10\,mm$ of the thick end of a $200\,\mu l$ pipet tip was glued into the lid. To sustain humidity the chamber was filled with water and sealed with Parafilm.

2.2.2 Sample holder - root without gel

With this mounting technique the root can be observed outside any gel, without light scattering of the gel. The root maintains its natural mobility, which can be problematic for imaging older parts of the plant but is most suitable to image the root tip of young seedlings. Seeds were sowed on micro chambers made of the thin end of a $200\,\mu l$ micro pipette tip filled with 1/2 MS-medium containing $0.5\,\%$ Phytagel. The micro chambers were cultured in a petridish ($60\,mm$ in diameter) with an perforated steel plate inset (Fig. 2.3 A, C, E). Once the root grew through the gel it continuous growing in a liquid 1/2 MS-medium (Fig. 2.3 A). In the microscope chamber the sample holder was mounted with a steel ring holder (Fig. 2.3 B, D).
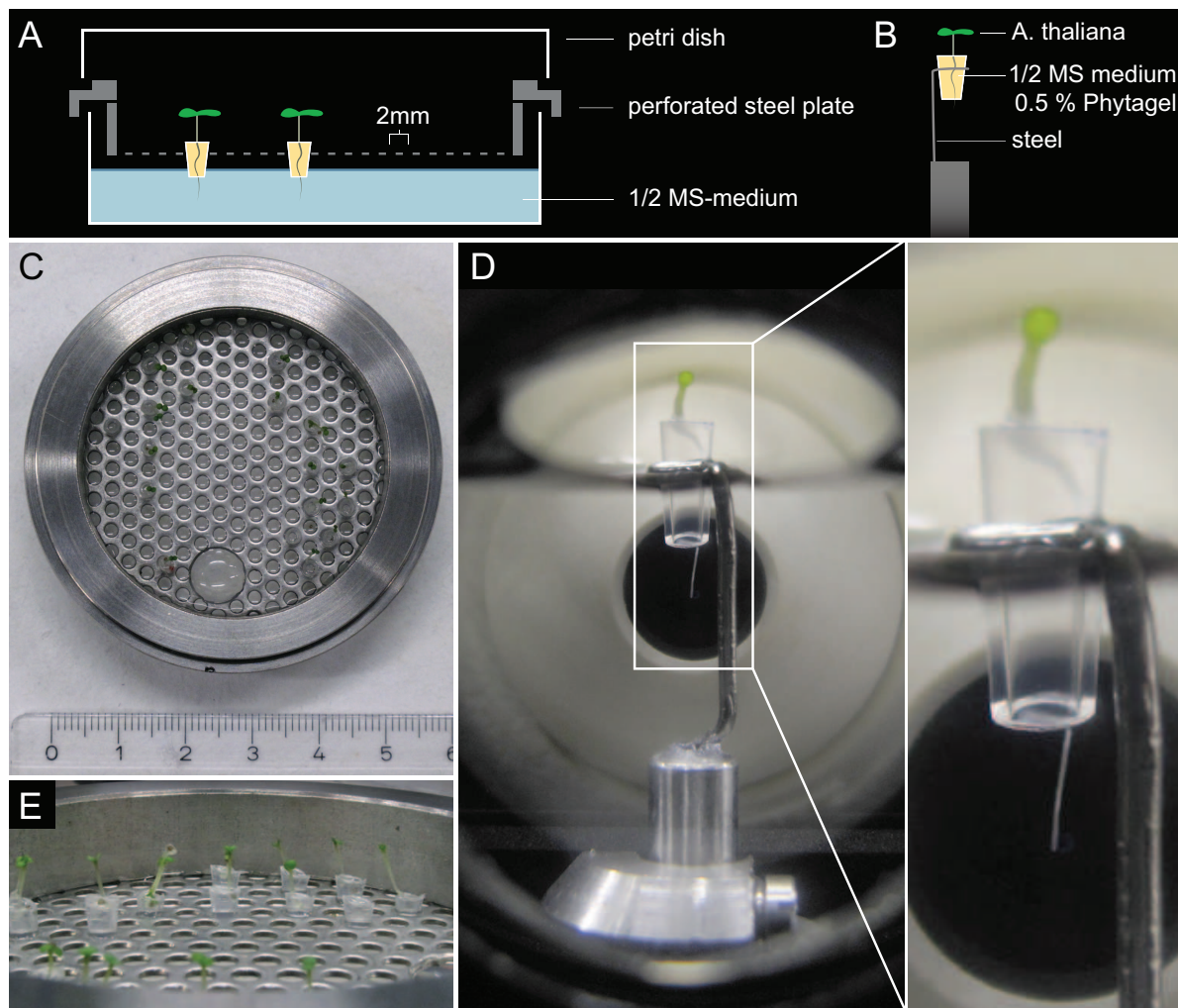
Figure 2.3: Sample holder - Root without gel. Seeds were sowed on custom-designed microchambers made of a cutted micropipette tip ($200\,\mu l$ pipette tip) filled with Phytagel ($0.5\,\%$, 1/2 MS-medium). (A) The microchambers were cultured in a petridish ($60\,mm$ in diameter) with a perforated steel plate inset. The petri dish was filled with liquid 1/2 MS-medium. A steel ring holder was used to mount the sample in the microscope chamber.

2.2.3 Sample holder - root on the surface of gel

This sample holder combines several advantages. First, the plant grows on the surface of a Phytagel, which is the common way for plant culturing in the laboratory. Second, the root can be imaged outside any gel and is mounted on the gel at the same time. Third, the plant can be extruded up to $20\,mm$ from the capillary. This allows the imaging of any desired part of the plant. For sample preparation, the capillary was pushed $1.5\,mm$ deep (half of the diameter) into the Phytagel at about $10\,mm$ below the root tip and then slided carefully over the root until the capillary reached the leaves and was then

lifted. The capillary was further pushed into Phytagel to fill the capillary. A carbon rod was inserted from the top, behind the plant. The capillary was pushed into Phytagel in order to extrude the plant up to the region of interest (0-$4\,mm$ above the edge of the capillary). A drop of $2\,\%$ agarose was placed above the region of interest in order to mount the root onto the Phytagel. The plants were kept in the custom made chambers described in Fig. 2.1 until imaging.
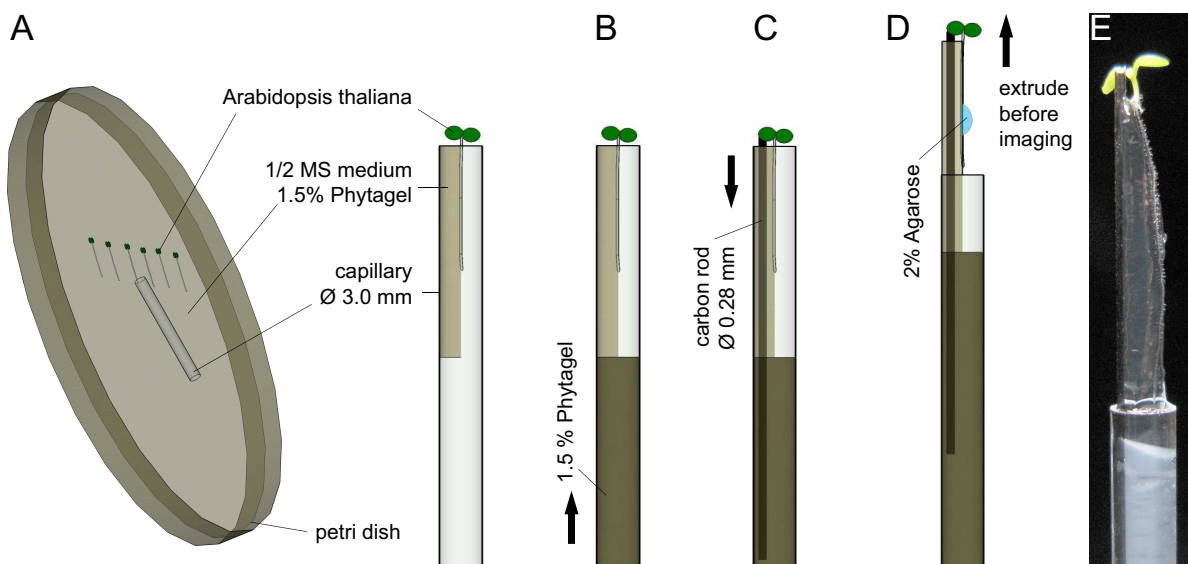

Figure 2.4: Sample holder - Root on the surface of gel. (A) *Arabidopsis thaliana* seedlings grew on vertically positioned petri dishes filled with $1/2$ MS-medium containing $1.5\,\%$ Phytagel. A single seedling was dug up with a capillary. (B) The capillary was then pushed into $1.5\,\%$ Phytagel to fill the capillary. (C) A carbon rod was placed inside the gel behind the plant. (D) The plant was extruded up to the region of interest by pushing it again into Phytagel. A drop of $2\,\%$ agarose fixed the plant on the gel. (E) A photo of the plant on the sample holder ready for microscopy. **Supplemental Movie-2.4**.

2.2.4 Gravity-stimulation for lateral root induction

The formation of lateral roots can be induced by bending the primary root (Lucas et al., 2008; Ditengou et al., 2008). Lateral roots emerge always on the outer side of the bend (Laskowski et al., 2008; Smet et al., 2007; Richter et al., 2009). One of the first molecular components that identify lateral root founder cells is the transcription factor GATA23 (De Rybel et al., 2010). Gravity-stimulated roots were used and the expression of the promoter of GATA23 to spot the region of lateral root emergence.

In order to test how long the gravity-stimulation has to last six days old plants were rotated by 90° for different periods of time. After $3\,h$, $6\,h$, $9\,h$ and $12\,h$ the plates were

returned back to the previous position and the number of lateral roots that appeared were counted three days later. In 42 % of the plates the primary roots show lateral emergence at the outside of the bend, when stimulated for 3 h, 60 % after 6 h and 80 % after 9 h of stimulation (Fig. 2.5). The first cell division occured 7 - 15 h after the gravity-stimulation. In order to stimulate the root in a reasonable way without missing the first division roots were stimulated for 6 h before recording.
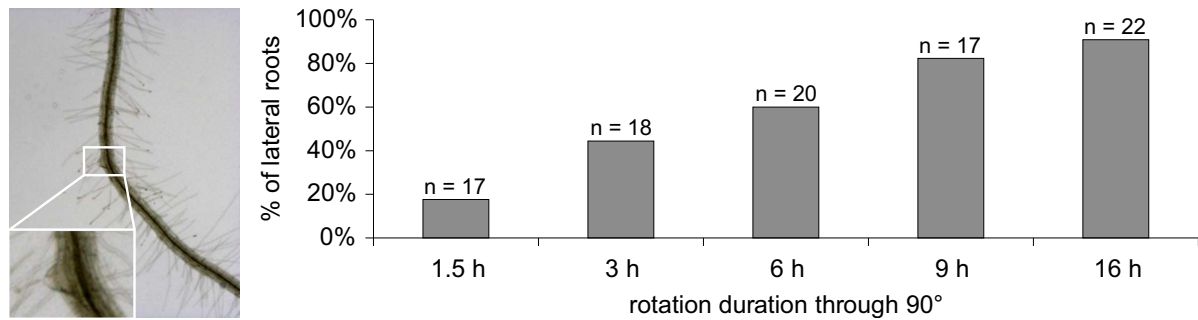

Figure 2.5: Lateral root induction by gravity-stimulation. Seven days old plants were rotated through 90° for different periods of time. The number of emerged lateral roots in the region of the bend were counted, three days later. In total, 94 plants from three independent experiments were analyzed. **Supplemental Movie-2.5**.

2.2.5 Sample preparation of rice segments

The deepwater rice *Oryza sativa* L. ssp. *indica*, cultivar Pin Gaew 56 (PG56), was obtained from Dr. Bianka Steffens (Christian-Albrechts-Universität zu Kiel, Kiel, Germany). Segments of about $20\,cm$ of the 13 weeks old plants were excised at the third node of the stem (Steffens and Sauter, 2005). The segments were further cut to a length of $7\,cm$ in order to fit into the microscope chamber. A metal rod ($3\,mm$ in diameter, $30\,mm$ long) was stucked carefully into the lacuna of the rice segment and then placed into the microscope chamber. A snap-cap vials was placed on top of the chamber in order to maintain humidity and was sealed with Parafilm. The light intensity was set to $150\,\mu mol/m^2/s$ at the upper end of the segment. The liquid medium in the microscope chamber contained $150\,\mu M$ Ethephon (2-Chloroethylphosphoric acid) and $100\,\mu M$ GA3 (gibberellic acid). The fluorescence membrane marker $1\,\mu g/ml$ ($1.65\,\mu M$) FM 4-64 was used for visualization.
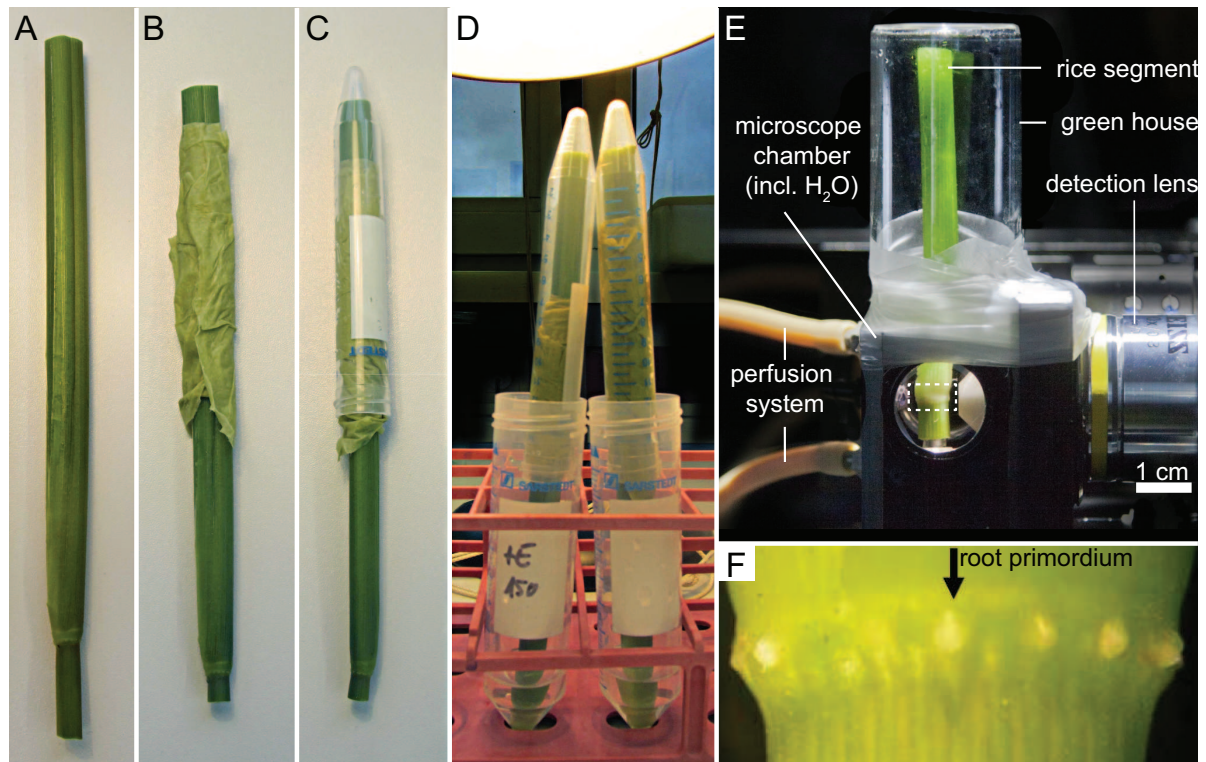
Figure 2.6: Rice segment preparation for microscopy (A) $20\,cm$ long rice segment. (B, C) Wet paper and a $15\,ml$ Falcon tube protects the segment from dehydration during transportation. (D) Test setup with $150\,\mu mol/m^2/s$ at the tip, $35\,\mu mol/m^2/s$ at the bottom. The segments in $50\,ml$ Falcon tubes containing tab-water with $150\,\mu M$ Ethephon. (E) Prior to imaging, the segments were shortened to $7\,cm$ and such that the node was $7\,mm$ above the lower edge. The segment was stucked on a metal rod which was mounted inside the microscope chamber. The chamber was perfused with 1/2-MS medium. A snap-cap vial was placed upside down and sealed with Parafilm on top of the chamber in order to maintain humidity. (F) Close-up of the third node region where adventitious root primordia are located. Pictures in A, B, C, D and F were kindly provided from Dr. Bianka Steffens.

2.3 Reagents, dyes and drugs

2.3.1 List of reagents, media and accessories

Table 2.2: Material and reagents

article	company	article number
agarose low melt	Carl Roth, Karlsruhe, Germany	6351.2
capillaries	Hilgenberg GmbH, Malsfeld, Germany	1470072
carbon rods	Conrad Electronic, Wels, Germany	275214 - 62
culture tubes "de Wit"	Duchefa, Haarlem, Netherlands	W1607.0750
D-Saccharose	Carl Roth, Karlsruhe, Germany	4621.1
ethephon	received from Dr. Bianka Steffens	
fluorescent lamp (23 W, 6500 K)	Philips, Amsterdam, Netherlands	8727900926002
fluorescent microspheres	Invitrogen, Eugene, Oregon, USA	T-7280
FM 4-64	Sigma-Aldrich, St. Louis, MO, USA	S6689
gibberellic acid	received from Dr. Bianka Steffens	
flexible fiber optic light guide	Edmund optics, Barrington, USA	39-370
Hellmanex II	Hellma Analytics, Müllheim, Germany	320.002
MES, low moisture	Sigma-Aldrich, St. Louis, MO, USA	M3671-50G
Murashige Skoog (MS) Medium	Duchefa, Haarlem, Netherlands	M0222.0050
Phytagel	Sigma-Aldrich, St. Louis, MO, USA	p8169-500G
potassium hydroxide	Carl Roth, Karlsruhe, Germany	P747.1
saccharose	Carl Roth, Karlsruhe, Germany	4621.1
servo motor HS-56HB	HiTec, Bretten, Germany	33056S
snap-cap vials	Carl Roth, Karlsruhe, Germany	lc84.1
sodiumhypochloride	Carl Roth, Karlsruhe, Germany	9062.3
TritonX-100	Carl Roth, Karlsruhe, Germany	3051.3

2.3.2 Membrane fluorescent dye FM4-64

The membrane was stained with the styryl dye FM 4-64 which has an excitation/emission maximum at $515/640\,nm$. Roots were incubated with $5\,\mu M$ for $10\,min$ before imaging. The concentration in the microscope chamber was $1\,\mu M$. The dye was excited at $488\,nm$, the emission was filtered with a $607/70\,nm$ bandpass filter.

2.3.3 Multifluorescent microspheres

In LSFM the foci of the detection and the illumination paths need to overlap. Prior to each recording the objective lenses were aligned by using multifluorescent microspheres

embedded in a Phytagel cylinder. In order to have the same amount of particles within the field of view for the various types of objective lenses it requires different concentrations of multifluorescent microspheres. Therefore, the volume of the field of view was calculated, which depends on the objective lens and on the size of the camera chip. The magnification varies the field of vision in x and y, whereas the depth of focus (z) is determined by the numerical aperture (NA). Particles that are present in this volume are detected by the camera chip which has a defined size.

Dimensions of the Andor Clara camera chip:

$$x: \; 1392 \, px \; \cdot \; 6.45 \, \mu m \; = \; 8978.4 \, \mu m$$

$$y: \; 1040 \, px \; \cdot \; 6.45 \, \mu m \; = \; 6708.0 \, \mu m$$

Dimensions of the Andor Neo camera chip:

$$x: \; 2560 \, px \; \cdot \; 6.5 \, \mu m \; = \; 16640.0 \, \mu m$$

$$y: \; 2160 \, px \; \cdot \; 6.5 \, \mu m \; = \; 14040.0 \, \mu m$$

The depth of focus (z) depends mainly on the NA of the objective lens and can be calculated by the following equation:

$$z[nm] \; = \; 2 \cdot n \, \frac{\lambda}{NA^2}$$

Table 2.3: Volume of the field of view (FOV) for different objective lenses using the Andor Clara camera. The volume calculations for the 10× and 20× were performed using the thickness of the light-sheet (2.5× illumination lens: 5 μm) instead of the axial resolution because the light sheet is thinner than the depth of focus. The volume for the 40× and 63× was calculated using the axial resolution because the light sheet is equal or thicker than the axial resolution. Calculations for a given wavelength of $\lambda = 561 \, nm$ and a refractive index of $n = 1.33$ (water).

magnification	NA	resolution$_{axial}$	volume FOV [μl] Andor Clara	volume FOV [μl] Andor Neo
10×	0.3	16.58	$3.01 \cdot 10^{-3}$	$1.16 \cdot 10^{-2}$
20×	0.5	5.97	$7.53 \cdot 10^{-4}$	$2.90 \cdot 10^{-3}$
40×	0.8	2.65	$9.99 \cdot 10^{-5}$	$3.84 \cdot 10^{-4}$
63×	1.0	1.49	$2.26 \cdot 10^{-5}$	$8.72 \cdot 10^{-5}$

The particular end-concentration can be calculated by the following equation:

$$concentration_{stock} \times volume_{stock} = concentration_{end} \times volume_{end}$$

Some companies indicate the particle concentration in volume %. In order to get concentration in particles/ml the volume of a single particle was calculated by the formula for the volume of a sphere:

$$Volume\ of\ a\ sphere = 4/3 \cdot \pi \cdot r^3$$

2.3.4 Phytagel versus agarose

Phytagel is a standard for plant culture in laboratory. It is used instead of soil in order to control nutrient composite. Furthermore it is transparent and thereby useful for microscopic root system observations. Phytagel is a polysaccharide produced by the bacterium *Pseudomonas elodea*. Compared to other gelling agents, it is stiffer while being clearer at same concentrations (Fig. 2.7). To illustrate the difference in transparency between Phytagel and agarose $100\,ml$ Schott bottles ($56\,mm$ in diameter, glass wall thickness of $2.6 \pm 0.6\,mm$) were filled with 1/2 MS medium with different concentrations of Phytagel or agarose. The identical solutions were used to measure the optical density and the refractive index. The OD measurements were performed within $1\,h$ of gel preparation with the Tecan Infinite M200 ($10\,mm$ cuvette thickness). The refractive index was measured with Rudolph Research: J257 Automatic Refractometer. The index of agarose varies in the third and Phytagel in the fourth position (Fig. 2.7 C).
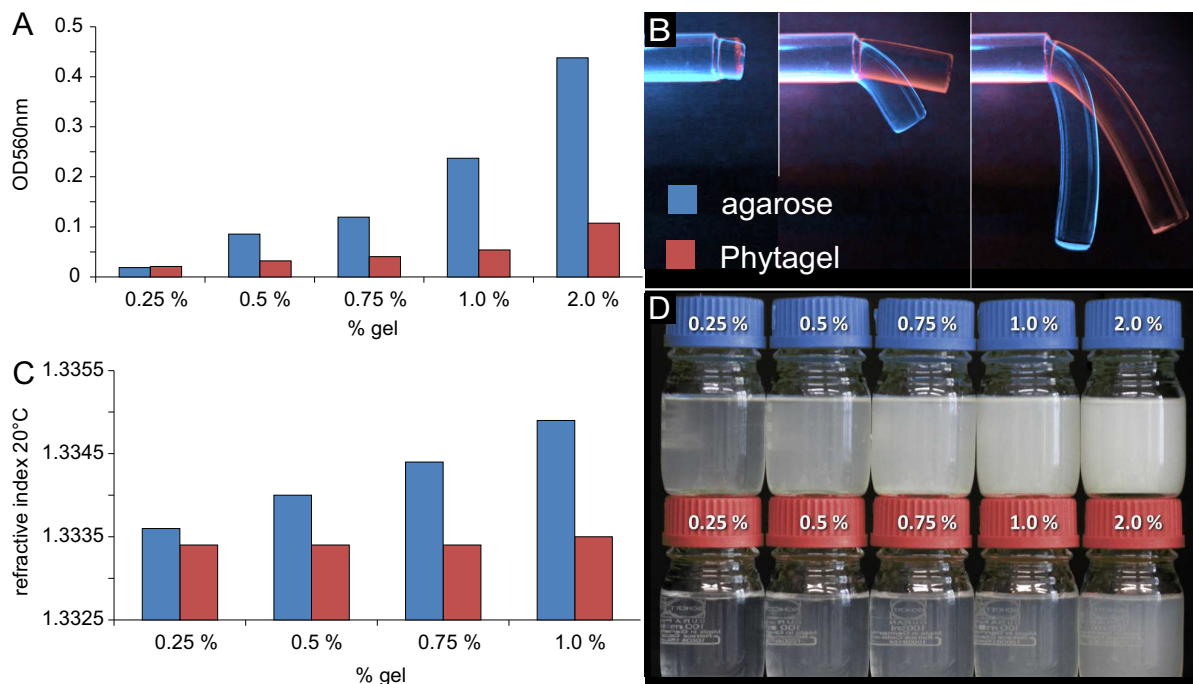
Figure 2.7: Optical and mechanical properties of Phytagel and agarose. (A) The optical density and (C) the refractive index of $1/2$ MS medium containing different concentrations of Phytagel or agarose. (B) Agarose and Phytagel in 1% concentration extruded from a capillary ($3\,mm$ in diameter). (D) Bottles filled with the same media used in A and C photographed in front of a black card board and daylight. **Supplemental Movie-2.7**.

2.4 The monolithic Digital Scanned Light-sheet Microscope

The name Light Sheet-based Fluorescence Microscopy (LSFM) describes the technology. There are various implementations of LSFM, for example, a light-sheet can be formed either by a cylindrical lens or by scanning a focused laser beam up and down in synchrony with the camera exposure time. A microscope with a scanned light-sheet is termed Digital Scanned Light-sheet Microscope (DSLM). The microscope used in this work is an improved version of the DSLM described by Keller et al. (2010). The main difference is that all optical parts are built in a single aluminum block, therefore it's called monolithic-DSLM (mDSLM). A four motors stage blow the microscope chamber move the plant along x/y/z and rotate it around the vertical axis, which is parallel to gravity and orthogonal to the optical illumination and detection axes. The filter wheel is uncoupled from the aluminum block and mounted separately on the optical table. Green fluorescent proteins (GFP) and yellow fluorescent proteins (YFP) were excited at $488\,nm$ by a diode

laser and detected between 500-550 nm. The red fluorescent protein was excited at 561 nm by a diode-pumped solid state (DPSS) laser and detected between 572-642 nm. Images are captured with cameras from Andor, either Clara (CCD) or Neo (CMOS).

Different pairs of objective lenses can be used. There are two air objective lenses (2.5× and an 5×) for the illumination path, and four water dipping objective lenses (10×, 20×, 40× and 63×) for the detection path available (Tab. 2.4). The two illumination objective lenses create different properties of the light sheet. The light sheet thickness within the focal area is thinner in the 5× (ca. 2.5 μm) compared to the 2.5× (ca. 5 μm), but the focal area is also shorter (Fig. 2.9 B). The 5× was used for high magnification lenses (40× and 63×), the 2.5× for lower magnification lenses (10× and 20×).

Table 2.4: **Objective lenses used in the mDSLM**.

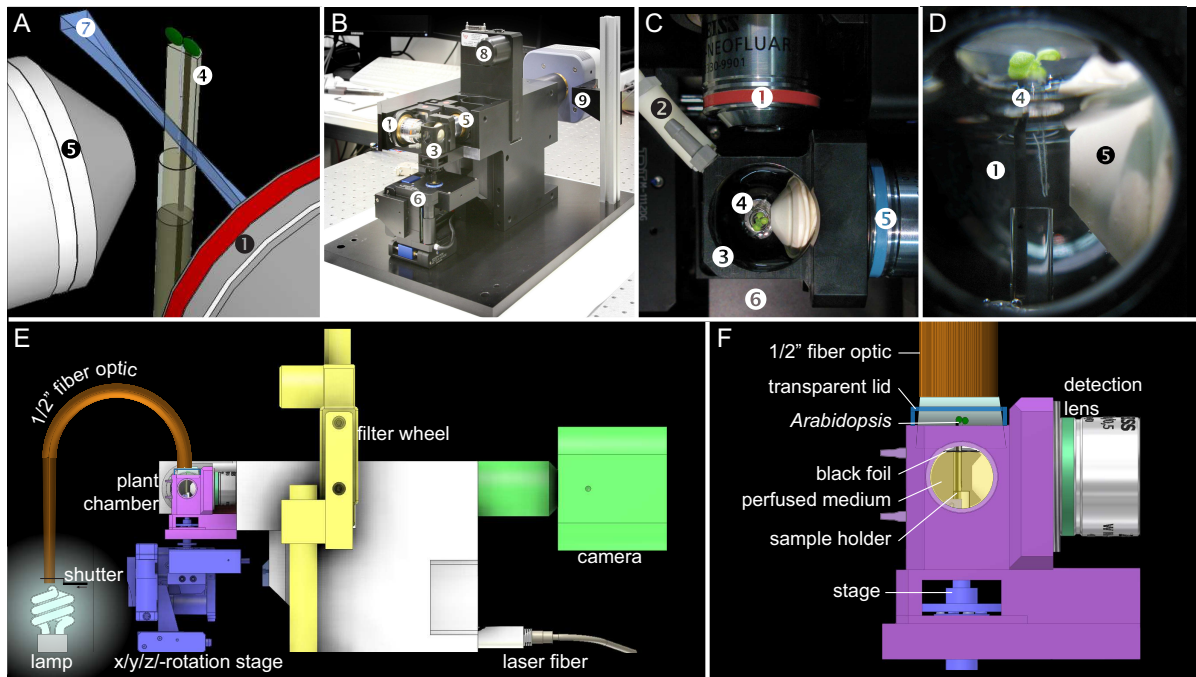|	objective class	magnific.	NA	work. dist. [mm]
illumination lenses	EC Epiplan-Neofluar	2.5×	0.06	15.1
	EC Plan-Neofluar	5×	0.16	18.5
detection lenses	W N-Achroplan	10×	0.3	2.6
	W N-Achroplan	20×	0.5	2.6
	W N-Achroplan	40×	0.75	2.1
	W N-Apochromat	63×	1.0	2.4

Figure 2.8: Arabidopsis in the monolithic Digital Scanned Laser Light Sheet-based Fluorescence Microscope (mDSLM). (A) Perspective sketch of the plant specimen holder in front of the two objective lenses. Only the fluorophores in a thin planar volume that overlaps with the focal plane of the detection objective lens are excited. Thus fluorophores outside this volume do not blur the image and are not subjected to photo bleaching. (B, E) The central components of the mDSLM are mounted on a plate. All optical components are inside a single aluminum block. Four motors below the specimen chamber move and rotate the plant. The filter wheel is uncoupled from the aluminum block. Images are captured with cameras from Andor, either Clara or Neo. A flexible optical glass fiber guides the light coming from a small fluorescent lamp above the plant in the microscope's specimen chamber. (C) Top view of the specimen chamber. (D, F) Side-view into the chamber with the root in front of the detection lens. The plant grows in an upright position. While the leaves remain in the air, the root system is perfused with an liquid medium. Legend: 1: illumination objective lens, 2: perfusion system, 3: specimen chamber, 4: *A. thaliana* in capillary, 5: detection objective lens, 6: microscope stage, 7: laser light sheet, 8: filter wheel, 9: camera. **Supplemental Movie-2.8**.
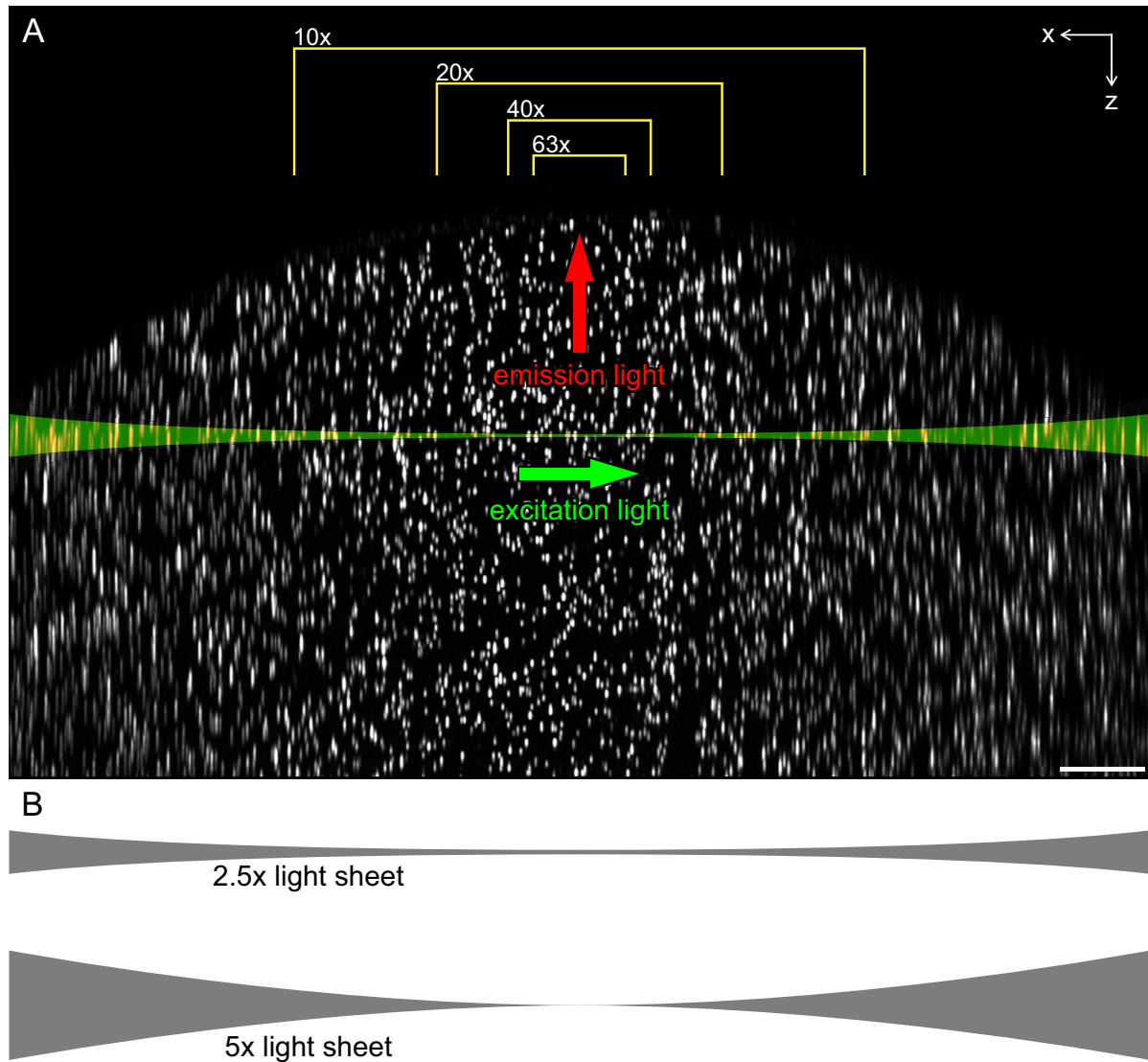
Figure 2.9: Illustration of the illumination and detection properties in the mDSLM. (A) Images of multifluorescent microspheres in a 1 % agarose gel cylinder (top view, x-z reslice). The excitation light sheet illuminates fluorophores in a small volume which overlaps with the focal plane of the detection lens. Yellow outlined areas delineate the field of view for different detection lenses using the Andor Clara camera. Images were recorded using the 2.5× illumination lens and the 10× detection lens in combination with the Andor Neo camera chip, which is four times as large as the Andor Clara camera chip. (B) Two different illumination lenses with different light sheet characteristics. The 5× illumination objective lens creates a thinner light sheet (2.5 μm in the focus) but has a shorter focus area. The 2.5× illumination objective lens creates a more homogeneous, but thicker light sheet (5 μm in the focus area). The 2.5× was used for lower magnification detection lenses (10× and 20×), the 5× was used for higher magnification detection lenses (40× and 63×). Scale bar: 100 μm.

2.4.1 Plant illumination system

The plant is inserted from above but is held from below. Thus, the opening remains accessible for diurnal illumination of the leaves. The light source for plant leaves illumination stems from a small fluorescent lamp with the same spectral quality as common fluorescent lamps in plant incubators (Fig. 5.5 on page 142). A flexible glass fiber with a diameter of $1.22\,cm$ guides the light towards a location above the plant. The optimal light intensity for Arabidopsis is 120-140 $\mu mol/m^2/s$. The maximum intensity in the mDSLM of $260\,\mu mol/m^2/s$ was measured behind the glass fiber optic and can be adjusted by changing the distance between lamp and glass fiber. A shutter closes the light path and turns the light off in the microscope chamber whenever a stack of fluorescence images is recorded. A standard time switch for the lamp generates a diurnal cycle (Fig. 2.10). The shutter is operated by the data acquisition software of the mDSLM. The microscope's real-time-controller triggers (TTL-signal) an Arduino board which then drives a motor. The program was written by Prof. Ernst Stelzer and extended by the perfusion system control by Sven Plath (see supplement material on page 179). The shutter is made of a rigid cardboard covered with a short felt.
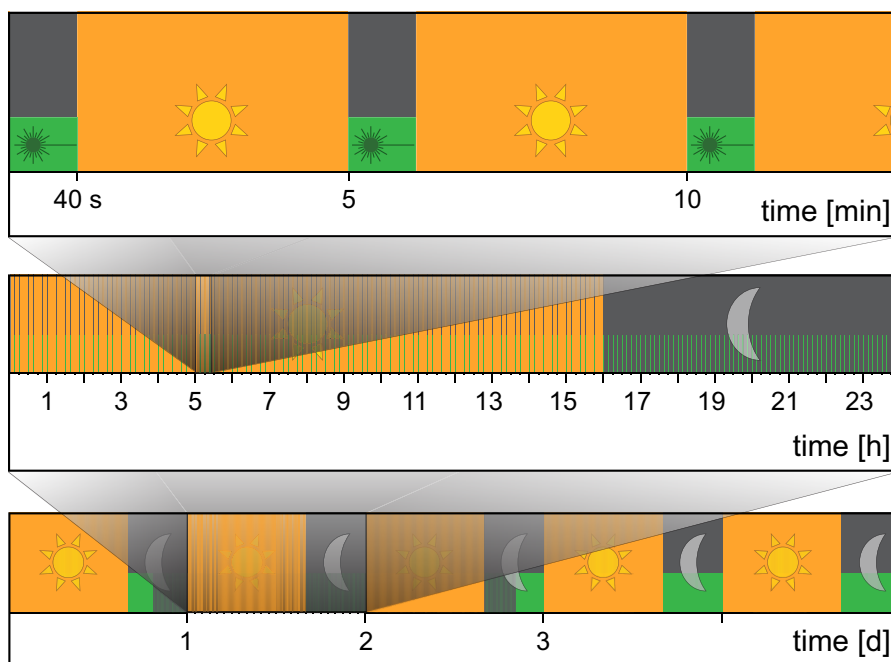
Figure 2.10: Experimental protocol for recording Arabidopsis in the mDSLM. The three panels illustrate how recording interval and plant illumination are orchestrated. The recording of an image stack (e.g. 233 planes, two channels) takes about $40\,s$, subsequently the plant illumination is switched on for $4\,min$ and $20\,s$ until the next recording starts. After a $16\,h$ day the plant illumination is turned off for an $8\,h$ night. This procedure is repeated for every day the plant resides in the microscope's specimen chamber. **Supplemental Movie-2.10**.

The Arabidopsis root system architecture shows significant differences when it is exposed to light (Fig. 2.11 A, B). Due to this altered phenotype the root system was shaded by covering the water surface in the mDSLM microscope chamber with the same black plastic foil as in the transparent cultivation chambers (Fig. 2.11 C, D). Thereby, the roots were illuminated with considerably less light than the leaves. Measurements of the camera background in light and darkness conditions revealed that by covering the water surface the amount of light detected by the camera was reduced to 42 %.
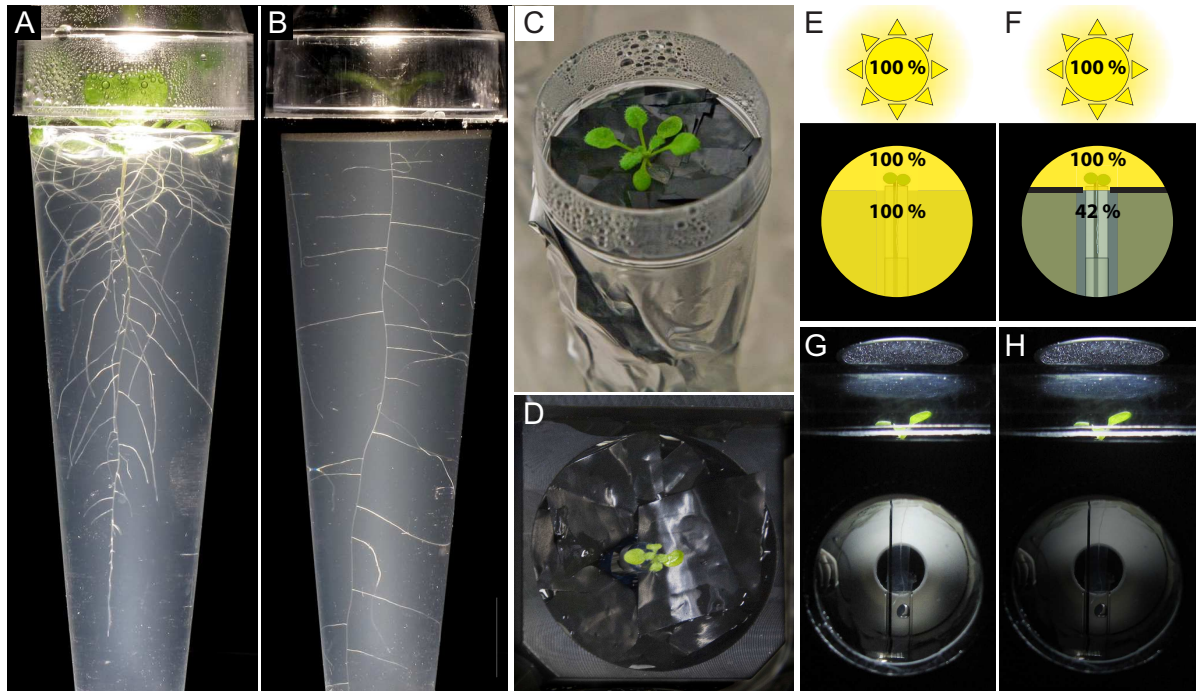

Figure 2.11: Light conditions in the mDSLM chamber. The root system has a different morphology when exposed to light. (A) Three weeks old Arabidopsis plant grown in transparent cultivation chambers filled with 1/2 MS medium containing 0.3 % Phytagel. (B, C) Arabidopsis plant grown in a cultivation chamber that was covered with aluminum foil and black plastic foil. Lateral roots continue to grow towards gravity in light conditions, whereas in darkness they grow straight at a certain angle away from the primary root. (D) Black plastic foil was used to cover the water surface in the microscope chamber. (E, F) Illustration of the light situation in the microscope chamber. (G, H) Photos of the plant in the microscope chamber w/wo covering the water surface.

2.4.2 Perfusion system

The plant is placed in a medium-filled chamber close to the common focal point of the two objective lenses. The perfusion system was driven by a peristaltic pump (ISMATC, model ISM 832c). The flow speed of $0.55\,ml/min$ exchanges volume of $13\,ml$ in the

microscope chamber in approximately $24\,min$. The microscope chamber has three outlets for the perfusion system. In most cases the upper outlet was used. In order to image regions that are close beneath the leaves, the water level can be adjusted in order to keep the leaves in air (Fig. 2.12). Therefore, the outlet in the middle was used in combination with an angled plastic tube combiner which was modified (one of end was sealed and an additional whole in the middle part was drilled at an right angle to the flow direction) and plugged into the middle outlet. By rotating this part the outlet was adjusted to the desired height.
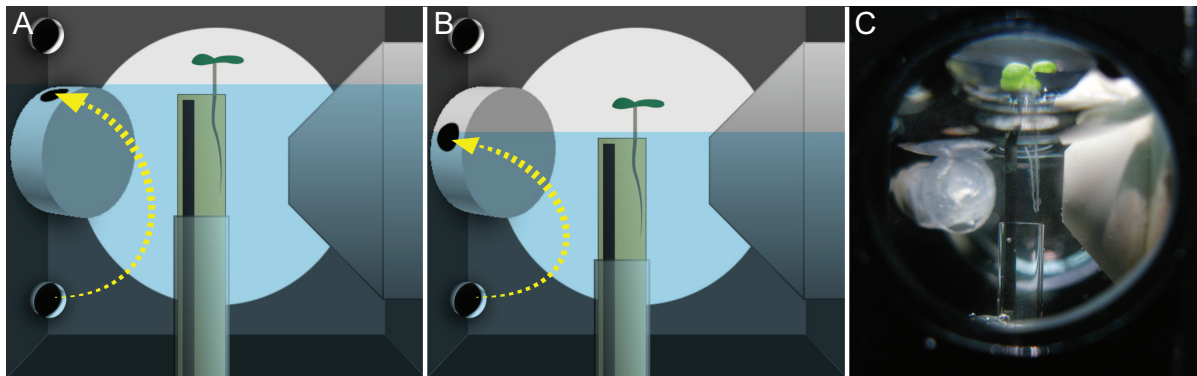

Figure 2.12: Adjustable perfusion outlet for variable water level. Side view of the mDSLM microscope chamber. A modified angled plastic tube combiner was plugged in the middle outlet. By rotating the new outlet the water level was adjusted (A, B). (C) Side view of the mDSLM microscope chamber. **Supplemental Movie-2.12**.

2.4.3 Advanced application of the mDSLM

Technical features of the mDSLM that allow for advanced application had to be approved during the developmental testing phase of the mDSLM and are described in the following sections.

Multispecimen - successive recording of various regions

The field of view of a microscope is limited to the magnification and the size of the camera chip. Sometimes, big objects need a larger field of view. The microscope software allows to specify and position multiple z-stacks in the multiple specimen option. During the acquisition mode these z-stacks are recorded consecutively. The multiple specimen option can be used to record multiple regions (Fig. 2.13) or to capture and stitch a series of stacks to a larger panorama image together (Fig. 3.2 on page 53). The precision

was good, during time lapses no wiggling between time points could be observed. The multiple specimen option was further used to record multiple channels subsequently.
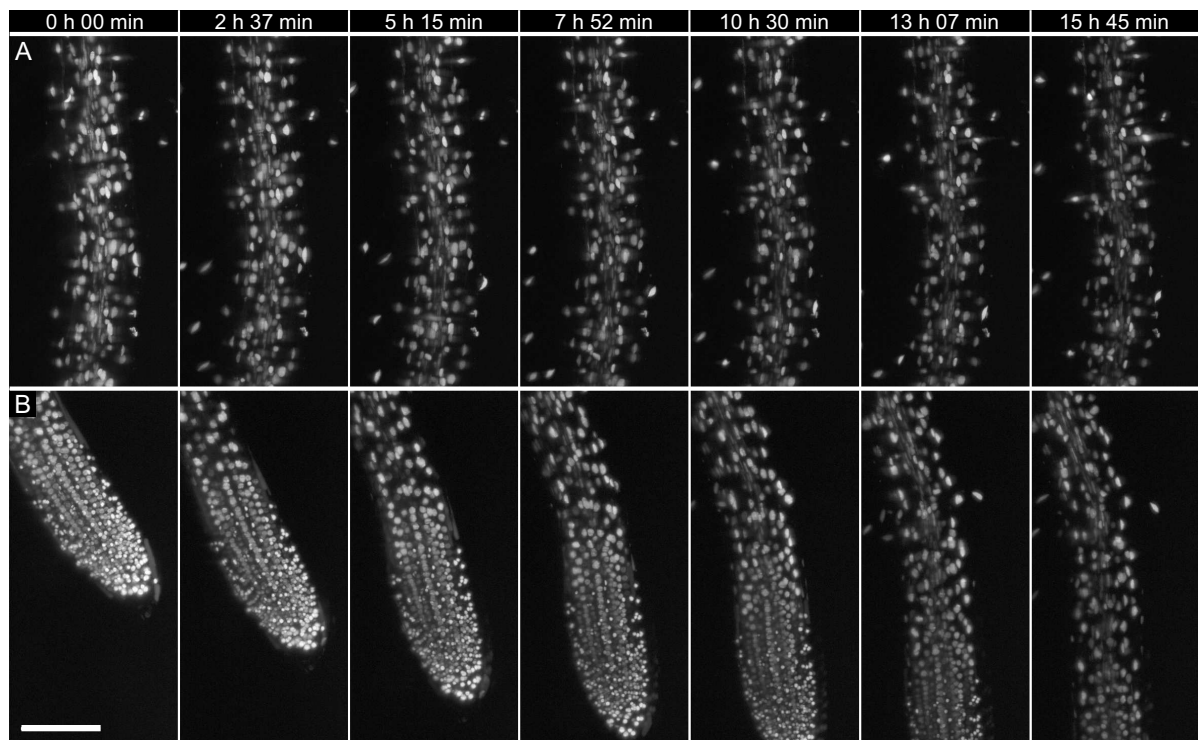

Figure 2.13: Recording multiple regions of interest at the same time. Maximum intensity projections of seven time points out of 126 of two regions $1100\,\mu m$ apart. (A) A region above the root tip, where a lateral root was supposed to grow. But, it did not grow. (B) At the same time the primary root tip developed. The six days old Arabidopsis express UBQ10::H2B-RFP. Scale bar: $100\,\mu m$. Detailed recording metadata on page 155.

Multiple angle acquisition

Deep inside of large samples light absorption and scattering increases which causes a loss of signal inside the sample. The sample mounting on the rotation stage allows to acquire images of the same region along multiple directions. The different views can increase the overall information and reduce the optical artifacts caused by scattering of thick samples (Verveer et al., 2007). To illustrate this a root tip along five different view points was recorded (30° apart) and the views were combined using an affine registration in Amira software (Fig. 2.14). Compared to the single view acquisitions, the merged image is evenly bright along all directions. Furthermore, the multiple angle acquisition was successfully applied to a time lapse recording of a lateral root formation process (Fig. 2.15).
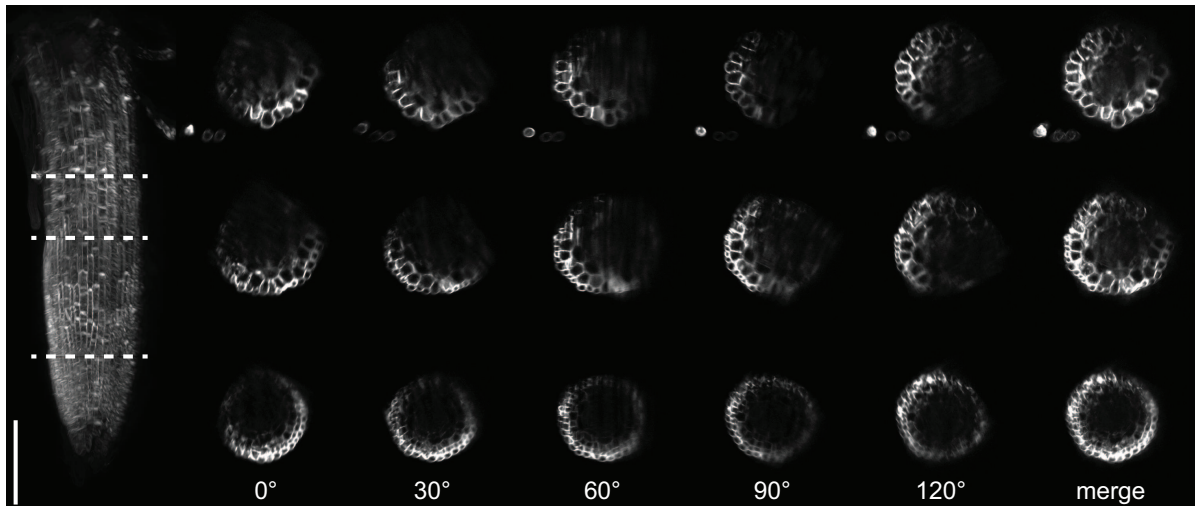
Figure 2.14: Recording along multiple angles of a primary root. Left, maximum intensity projection of the merged stacks. The dashed lines indicate the position of the optical transverse section presented in the panel showing each angle of acquisition and the maximum projection merge. The five angles of acquisition were aligned using *Amira*. Scale bar: $100\,\mu m$. The 4 days old transgenic Arabidopsis express 35S::LTI6b-GFP. Detailed recording metadata on page 154. **Supplemental Movie-2.14**.

Figure 2.15: Time lapse recording along multiple directions. (A) Maximum intensity projections of image stacks along two angles (0°, 45°) in the last time point of the time lapse. (B) Enlarged view of the dashed boxed area in A. The six days old transgenic Arabidopsis express UBQ10::H2B-RFP. Scale bar: A) $50\,\mu m$, B) $20\,\mu m$. Detailed recording metadata on page 173. **Supplemental Movie-2.15**.

Spatial resolution

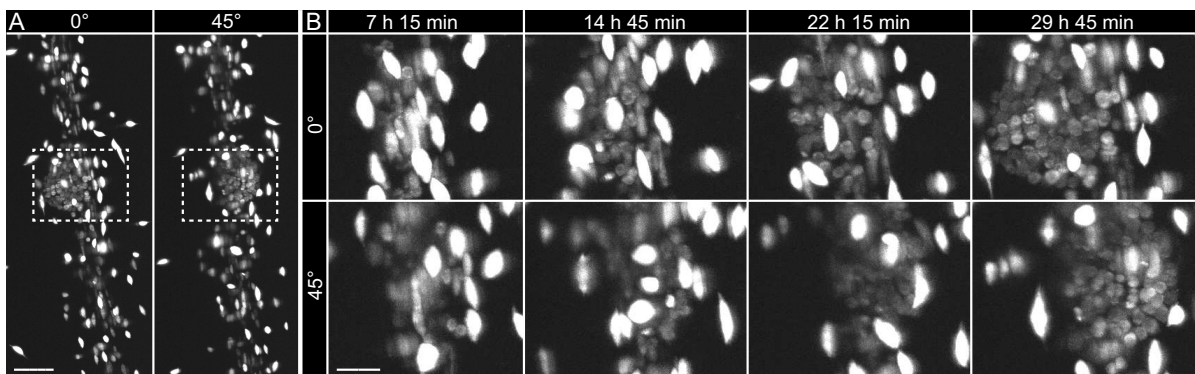The signal to noise ratio plays a crucial role in the quality of an image. In a light sheet-based fluorescence microscope the signal to noise ratio is much higher compared to other fluorescent microscopes (Keller and Stelzer, 2008), because only an emission filter and a tube lens is in between the detection lens and the camera. The image quality further benefits from high dynamic range of CCD or CMOS cameras.

The resolution of an optical system is mainly dependent on the objective lens that is used in the detection path and the pixel-pitch on the camera chip. In a light sheet-based fluorescence microscope the axial resolution mainly depends on the thickness of the light sheet and a true optical sectioning ability with a good axial resolution is preexisting. In a cross-section of the root, the thinnest diameter of a cell wall measured (full width at half maximum) was $0.77\,\mu m$ in x-y. The thinnest membrane in axial direction was measured with $2.45\,\mu m$, which reflects the thickness of the light sheet (Fig. 2.16). Cell contours are very well resolved across the entire width of the root (Fig. 2.16). The cell layers epidermis, cortex, endodermis and pericycle could be identified, but in the central cylinder cell contours were less well resolved. The use of long working distance objective lenses allow to capture the entire volume of large objects. The properties of the light sheet change deep inside tissue due to scattering and dense objects that create shadows. Fig. 2.17 shows to what extend small Golgi-vesicles can be detected at different depths. These vesicles are still well resolved in the endodermis cell layer (Fig. 2.17 (3)). In the central cylinder endosomes are still visible although the image starts to get blurry which is caused by out of focus light due to scattering.
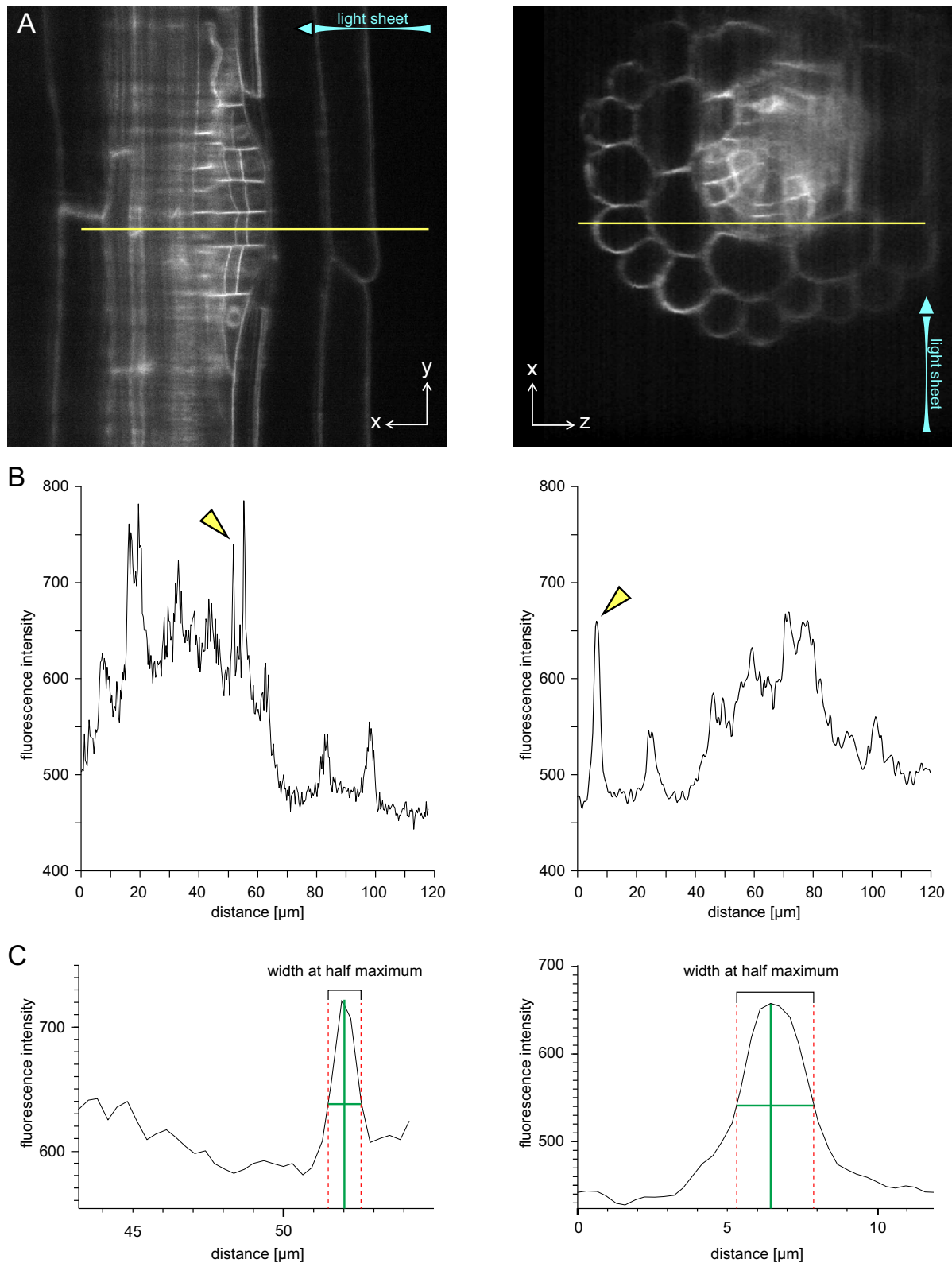
Figure 2.16: Intensity profile along xy and xz. Single slice of an image stack through the central plane of an Arabidopsis main root along x-y (left) and x-z (right). The six days old Arabidopsis express UBQ10::YFP-PIP1;4. The fluorescence intensity signal along the yellow lines (left and right) is plotted in B. (B) Yellow arrowheads point at an intensity peak which is enlarged in C. (C) Full width at half maximum of the intensity peak indicates a spatial resolution of approximately $0.77\,\mu m$ in x-y and $2.45\,\mu m$ in x-z direction. Images were collected with the $40\times/0.75$ W objective lens for the detection and the $5\times/0.16$ was used in the illumination path. YFP was excited with $488\,nm$ diode laser, fluorescence was filtered with a 534/30 band-pass filter. Detailed recording metadata on page 162.

Figure 2.17: *Trans-***Golgi network vesicles deep within the primary root**. Image stack recording of a Arabidopsis root expressing 35S::GFP-RabA1d. (A) 3D reconstruction of a stack of images recorded with the $63\times/1.0$ W objective lens for the detection and the $5\times/0.16$ was used in the ill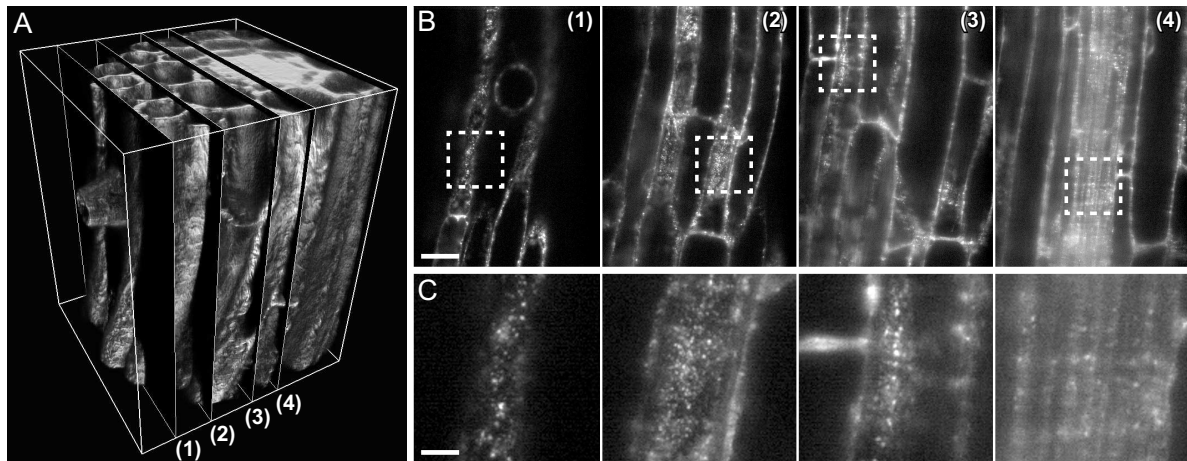umination path. Single sections at different z-depths ((1): z $= 0\,\mu m$, (2): z $= 16.5\,\mu m$, (3): z $= 36.8\,\mu m$, (4): z $= 50\,\mu m$) are depicted in (B). (C) Magnification of the boxed dashed area. Scale bar: B) $20\,\mu m$, C) $5\,\mu m$. Detailed recording metadata on page 156. **Supplemental Movie-2.17**.

Recording speed

The recording speed is limited due to waiting processes while the stage moves in between two z-planes. Furthermore, the recording speed reaches $5\,fps$ at maximum in a two channel acquisition mode because of a waiting process (ca. $200\,ms$) while the filter wheel changes the emission filter. The speed can be raised to $7\,fps$ by a successively channel recording, i.e. the filter does not change until the complete z-stack of the first channel was recorded). The speed can be further significantly increased by using the binning option of the Andor Clara camera ($14\,fps$ in single plane, $11\,fps$ in a stack recording). The binning modus lowers the resolution but increases the signal to noise ratio dramatically. A maximum frame rate of $25\,fps$ was achieved by recording a small region of interest in a single plane using binning 2×2. In summary, the recording speed can be increased by 1) a short exposure time. There is a limit of approximately $20\,ms$, because the scanning process of the light sheet takes some time, 2) a small region of interest, 3) the use of camera binning and 4) the successively channel recording (Tab. 2.5).

Most long term time lapse recordings were performed with a frame rate of $11\,fps$ which allowed to record one time point within $40\,s$ (exposure time of $35\,ms$, binning 2×2 and successively recording of two channel consisting of 233 planes).

Table 2.5: Recording speed in the mDSLM.

channel	z-planes	field of view	binning	frame rate
simultaneous	stack	full frame	1×1	5
successively	stack	full frame	1×1	7
successively	stack	full frame	2×2	11
successively	single plane	full frame	2×2	14
successively	single plane	region of interest	2×2	25

CUDA online deconvolution feature

Image quality suffers from optical distortions by the point spread function of the detection objective lens. These known distortions can be recovered by the Richardson-Lucy deconvolution. The microscope software has the ability to compute an Richardson-Lucy deconvolution algorithm online, i.e. during the recording process. The calculation is done for each image (i.e. 2D) and computed on the PC's graphics processing unit (GPU) using the Nvidia CUDA platform. Fig. 2.18 shows images of a microtubule labeled transgenic Arabidopsis root that were deconvolved by a different number of iterations. Microtubules are much better separated in the deconvolved images. When a high number of iteration (>10) was computed structures (artifacts) appear in the background that were not visible in the raw data. The deconvolution was implemented by Christian Harak during an internship at the EMBL in Heidelberg.
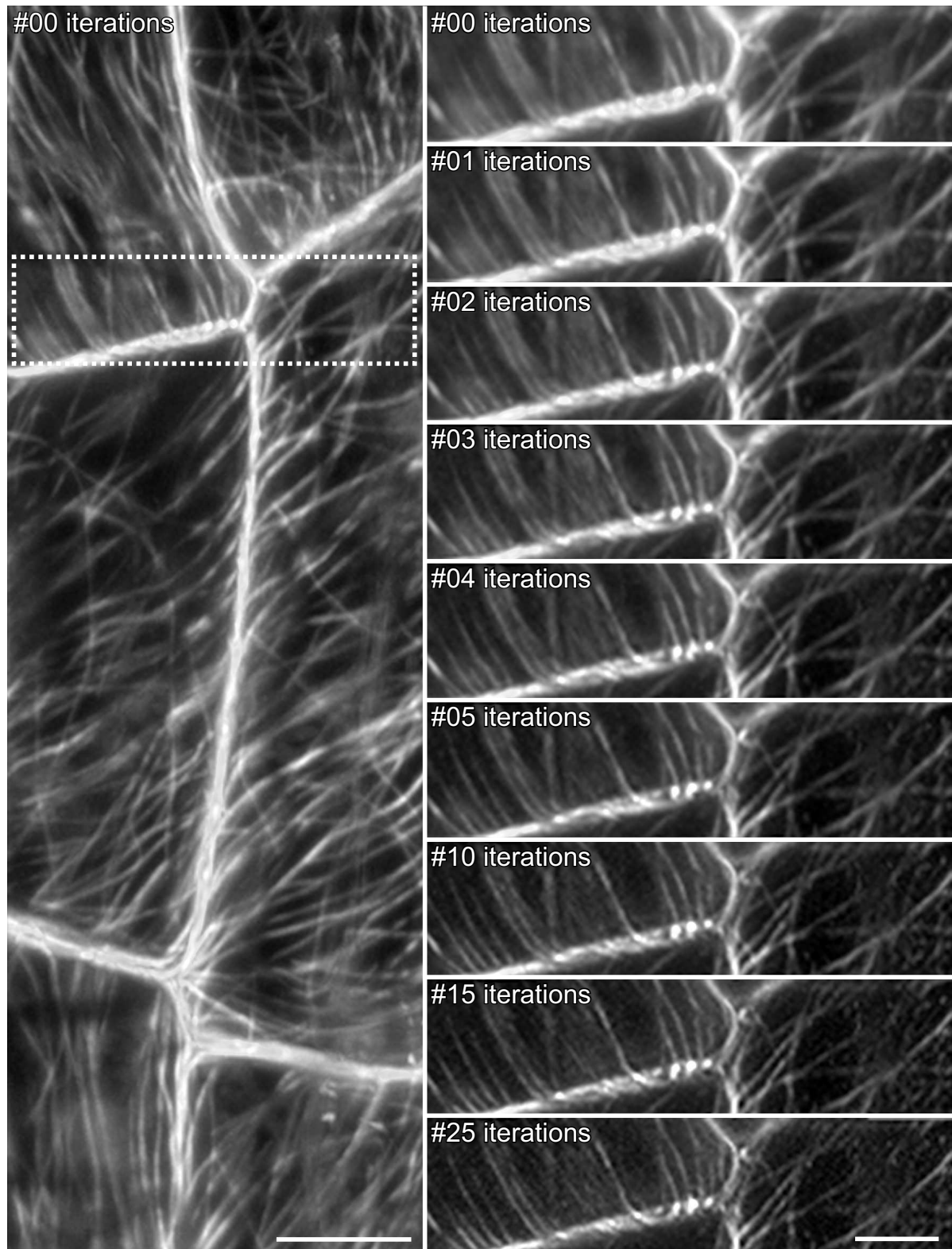
Figure 2.18: CUDA online deconvolution. (A) Microtubules in the epidermis cell layer of a transgenic Arabidopsis plant expressing 35S::GFP-MAP4. The overview on the left was recorded without deconvolution. The dashed box area is enlarged on the right. Different number of iterations of the Richardson-Lucy deconvolution were computed. Scale bar: $10\,\mu m$ (overview), $5\,\mu m$ (detail).

Structured illumination
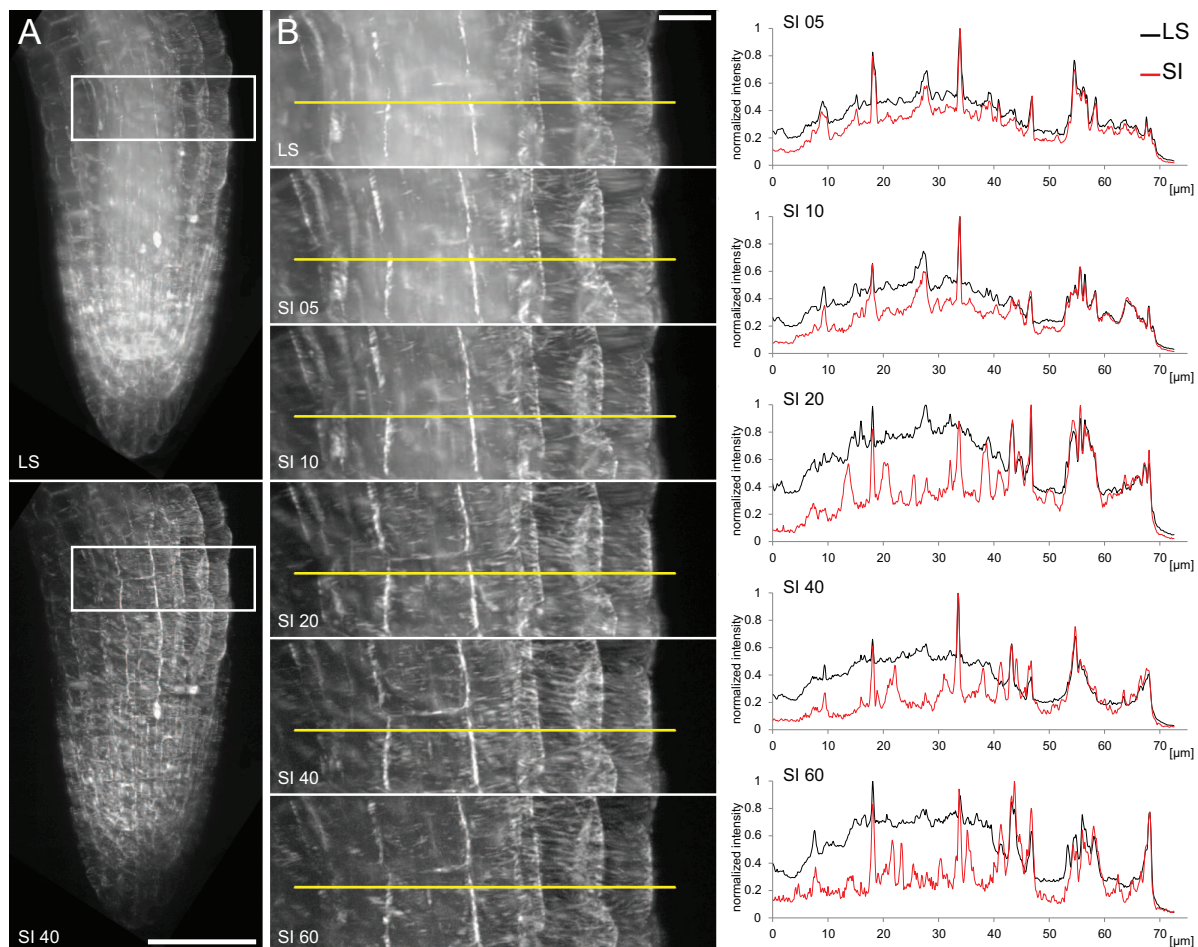
Figure 2.19: Gain in image quality for different SI pattern. Comparison of standard light-sheet illumination (LS) and structured illumination (SI05, SI10, SI20, SI40 and SI60). (A) Maximum-intensity projections of the Arabidopsis root expressing the microtubule marker 35S::MAP4-GFP. The boxed area is magnified in B. (B) The yellow line indicates the position of the intensity profile depicted in the diagram. In all plots the raw intensity values were normalized to the maximum intensity in each image. Scale bar: (A): $50\,\mu m$, (B): $10\,\mu m$.

Multicellular organisms scatter light which lowers the contrast inside the specimen. Incoherent structured illumination can improve the image quality (Keller et al., 2010). The intensity of the illuminating laser beam is modulated in synchrony with the scanning process, which creates a striped pattern of light. The acquisition of three spatial phase shifts of this pattern allows to illuminate the complete field of view. A processing algorithm combines the three images and thereby discriminates scattered background light against high contrast signal (Neil et al., 1997). The contrast was analyzed by comparing the normalized intensities of images acquired with a continuous light sheet

(LS) with different patterns of structured illumination (SI) along a line in a maximum intensity projection (Fig. 2.19). The application of SI improved the contrast significantly, i.e. in the maximum intensity projection more visual features can be seen.

2.5 Image processing

Due to the large amount of data, which is produced during a recording acquisition, the data handling and processing has become an important role in the analysis and visualization. Crucial steps in preprocessing steps or the analysis are described in the following section.

2.5.1 Fiji

Fiji is a very powerful open source image processing package and was used for numerous visualizations, measurements and image processing steps, e.g. projections along all directions, cropping, rotation, intensity plots, angle measurements, kymographs, 3D viewer, BigDataViewer, etc.

A main important data preprocessing step was to correct for movements or a drift of the plant using the plugin *Correct 3D drift*. The complete dataset of a recording was loaded as *virtual hyperstack* via the plugin Bio-Formats Importer. The plugin *Correct 3D drift* registers and transforms (x/y/z translation) the time points based on the grey level intensities (Pietzsch et al., 2012). The plugin saves each z-plane in a single tif-file, which can generate several hundred thousands images in one folder. These images were combined into z-stacks for each time point using a *Mathematica* script written by Alexander Schmitz.

2.5.2 Adobe After Effects

Adobe After Effects is highly integrated in other *Adobe* graphic applications like *Illustrator* or *Photoshop* and an ideal tool for creating and editing video footages. The software has a very powerful motion-tracking tool which is an ideal tool to analyze microscopic data, e.g. particle tracking, drift corrections, growth measurements (Maizel et al., 2011; Lucas et al., 2013). Image sequences can be imported in $8\,bit$, $16\,bit$ or $32\,bit$. A main limitation is that it only works with two-dimensional footages, although a 2.5-D visualization is possible (2D images in a 3D space).

Most of the movies were processed and annotated with *Adobe After Effects*. Furthermore the software was used:

- to track endosomal compartments (e.g. Fig. 3.12 on page 64)

- to correct a drift and measure the growth rates of root hairs (e.g. Fig. 3.16 on page 68)

- to measure the width, height and length of lateral root primordia (e.g. Fig. 3.28 on page 81)

- to dissect the fluorescence signal from lateral root overlaying tissue by retouching (e.g. Fig. 5.6 on page 143)

- to follow the further development of cell files during the lateral root emergence by animating a semi-transparent mask (Fig. 3.48 on page 99)

2.5.3 Nuclei tracking and visualization with Mathematica

Cell lineage tracing was performed with the program *TrackGen* written by Alexander Schmitz in *Mathematica*. *TrackGen* allows to manually track the lineage of individual cell nuclei in time series datasets and offers comprehensible visualization tools (Fig. 2.20). The images were loaded into the program as 8-bit RGB tif (one time point as one file) including two channels (green-mebranes, red-nuclei). Arrow keys allow to navigate through time and z-planes.

Objects were manually identified by clicking on a nucleus. The Object ID number, three-dimensional position (x/y/z), the current time point and its precursor was saved. For the first data set (#121204) every nucleus in every time point was identified, creating 21,219 objects. In all other data sets only the first and last occurrence of each cell nucleus was identified which reduced the number to approximately 1,000 objects. All data was then exported to a XLSX file (Tab. 2.6). A compressed graph representation for each founder cell gives an overview of the cell lineage and associated information (Fig. 2.21).
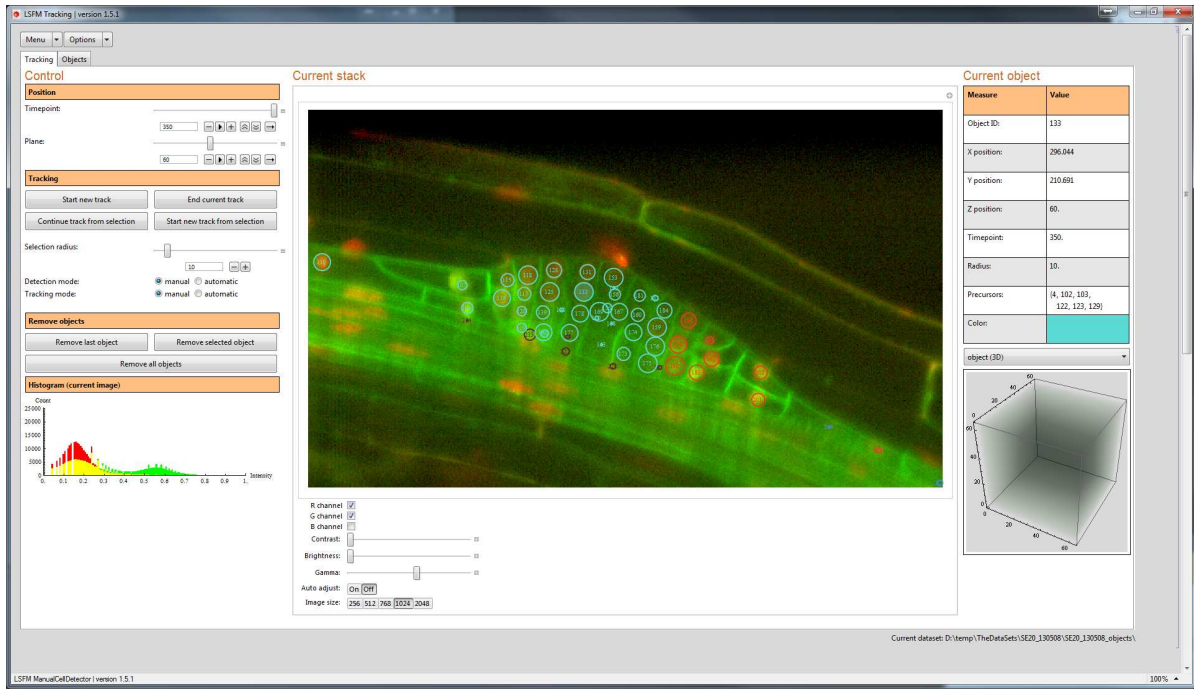
Figure 2.20: Graphical user interface of the cell tracking programm _Trackgen_ written by Alexander Schmitz.

Table 2.6: Cell lineage object list in _Excel_. Position, time point and the list of precursor were saved for the first and last occurrence of each nucleus.

	A	B	C	D	E	F
1	ObjectID	X	Y	Z	Timepoint	Precursors
2	9	179.2	333.9	70	1	{}
3	9	177.2	337.8	69	8	{}
4	368	194.8	328.1	69	9	{9}
5	368	200.6	333.3	73	69	{9}
6	369	161.6	343.0	69	9	{9}
7	369	120.6	361.9	69	64	{9}
8	370	128.5	358.0	69	65	{9, 369}
9	370	111.5	354.7	72	300	{9, 369}
10	371	110.9	363.2	69	65	{9, 369}
11	371	6.2	397.0	65	153	{9, 369}
12	372	20.5	394.4	65	154	{9, 369, 371}
13	372	40.6	378.1	71	300	{9, 369, 371}
14	373	1.6	402.2	65	154	{9, 369, 371}
15	373	1.0	394.4	72	300	{9, 369, 371}
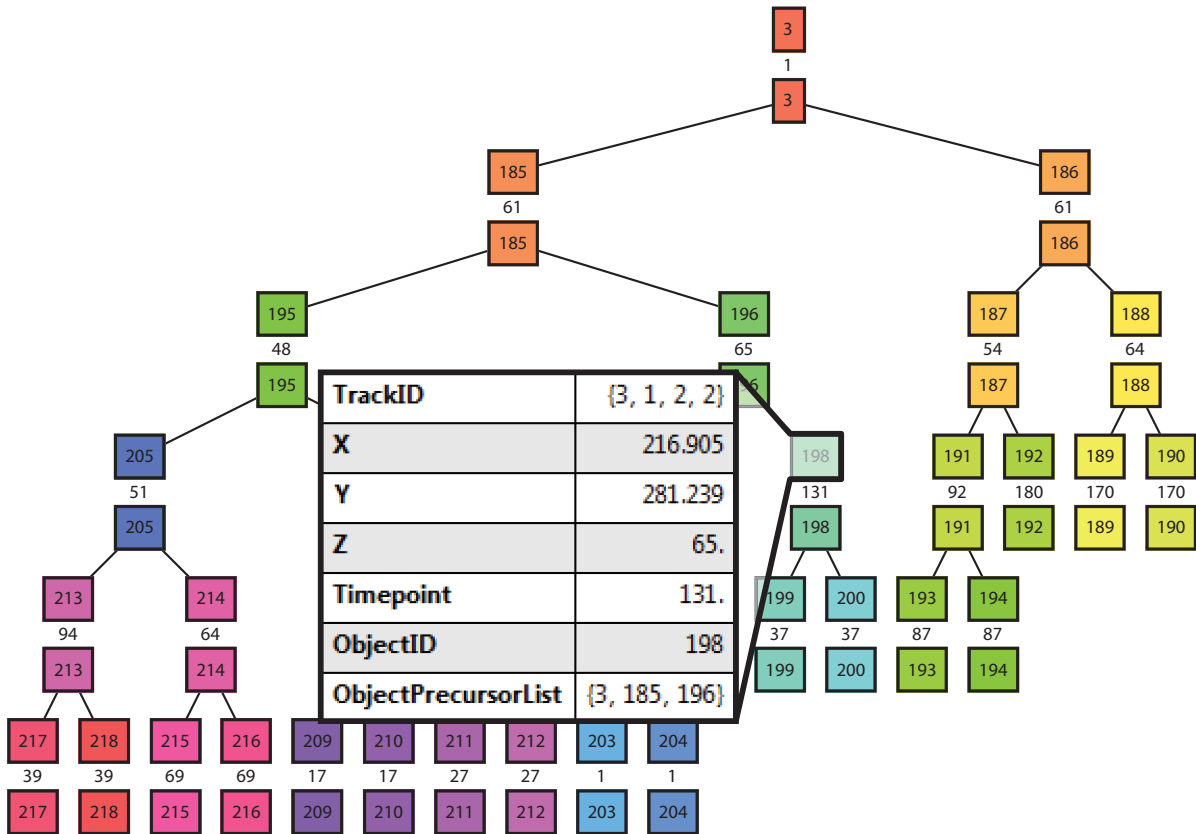
Figure 2.21: Typical lineage tree of founder cell #3 in data set #130607. Each color and number in a box represents an object ID. The number between the ID-boxes represent the time span between the first and the last occurrence of the object. By moving the pointer over an ID-box the detailed information of the position and precursor list is displayed.

The objects identified in *TrackGen* were visualized using a second program *TrackAlyzer* written in *Mathematica* by Alexander Schmitz. *TrackAlyzer* provides an interface for comprehensive visualization and analysis of the cell lineages in three dimensions as a function of time (Fig. 2.22). All properties of lineages or single cell nuclei and their divisions can be highlighted individually. For example, *TrackAlyzer* was used to color code cell division angles, cell lineages that belong to the same cell file or cell layers (Fig. 2.23).

In order to compare the data sets Alexander Schmitz performed an affine transformation of the nuclei coordinates consisting of a translation and a rotation, in order to have standardized and comparable views on the data sets (side-, front-, radial-view, Fig. 2.24). In all visualizations the root tip is downwards and the shoot is upwards (the radial view looks shootwards). Since objects were identified only in their first and last occurrence, the positions in between were interpolated.
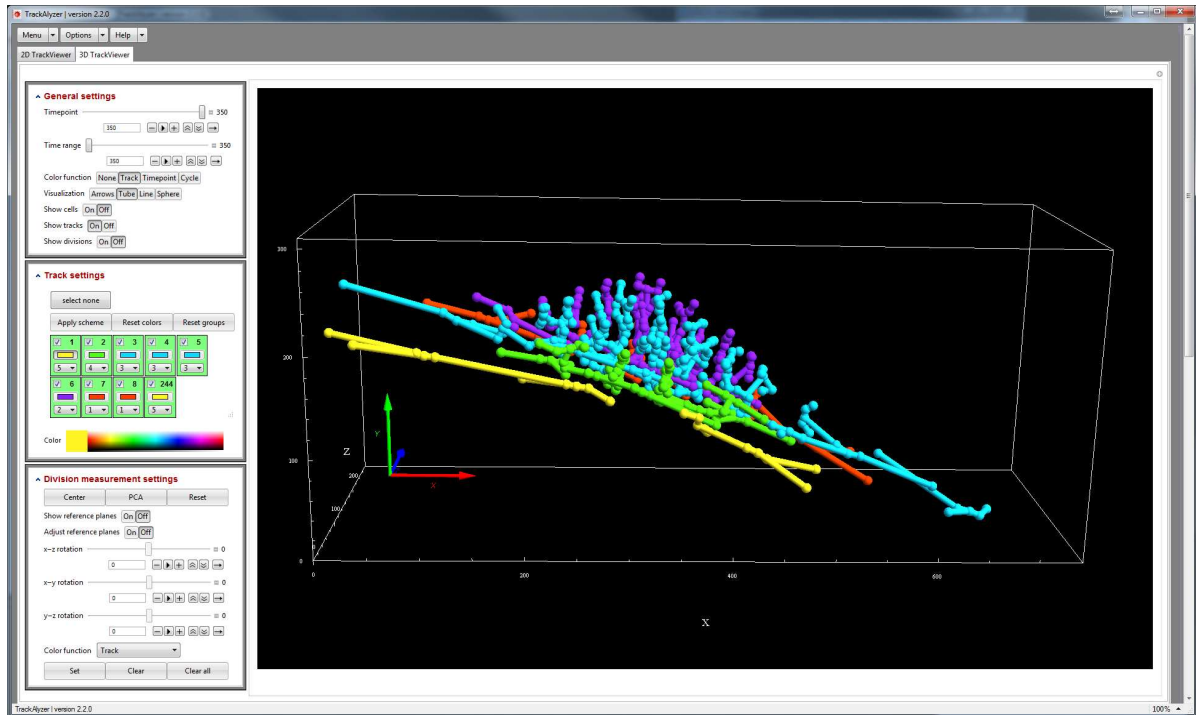
**Figure 2.22: Graphical user interface of the analysis program *TrackAlyzer* written by Alexander Schmitz**.
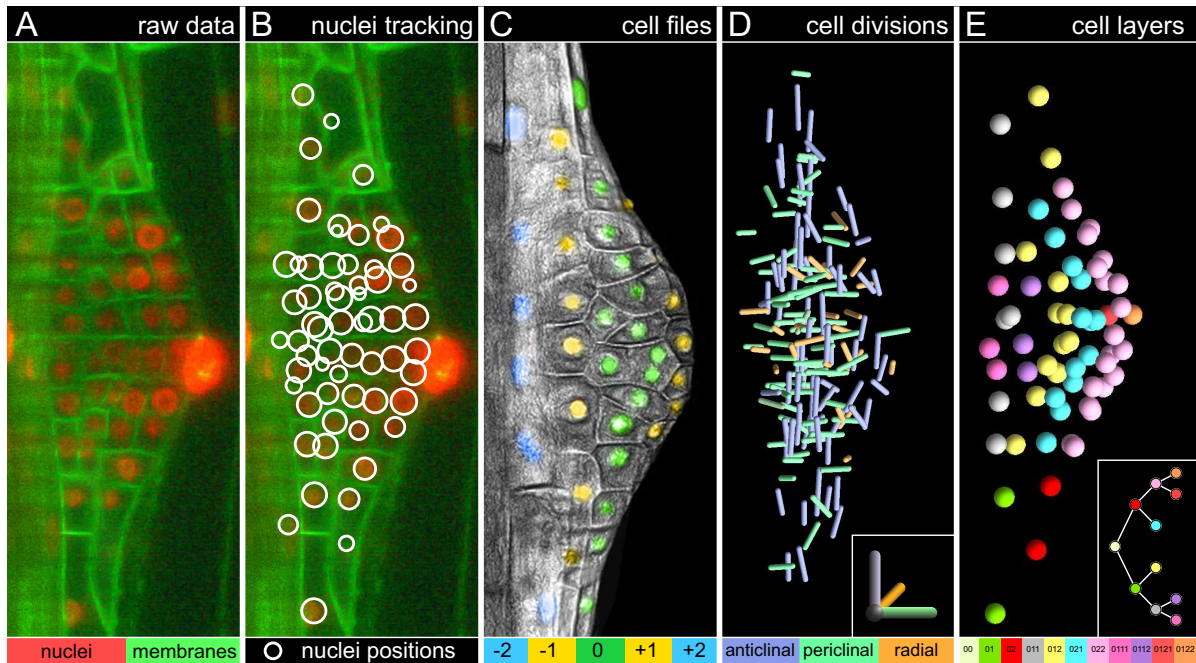
Figure 2.23: Cell nuclei tracking and visualization of quantitative properties. (A) Single slice ($55.8\,\mu m$ deep inside the root) of #120830 at $33\,h\,34\,min$ post gravity-stimulation. (B) Identified nuclei positions are superimposed on the single slice in A. (C) Objects overlaid with the membrane channel raw data. Each color labels the cells that derive from one cell file. (D) Based on the angle of division each cell division event was classified as anticlinal, periclinal or radial. (E) Central cell file color coded based on the history of periclinal division.
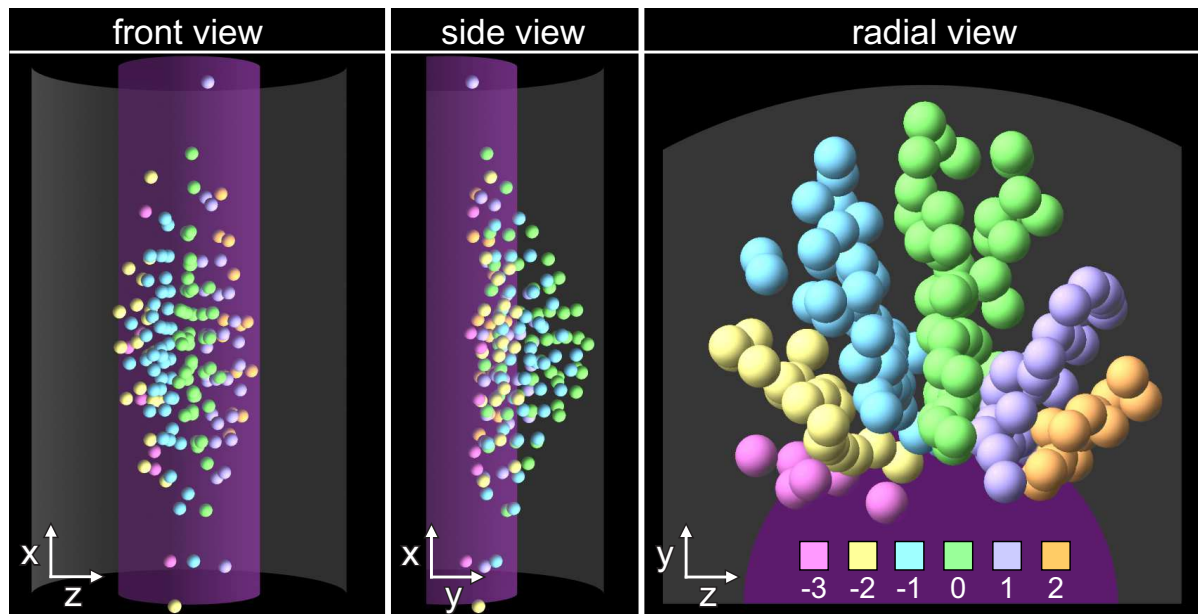
Figure 2.24: Canonical views of a virtual lateral root primordium. The root primary axis is oriented vertically such that the plant shoot is located upwards and the root tip is oriented downwards. Three main view directions can be distinguished: front, side and radial. The radial view corresponds to a transverse view along the main root. Colored spheres indicate the spatial distribution of cell nuclei in all contributing cell files of dataset #121204 at $39\,h\,25\,min$ post gravity-stimulation. Cell nuclei that derived from the same cell file share the same color. The cell file contributing most is termed master cell file and labeled with index #0. Cell files to the left are labeled with negative indices, whereas cell files to the right are labeled with positive indices. The primary root is schematically indicated in grey and the vasculature as a purple cylinder.

3 Results
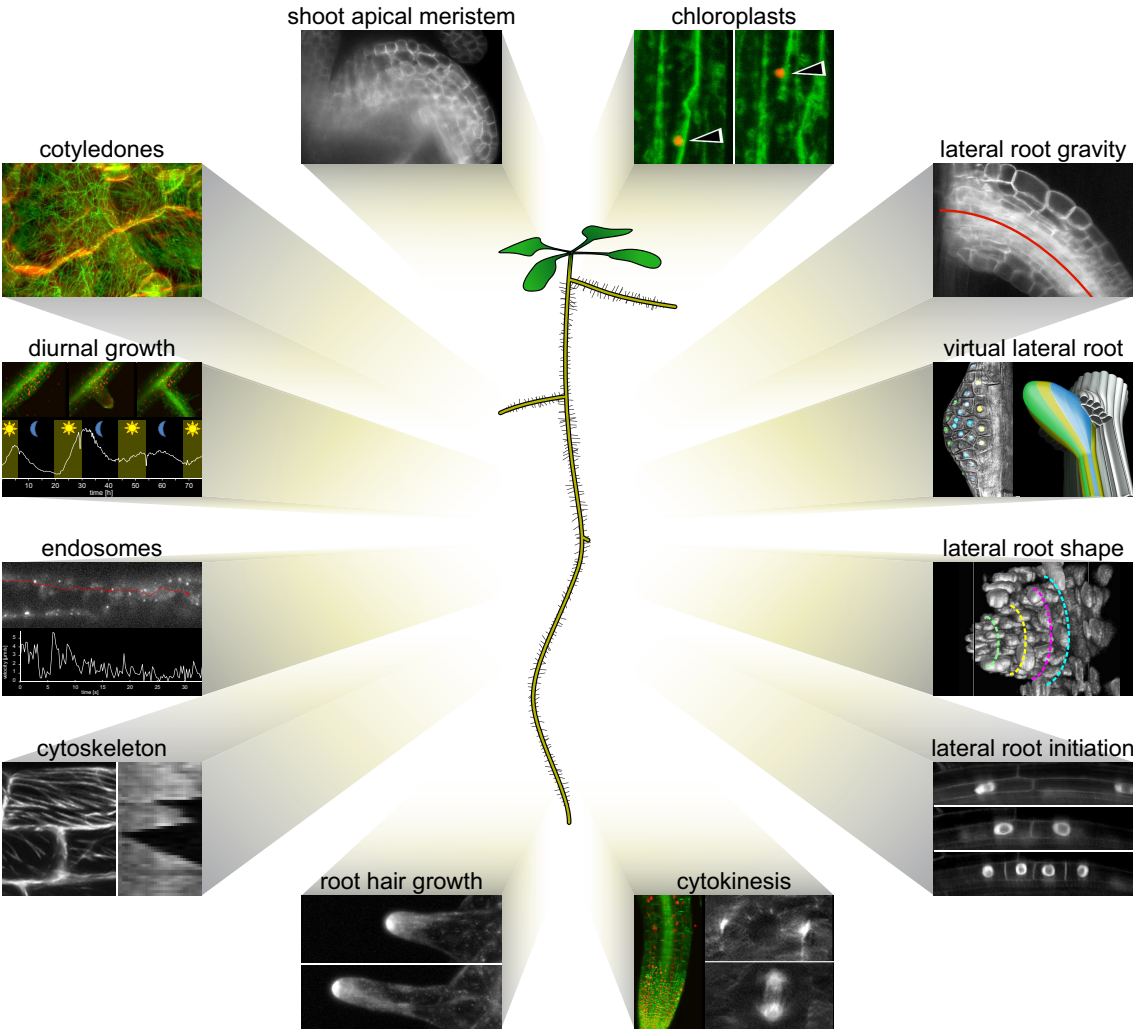
Figure 3.1: Imaging diverse regions of Arabidopsis with LSFM.

The results of this work can be divided into two main parts. The establishment of the method that allows to capture various parts of a plant in close-to-natural conditions, and the comprehensive analyses of lateral root formation. The following chapters show recordings of leaves and other aerial parts of the plant as well as the tip of the root, root hairs and lateral roots (Fig. 3.1). The time scales of the recordings range from seconds for intracellular dynamic observations to a couple of days for the study of organ growth. The quantitative analysis of cell lineage tracking during lateral root formation shows unprecedented details of post-embryonic organogenesis in plants.

chapter	publication	page
imaging conditions	Maizel et al., 2011, *ThePlantJournal*	52
lateral root gravity	Rosquete et al., 2013, *Current Biology*	59
cytoskeleton		62
endosomes		64
chloroplasts		64
root hair growth	Berson et al., 2014, *BMC Plant Biology*	66
cytokinesis	Berson et al., 2014, *BMC Plant Biology*	69
cotyledons		73
shoot apical meristem		73
rice, *Oryza sativa*		76
lateral root initiation	Vermeer et al., 2014, *Science*	77
lateral root shape	Lucas et al., 2013, *PNAS*	79
the virtual lateral root	Wangenheim et al., *in progress*	83

3.1 Plant imaging in the mDSLM

3.1.1 Non-invasive long term imaging of Arabidopsis

In the microscope chamber the plant grows in an upright position with its leaves in the air and its roots in liquid medium. The medium is constantly exchanged via a perfusion system. A light source illuminates the leaves and ensures photosynthetic activity in a diurnal fashion. In addition the root system is shaded as if it grows in the soil. The growth conditions in the monolithic Digital Scanned Light Sheet Microscope (mDSLM) allow to study dynamics of plant growth at organ, cellular and sub-cellular levels over periods of time, ranging from seconds to days.

Plant growth was documented to quantify whether the plant shows regular growth rates or continued growing once the recording process was done. The average growth rate of the primary root was $150\,\mu m/h$ which is similar to that reported in literature (Beemster and Baskin, 1998; Smet et al., 2007). The growth of the lateral root was recorded for up to $90\,h$ without any morphological signs of damage (Fig. 3.2). The plant maintained another $36\,h$ in the microscope without imaging to see whether it continued growing (Fig. 3.2 C). In total the plant maintained $123\,h$ ($>5\,d$) in the mDSLM microscope chamber. After the imaging process the sample holder was placed in a petridish with regular 1/2 MS-medium containing $1\,\%$ sugar and $1.5\,\%$ Phytagel. Several weeks after imaging the plant developed further like plants that where not imaged (Fig. 3.2 D). Taken together, the results suggests that the damage to the plant induced by handling, imaging and maintaining in the microscope chamber can be kept to a minimum and allow observations over periods of days.
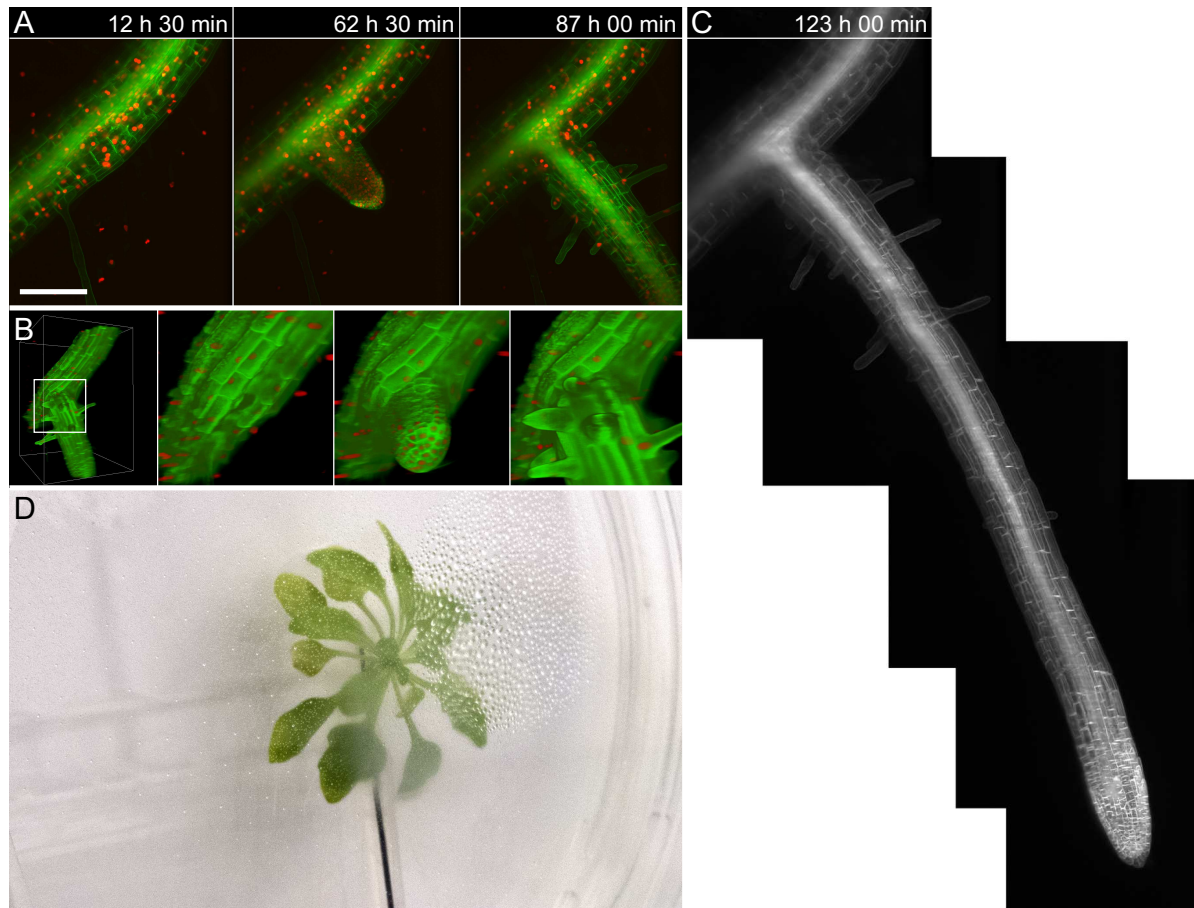
Figure 3.2: Lateral root growth in Arabidopsis - quality control. (A) Maximum-intensity projections at three of in total 350 indicated time points ($90\,h$ recording time, $15\,min$ interval). The seven day old seedling stably expresses 35S::H2B-RFP (red, nucleus label) and 35S::LTI6b-GFP (green, membrane label). (B) A 3D reconstruction shows an overview (left) and three more detailed 3D reconstructions at the same time points as in (A), which illustrates the outgrowth of the lateral root. C) Panorama stitch of five stacks recorded $36\,h$ after the time lapse recording to evaluate further root development. Overall, the plant was in the microscope chamber for 120 h. (D) Arabidopsis plant in the mDSLM sample holder capillary inside of a petri dish seven weeks after the imaging acquisition. Scale bars $100\,\mu m$. Detailed recording metadata on page 161. **Supplemental Movie-3.2**.

3.1.2 Light and growth

Diurnal pattern of lateral root growth

By following the growth of a lateral root, we observed that its growth rate was variable and coincided with the periods during which the plant was illuminated (Fig. 3.2). The fluorescence intensity of the overexpressed fusion protein (35S::LTI6b-GFP) increased at the beginning of the day and decreased during the night.
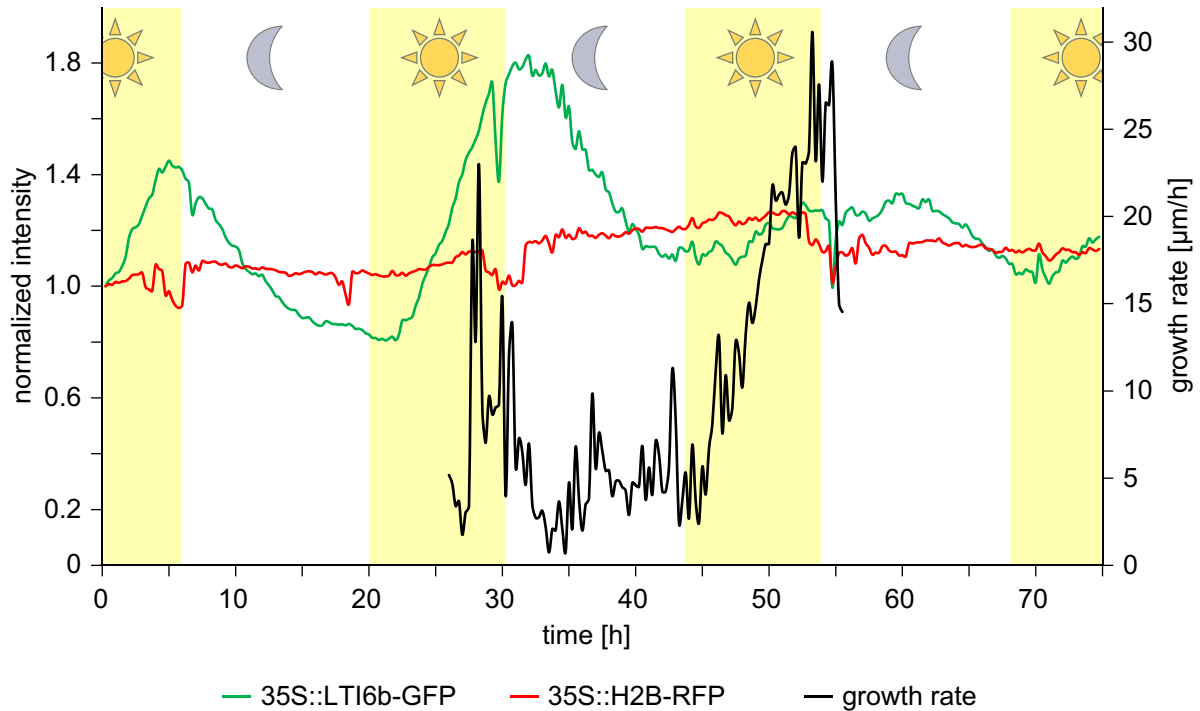
Figure 3.3: Diurnal activity pattern of Arabidopsis. The mean fluorescence intensity and the growth rates were measured in the recording dataset shown in Fig. 3.2. The seven days old seedling stably expresses H2B-RFP (red, nucleus label) and LTI6b-GFP (green, membrane label) under the control of the constitutive active promoter 35S-promoter from the Cauliflower mosaic virus (CaMV). The fluorescence intensity values in the average intensity projections were measured and normalized to the initial value (green and red lines). The growth rate of the lateral root (black line) was measured by tracking the tip by means of the software *Adobe After Effects*.

The growth rates peaked at dusk, which reminds of the diurnal growth rhythm displayed by the shoot (Nozue and Maloof, 2006), in contrary to what was observed by Yazdanbakhsh and Fisahn (2009), where the primary root growth peaked at dawn. Because of this obvious controversy an analysis of the growth rates according to the daytime was performed. Plant were cultured in a $12\,h$ day/$12\,h$ night rhythm and the root system was photographed twice a day (Fig. 3.4). The growth of the 21 primary (10 with sugar, 11 without sugar) and 89 lateral roots (54 with sugar, 35 without sugar) was measured at the end of each day (11 days) and each night (12 nights) and compared with and without saccharose in the medium in order to evaluate the influence of a direct sugar supply.
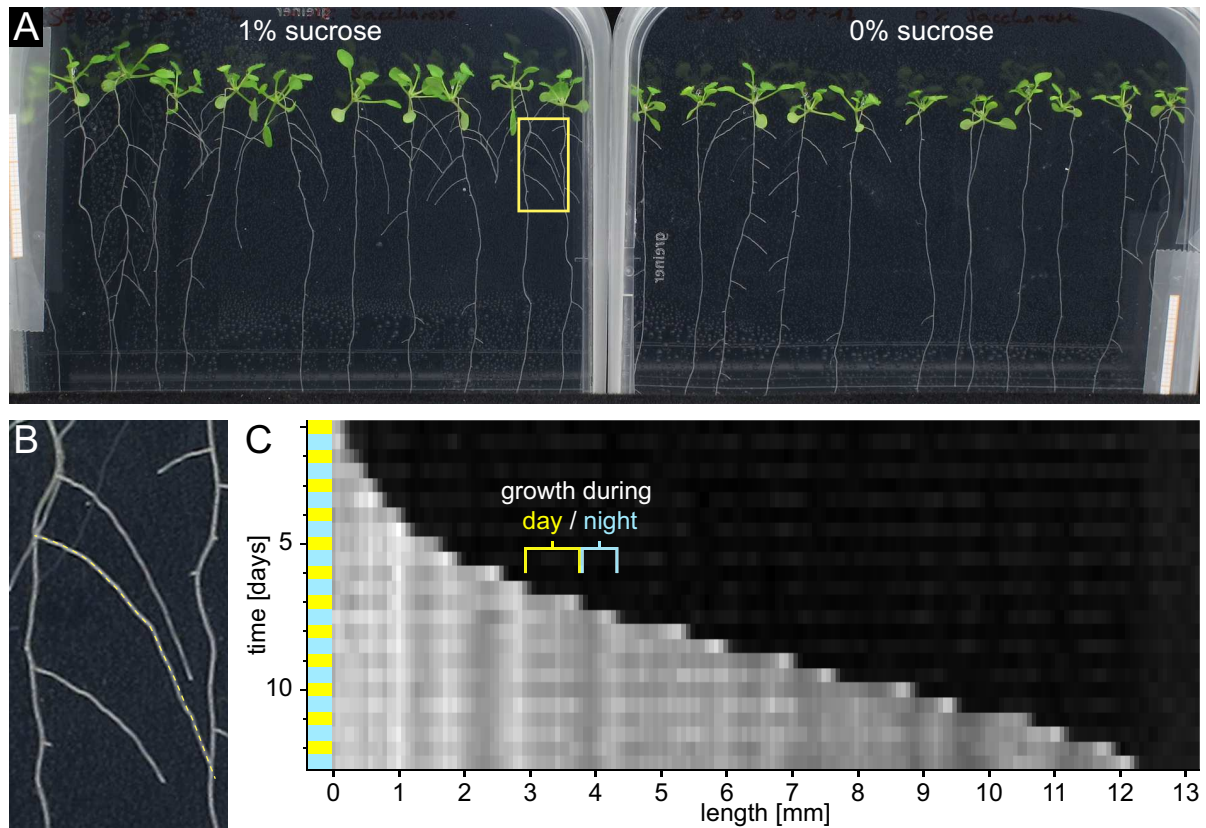
Figure 3.4: Diurnal root growth in Arabidopsis. (A) Time lapse recording of Arabidopsis seedlings. The plants grew in a petridish in a $12/12\,h$ day/night rhythm. Images were captured in the morning and evening. (B) Detail of the yellow box in A. The yellow line is plotted as a Kymograph in C. (C) Kymograph of a lateral root as a function of time. The growth was measured from 21 plants, i.e. 21 primary roots (10 with sugar, 11 without sugar), 89 lateral roots (54 with sugar, 35 without sugar), 11 days and 12 nights. Overall, $1.45\,m$ roots were measured.

The growth rate of young lateral roots is relatively low but accelerates with time until they reach a maximum growth rate of about $75\,\mu m/h$ at about five days after emergence (Fig. 3.4 C). For the mean growth speed, only fast growth rates were taken into account, i.e once the root growth was linear. During the day, the primary roots with sugar grew with $370\,\mu m/h$, lateral roots with $75\,\mu m/h$ (Tab. 3.1). The roots grew about $50\,\%$ less at night. Roots without sugar grew about $75\,\%$ compared to the growth with sugar, but again, the night to day ratio showed $50\,\%$ of the growth at night (Tab. 3.1). The statistical analysis confirms the observation made in the mDSLM microscope chamber.

Table 3.1: Growth rates of primary roots and lateral roots during day- and night time, w/wo sugar. The growth was measured from 21 plants, i.e. 21 primary roots (10 with sugar, 11 without sugar), 89 lateral roots (54 with sugar, 35 without sugar), 11 days and 12 nights. Overall, $1.45\,m$ roots were measured.

growth rate	w/ saccharose		wo/ saccharose	
$[\mu m/h]$	primary root	lateral root	primary root	lateral root
daytime	367.8 ± 71.6	75.1 ± 37.5	302.7 ± 75.7	57.5 ± 39.3
	(n = 47)	(n = 374)	(n = 70)	(n = 196)
nighttime	199.5 ± 39.3	44.0 ± 22.9	144.3 ± 43.4	29.9 ± 18.8
	(n = 52)	(n = 377)	(n = 65)	(n = 109)
night/day ratio	0.54	0.59	0.48	0.52

Shading the root system - lateral root growth in light versus darkness conditions

Lateral roots usually emerge at a right angle out of the primary root. Immediately after emergence lateral roots establish a well-defined angle with respect to the gravity vector, called the gravitropic set-point angle (GSA, see chapter 3.1.3 on page 59) (Digby and Firn, 1995; Rosquete et al., 2013). However, upon emergence the direction of growth depends on environmental conditions. We observed that the growth direction of the lateral roots is affected by light (Fig. 3.5). When roots are exposed to light they follow the gravity and grow constantly downwards, whereas roots in darkness grow straight at an angle of $70.1° \pm 9.6°$ (Fig. 3.6). Due to this altered phenotype the root system was covered in the microscope chamber and thereby exposed to considerable less light than the leaves (Fig. 2.11 on page 33).
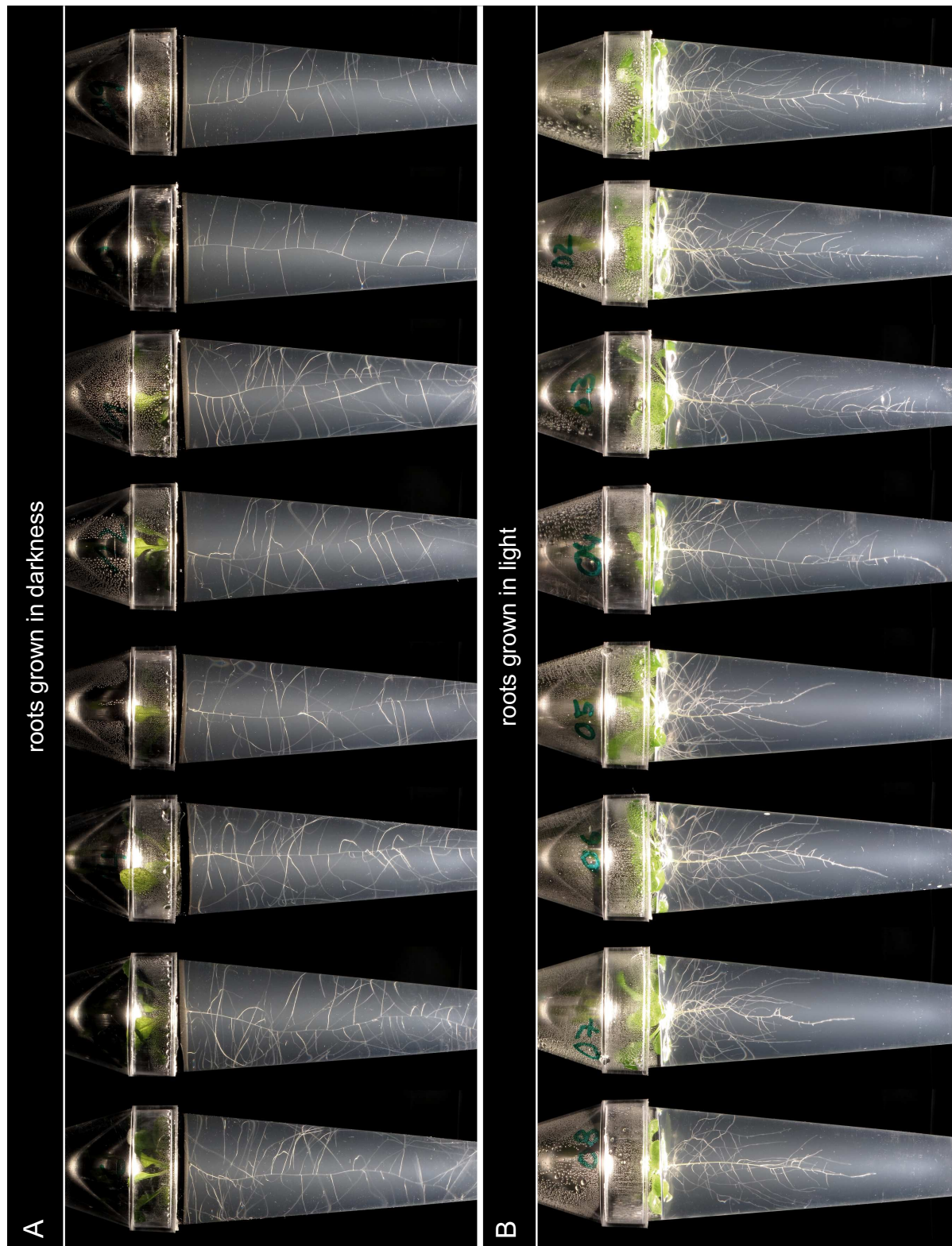
Figure 3.5: Root system of Arabidopsis grown in light versus darkness conditions. A) Two weeks old Arabidopsis plants in transparent pots filled with 1/2 MS medium containing 0.3 % Phytagel. The outside of the pots was covered by an aluminum foil, the surface of the gel inside the pot was covered by small pieces of a plastic sheet. B) Same conditions as in A but without covering the root system from light. This experiment was repeated five times with similar results (roots in light conditions n=74, roots in darkness conditions n=77).
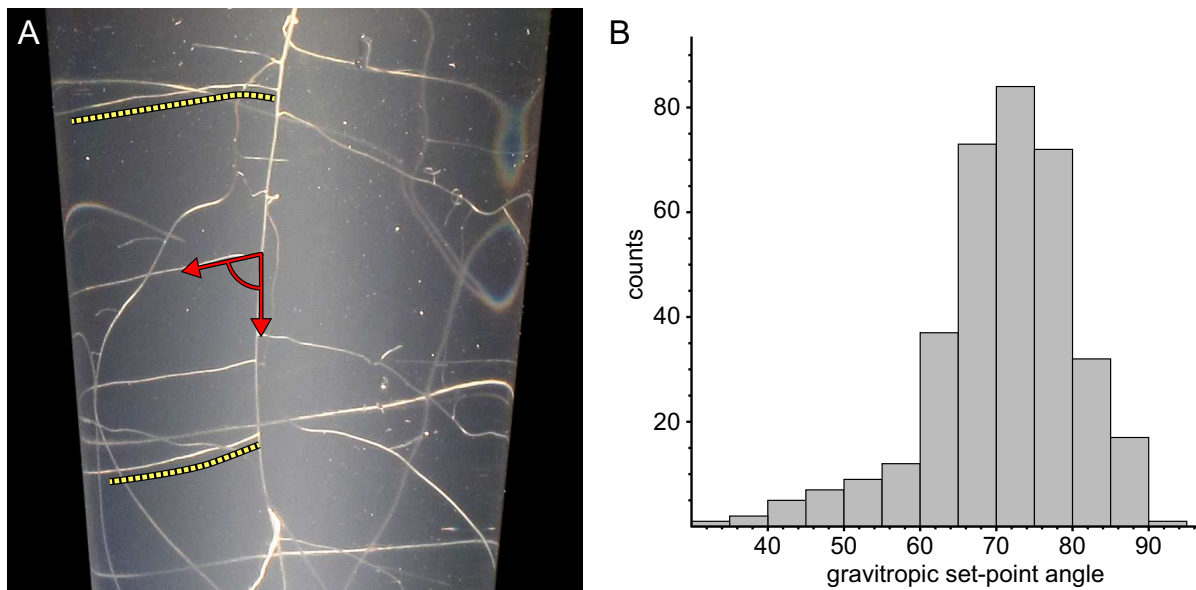
Figure 3.6: Lateral roots growth angle relative to the gravity vector. (A) The three weeks old Arabidopsis root was grown in dark conditions. Red arrow indicate the lateral root growth angle with respect to the vector of gravity. The yellow dashed lines highlight lateral roots that initially emerge orthogonal to the main root and establish the particular angle during growth. (B) Distribution of lateral root growth angle. In total, 352 lateral roots were measured from 35 plants in four independent experiments.

Interval illuminated light conditions don't impair growth

Plant growth is influenced by many abiotic factors, e.g. the light environment. Photoreceptors such as phytochroms, cryptochromes or phototropins modulate processes that are linked to the circadian clock, e.g. transpiration, cell elongation or flowering time. An interrupted night by a short period of light can simulate a long day, i.e. long-day plants start flowering although the real day is still a short day (Weiler and Nover, 2008). However, it is not known whether a disruption of the day by a short period of darkness would have an effect on plant growth. This condition was simulated in the plant incubator to test whether the interval illumination during the day in the mDSLM affects the phenotype of the plants. A common way to assess changes in root development is to determine the lateral root density (Dubrovsky et al., 2006). The number of emerged lateral roots was compared in different illumination conditions. Six days old plants (grown in long day conditions (16/8)) were transferred to different light conditions. The control plants continued growing in the 16/8 long day condition. The second condition simulated the illumination interval in the microscope chamber, i.e. in the 16/8 long day, the light was turned off every $5\,min$ for a $1\,min$ period of darkness ($1\,min$ darkness, $4\,min$ light). In

the third condition, the plants were continuously exposed to light but the period was reduced to the same total amount of light per day as in the interval condition ($12.8\,h$ instead of $16\,h$). Plants in $16\,h$ light per day had twice as much lateral roots than plants with $12.8\,h$ light per day (Tab. 3.2). The plants in the $12.8\,h$-interval illumination conditions had slightly less lateral roots than in the $12.8\,h$-continuously illuminated condition. This suggests that the quality of the light (continuously or interval) does not impair the number of lateral roots, only the amount of light per day does.

Table 3.2: Number of lateral roots per plant under different light conditions. A single experiment was performed.

hours of light / day	number of plants	number of lateral roots	lateral roots/plant
16	50	510	10.2
12.8 (interval illumination)	43	215	5.0
12.8	47	258	5.5

3.1.3 Gravitropic set-point angle establishment in lateral roots

Most plant imaging methods have relied on a horizontal positioning of the plant between coverslips. Mounting the plant parallel to gravity allows the study of root growth in their natural orientation. By recording the root with a plasmamembrane marker the establishment of this angle could be observed at a cellular level, which was not described so far.

In Arabidopsis lateral roots grow at a particular angle to the gravity vector. The so called Gravitropic set-point angle (GSA) defines the angular growth of an organ with respect to the gravity vector (GSA = 0° for positive and 180° for negative orthogravitropism). It is very likely that an asymmetric distribution of auxin is involved in controlling this growth as auxin is a key player in differential growth of various tissues (Kleine-Vehn and Friml, 2008). With LSFM the dynamics of outgrowing lateral roots establishing the GSA was observed at cellular level. The result was a contribution to the paper *An Auxin Transport Mechanism Restricts Positive Orthogravitropism in Lateral Roots* in which a role for the PIN auxin efflux transporters in response to gravity of lateral roots in Arabidopsis is described (Rosquete et al., 2013). Numerous hints revealed that an asymmetric distribution of auxin in the lateral root tip supported by PIN-proteins can be linked to the establishment of the GSA (Rosquete et al., 2013).

Young lateral roots emerge at a right angle to the primary root. Before emergence, the lateral root is made up of small cells and a defined elongation zone lacks. A kymograph along the upper side and the lower side of the root was used to measure the dynamics of cell elongation of five cells in each of the epidermis cell files. While the cells constantly grow, cells on the upper side elongate more compared to cells at the lower side of the root (Fig. 3.7).
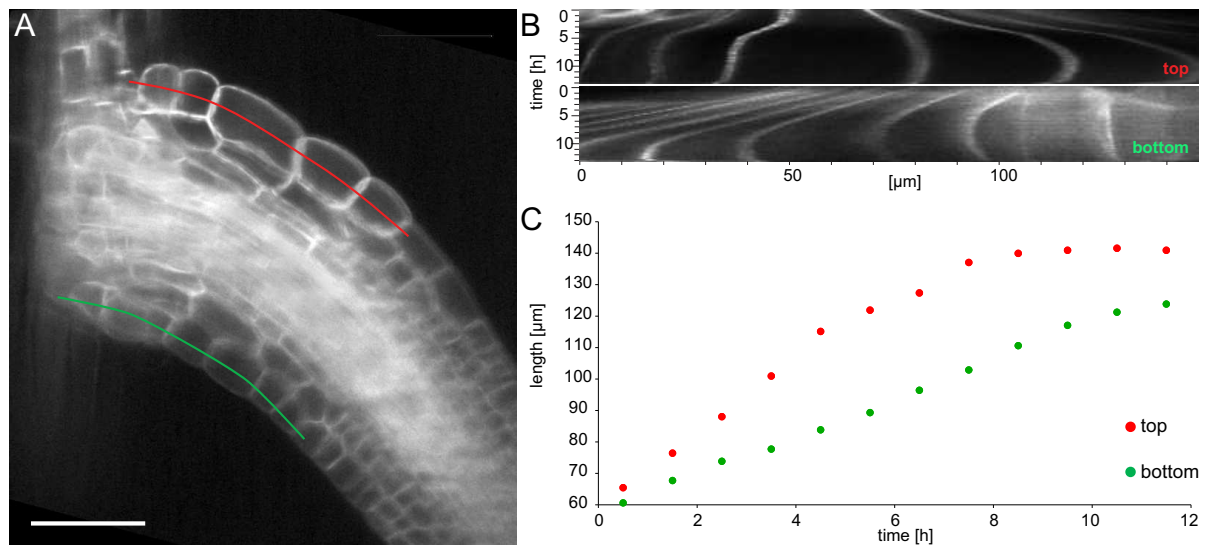

Figure 3.7: GSA formation in lateral roots (A) Live imaging of an emerging lateral root. The six days old Arabidopsis expresses 35S::LTI6b-GFP (plasmamembrane label) was recorded every 15 min for a time period of 38 h. The red and green line denote the top and bottom epidermis cell files. The pixels along these lines are plotted as a function of time (B). The length of five connected cells of the bottom and top cell files was summed and plotted against time (C). Scale bar: 50 μm. Detailed microscopy metadata on page 169. **Supplemental Movie-3.7**.

The triple mutant *pin3 pin4 pin7* showed a GSA closer to 90° (Rosquete et al., 2013). Dynamic live imaging of the *pin3 pin4 pin7* triple mutant should have confirmed this result. Since the mutant does not express a fluorescence protein the root was stained with the membrane dye FM 4-64. In two recordings the GSA was found to be close to 90° (Fig. 3.8, A). Cell length measurements of the upper and lower epidermis cell files showed a similar elongation of cells on both sides (Fig. 3.8, B). But, control experiments with FM 4-64 dye stained wildtype roots showed unexpected wavy phenotypes in the further development of the lateral roots (Fig. 3.8, C). Because of the potential toxic effect of the FM 4-64 on the directional growth of lateral roots this result was not included in the manuscript. A transgenic plasmamembrane marker could have been used to study the cell elongation dynamics in this mutant.
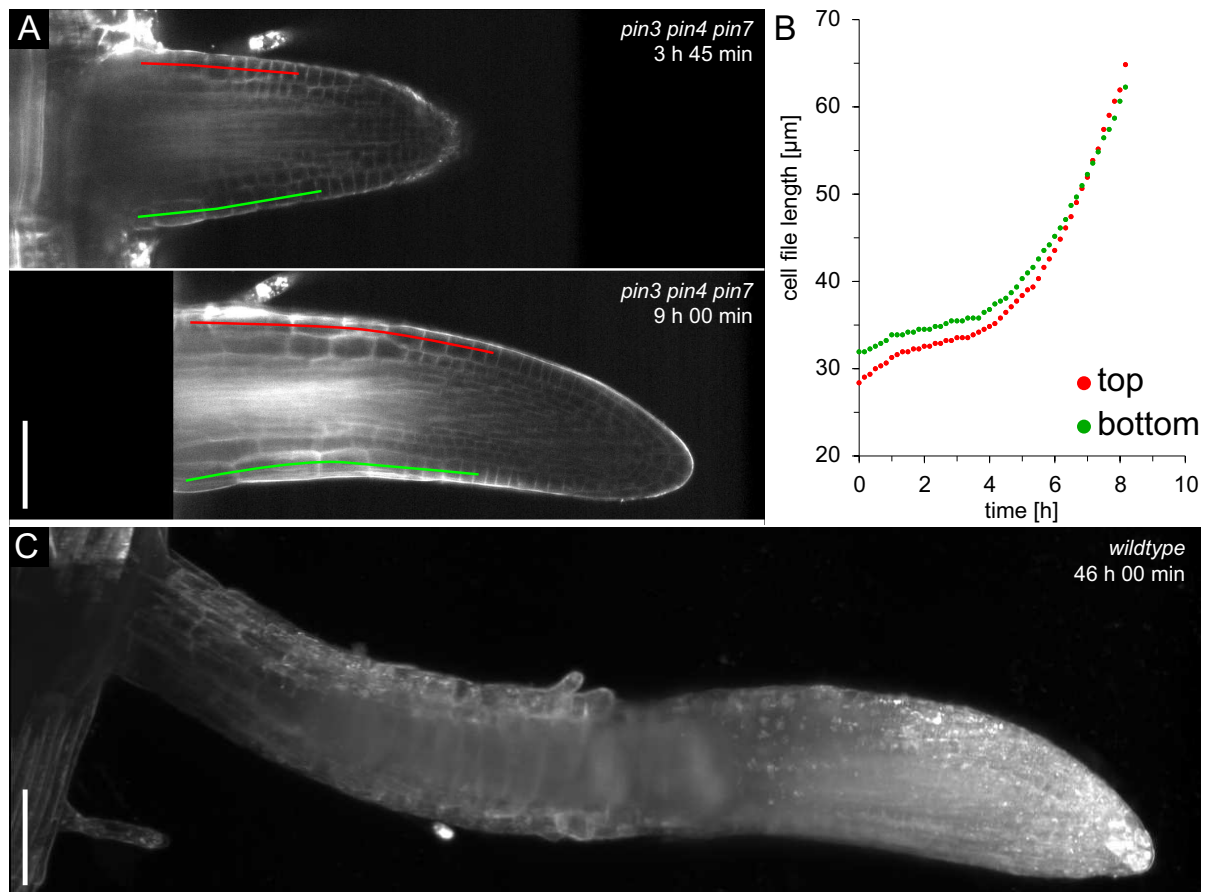
Figure 3.8: Lateral root GSA formation in *pin3 pin4 pin7* triple mutant and wildtype. (A) Two time points of the time lapse recording in a single longitudinal section of the *pin3 pin4 pin7* triple mutant labeled with the membrane dye FM 4-64. The length of five connected cells of the top and the bottom cell file was summed and plotted against time (B). (C) Last time point of a control experiment with a wildtype plant labeled with FM 4-64. Detailed microscopy metadata of the PIN-mutant recording on page 170 and wildtype recording on page 171. Scale bar: $50\,\mu m$ (A), $100\,\mu m$ (B). **Supplemental Movie-3.8**.

3.1.4 Dynamics of the cytoskeleton and endosomal compartments

Intracellular vesicle transport processes are essential tasks within a cell to maintain the membrane and protein homeostasis. The delivery, recycling and depletion of molecules play a key role to ensure the correct distribution of all compounds within the cell. A quick response (seconds) in the protein distribution allows the cell to cope with environmental changes. The recording of such dynamics, especially the fast moving endosomes is a serious challenge for imaging techniques. Such small vesicles, having only a few hundred nanometers in diameter, require a high magnification and a high acquisition speed to

capture the up to $10\,\mu m/s$ fast movements. In plant cells vesicles are transported mainly by the motor protein myosin which moves along the actin cytoskeleton. Light Sheet-based Fluorescence Microscopy combines spatial resolution, acquisition speed and large volume recording with high signal-to-noise ratio. In addition, the special plant mounting, large field of view imaging allows the observation of whole organs and the endosomes distribution during developmental processes. For example, the subcellular localization of RabA1d labeled vesicles during cell plate formation and root hair growth respectively was analyzed from one and the same recording (Fig. 3.16 and Fig. 3.20).

Dynamics of microtubules and actin

The cytoskeleton is involved in many dynamic processes within a cell such as mitosis, the association with the cellulose-synthase at the plasmamembrane (Paredez et al., 2006), the positioning of the nucleus (Ketelaar et al., 2002), or the transport of endosomal compartments. Imaging these processes require a high spatial as well as temporal resolution. LSFM was used to record the dynamic of microtubules assembly and disassembly (Fig. 3.9) as well as the dynamics of the actin filaments (Fig. 3.10 and 3.11). The results show that the microscope is able to capture such dynamic events at a high temporal resolution with a very good signal to noise ratio.
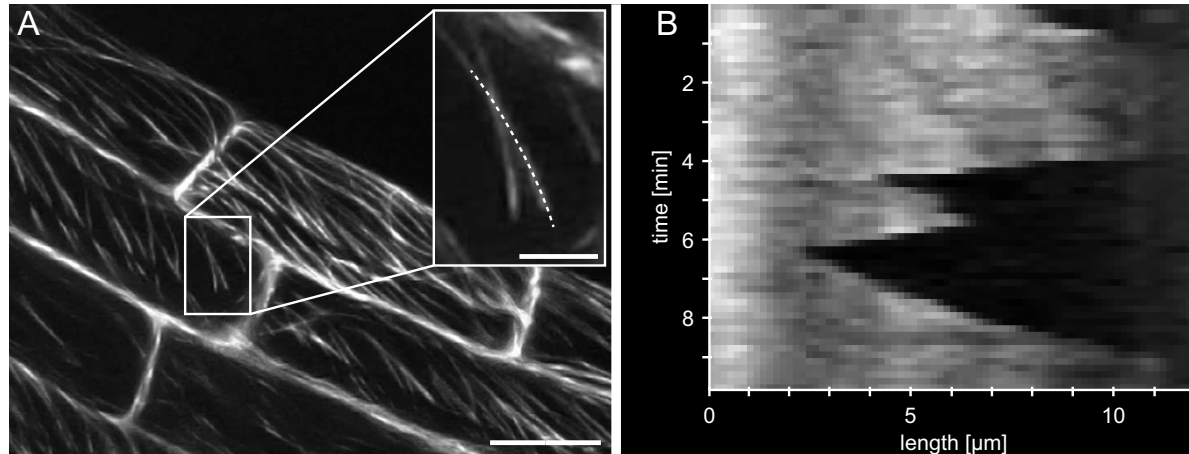
Figure 3.9: Growing and shrinking of microtubules. (A) Root epidermis cells of a five days old Arabidopsis expressing 35S::GFP-MAP4. The dashed line indicates a growing and shrinking microtubulus. (B) Kymograph of the yellow dashed in (A). A stack of 47 planes was recorded every $10\,s$ for a period of $10\,min$ with a $40\times/0.75$ objective lens in the detection path and a $5\times/0.16$ objective lens in the illumination path. Scale bar: $20\,\mu m$ (overview), $5\,\mu m$ (detail). **Supplemental Movie-3.9**.
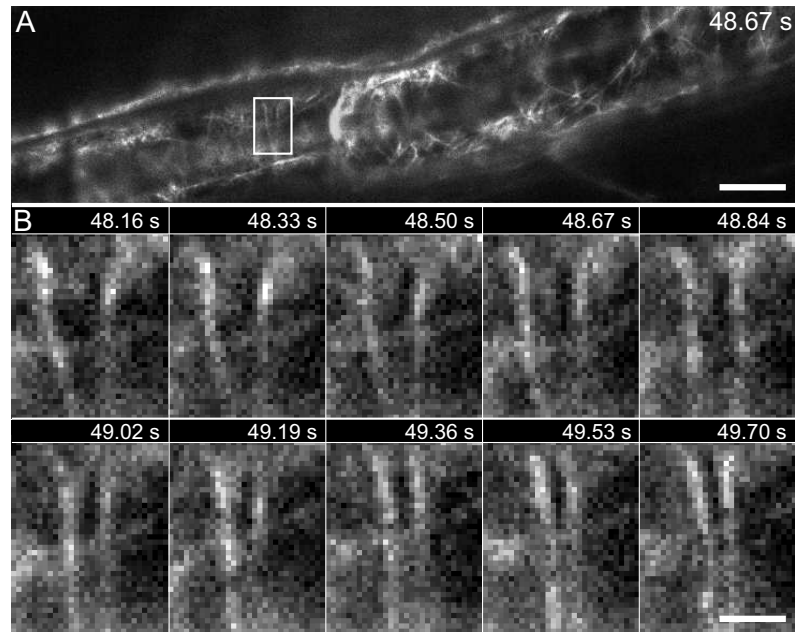
Figure 3.10: Dynamic of actin filaments. (A) Single slice of a root epidermis cell of a six days old Arabidopsis expressing 35S::GFP-Talin. (B) Montage of the boxed area in A at several indicated time points. Two bundels of actin filaments move towards each other in a time period of $1.5\,s$. A single plane was recorded at $5.8\,fps$ for $2\,min$ with a $40\times/0.75$ objective lens in the detection path and a $5\times/0.16$ objective lens in the illumination path. Scale bar: $10\,\mu m$ (overview), $2\,\mu m$ (detail). **Supplemental Movie-3.10**.
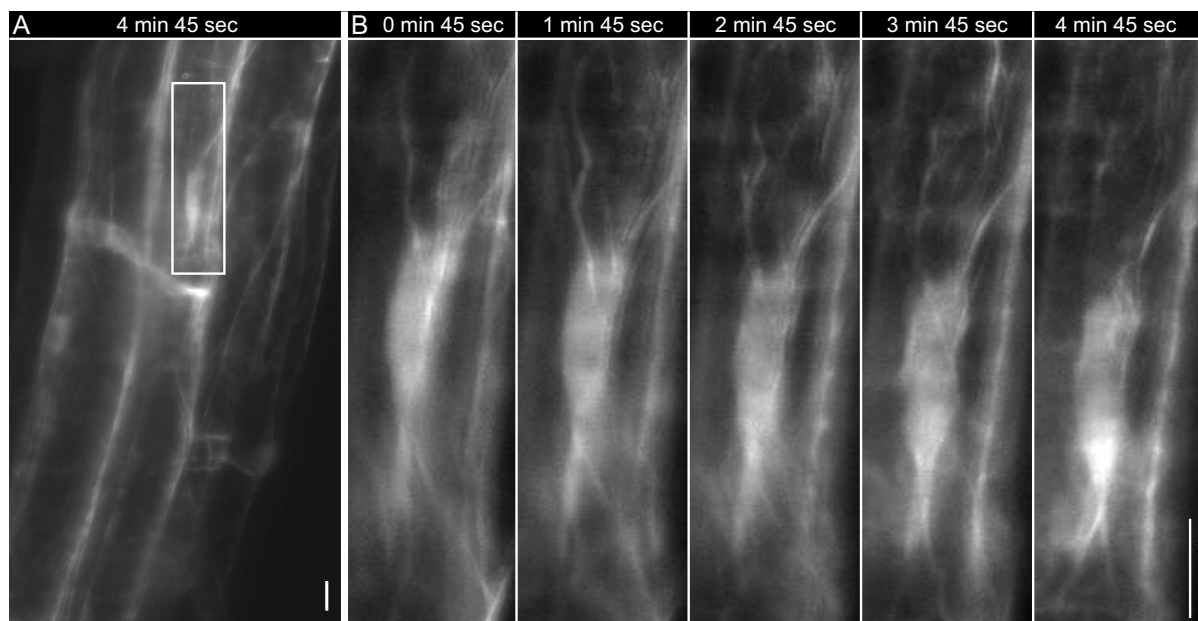
Figure 3.11: Actin around the nucleus. (A) Sum-projection of a stack of 10 planes in the cortex layer. The last time point of a time lapse recording of a seven days old Arabidopsis expressing 35S::GFP-Talin is shown. (B) Five time points of the time lapse recording. The stack of images was recorded every $15\,s$ for a time period of $5\,min$. The boxed area is enlarged in B. Scale bar: $10\,\mu m$. Detailed microscopy metadata on page 158. **Supplemental Movie-3.11**.

Dynamics of endosomal compartments

The dynamic movement of chloroplasts was observed in the hypocotyl (Fig. 3.12) as well as stromule membrane protrutions of plastids in root cells (Fig. 3.13). Single endosomal compartments move with up to several $\mu m/s$, thus trajectory tracking requires a high temporal resolution. The mDSLM allows a recording speed of up to $25\,fps$. In combination with a high magnification it was possible to follow the fast moving endosomal compartments (Fig. 3.14). The RabF2a-labeled endosomes (late endosomes) show an average speed of $2.3\,\mu m/s$ and a maximum speed of $5.8\,\mu m/s$ (Fig. 3.14). An endosome labeled with GFP-RabA1d moves much faster with an average speed of $5.4\,\mu m/s$ and show a maximum speed of $10\,\mu m/s$ (Fig. 3.15). The difference in the speed of these two different endosomal compartments confirms previous results using spinning-disc confocal microscopy where the speed of several endosomal compartments was compared with statistically relevant evidence (diploma thesis Wangenheim (2009), and von Wangenheim et al., *submitted in Plant Physiology*). The results show that light-sheet microscopy can be used to characterize the organization, dynamics and interactions of endosomal compartments and the image quality is comparable to other fluorescent microscope techniques that are characterized by high frame rates with a high signal to noise ratio, such as spinning-disc confocal microscopy.
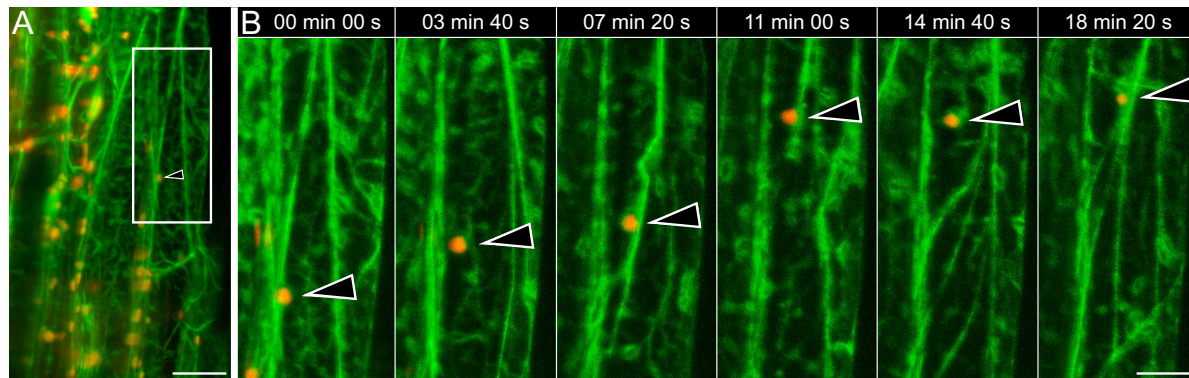
Figure 3.12: Chloroplast movement. A time lapse recording of a five days old Arabidopsis expressing the actin marker 35S::GFP-Talin (green channel). (A) Overview of epidermis cells in the hypocotyl. The boxed area is enlarged in B). (B) Six time points out of 60. The arrowhead highlights a chloroplast which moves through the cell. The chloroplast's autofluorescence (red channel) was excited at $488\,nm$ and the emission was filtered using a 514 longpass filter. Images were collected every $20\,s$ with the $63\times/1.0$ objective lens in the detection path and the $5\times/0.16$ objective lens in the illumination path. (green: actin, red: chloroplasts autofluorescence). Scale bar: $20\,\mu m$. Detailed microscopy metadata on page 160. **Supplemental Movie-3.12**.
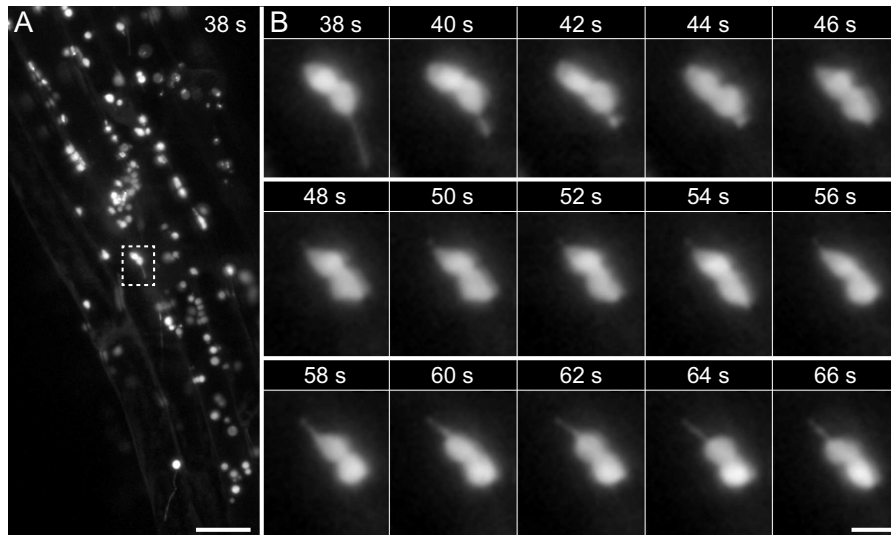
Figure 3.13: Membrane dynamic in plastids. Time lapse recording of a 5 days old Arabidopsis root expressing the plastid marker 35S::SSU-GFP (SSU - small subunit of ribulose-1,5-bisphosphate carboxylase). (A) Overview, the dashed boxed area is enlarged in (B). (B) Time series of the recording at indicated time points. Images were collected every $2\,s$ with the $40\times/0.75$ objective lens in the detection path and the $5\times/0.16$ objective lens in the illumination path. Scale bar: A) $20\,\mu m$, B) $2\,\mu m$. Detailed microscopy metadata on page 159. **Supplemental Movie-3.13**.
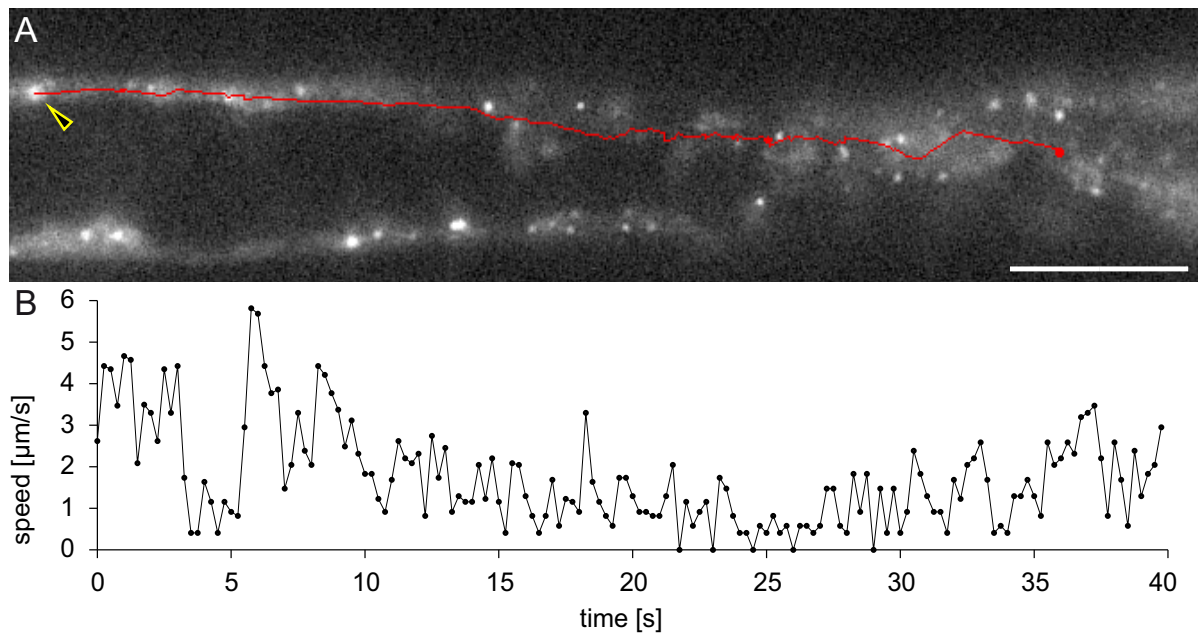
Figure 3.14: Tracking of late endosomes. (A) The first time point of a single plane time-lapse recording of an Arabidopsis root hair. The six days old plant expresses the late endosome marker UBQ10::YFP-RabF2a. The yellow arrowhead highlights an endosome which moves through the cell. The red colored line indicates the trajectory of the endosome in a time period of $40\,s$. Tracking was performed using the *Manual Tracking* plugin in *Fiji*. Its speed as a function of time is shown in B. Images were recorded at a rate of $4\,fps$ with the $63\times/1.0$ objective lens in the detection path and the $5\times/0.16$ in the illumination path. Scale bar: $10\,\mu m$. **Supplemental Movie-3.14**.
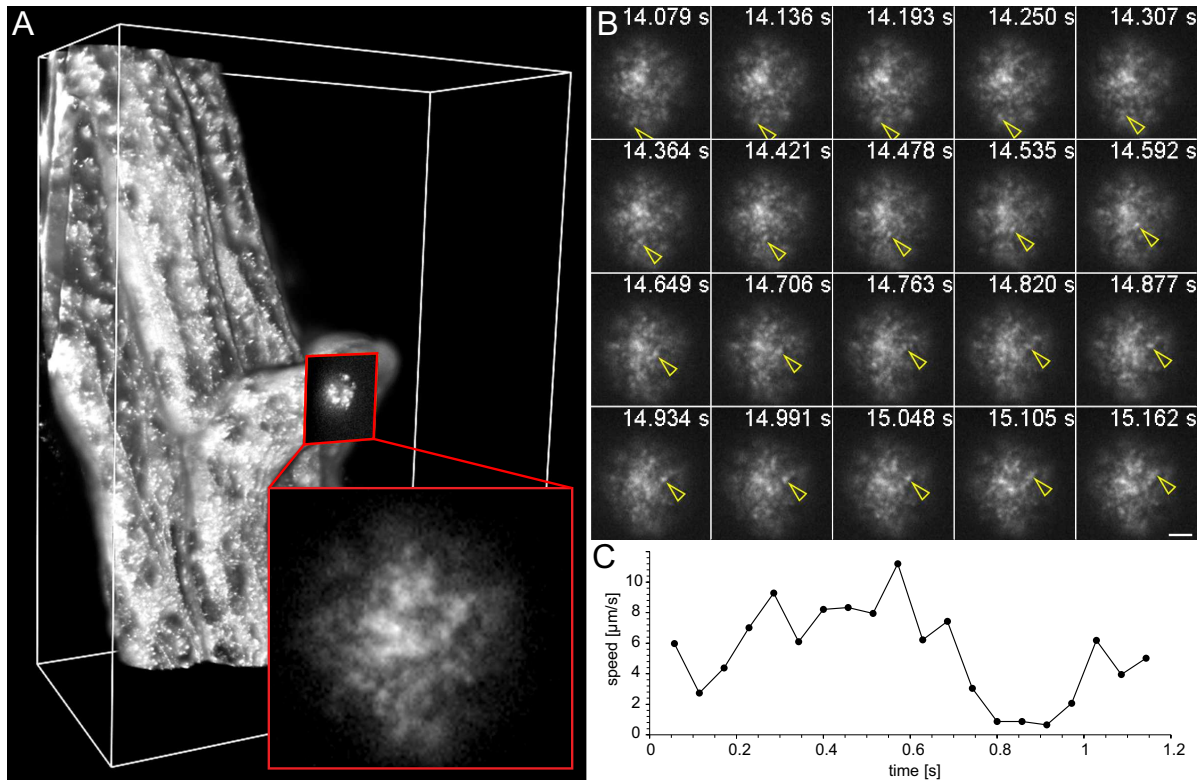
Figure 3.15: Endosome tracking in a growing root hair tip. (A) 3D-reconstruction (overview) of a part of the primary root of a five days old Arabidopsis expressing 35S::GFP-RabA1d. The red box highlights the region of interest at the tip of a growing root hair which was recorded in a single plane. (B) Montage of the single plane (red box in A) at different time points. The yellow arrowhead highlights an endosome which was tracked manually by means of the software *Adobe After Effects*. (C) Speed diagram of the tracked data. Images were collected with the $63\times/1.0$ objective lens in the detection path and the $5\times/0.16$ objective lens in the illumination path with a frame rate of $17.54\,fps$ (Andor Clara, 2×2-binning was used). Scale bar: $2\,\mu m$. **Supplemental Movie-3.15**.

Oscillating root hair growth

The small Rab-GTPase A1d (RabA1d) is localized at vesicles that accumulate in the tip of growing root hairs (Ovečka et al., 2010; Asaoka et al., 2013). It is very likely that these endosomes are involved in the growth process but so far there was no evidence whether the localization in the root hair tip can be correlated with the growth rate of the root hair. To correlate this the growth rate and the fluorescence signal of GFP-RabA1d was measured in growing root hairs. A stack of 388 images was recorded every $2\,min$ for a time period of $10\,h$, in total 1.15 terabytes of data was generated. Each time point consists of $2,145$ megapixel (voxel size x/y/z $= 0.16\,\mu m/0.16\,\mu m/0.645\,\mu m$). To extract the needed information from such a big dataset was a challenge. The root hairs grow more or less perpendicular to the surface of the cylindrical shaped main root, thus, the

position and orientation of each root hair varies. To analyze the growth of a root hair, the stack of images was cropped to a smaller region. The resulting mini-stack was scaled in z to obtain voxels that can be rotated without distortions (Fiji-Plugin TransformJ: Scale, interpolation scheme: linear). The dataset was rotated in order to have a side view on the root hair. After background subtraction, the image stack was flattened using a sum-projection. These images were imported in *Adobe After Effects*. First, the image sequence was tracked and stabilized around the primary root to correct for any movements or drifts (a distinctive region, e.g. contact point of two cells, was followed in each frame of the sequence). Then, the root hair tip was tracked. The coordinates where used to calculate the displacement d between two time points:

$$d \;=\; \sqrt{(x_t - x_{t-1})^2 + (y_t - y_{t-1})^2}$$

the growth rate in $\mu m \,/\, min$ was calculated by including the pixelsize px in μm and the recording interval time t in min:

$$growthrate \;=\; \frac{d \cdot px}{t}$$

In order to measure the fluorescence intensity in the tip region the tracked coordinates were used to reverse translate and thereby stabilize the footage around the tip. These images were exported as tifs and imported in *Fiji*. The fluorescence intensity was measured in an area of $77\,px^2$. Overall the root hairs grow more or less continuously but sometimes they show an oscillating growth pattern (Fig. 3.16 C-G). Furthermore, during the oscillating growth, an increase in the fluorescence intensity is accompanied with an increase in growth rate (Fig. 3.16 C). The correlation coefficient for the time frames 150-$250\,min$ in Fig. 3.16 C is 0.72, reflecting a strong temporal correlation between apical RabA1d accumulation and tip growth. This corroborates the hypothesis that RabA1d labeled endosomes contribute to cell expansion.

The correlation coefficient was calculated with the following equation ($\overline{x}$ and $\overline{y}$ are sample means of the two matrices):

$$Cor(X, Y) = \frac{\sum (x - \overline{x})(y - \overline{y})}{\sqrt{\sum (x - \overline{x})^2 \sum (y - \overline{y})^2}}$$
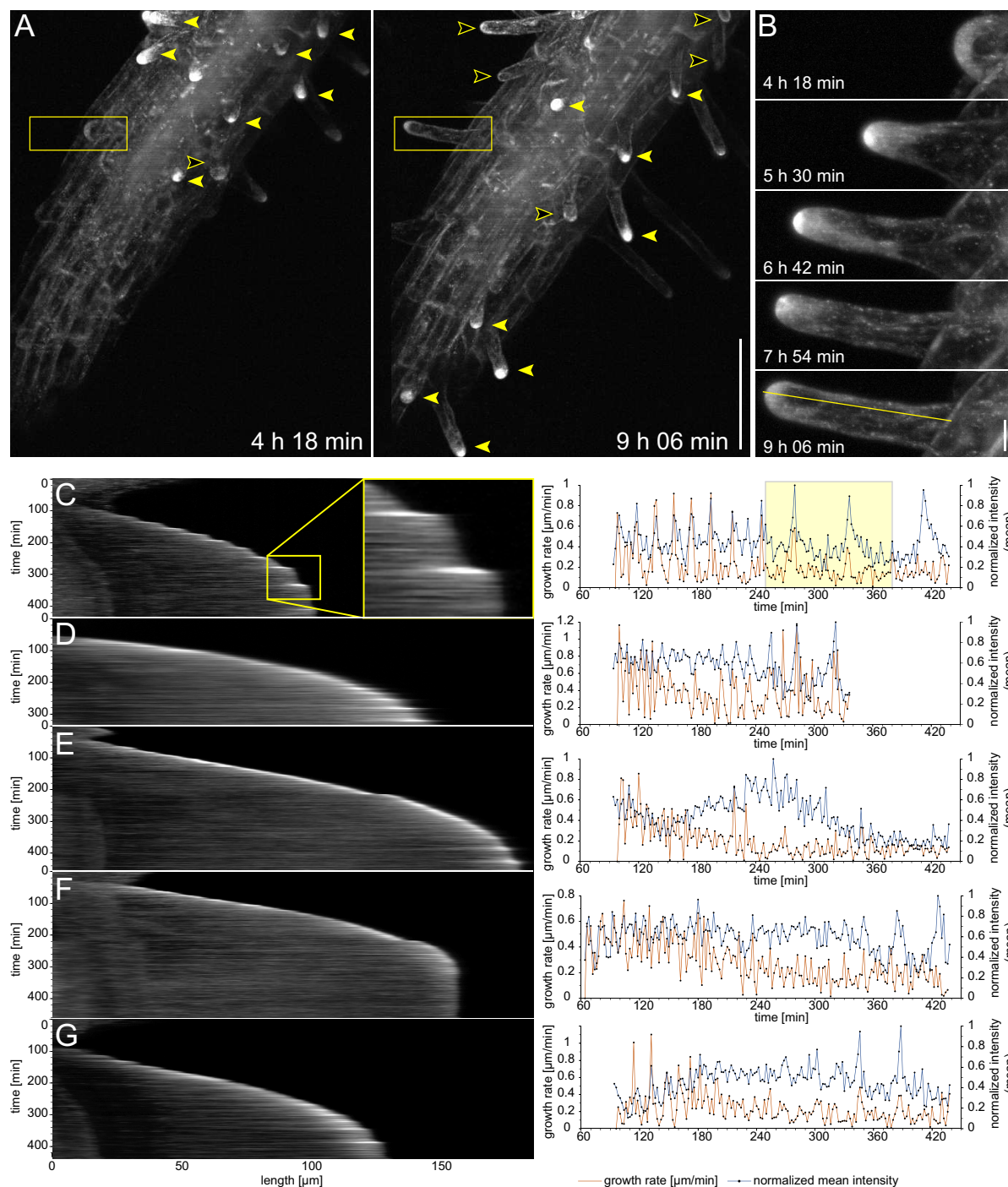
Figure 3.16: Oscillating root hair growth. Time lapse recording of a five days old Arabidopsis root expressing 35S::GFP-RabA1d. (A) Maximum-intensity projections of two indicated time points. Filled arrowheads highlight growing root hairs, empty arrowheads non-growing root hairs. The boxed area is enlarged in B. (B) The tip-accumulation of GFP-RabA1d increased in steady state growing root hairs. The yellow pixel line is plotted in C as a function of time (kymograph). (C) Kymograph of the root hair shown in B. Growth rates and mean fluorescence intensities are plotted in the diagram on the right. The yellow area in the diagram corresponds to the yellow box in the kymograph. An increase in fluorescence intensity correlates with an higher growth rate. (D-G) Kymographs and growth analysis of five growing root hairs. Scale bar: A) $100\,\mu m$, B) $10\,\mu m$. Detailed recording metadata on page 157. **Supplemental Movie-3.16.1**, and **Supplemental Movie-3.16.2**.

Cell plate growth dynamics

microtubules (GFP-MAP4) | plasmamembrane (FM4-64 dye) | merge
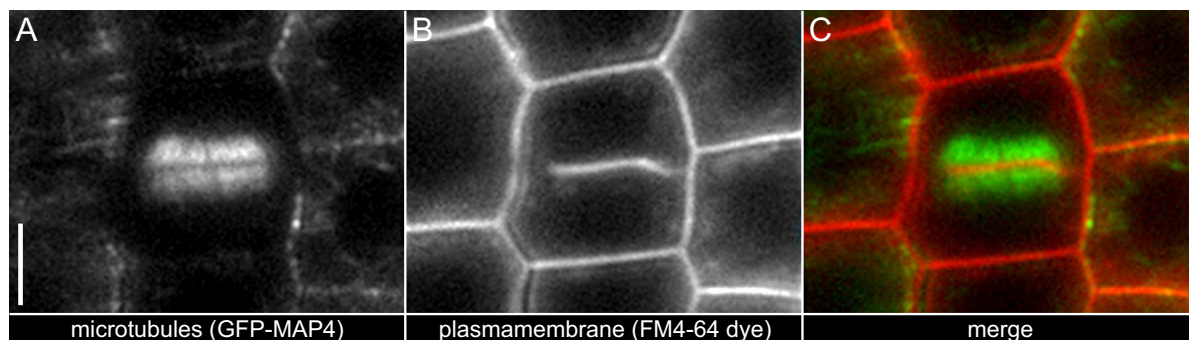
Figure 3.17: Phragmoplast in a cortex cell during cytokinesis. The phragmoplast is a structure made of cytoskeleton, membrane and vesicles that built the cell plate in between two daughter cells during cytokinesis. Single optical slice through a cortex cell in the root tip of a five days old transgenic Arabidopsis plant that expresses 35S::GFP-MAP4. (A) Microtubules, (B) plasmamembrane, labeled with FM4-64 dye, (C) merge of both channels. Images were collected with a $40\times/0.75$ objective lens in the detection path and a $5\times/0.16$ in the illumination path. Scale bar: $5\,\mu m$.

Besides the localization in growing root hairs, GFP-RabA1d labeled endosomes were also found at the margins of growing cell plates. The cell plate is built by means of the phragmoplast, a structure made of cytoskeleton, membrane and vesicles (Fig. 3.17). The localization of GFP-RabA1d at the growing cell plate during cytokinesis suggests a role in delivery of membranes/cargo for cell plate formation and membrane recycling at margin domains (Fig. 3.18). The cell plate formation of a transgenic plant that expresses the trans-Golgi network localized fusion protein GFP-RabA1d was recorded in order to quantify the dynamics of this process (Fig. 3.20). The size and the total time a cell plate was visible in the fluorescence image was measured. For a comparison another transgenic plant line expressing the microtubule marker GFP-MAP4 was analyzed (Fig. 3.21). The growth rate averaged on the entire process of $0.38 \pm 0.12\,\mu m/min$
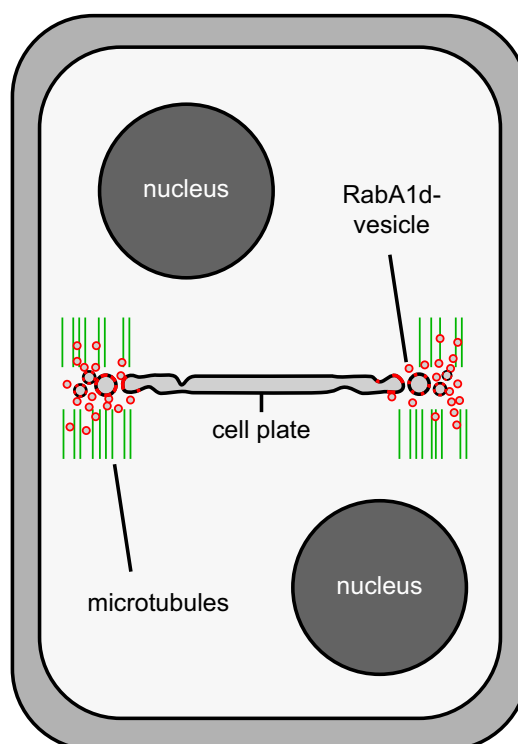
Figure 3.18: RabA1d-labeled endosomes located at the growing cell plate. The phragmoplast is a structure made of cytoskeleton (green) and endosomes (red). Both are involved in the delivery of new or recycled material to the margins of the growing cell plate during cytokinesis.

for the RabA1d-plants (Tab. 3.3) was comparable to the $0.42 \pm 0.13 \, \mu m/min$ for the MAP4-plants (Tab. 3.4, Fig. 3.19 A). However, some differences were observed between cell types (Fig. 3.19 B). In almost every cell, the cell plate did not reach all cell borders at the same time. In the end it took more time to finish the process which decreases the overall growth rate. Much higher growth rates were measured during the steady state growth of the cell plate formation, $1.26 \pm 0.19 \, \mu m/min$ (n=11) for RabA1d-plants and $1.12 \pm 0.44 \, \mu m/min$ (n=11) for MAP4-plants.
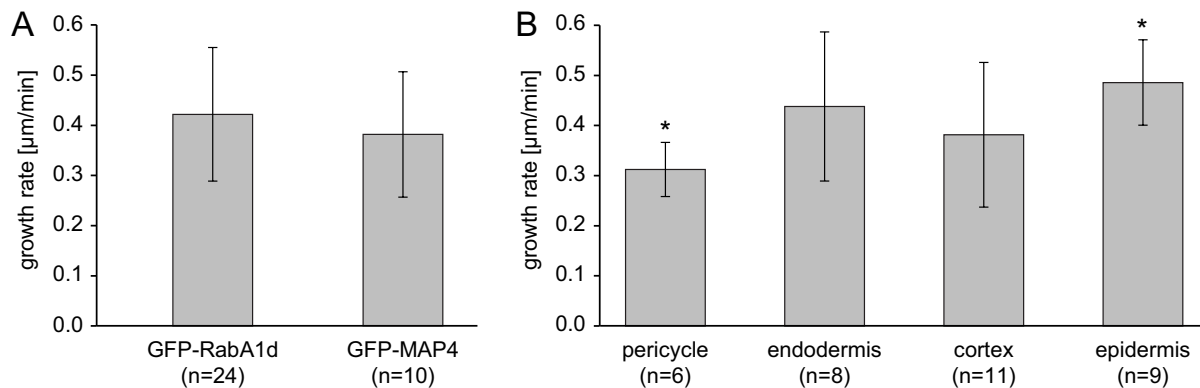
Figure 3.19: Cell plate growth rates in various tissues of two different transgenic Arabidopsis plants. (A) Comparison of cell plate growth rates in Arabidopsis plants expressing 35S::GFP-RabA1d and 35S::GFP-MAP4 showed no significant difference (p-value >0.05). (B) Growth rates of cell plates in cells from different types of tissues showed no significant difference (t-test >0.05) instead of epidermis versus pericycle (p-value <0.05). The statistical analysis was performed with the help of Sabine Fischer using a Wilcoxon rank sum test with Holm's correction.
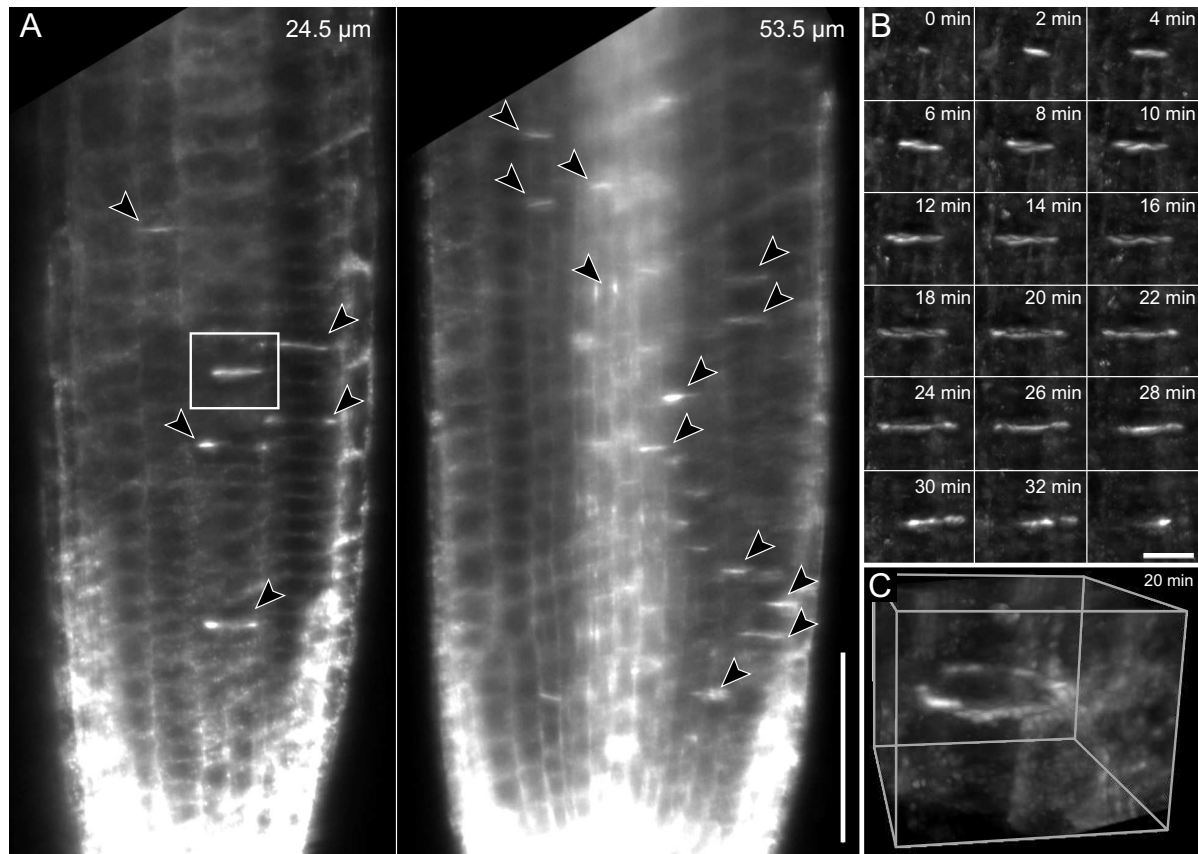
Figure 3.20: GFP-RabA1d accumulates at growing cell plate. (A) Single planes of one time point at indicated depths inside the primary root. The GFP-RabA1d labeled vesicles accumulate at cell plates during cytokinesis (arrowheads). The boxed area highlights a cell plate which is enlarged and depicted B. (B) Time-lapse imaging of cell plate formation starting with a small spot like structures in the middle of the cell and followed by a formation of a ring-like structure at the margins of the growing cell plate. (C) Three-dimensional reconstruction of the cell plate in B at time point $20\,min$. Images were collected every $2\,min$ with a $40\times/0.75$ objective lens in the detection path and a $5\times/0.16$ objective lens in the illumination path. Scale bar: A) $50\,\mu m$, B) $10\,\mu m$. Detailed recording metadata on page 157. **Supplemental Movie-3.20**.

Table 3.3: Cell plate growth in 35S::GFP-RabA1d transgenic plants. Time period, diameter and growth rate is displayed for the complete process of cell plate growth. Two plant were measured.

number of cell plates	time period		diameter		growth rate	
	$[min]$	+/-	$[\mu m]$	+/-	$[\mu m/min]$	+/-
total (n=24)	32.4	8.0	13.5	4.7	0.42	0.13
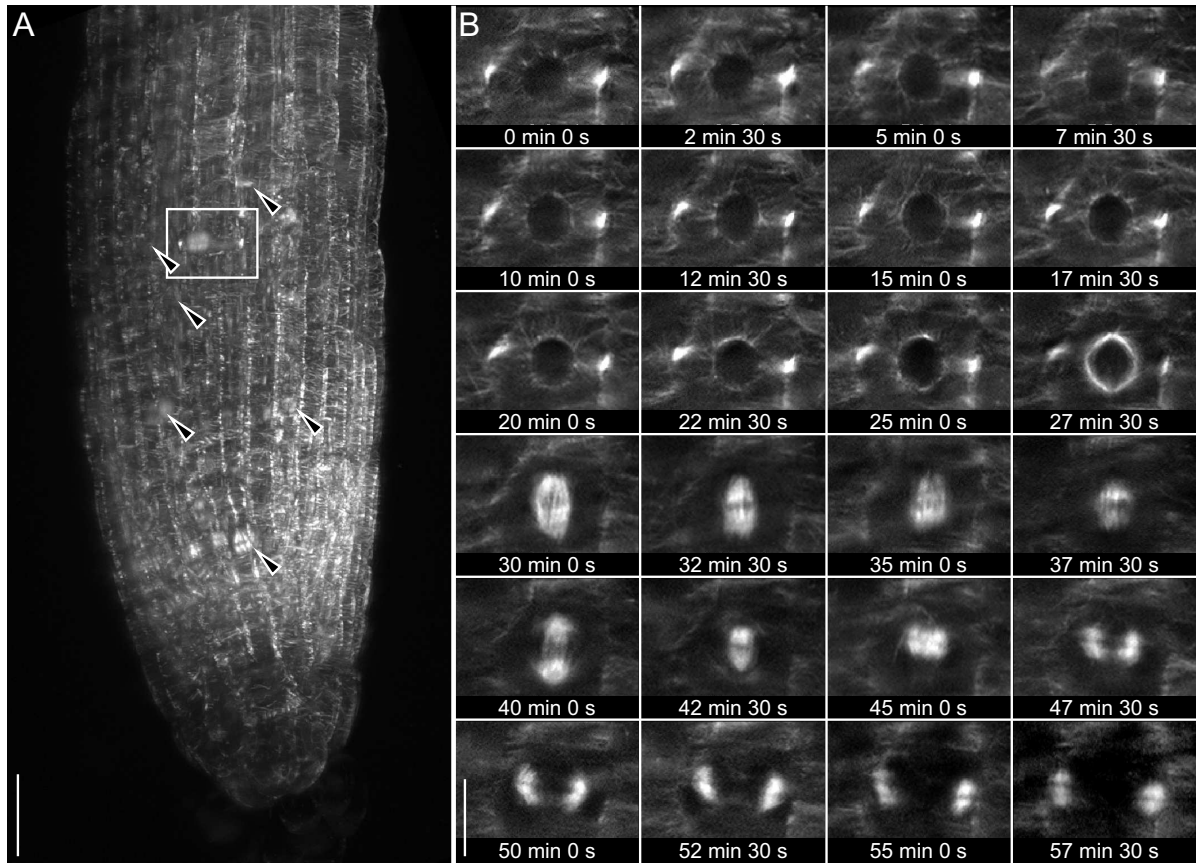
Figure 3.21: Microtubule organization during cytokinesis. (A) Maximum intensity projection of the first time point of a time lapse recording. The five days old Arabidopsis expresses 35S::GFP-MAP4. Cell divisions are indicated by arrowheads. (B) Division of a single cell. Each picture corresponds to the boxed area in A and represents a single plane located $19.5\,\mu m$ deep inside the root (cortex layer). The preprophase band (0 - $25\,min$), the nuclear envelop break down and spindle formation (27.5 - $35\,min$), the separation of chromosomes (37.5 - $40\,min$), the phragmoplast (42.5 - $57.5\,min$). Images were collected every $2.5\,min$ with a $40\times/0.75$ objective lens in the detection path and a $5\times/0.16$ objective lens in the illumination path. Structured illumination (SI10) and CUDA deconvolution (5 iterations) was used. Scale bar: (A) $20\,\mu m$, (B) $10\,\mu m$. **Supplemental Movie-3.21**.

Table 3.4: Cell plate growth in 35S::GFP-MAP4 transgenic plants. Time period, diameter and growth rate is displayed for the complete process of cell plate growth. Three plants were measured.

number of cell plates	time period		diameter		growth rate	
	$[min]$	+/-	$[\mu m]$	+/-	$[\mu m/min]$	+/-
total (n=10)	33.5	9.0	12.1	2.4	0.38	0.12

3.1.5 Hypocotyl parts of the plant

For microscopy the root is a grateful specimen because it is relatively transparent compared to aerial parts of the plant and can be maintained in water, which allows the use of water dipping lenses. Imaging aerial parts of a plant is a challenge, because of a wax cuticular, autofluorescence of chloroplasts and air in between the cells. Nevertheless, there is a strong interest in understanding growth processes of the shoot apical meristem or the formation of stomata in leaves. To see whether LSFM could be an applicable tool images from different aerial parts were collected.

Cotyledons

To test the imaging penetration depth into cotyledons of Arabidopsis a microtubule marker was recorded (Fig. 3.22). The sample was placed in a 45° angle for an optimal penetration of the light-sheet into the tissue. The microtubules as well as the cell contours (stained with FM4-64 dye) were very well resolved in the epidermis cell layer, the fluorescence signal drops rapidly in deeper cell layers, i.e. structures $50\,\mu m$ inside (second cell layer) cannot be resolved (Fig. 3.22 B).

Shoot apical meristem

The shoot apical meristem (SAM) is located at the very tip of the shoot and is besides the root apical meristem the second location where organogenesis occurs. A two months old plant was placed right next to the microscope (Fig. 3.23 A). The SAM overlaying tissue was carefully removed prior to imaging. In the microscope chamber a furcated carbon rod was used to carefully clamp the shoot in front of the detection lens (Fig. 3.23 B). The rest of the plant remained intact and received the same culturing conditions as prior to the experiment (light, temperature). Cells in the SAM are very well resolved and cell contours can be recognized for at least three cell layers deep inside the tissue.
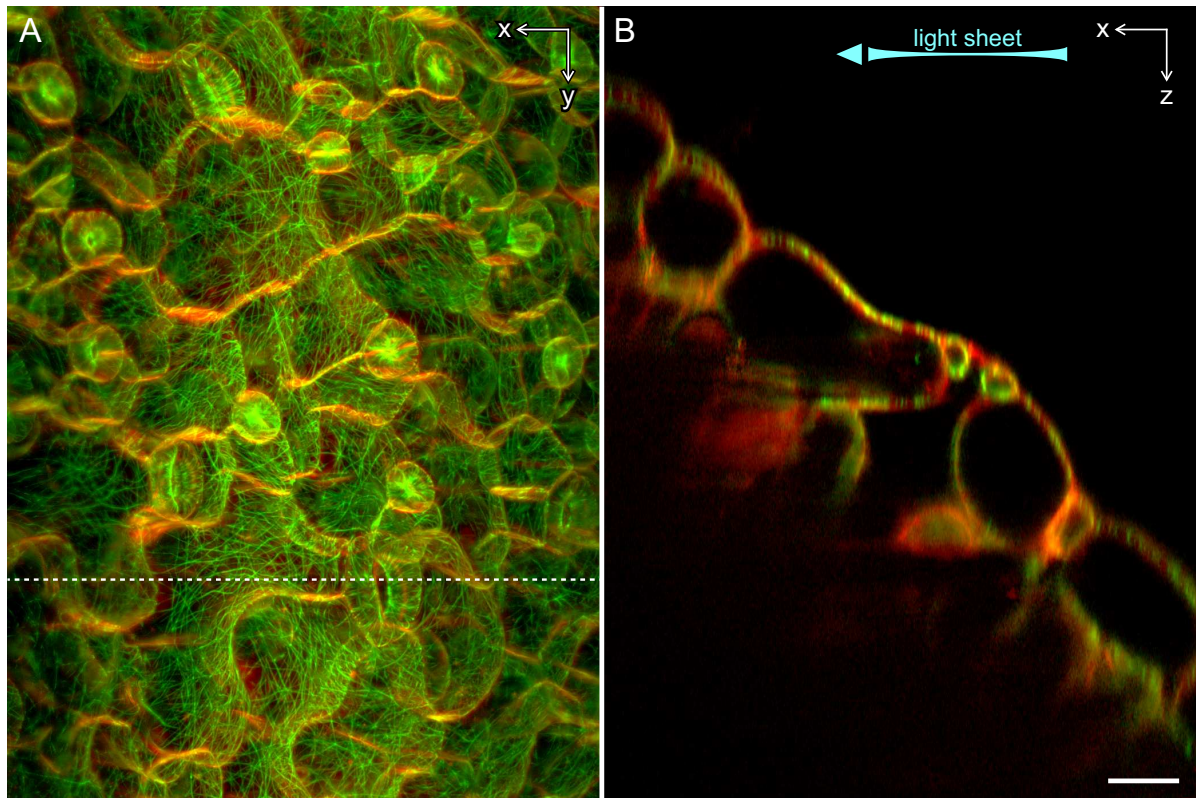
Figure 3.22: Microtubules and plasmamembrane in cotyledons of Arabidopsis. A four days old Arabidopsis expressing the microtubules marker 35S::GFP-MAP4 (green) was labeled with $5\,\mu M$ of the membrane marker FM4-64 dye (red). (A) Maximum intensity projection. The dashed line indicates the transverse section shown in B. (B) Single slice (x-z) along the dashed line in A. The stack of 357 images was collected with the $40\times/0.75$ objective lens in the detection path and the $5\times/0.16$ objective lens in the illumination path. Images were recorded with structured illumination (SI10). Scale bar: $20\,\mu m$. **Supplemental Movie-3.22**.
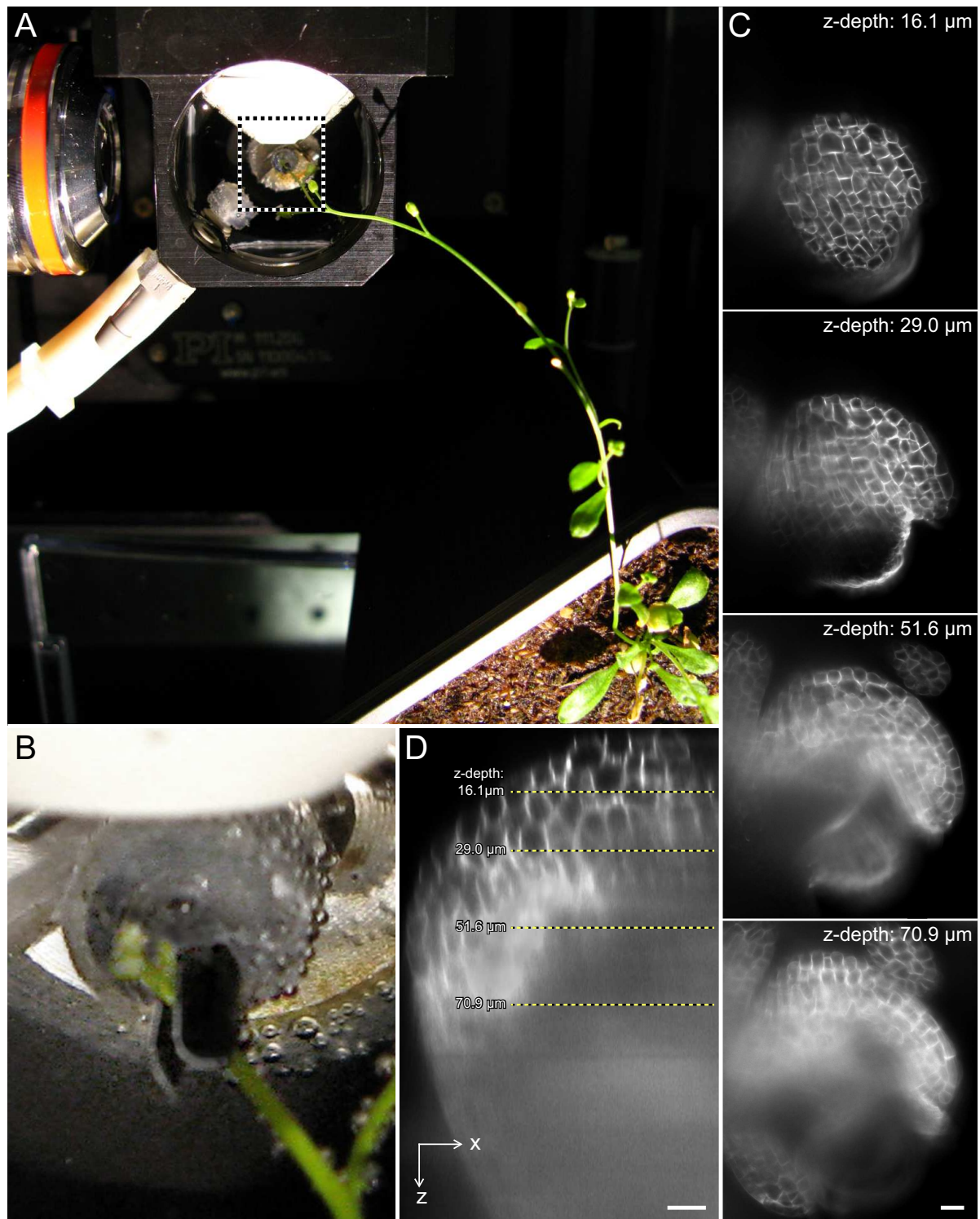
Figure 3.23: Imaging the shoot apical meristem of Arabidopsis. (A) A two months-old Arabidopsis expressing the membrane marker 35S::LTI6b-GFP in the mDSLM microscope chamber (top view). The dashed box area is enlarged in B. (B) The stem of the apical tip clamped using a furcated carbon rod. (C) Four single optical slices of an image stack at indicated depths. (D) Single slice along the x-z axis. Images were collected with the $40\times/0.75$ objective lens in the detection path and the $5\times/0.16$ objective lens in the illumination path. Scale bar: C) and D) $10\,\mu m$. Detailed microscopy metadata on page 153.

3.1.6 *Oryza sativa* adventitious root emergence

Besides the model organism *Arabidopsis thaliana* rice (*Oryza sativa*) is important to study because of the wide use as basic food. When the deep water rice is flooded by water adventitious roots rapidly emerge from the stem. In cooperation with Bianka Steffens (University of Kiel) the dynamic process of emergence of adventitious roots should be recorded with LSFM. The imaging of such a large object ($1\,cm$ in diameter, $7\,cm$ long) in the mDSLM microscope chamber was a challenge. The borders of the stage had to be extended from $1500\,\mu m$ to $2000\,\mu m$ in all directions ($\pm$ x and z) in order to accommodate the segment in the focal plane of the detection lens.
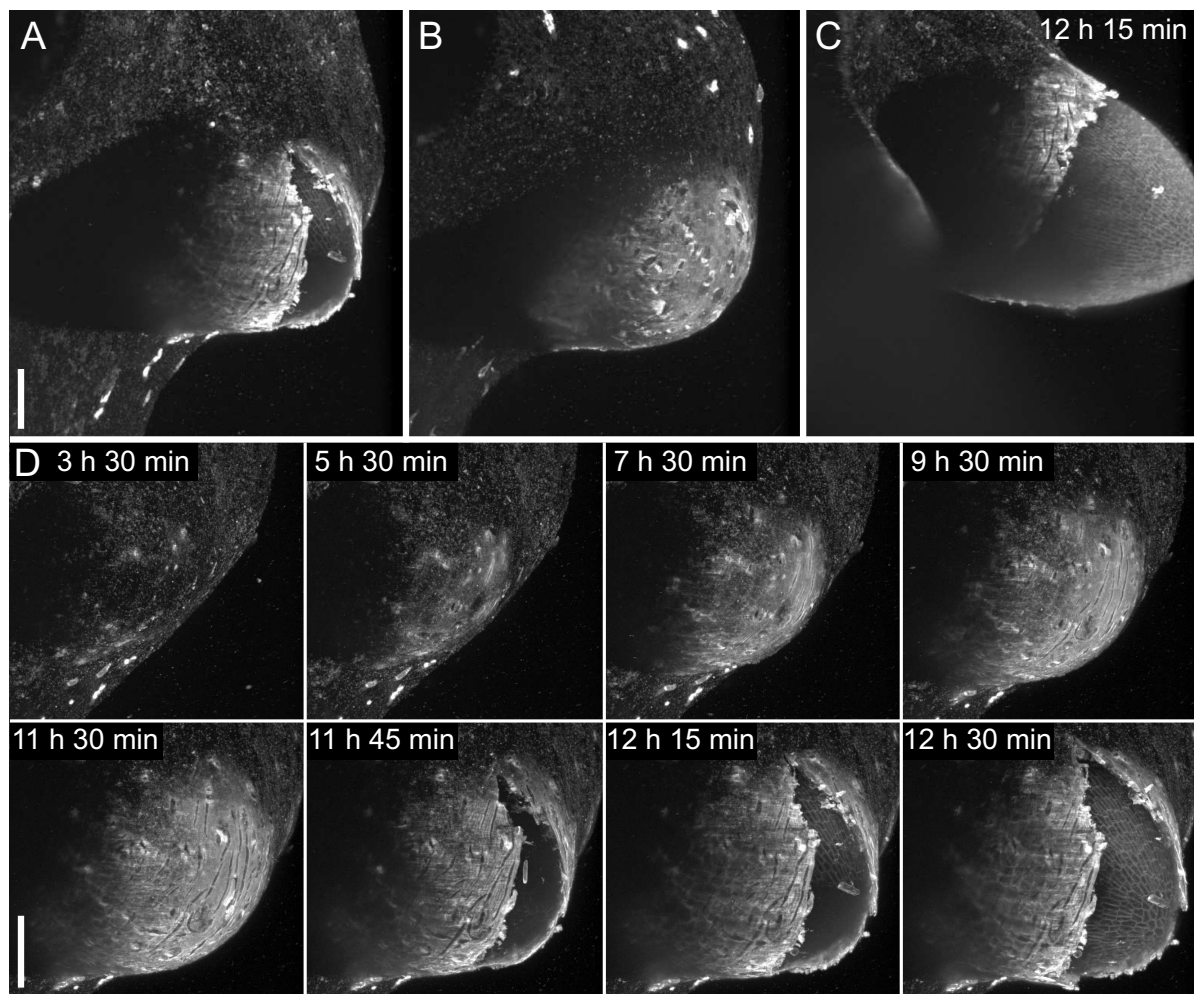
Figure 3.24: *Oryza sativa* adventitious root emergence. (A, B, C) Simultaneous recording of three adventitious root primordia at the same rice segment. The maximum intensity projection of one time point out of 51 is shown. (D) Eight time points of the time lapse shown in A. Images were collected with the $10\times/0.3$ objective lens in the detection path and the $2.5\times/0.06$ objective lens in the illumination path. Scale bar: A), B), C) and D) $100\,\mu m$. Detailed microscopy metadata on page 178. **Supplemental Movie-3.24**.

The rice-segments were stained with FM4-64. Adventitious root emergence were successfully recorded every $15\,min$ for at least $12\,h$ at multiple regions around the segment (Fig. 3.24). In the beginning the primordia were visible as bulge. In the course of time the intensity of fluorescence increased and grooves appeared at the tip of the growing bulge. The tissue ruptured within minutes and the adventitious lateral root emerged.

3.2 Lateral root formation in Arabidopsis

In Arabidopsis, lateral roots derive from a number of founder cells in the pericycle cell layer. The procedure of the first divisions seem to follow a certain pattern, as it is reported several times (Malamy and Benfey, 1997; Casimiro et al., 2001; Dubrovsky et al., 2001). Nevertheless, detailed studies of the cell lineages during the formation process do not exist so far. Besides the cell division pattern the lateral root primordium has to pass through several overlaying layers of tissue. The analysis of the morphology of cells and tissues as well as the study of cell division patterns would improove the understanding of organogenesis in plants.

Gravity-stimulation was used to induce lateral root initiation. The region where cells start to divide was spotted by the activity of a lateral root primordium specific promoter (GATA23::GFP-GUS). In addition, this plant line expresses a nuclear marker (UBQ10::H2B-RFP) and a plasma membrane marker (UBQ10::YFP-PIP1;4) for the simultaneous recording of cell nuclei and cell contours. Very well-resolved spatial and temporal recordings of lateral root initiation, growth and emergence for several plants were achieved that allows to analyze morphogenesis and cellular lineaging of the complete process of lateral root formation.

3.2.1 First cell divisions of lateral root formation

A lateral root primordium originates from nine to eleven founder cells, that are located in five to eight cell files. Prior to the first division, the nuclei of two pericycle cells within the cell file adjacent to the xylem pole migrate towards each other (Fig. 3.25 A, B). The average time point of this process was observed to occur about $7\text{-}15\,h$ after gravity-stimulation. Each of these two opposing pericycle cells divide asymmetrically creating a smaller and a larger daughter cells (Fig. 3.25 C). In the second division cycle the small center cells divide periclinal whereas the two larger cells again divide asymmetrically (Fig. 3.25 D). The upper cell (towards the shoot) divides anticlinal but the division of

the lower cell (towards the tip of the root) is neither anticlinal nor periclinal, the cell just splits off a corner. This observation shows, although the divisions of first two cell cycles seem to be stereotypical, several exceptions were observed. When a single founder cell contributed to the primordium, an additional initial anticlinal division generates two daughter cells which then follow the sequence described.
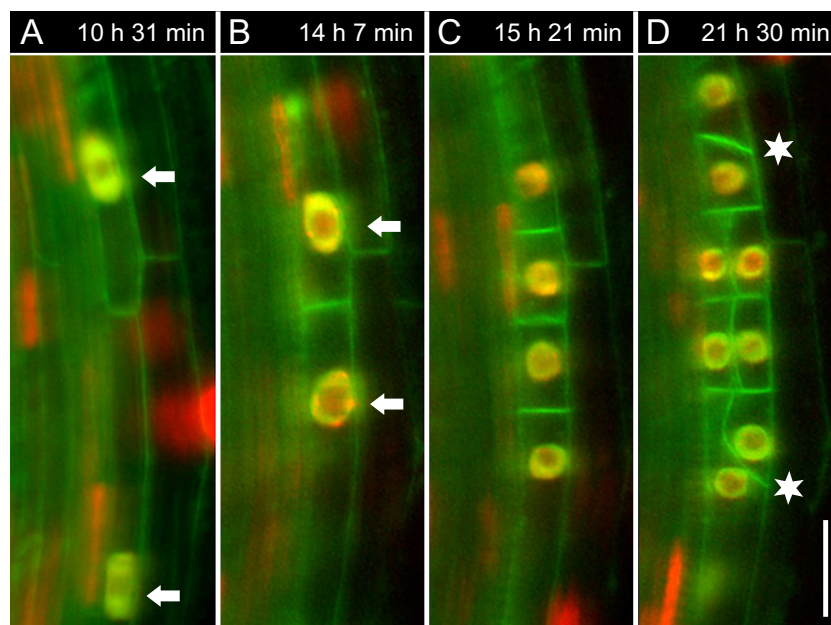
Figure 3.25: First two consecutive cell divisions of lateral root formation. Single slices of one of the center pericycle cell files of time lapse recording number #121114. (A and B) The cell nuclei of two neighboring pericycle cells migrate towards each other (arrows). (C) Both cells divide anticlinal creating one small and one larger daughter cell (C). (D) In the subsequent cell cycle, the two smaller daughter cells in the center divide periclinal. The upper cell of the two larger cells divide anticlinal (upper star), whereas the lower cell divides neither anticlinal nor periclinal, but rather splits off one corner (lower star). The seven days old Arabidopsis seedling expresses GATA23::GUS-GFP-NLS, UBQ10::YFP-PIP1;4 and UBQ10::H2B-RFP. Images were collected with the $40\times/0.75$ objective lens in the detection path and the $5\times/0.16$ objective lens in the illumination path and camera binning 2×2. Scale bar: $20\,\mu m$. Detailed microscopy metadata on page 163. **Supplemental Movie-3.25**.

While the primordium develops the endodermis, a watertight epithelium overlaying the pericycle, shrinks and seems to actively create room for the emerging lateral root. In contrast, the cortex and epidermis do not shrink but are pushed to the side during the lateral root emergence. The question arose, whether the shrinkage of the endodermis and the swelling of the pericycle is a simultaneous process or a consecutive one. To answer this question the area of three pericycle cell files that will divide and three overlaying endodermis cells were measured in a cross section of the main root of dataset #121114. For each of the 60 time points the areas were outlined with a polygonal

lasso tool in the software *Amira*. An almost doubling of the area of the pericycle cells could be observed ($184.1\,\mu m^2$ to $328.3\,\mu m^2$ over the time period of $3\,h\,35\,min$) and the endodermis maintained its area. On account of this observation a dynamic morphological study revealed that swelling of the pericycle comes first and shrinkage of the endodermis follows. This was a contribution to the paper *A spatial accommodation by neighboring cells is required for organ initiation in Arabidopsis* (Vermeer et al., 2014). Vermeer et al. (2014) further showed that no pericycle swelling and no cell division occurred when auxin-signaling is blocked specifically in the endodermis (Vermeer et al., 2014). Thus, it seems that signals coming from the endodermis are required for the early steps in lateral root initiation.
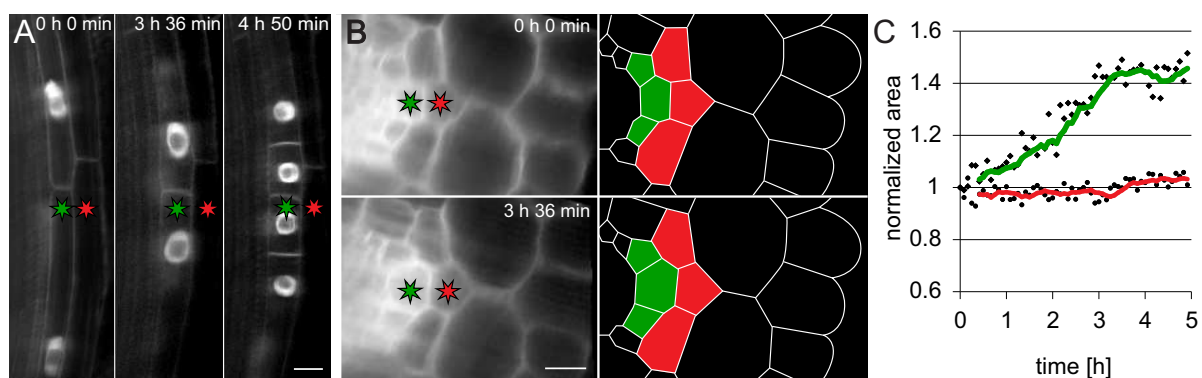
Figure 3.26: Pericycle cells swell prior to their first division. Cell area analysis of the recording shown in Fig. 3.25). (A) Single slice of two dividing pericycle cells. (B) Radial views of A at $t = 0\,h$ and $t = 3.58\,h$ and a sketch of the membranes on the right. Pericycle is indicated with yellow asterisk and/or filled area, endodermis with red asterisk and/or filled area. (C) The sum area of the three cells normalized to the initial value is plotted. The yellow and red lines are sliding window averages over six time points. **Supplemental Movie-3.26**.

3.2.2 Shape analysis - height, length, width and volume

During the formation and emergence of lateral roots the overlaying tissues exerts a mechanical and biomechanical constraint on the primordium which is likely to influence the lateral root morphogenesis. While the lateral root emerges the cortex and epidermis cells are pushed apart. Indeed, the recordings detected a rupturing of the lateral root overlaying tissue within minutes. In between two consecutive time points during the rupturing a lateral root grew $12\,\mu m$ (Fig. 3.27). This growth rate is much higher than the average growth rates of 2-$3\,\mu m/h$. The rapid growth during emergence was observed several times but not always, i.e. in most cases the overlaying tissue opened gradually and not abruptly.
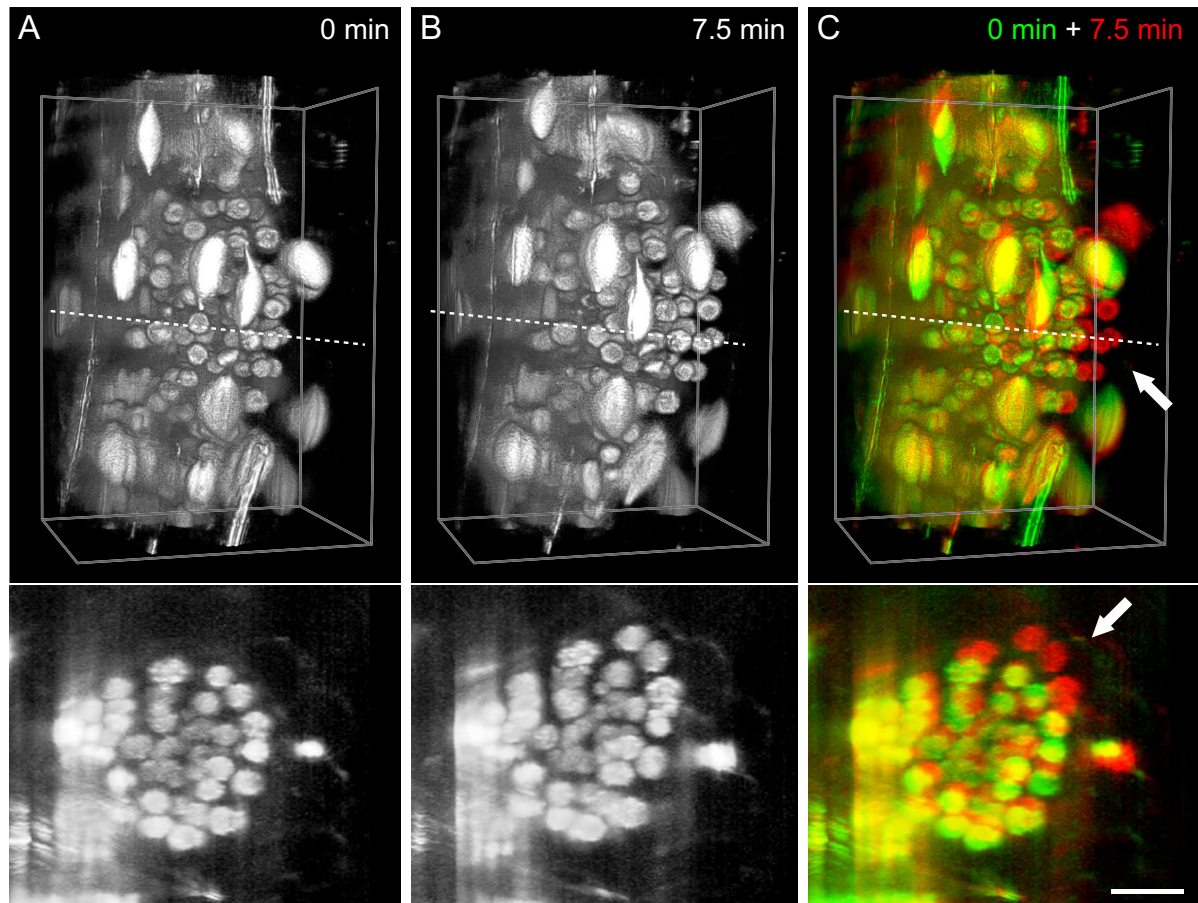
Figure 3.27: Lateral root quickly grows when overlaying tissue ruptures. Time lapse recording of a lateral root primordium that stably expresses UBQ10::H2B-RFP. A stack of images was collected every $7.5\,min$ for a period of $9\,h$. (A) 3D reconstruction of the time point before the overlaying tissue ruptured. The dashed line indicates the position of a cross section that is depicted in the lower panel. (B) The next time point, $7.5\,min$ later. (C) Merge of the two time points indicated in different colors ($0\,min$-green, $7.5\,min$-red). The position of the nuclei changed rapidly in between to consecutive time points highlighted by arrows. Detailed microscopy metadata on page 175. **Supplemental Movie-3.27**.

The shape of three lateral root primordia during the process of emergence were analyzed in order to quantify the dynamic shape development. The outline of the primordium was manually segmented in two-dimensional sections along the radial section and the longitudinal section of the primordium with the software *Amira*. The width, height and length of the primordium at a constant distance ($15\,\mu m$) to the tip of the primordium was extracted from the segmented shape by means of *Adobe After Effects*. The primordia became continuously rounder when they developed and emerged through the overlaying tissue (Fig. 3.28 and Fig. 3.29).
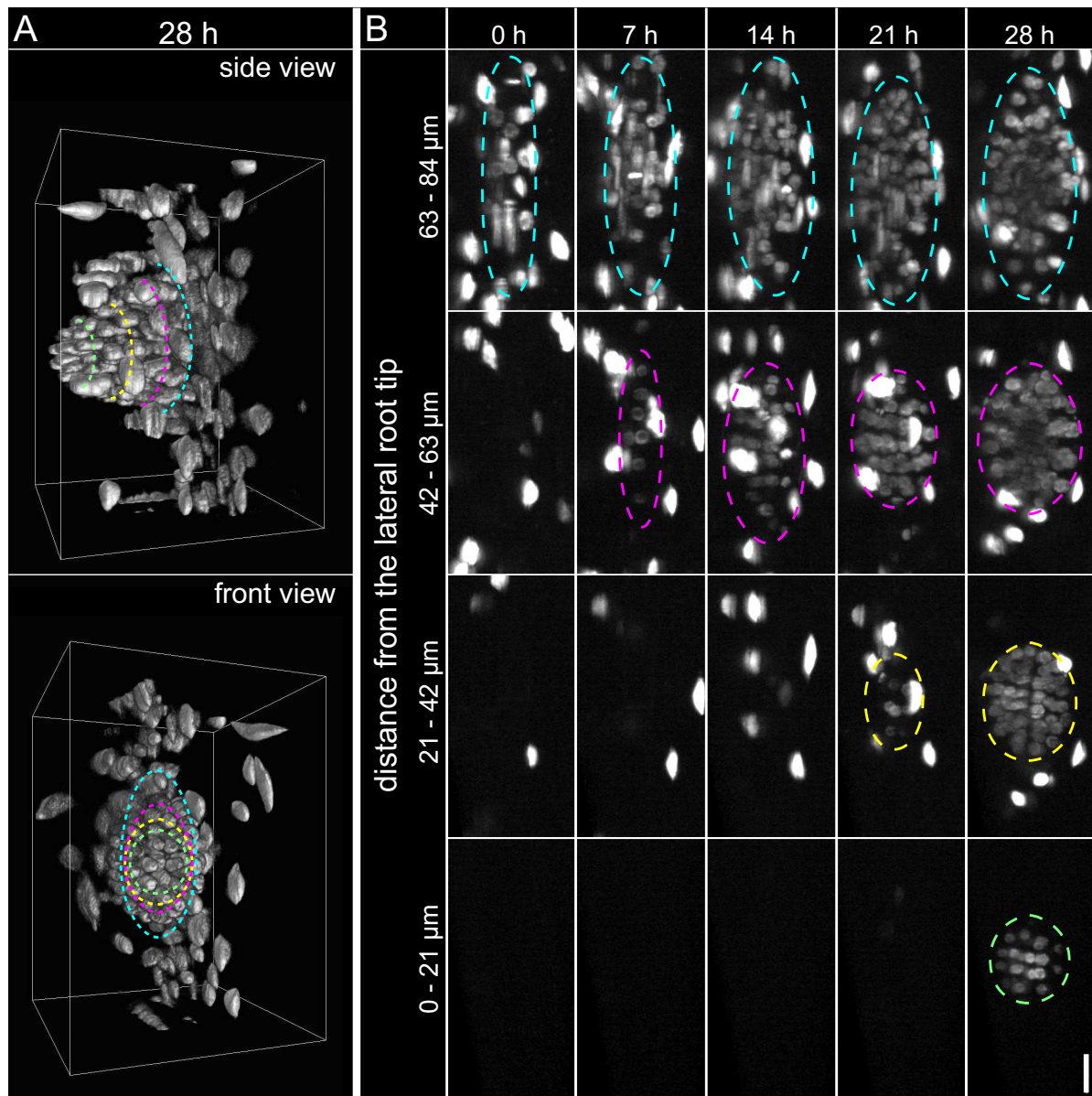
Figure 3.28: Lateral root primordium shape analysis. (A) Side view and frontal view of the 3D reconstruction of the primordium in the last time point of the recording. Colored dashed lines represent the position of four sections that are presented in B. (B) Four sections at different distance from the tip of the lateral root primordium at indicated time points. The dashed lines delineate the primordium. The primordium is observed from the top and growing toward the observer (frontal view). The six days old Arabidopsis expresses UBQ10::H2B-RFP. Images were collected with the $20\times/0.5$ objective lens in the detection path and the $2.5\times/0.06$ objective lens in the illumination path. Detailed microscopy metadata on page 173.
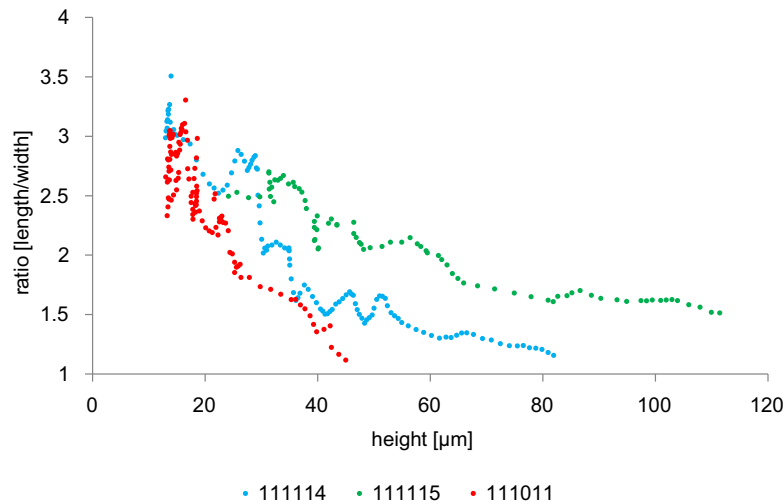
Figure 3.29: Length/width ratio during lateral root development. Development of the length/width ratio according to height for three individual lateral root primordia. Three independent plants (red, green, blue) were analyzed at a constant distance from the tip of the primordium ($15\,\mu m$) and plotted as a function of the primordiums height. Detailed microscopy metadata on page 172 - 174. **Supplemental Movie-3.29**.

To test whether a precise patterns of cell division is important on the lateral root primordium morphogenesis the *aur1-2 aur2-2* double mutant was analyzed. This mutant lacks the key α-Aurora kinases that are required to correctly position the cell wall, especially in asymmetric divisions. The morphology of the primordium in *aur1-2 aur2-2* was rather flexible compared to the monotonously growing wild type (Fig. 3.30 A). The continuous radialization (lengt/width ratio) observed in the wild type was replaced by an irregular decrease in the *aur1-2 aur2-2* mutant (Fig. 3.30 B and C). Thus, the defect in the orientation of cell divisions impairs the shape of the primordium, which in turn is influenced by mechanical properties of the surrounding tissue.
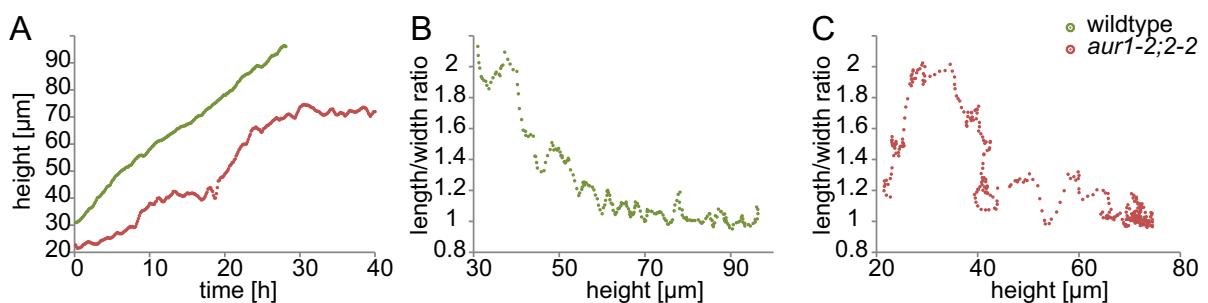
Figure 3.30: Dynamics of growth in height of primordia in *aur1-2aur2-2* double mutant and wild type. Both, wild-type and *aur1-2 aur2-2* double mutant expresses the PIN1::PIN1-GFP construct. (A) Growth in height as a function of time. (B and C) Length/width ratio as a function of the primordiums height for (B) wild-type and (C) *aur1-2 aur2-2* double mutant. Detailed microscopy metadata on page 176 (wild type) and page 177 (*aur1-2 aur2-2*) **Supplemental Movie-3.30**.

3.2.3 The virtual lateral root primordium - lineage tracing in lateral root formation

The complete process of lateral root formation was captured in its three dimensions in order to encompass all divisions of all involved cells. Quantitative analyses of lateral root formation in terms of the spatial and temporal patterns of cell division as well as cellular contribution and primordium growth parameters were successfully performed. Similarities and differences among these datasets were identified. Furthermore, the *aur1-2 aur2-2* double mutant was successfully recorded, analyzed and compared with the wild type data.

Five time lapses showing lateral root formation

Gravity-stimulated transgenic plants were recorded that expresses GFP coupled to a nuclear localization signal under the control of a promoter which is specifically active during lateral root initiation (GATA23::GFP-GUS-NLS). Furthermore, the plants express a nuclear marker (UBQ10::H2B-RFP) and a plasmamembrane marker (UBQ10::YFP-PIP1;4) to image cell nuclei and cell contours during lateral root formation (Fig. 3.31). The signal of YFP and GFP were captured in a single channel, in a second channel the fluorescence of RFP was captured. A total of five datasets could be obtained which allowed for cell tracking. The time lapse of the five recordings are summarized in Fig. 3.32 - 3.36. The longest period of a recording was $60\,h$. As a quality control the fluorescence intensity in each time point was measured in a sum-projection and plotted against time (Fig. 3.37). The time course of the fluorescence intensity is not easy to interpret because e.g. the membrane channel includes also the activity of the promoter GATA23 which drops with the development of the primordium. But the curves show no obvious bleaching but rather an increase in fluorescence due to the growth of the lateral root (Fig. 3.37). The recording #120830 was stopped because the plant fell off the sample holder into the water during the night and the fluorescence intensity dropped to almost zero. The fluorescence intensity also dropped in dataset #130607 in the night to day 3 but the recording was not stopped. The next day, the fluorescence signal came back and in the end the lateral root emerged from the main root (Fig. 3.37).
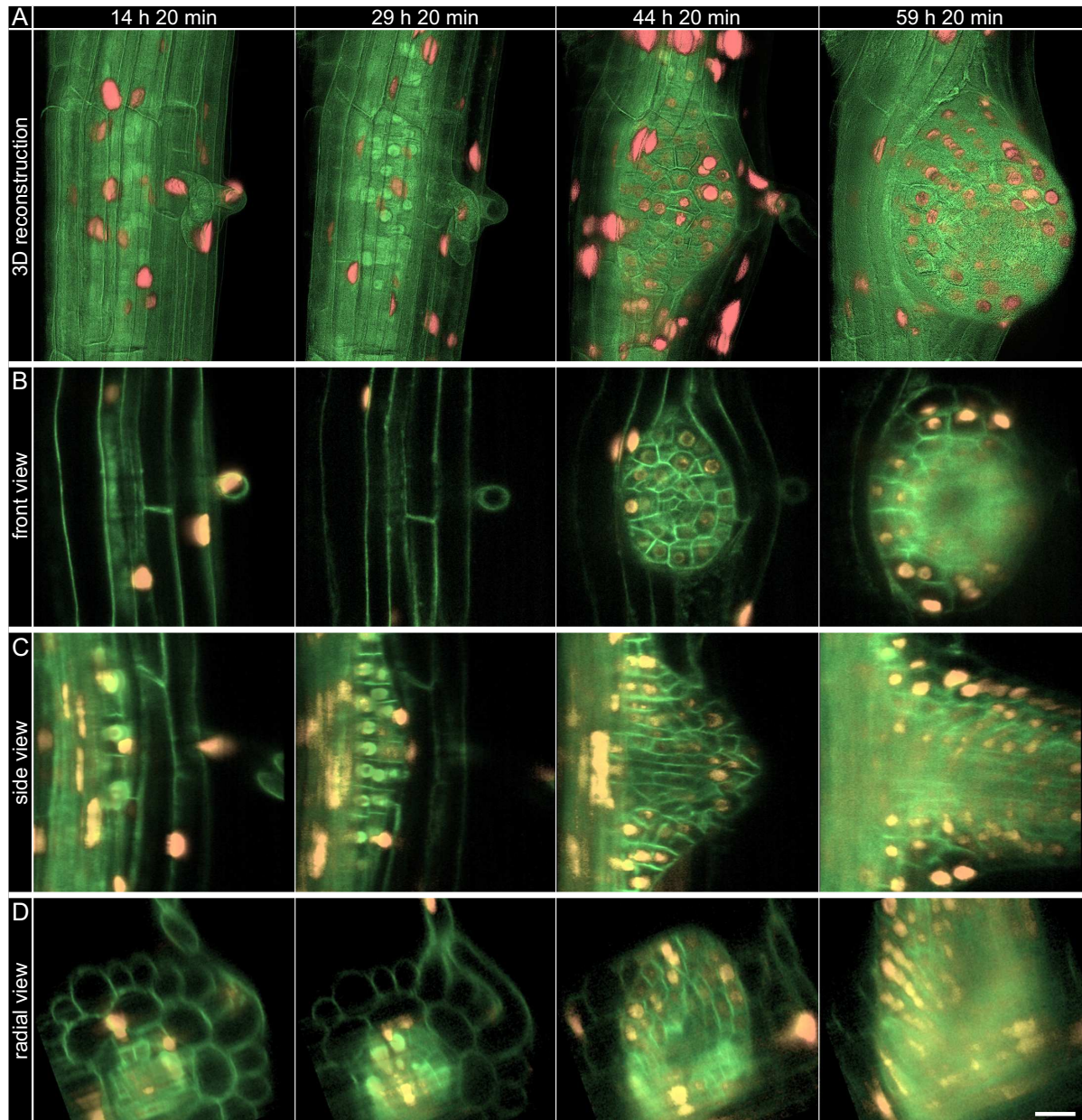
Figure 3.31: Recording of the entire process of lateral root formation. (A) Three-dimensional reconstruction of the lateral root growing out of the primary root (dataset #121204). (B) Single slices along x-y (front view) $10\,\mu m$ inside the epidermis cell layer. (C) Single slices along z-y (side view) $80\,\mu m$ deep inside the primary root. (D) Single slices along y-z (radial view) through the center of the primordium. The six days old Arabidopsis stably expresses UBQ10::YFP-PIP1;4 (membranes, green), UBQ10::H2B-RFP (nuclei, red) and GATA23::GUS-GFP-NLS (promoter activity, nuclear localization signal, green). Time points are relative to gravity-stimulation. Images were collected with the $40\times/0.75$ objective lens in the detection path and the $5\times/0.16$ objective lens in the illumination path and camera binning 2×2. Scale bar: $20\,\mu m$. Detailed recording metadata on page 164. **Supplemental Movie-3.31**.

Figure 3.32: Time lapse recording #120803. Five time points of a longitudinal section (side view) and a transverse section (radial view). Time is relative to the point of gravity-stimulation. The signal of UBQ10::YFP-PIP1;4 (membranes) and GATA23::GUS-GFP-NLS (nuclei) is shown. Images were collected with the 40×/0.75 objective lens in the detection path and the 5×/0.16 objective lens in the illumination path and camera binning 2×2. Scale bar: 20 μm. Detailed recording metadata on page 162. **Supplemental Movie-3.32**.
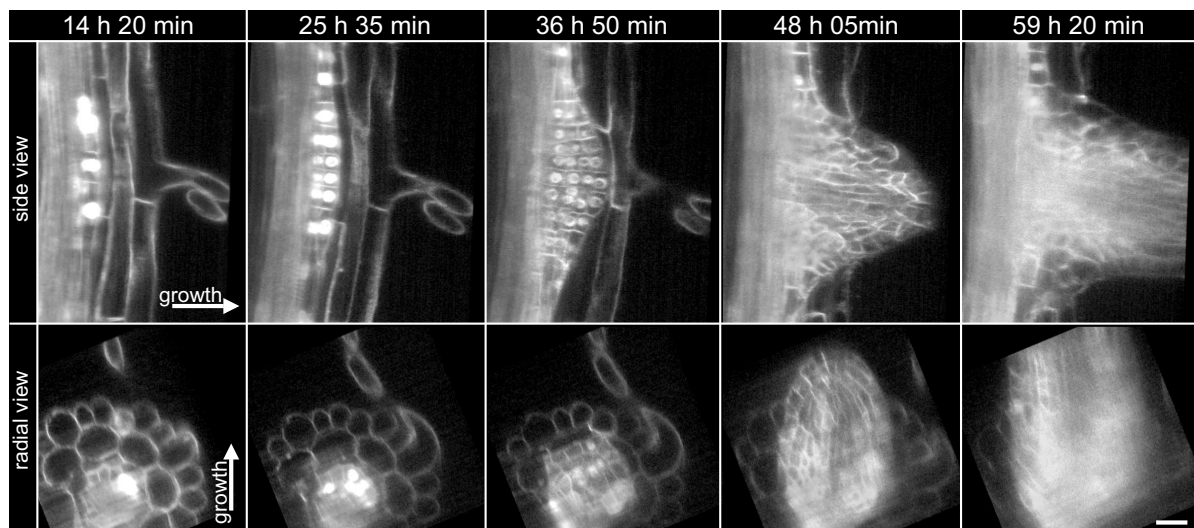
Figure 3.33: Time lapse recording #121204. Five time points of a longitudinal section (side view) and a transverse section (radial view). Time is relative to the point of gravity-stimulation. The signal of UBQ10::YFP-PIP1;4 (membranes) and GATA23::GUS-GFP-NLS (nuclei) is shown. Images were collected with the 40×/0.75 objective lens in the detection path and the 5×/0.16 objective lens in the illumination path and camera binning 2×2. Scale bar: 20 μm. Detailed recording metadata on page 164. **Supplemental Movie-3.33**.
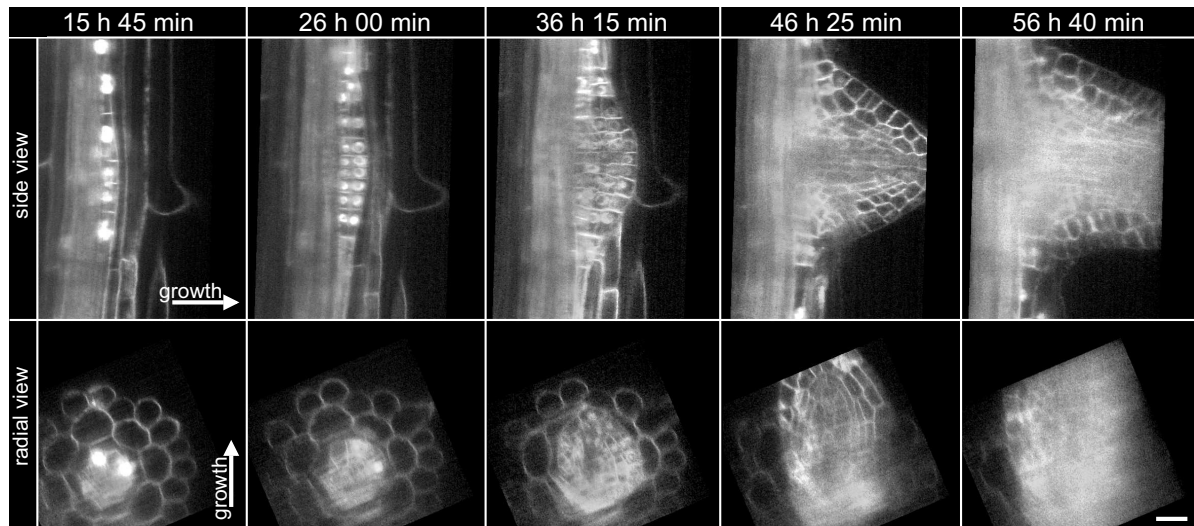
Figure 3.34: Time lapse recording #121211. Five time points of a longitudinal section (side view) and a transverse section (radial view). Time is relative to the point of gravity-stimulation. The signal of UBQ10::YFP-PIP1;4 (membranes) and GATA23::GUS-GFP-NLS (nuclei) is shown. Images were collected with the $40\times/0.75$ objective lens in the detection path and the $5\times/0.16$ objective lens in the illumination path and camera binning 2×2. Scale bar: $20\,\mu m$. Detailed recording metadata on page 165. **Supplemental Movie-3.34**.
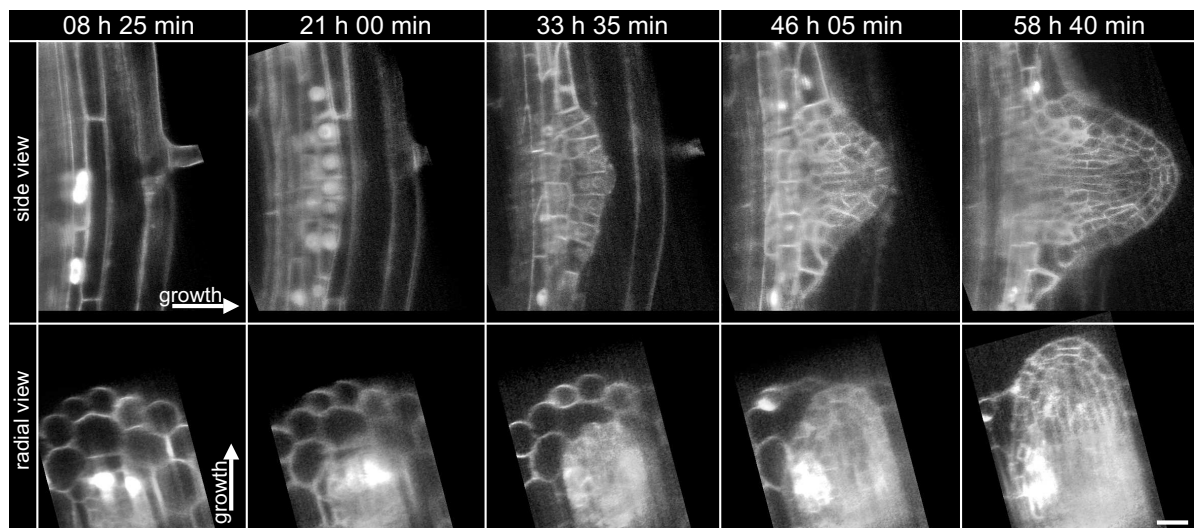
Figure 3.35: Time lapse recording #130508. Five time points of a longitudinal section (side view) and a transverse section (radial view). Time is relative to the point of gravity-stimulation. The signal of UBQ10::YFP-PIP1;4 (membranes) and GATA23::GUS-GFP-NLS (nuclei) is shown. Images were collected with the $40\times/0.75$ objective lens in the detection path and the $5\times/0.16$ objective lens in the illumination path and camera binning 2×2. Scale bar: $20\,\mu m$. Detailed recording metadata on page 166. **Supplemental Movie-3.35**.
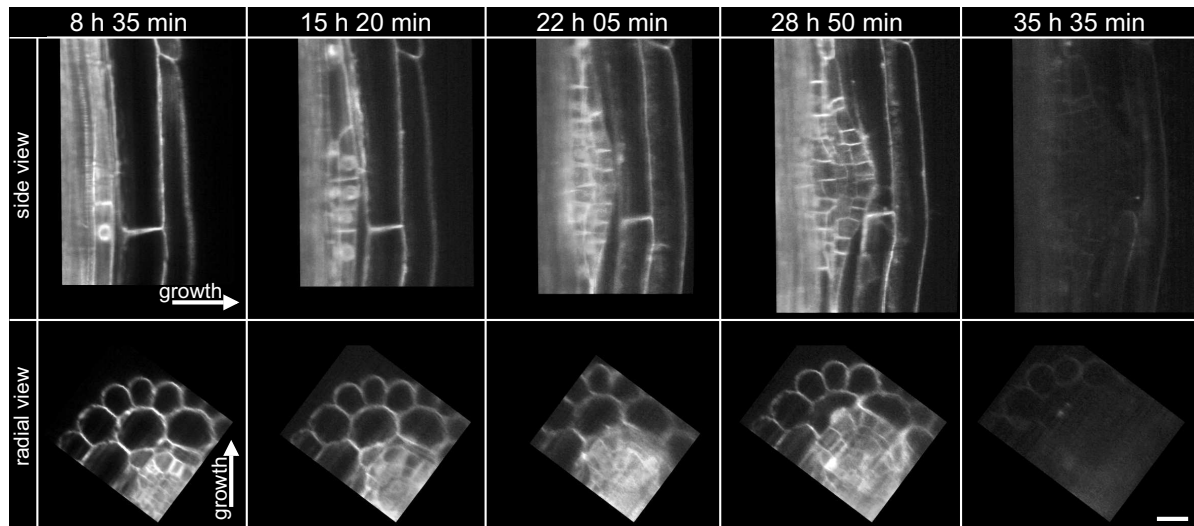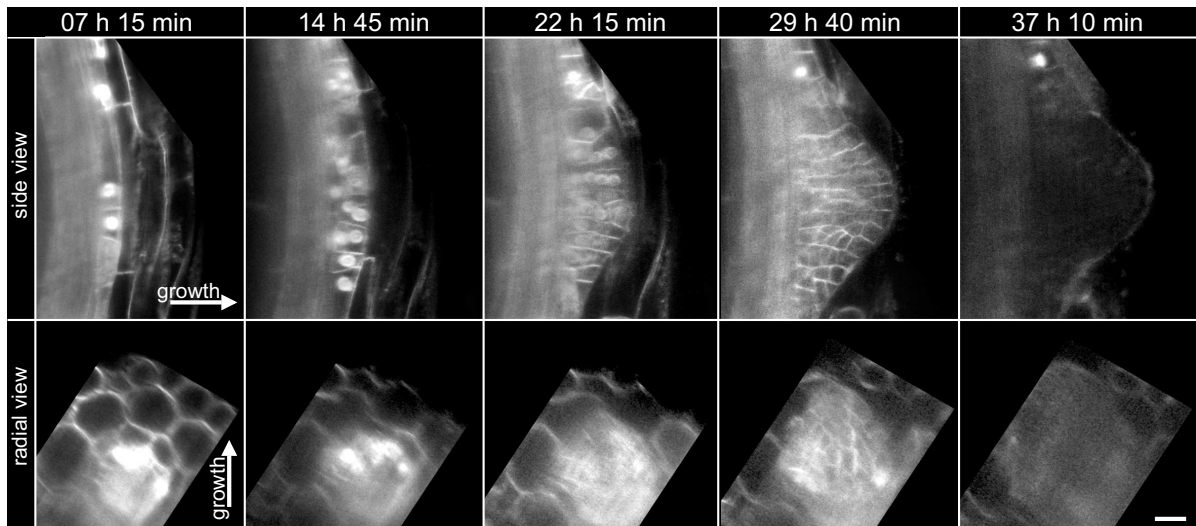
Figure 3.36: Time lapse recording #130607. Five time points of a longitudinal section (side view) and a transverse section (radial view). Only the first 37 h are shown, in total this recording took 64 h and the lateral root fully emerged. Time is relative to the point of gravity-stimulation. The signal of UBQ10::YFP-PIP1;4 (membranes) and GATA23::GUS-GFP-NLS (nuclei) is shown. Images were collected with the $40\times/0.75$ objective lens in the detection path and the $5\times/0.16$ objective lens in the illumination path and camera binning 2×2. Scale bar: $20\,\mu m$. Detailed recording metadata on page 167. **Supplemental Movie-3.36**.

#120830

#121204

#121211

#130508

#130607

light ● GATA23::GFP-NLS / UBQ10::YFP-PIP1;4 ● UBQ10::H2B-RFP
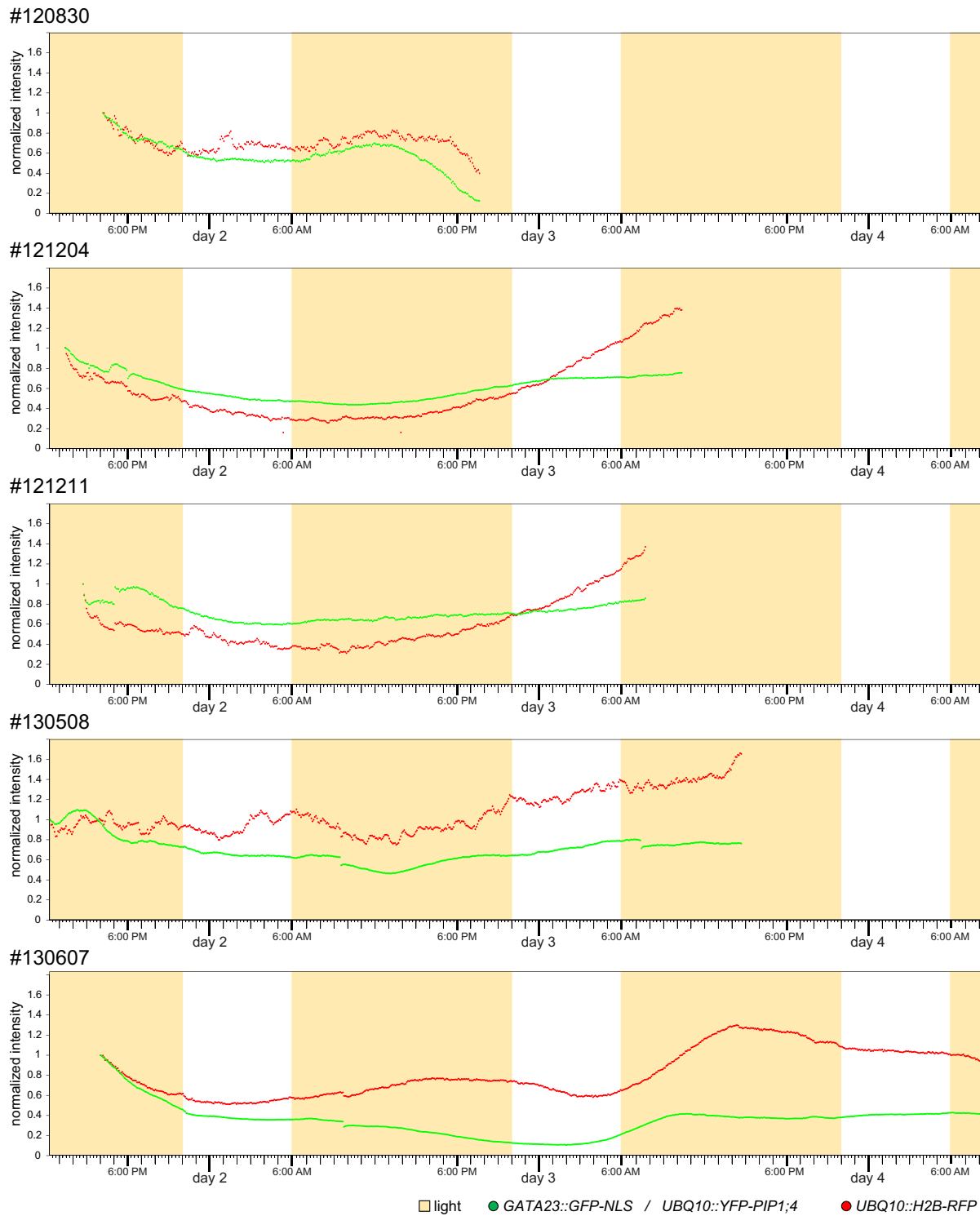
Figure 3.37: Fluorescence intensity as a function of time. The Arabidopsis plants stably expresses UBQ10::YFP-PIP1;4 (membranes, green), GATA23::GUS-GFP-NLS (nuclei, green) and UBQ10::H2B-RFP (all nuclei, red). The fluorescence intensity in each time point was collected in a sum-projection for each of the two channels, measured and normalized to the initial value. The yellow bars indicate when the leaves were illuminated.

3.2.4 The segmented data

All cell lineages could be traced back by the manual identification of the cell nuclei position and the tracking of cell divisions by means of the *Mathematica* program *TrackGen*, written by Alexander Schmitz. The second program *TrackAlyzer* was used to visualize and analyze the datasets. Fig. 3.38 shows the segmented nuclei locations in the first and last time point in all datasets. The plant were gravity stimulated at different day or night times and the recordings last between 15-64 h (Fig. 3.38 B).
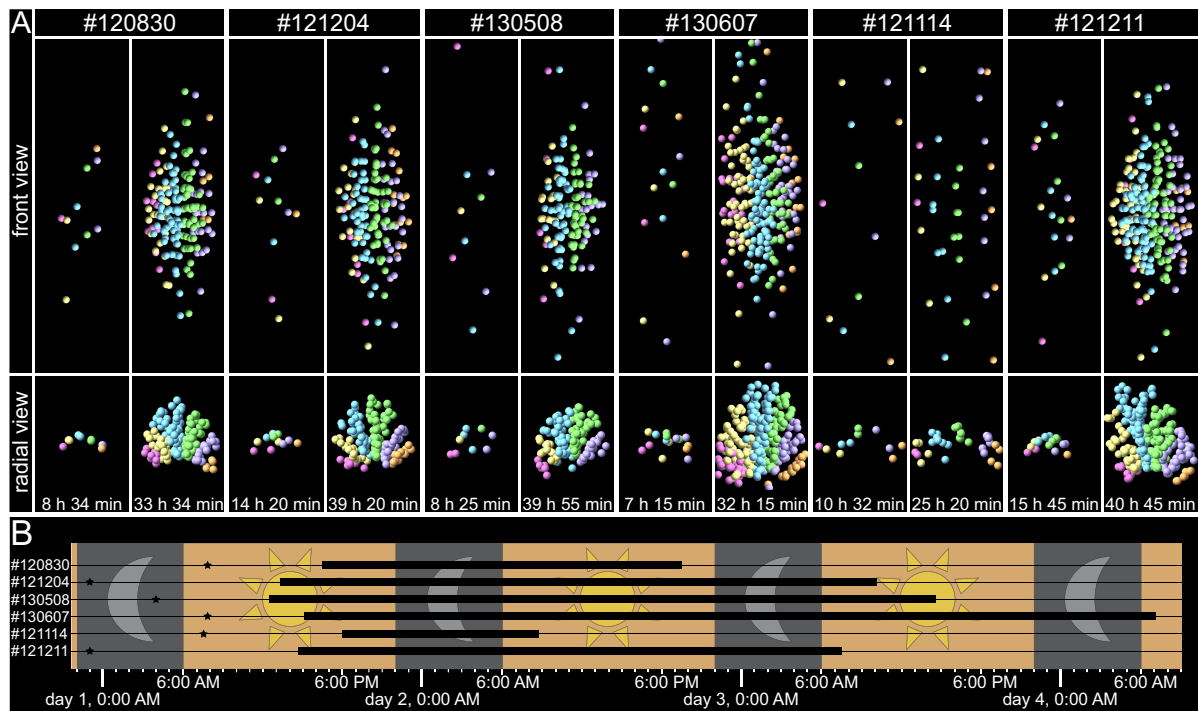
Figure 3.38: The datasets. Spatial distribution of cell nuclei in six individual lateral root primordia datasets (#120830, #121204, #130508, #130607, #121114, #121211). A) The first and the last time point are shown in the front view (upper panel) and in the radial view (lower panel). Time is relative to the point of gravity-stimulation. The position of the nuclei were tracked for 300 time points (25 h), except for #130508, which was tracked for 350 time points. Cells that are in the same cell file share the same color. B) The time course of each recording. The black star indicates the time point of gravity-stimulation, the black bar shows when the recording took place. **Supplemental Movie-3.38**.

In some datasets the first cell division already occurred (datasets #121204, #130607, #121211) before the recording started. The ancestors of this first division could be reconstructed, except for #121211. Two indications were used to reconstruct the ancestor. First, the time point when the next cell division occurs (the average time between two consecutive divisions is about 8 h). Second, the shape of the cell wall between two neigh-

boring cells. Newly formed cell walls have a straight shape and an edged connection to the parental cell walls compared to "old" cell walls (Fig. 3.39).
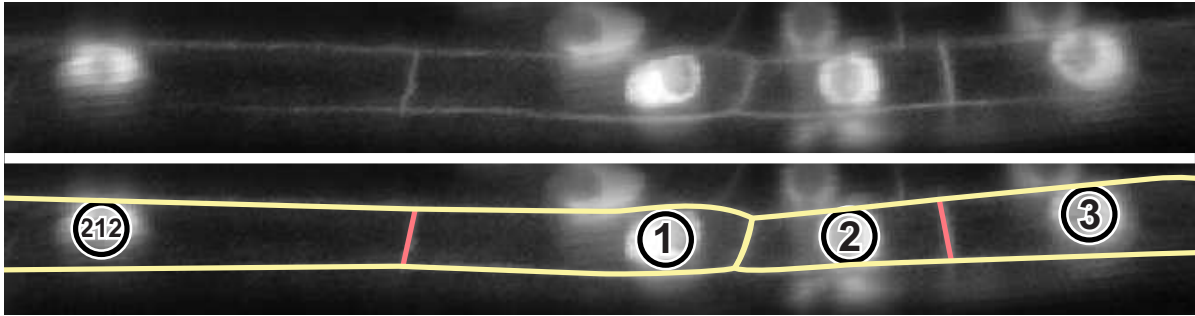
Figure 3.39: First time point of dataset #121204, single front-view section of a pericycle cell file. The recording started after the first division occurred. The precursor cells were identified by the duration to the subsequent division and the shape of the membranes. The cell with the ID #212 and #1 have the same precursor, and cell #2 and #3 have the same precursor. The cell wall between the ancestors has a more complex shape than the two other cell walls (red).

3.2.5 Growth rates and data synchronization

For a comprehensive comparison the datasets were synchronized. For a temporal synchronization, time point zero is the time point of gravity-stimulation. The number of cells at a given time point differ, e.g. dataset #121204 contains 33 cells whereas #130607 has 134 cells at $24\,h$ post gravity-stimulation. By synchronizing the datasets on a later time point where all primordia count the same number of cells (142 cells) the growth curves show a similar behavior with little individual variations (Fig. 3.40 B). In addition, fitting an exponential curve to the total number of cells revealed that the average cellular doubling time was $8\,h\,26\,min \pm 1\,h\,29\,min$ (Tab. 3.40). In conclusion, the overall growth behavior of the different datasets is similar, but due to the variations in the course of development, a synchronization on the actual number of cells was performed (Fig. 3.40 C). This allows to compare the primordia at a given developmental stage. All further analysis of the datasets were performed on the basis of this synchronization method.
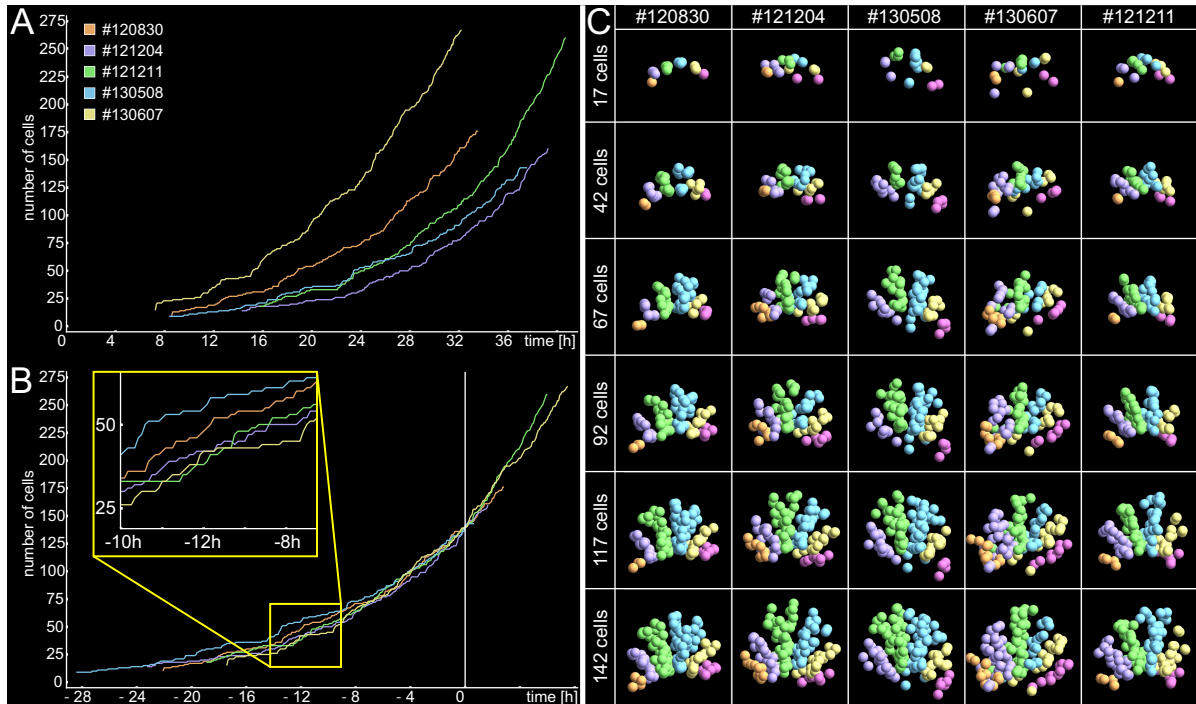
Figure 3.40: Three different types of data synchronization. The total number of cells of each lateral root primordium increases with time. (A) The datasets synchronized to the time point of gravity-stimulation show differences in the development at particular time points. (B) Datasets shifted to a later time point when all primordia consist of 142 cells. The overall progression of the total cell number shows a similar trend, although there are little differences (yellow box). (C) Synchronization on the actual number of cells. **Supplemental Movie-3.40**.

Figure 3.41: Growth rates and cellular doubling times.

	growth rate [%/min]	doubling time [h:min]
#120830	0.13	9:08
#121204	0.17	6:59
#121211	0.16	7:11
#130508	0.12	9:44
#130607	0.11	10:12
mean	0.14	8:26
STD	0.02	1:29

3.2.6 Shape analysis in the virtual lateral root data

The transition from ellipsoid to round previously described (chapter 3.29, page 82) was also observed in the virtual lateral root data. The calculations in Fig. 3.42 were performed in *Mathematica* by Alexander Schmitz based on the standardized (rotated)

datasets. To determine the height of the primordium the maximum distance of two objects along the y-axis in the master cell file was calculated. The width of the lateral root primordium was calculated by the maximum distance of two objects along the z-direction. The length of the primordium was computed by the maximum distance along the x-axis in the upper half (50 % of the height) of the primordium. The volume of the primordium was approximated using a convex hull. The overall progression of the shape of the primordia can be considered as similar and the length to width ratio decreases from 4 to 1.5, which confirms the transition from ellipsoid to a round shape described in chapter 3.29. Variations in the volume per cell show that the average size of a cell varies from plant to plant.
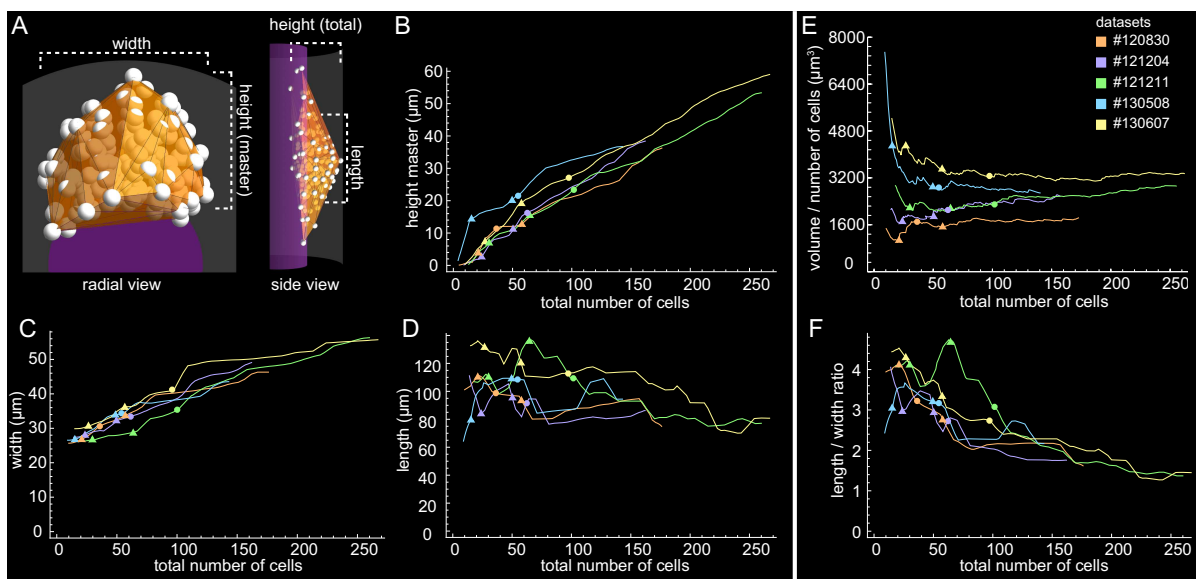
Figure 3.42: Height, width and volume measurements. (A) Convex hull around cell nuclei position of dataset #120830 in side and radial views. (B) The height was measured by taking the minimal and maximal distances between cell nuclei from the center cell file that contributes most to the primordium (master cell file). (C) The width was calculated by the largest distance of all cell nuclei positions in the radial view. (D) The length was measured at 50 % of the height. (E) Average volume per cell as a function of the total number of cells. The total volume was calculated using a convex hull. (F) Length to width ratio. The triangles highlight the first and second periclinal cell division, the circle the first radial division.

3.2.7 Founder cells contribution is variable and the future center position is unpredictable

A lateral root primordium derives from nine to eleven pericycle cells, that are organized in five to eight cell files. By following the lineages of these founder cells, the contribution

of each cell was quantified and showed variations at a common stage of 142 cells. For example, in dataset #130508, 60 % of the primordium consists of the progeny of two cells, whereas in dataset #130607 it required five founder cells to build up 60 % of the primordium.

The contribution of each founder cell seems to be dependent on where the future center of the primordium will be. Which pericycle cells become lateral root founder cells is defined by the position of the underlying protoxylem in the vasculature (Casimiro et al., 2003; Péret et al., 2009). But, what remains elusively is where the lateral root will emerge along the longitudinal axis of the primary root. In order to quantify this observation the center of the primordium was determined in the last time point of the recording in the side view (Fig. 3.43 D). This center was projected on the first time point. The position of the cell borders in each of the core cell files was measured relative to the subsequent center. Neither the position of the cells in the master cell files, nor the average center of the three core files matched with the real subsequent center of the primordium (Fig. 3.43, Tab. 3.5). This leads to the conclusion that the position of the subsequent center is not encoded in the initial position of cells (Fig. 3.43). Because of the reported influence of the endodermis on the initiation and emergence process (Vermeer et al., 2014), the position of the endodermis cell walls was projected on the actual center. No obvious link between the endodermis cell arrangement and the position of the future center of the lateral root primordium could be observed (Fig. 3.44).

Table 3.5: Relative position of the pericycle cell borders to the lateral root primordium future center in the initial time point.

	cell border position relative to the actual center [μm]			
	#-1	#0	#1	average
#120830	-37.7	-7.4	10.0	-11.7
#121204	13.2	23.2	12.6	16.3
#130508	-16.1	-53.5	-28.1	-32.6
#130607	33.5	-3.9	49.7	26.4
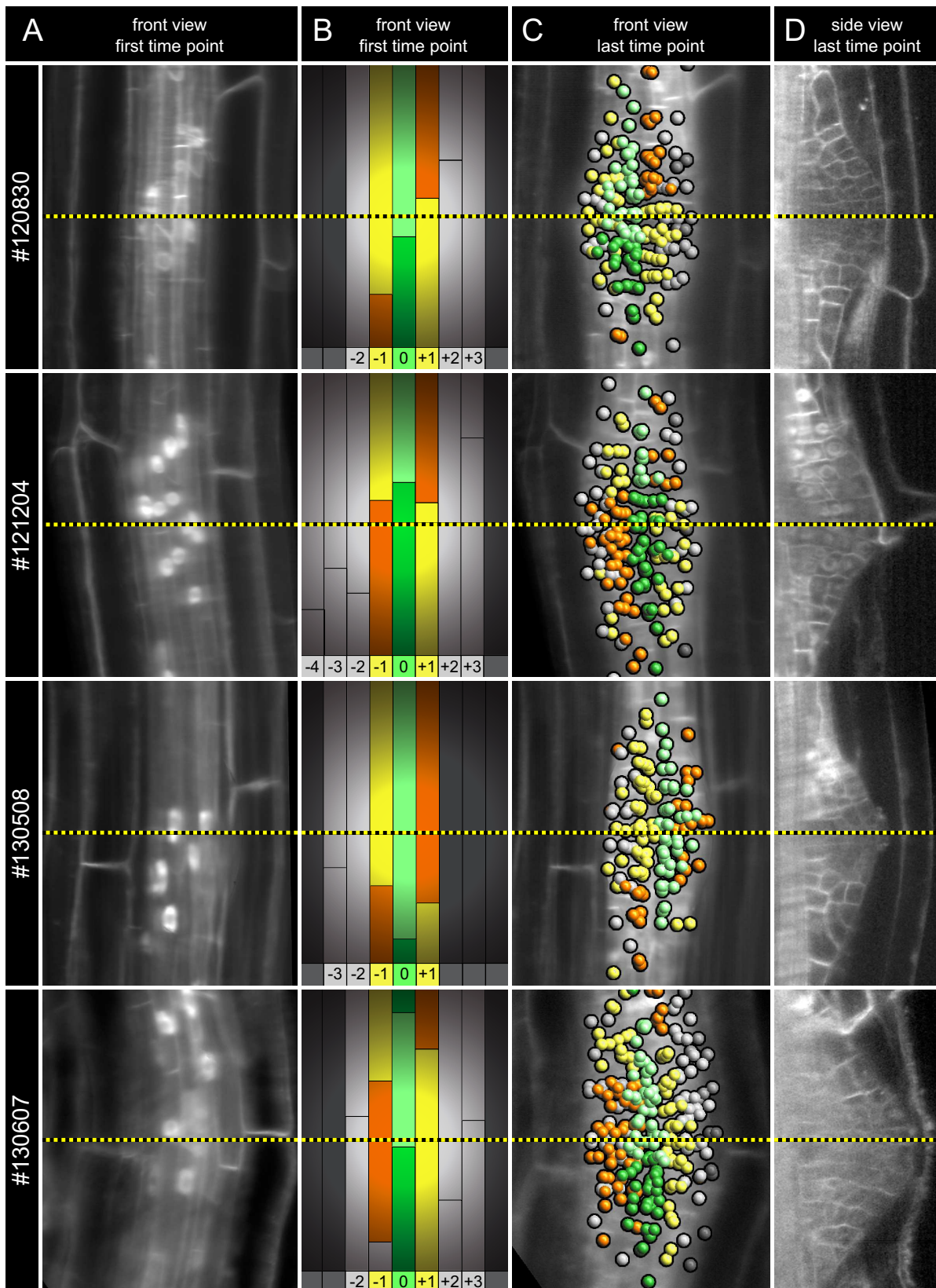
Figure 3.43: Founder cell position with respect to the future center of the lateral root primordium. (A) First time point of the membrane channel in the front view. (B) A sketch of the position of the cell boundaries. Cells in the master cell file are colored in light and dark green, respectively. The cells in the two flanking cell files are yellow or orange. (C) Objects overlayed with raw data in the front view of the last time point of cell tracking. Same color code as in B. (D) Single slice of the side view on the primordium was used to evaluate the center. First and last time points were manually registered in Amira in order to project the primordium center position on the initial situation. Yellow dashed line indicates the center of the primordium.
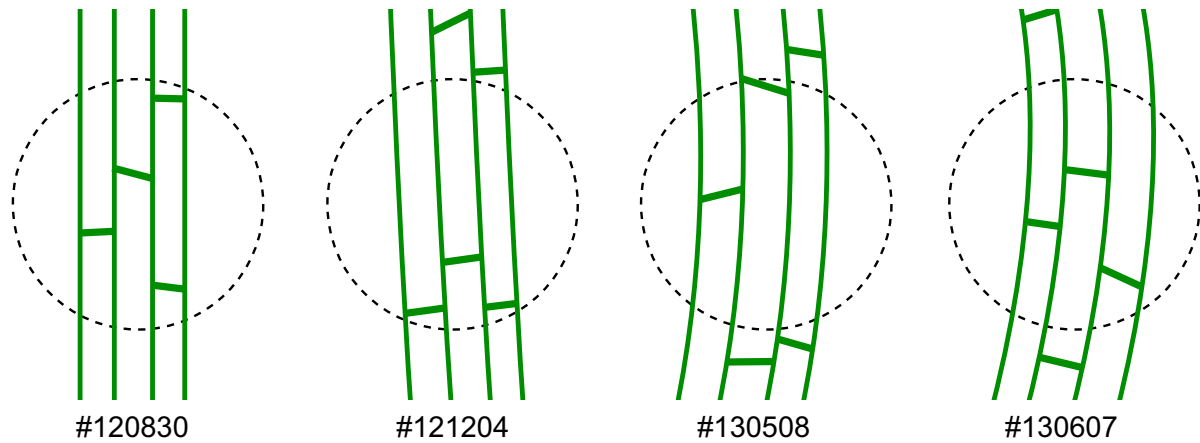
Figure 3.44: Endodermis cell borders and the position of the underlaying lateral root primordium. Front view, the endodermis cell borders were extracted from an initial time point of the recording and overlayed with the future center of the primordium (dashed circle).

3.2.8 Contribution of cell files is variable

The founder cells are located in five to eight pericycle cell files. At a developmental stage of 142 cells a core of three pericycle cell files contribute 109 ± 6 cells to the primordium (76 %) and the cell files that flank the core contribute 36 ± 6 cells (24 %). The central cell file in the core that is the highest is termed master cell file. In all datasets the master cell file contributes 44 ± 6 cells (31 %). In the first time points of the recording it seems obvious that cells in the master cell file swelled the most (Fig. 3.45). The master cell file is labeled #0 and colored green. Flanking cell files are colored alternately in yellow and blue. Cell files to the left are assigned with negative indices (#-1, #-2, #-3), cell files to the right are assigned with positive indices (#+1, #+2, #+3).
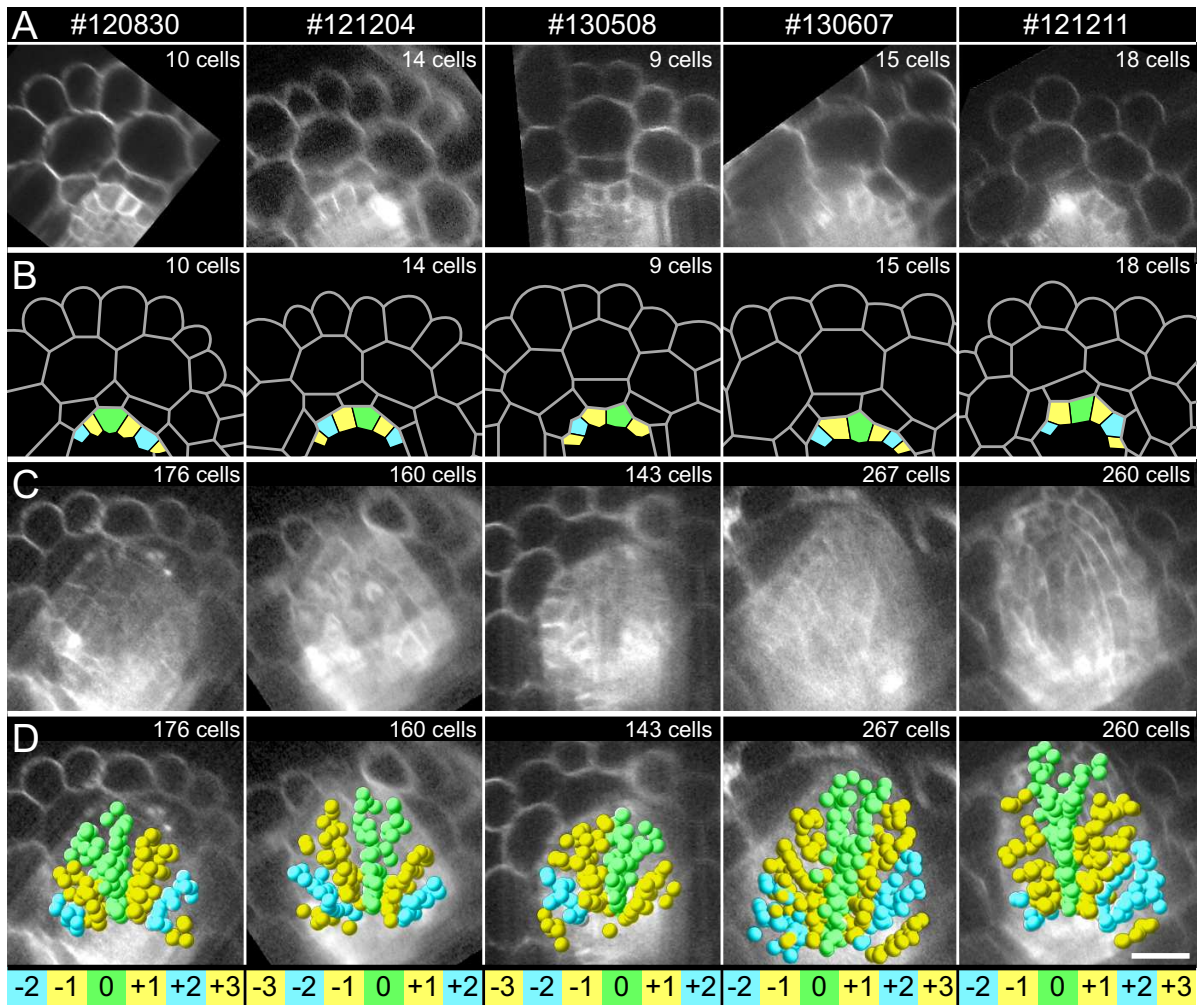
Figure 3.45: Cell files in the first and last time point of nuclei tracking. (A) Radial section of the membrane channel in the initial time point. (B) Sketch of the membranes in A. The master cell file is colored in green, the flanking cell files are alternately colored in yellow and blue. (C) Radial section (maximum intensity projection of 20 z-planes) in the last time point. (D) Objects in the radial view overlayed with the raw data in C. The master cell file is labeled #0 and colored green. The flanking cell files are alternately colored in yellow and blue and cell files to the left are assigned with negative indices (#-1, #-2, #-3), cell files to the right are assigned with positive indices (#+1, #+2, #+3).

In the radial view, it seems that most of the cells in the master cell file are located in the tip of the primordium. This observation can also be seen in single slices at different depths of the primordium in the frontal view (Fig. 3.46). The thickness of a cell file is increased by radial divisions, which mainly take place in upper regions of the primordium. But, no regularity in the occurrence of radial divisions was observed (Tab. 5.1 on page 141).
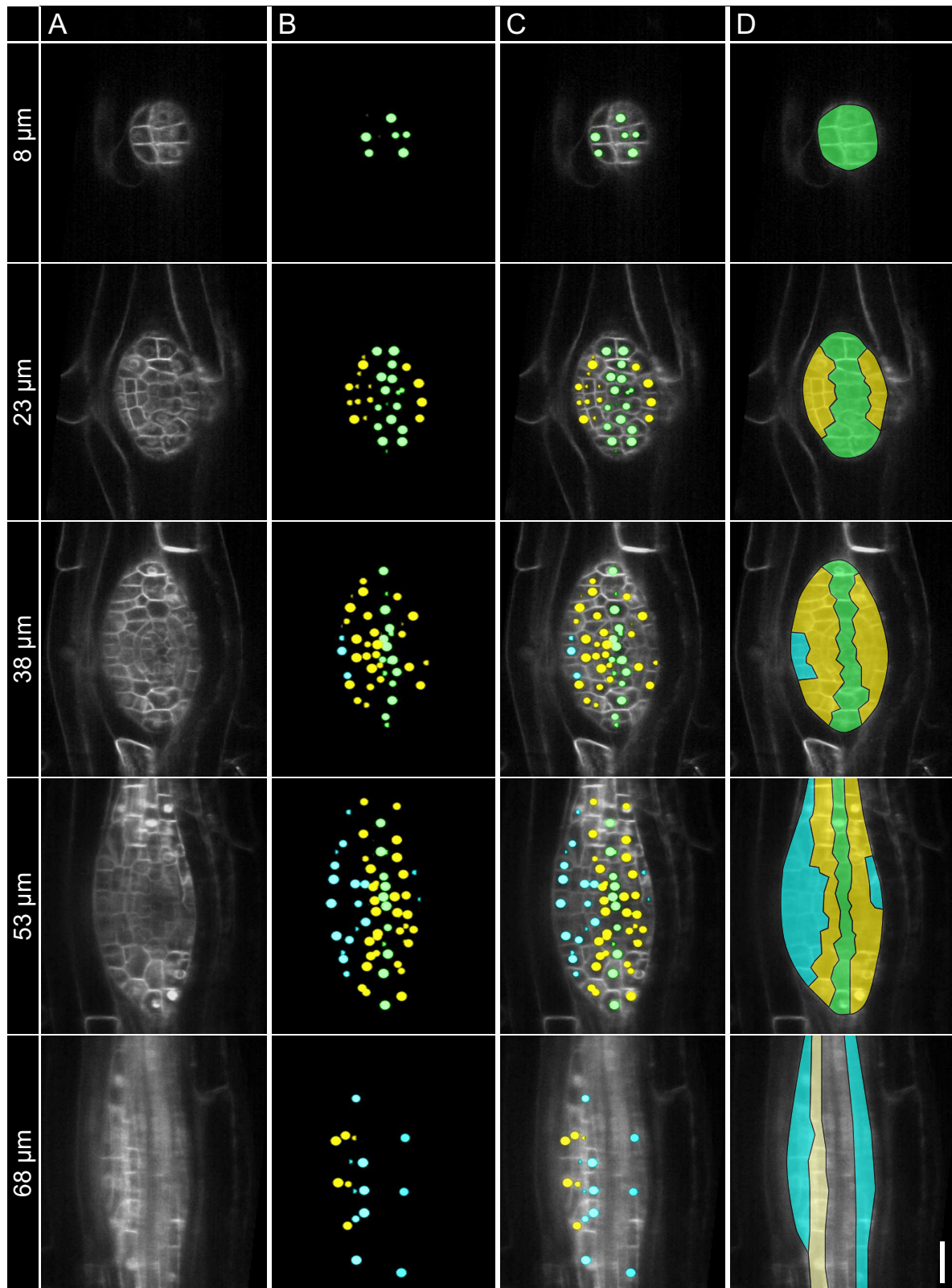
Figure 3.46: Cell file contribution in the last time point of dataset #121211. (A) Single slices of the membrane channel in front view at indicated depth from the tip of the lateral root primordium. (B) Nuclei objects in the corresponding image in A. (C) Overlay of A and B. (D) Sketch of the cell contours that belong to the same cell file. The master cell file contributes most to the tip whereas in deeper regions of the primordium only a thin row of cells can be seen. The flanking cell files make most of the base of the lateral root tissue and are excluded from the tip.

As a control and for visualization purposes the objects were overlayed with the raw image data of the membrane channel. Therefore, the objects were exported from *Mathematica* as 8-bit RBG images, and color coded according to the cell file belonging. The overlay of the objects with the raw data for single time points was performed in *Arivis*. In order to have an unobstructed view on the primordium from all sides the surrounding tissue was removed digitally in *Adobe After Effects* (Fig. 5.6 on page 143). The result of the overlay is exemplary shown for data set #121211 in Fig. 3.47 (Fig. 5.7–5.10 shows the other four datasets on page 144–145).
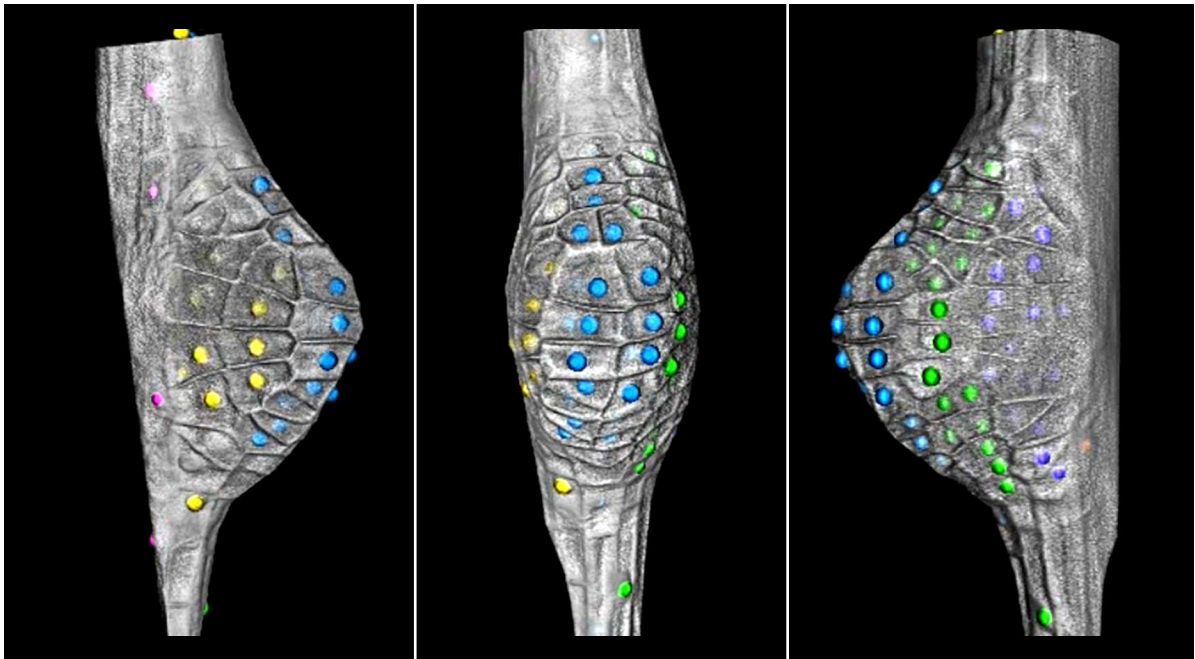
Figure 3.47: 3D overlay of the objects with the membrane channel in the last time point of dataset #121211. Front view (middle) and two angular views (left, right). Objects with the same color are located in the same cell file.

3.2.9 Contribution of flanking cell files increases during emergence

The cell lineage tracing revealed that the master cell file contributes most of the cells at a stage of 142 cells. However, the tracing was performed only on the first $24\,h$ and the actual emerging process was not analyzed, although most of the recordings continued until emergence of the root. In order to observe the further development of the cell files a transverse cross section of the membrane channel was overlayed with the objects (color

coded by cell file). In the last time point of the segmented data the contours of the cell files were highlighted with a colored area mask in *Adobe After Effects*. The subsequent development of the cell files was tracked manually by following the very well resolved cell contours. This reveals, that the tip of the lateral root is pushed out of the primary root by expanding cells at the base close to the vasculature. Thus, flanking cell files contribute more and more to the volume while the master cell file leaves a thin cell file behind (Fig. 3.48).
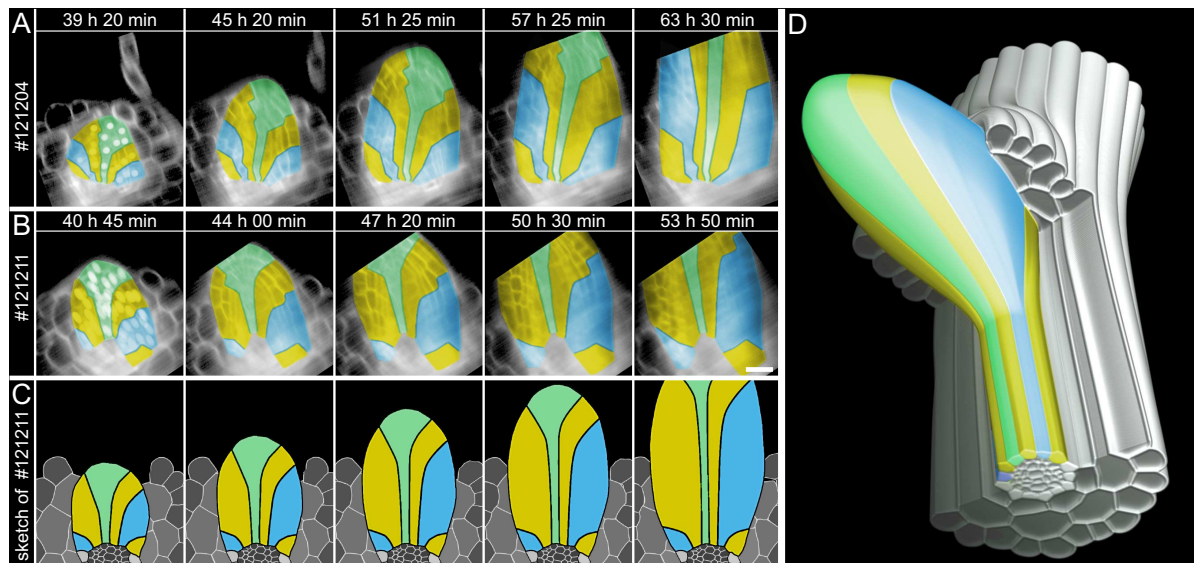
Figure 3.48: Cell file development in the future time course. A radial cut of the membrane channel trough the main root at different time points. The master cell file is colored in green, the flanking cell files are alternately colored in yellow and blue. The cell files highlighted in the last time point of nuclei tracking were followed in the further development by tracking the cell borders in dataset (A) #121204 and (B) #121211. (C) An illustrative drawing of B (#121211) shows the cell file development. (D) Three-dimensional rendering illustrates the cell file contribution of an outgrown lateral root. **Supplemental Movie-3.48**.

3.2.10 Layer assignment

Lateral root development has been separated into stages according to the number of cell layers that are generated (Malamy and Benfey, 1997). The virtual lateral root data allowed to reconstruct a cellular layering in order to see whether the sequence and time point of cell layer generation can be linked to a particular total number of cells and follows a certain regularity. The angle between the two daughter cells was calculated to a reference vector. The angle measurement was performed by Jens Fangerau. His algorithm takes the developing curvature of the primordium into account (Fangerau, 2014). By this, the cell divisions were classified into either anticlinal, periclinal or radial

(definition on page 12). Whenever a periclinal division occurs the two daughter cells were assigned to new cell layers. For example, the progeny of a founder cell located in layer #00 were assigned into two new layers termed #01 and #02. The cell layer closer to the main root received the lower number (#01), the layer further apart the higher number (#02). The datasets #121211 and #130607 could be analyzed until a total number of 260 which allowed the reconstruction of eight layers. Fig. 3.50 shows the layering in the last time point of all cell files in datasets #130607 (Fig. 5.12–5.15 shows the other four datasets on page 148–151).

The sequence of periclinal divisions is similar The nuclei coloring according to number of periclinal divisions in the Fig. 3.50 show that cells with a same color, i.e. they derive from the same number of periclinal divisions, are organized in a layered structure. However, this is only the case for cells in the center of the primordium, at the margins color code is more variable and no obvious sequence of periclinal divisions was found.

Furthermore, the occurrence of periclinal divisions correlates with a particular developmental stage, i.e. there is a regularity at which developmental stage periclinal divisions occurs in all data sets (Fig. 3.49 and Tab. 5.1 on page 141). The first periclinal division occurs at a stage of 24 ± 4.9 cells, the second periclinal division occurs when the primordium counts 56 ± 5.6 cells. In addition, the sequence of periclinal divisions is conserved, i.e. the second periclinal division occurs always in the outer layer before the inner layer (Fig. 3.51 and Fig. 5.11 on page 146).
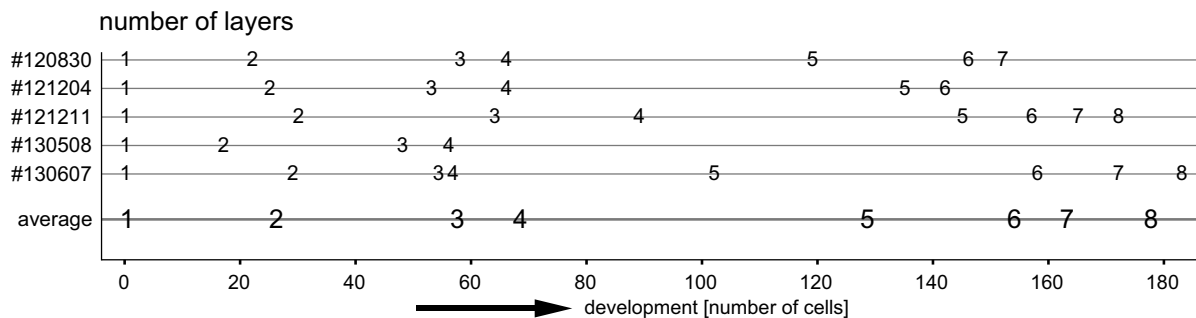
Figure 3.49: Time point of layer occurrence.
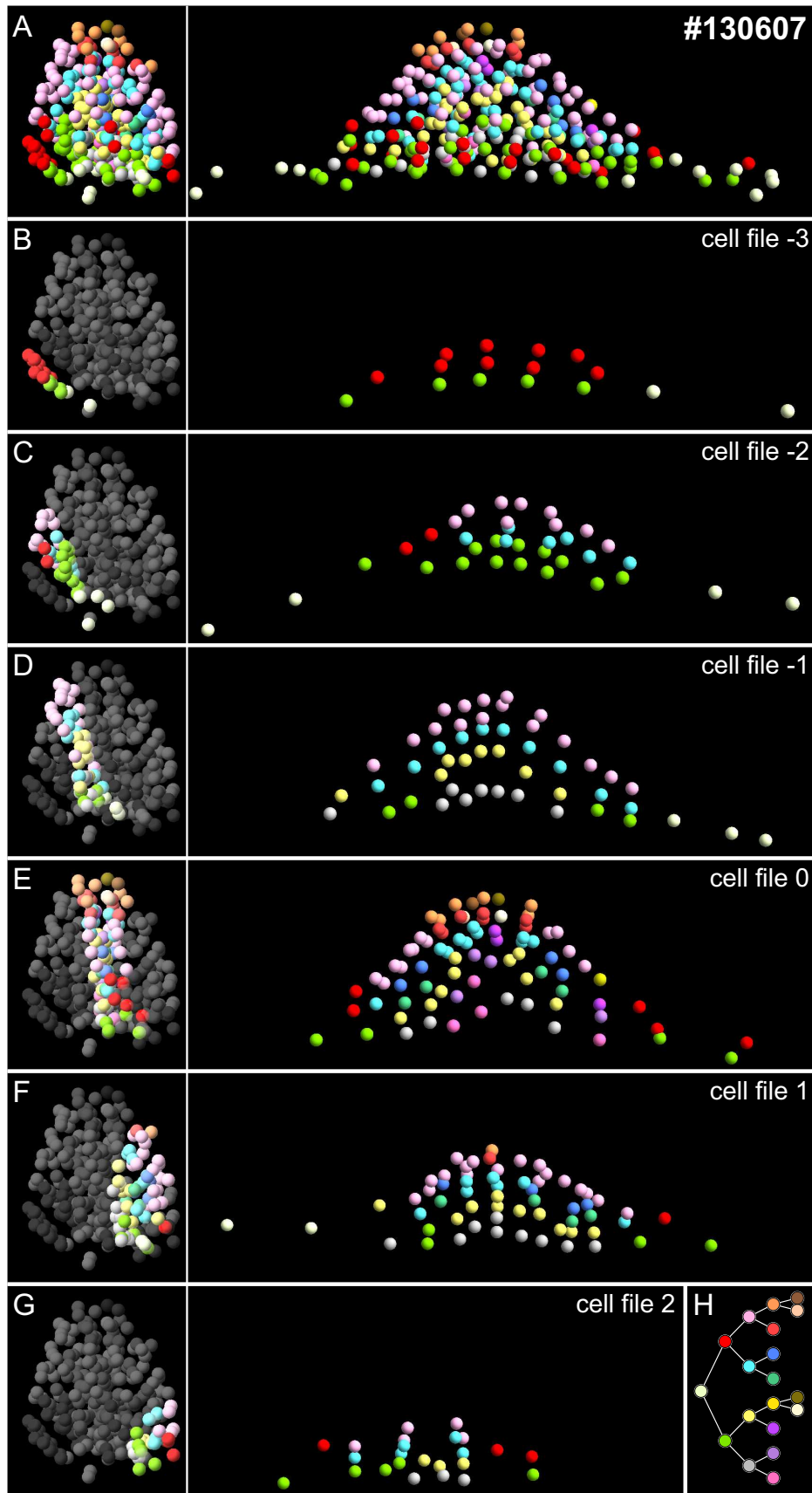
Figure 3.50: Layer assignment of the virtual lateral root #130607. The nuclei position in the last time point of the time lapse is shown in the radial view (left) and side view (right). (A) All nuclei objects. (B-G) Objects of a particular cell file. (H) Legend, colors indicate the history of periclinal divisions. **Supplemental Movie-3.50**.
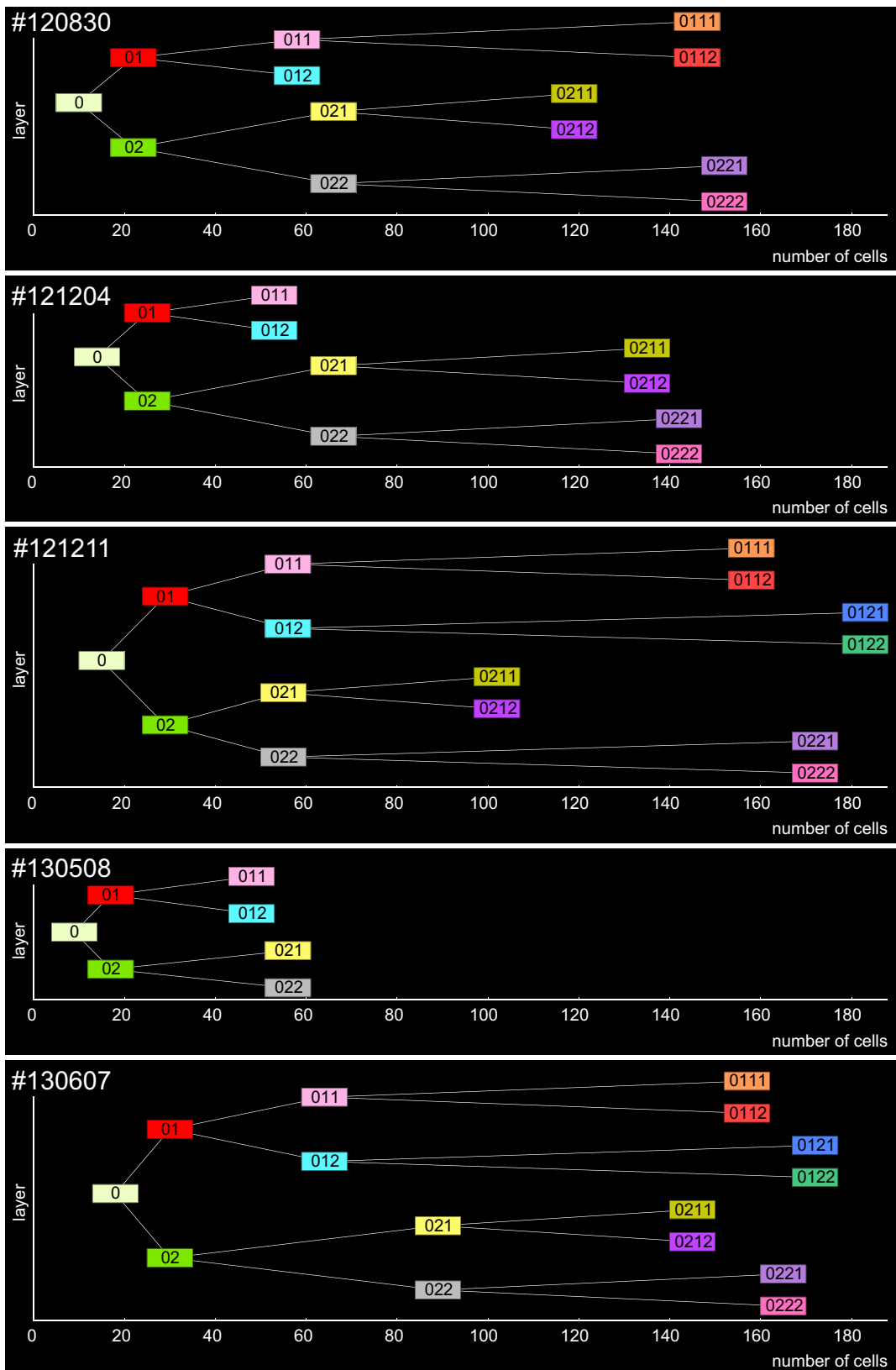
Figure 3.51: Lineage of layer generation.

Unexpected asymmetric cell division does not impair the formation process Although cells located in a particular layer derived from the same number of periclinal divisions, in dataset #130607 the sequence of periclinal divisions was disrupted by an unexpected asymmetric cell division within the center region of the primordium. This asymmetric cell division occurred in the second cell cycle in one of the small central cells (Fig. 3.52 A, B). The cell divided neither anticlinal nor periclinal but split off a corner. As a consequence, the larger daughter cell remains in both layers. In the next division round both daughters divide periclinal (Fig. 3.52 E) and as a result only three cell layer were formed instead of four. Although there was a unusual cell division changing the typical sequence of cell divisions, it seems that in the further development a typical organization of layers redevelops (Fig. 3.52 F, G).
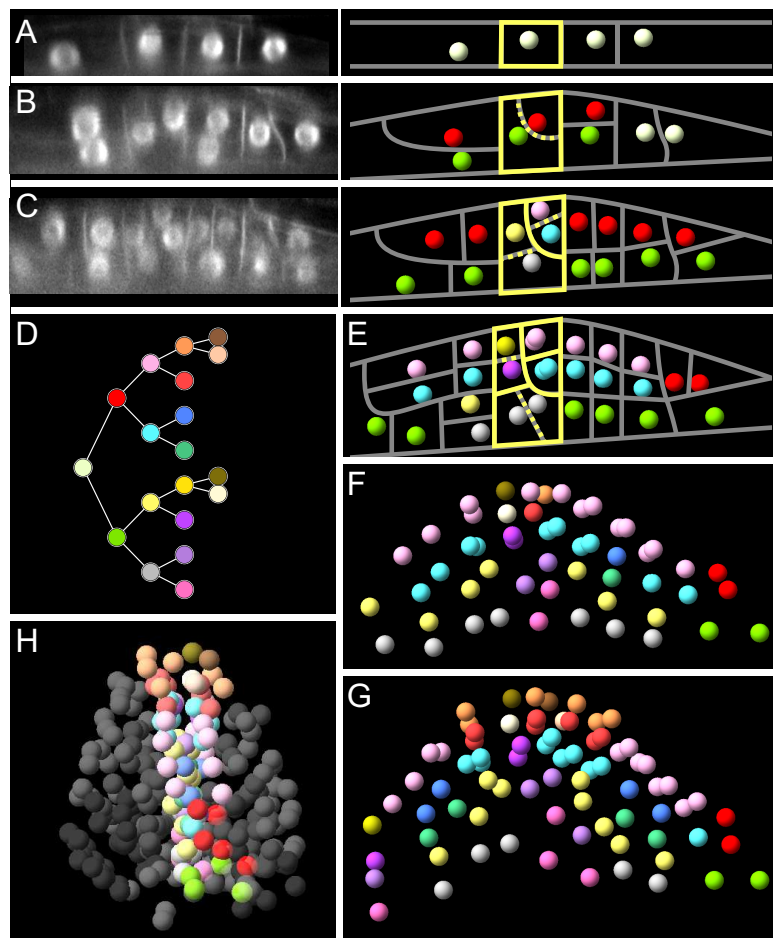
Figure 3.52: Unexpected asymmetric cell division in the center of the primordium. (A-G) Single longitudinal slice along the master cell file in dataset #130607 (left) and a sketch of the membrane and the positions of the nuclei position color coded according to the layer assignment (right). An asymmetric cell division in one of the small central cells is highlighted by the yellow boxed area. The cell split off one corner which leads to a different history of periclinal divisions. (D) Legend, colors indicate the history of periclinal divisions. (H) Same cell file in the radial view.

3.2.11 Transverse and longitudinal cell divisions

Oriented cell divisions are crucial for the morphology of developing organs. The correct positioning of cell walls is important especially in early steps of lateral root formation. To quantify when and where asymmetric cell divisions occur the plane of division was classified in two groups. Cell divisions that built the smallest cell wall area (Errera rule) were assigned as transverse. Cells that divide along their long side and thereby creating a long cell wall were assigned as longitudinal.

The *Big Data Viewer*-plugin in *Fiji* was used to create images of each cell file (side view) in dataset #120830, #121204 and #130508. All divisions were classified by measuring the geometry of the cell and the appropriate cell division rule was assigned. The divisions were summed up for each of the first four cell cycles. In the first cell cycle all divisions are anticlinal following the shortest wall rule. In the second cell cycle 50 % of the divisions were longitudinal. In contrast, in the third and fourth cell cycle only 20 % of the divisions were longitudinal (Fig. 3.53 and Tab. 5.2 on page 147). For example, some periclinal cell divisions occur although the mother cell is quite long (Fig. 3.55 cell file #-2 B). Those divisions seemed to occur preferentially at the margins of the primordium. The results suggest that the second cell cycle might play a crucial role in the early steps of lateral root formation.

	2. cell cycle	3. cell cycle	4. cell cycle
△ #120830	61.5 %	23.1 %	21.1 %
■ #121204	50.0 %	20.8 %	28.6 %
○ #130508	33.3 %	14.3 %	12.5 %
□ average	**48.3 %**	**19.4 %**	**20.7 %**
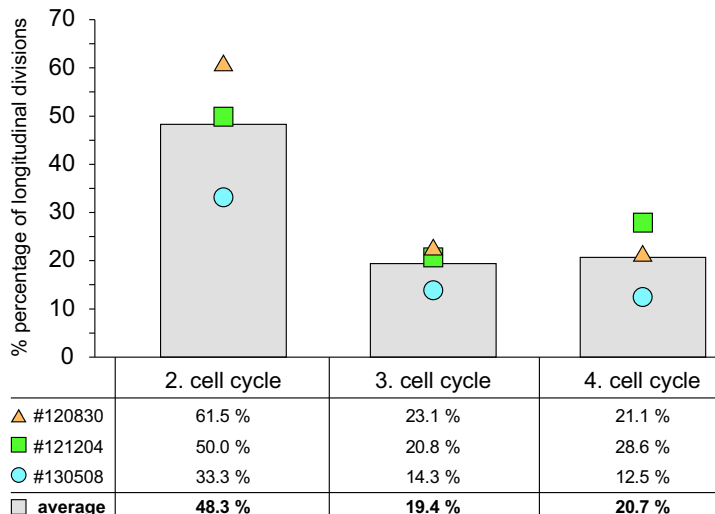
Figure 3.53: Percentage of longitudinal divisions (long cell wall) in the first four cell cycles.
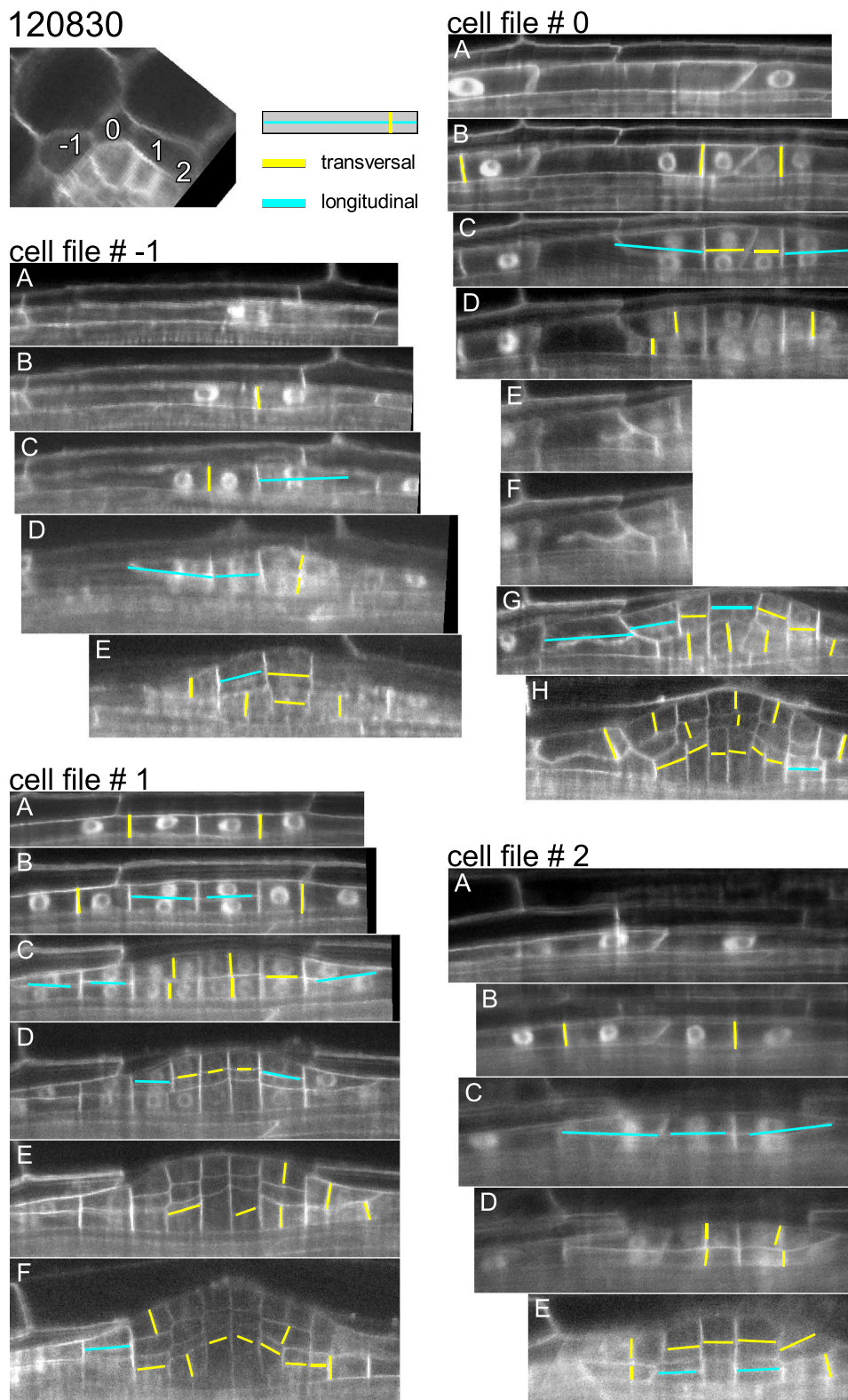
Figure 3.54: Transverse and longitudinal cell divisions in dataset #120830. Single sections along indicated cell files (overview upper left). The sections are shown at several time points (A-H). Cell divisions were assigned into two classes depending on the size of the cell wall relative to the cell dimensions. Yellow - transversal (shortest area wall), blue - longitudinal (long cell wall).

121204
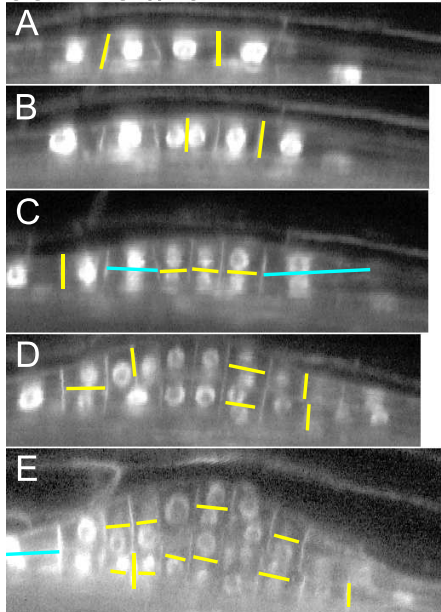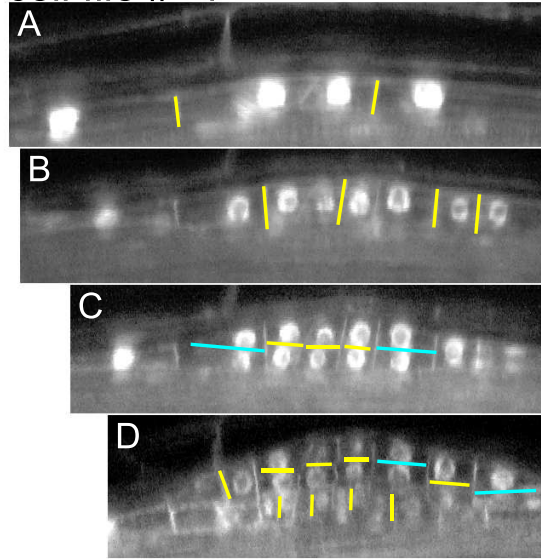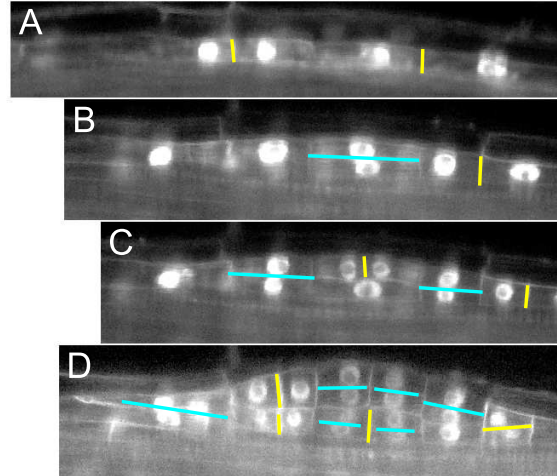
Figure 3.55: Symmetric and asymmetric divisions in dataset #121204. Single sections along indicated cell files (overview upper left). The sections are shown at several time points (A-E). Cell divisions were assigned into two classes depending on the size of the cell wall relative to the cell dimensions. Yellow - transversal (shortest area wall), blue - longitudinal (long cell wall).

130508
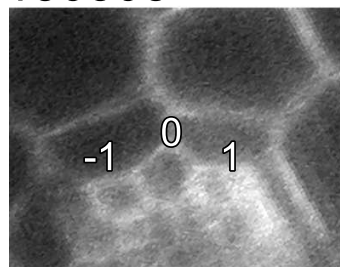
cell file # -1
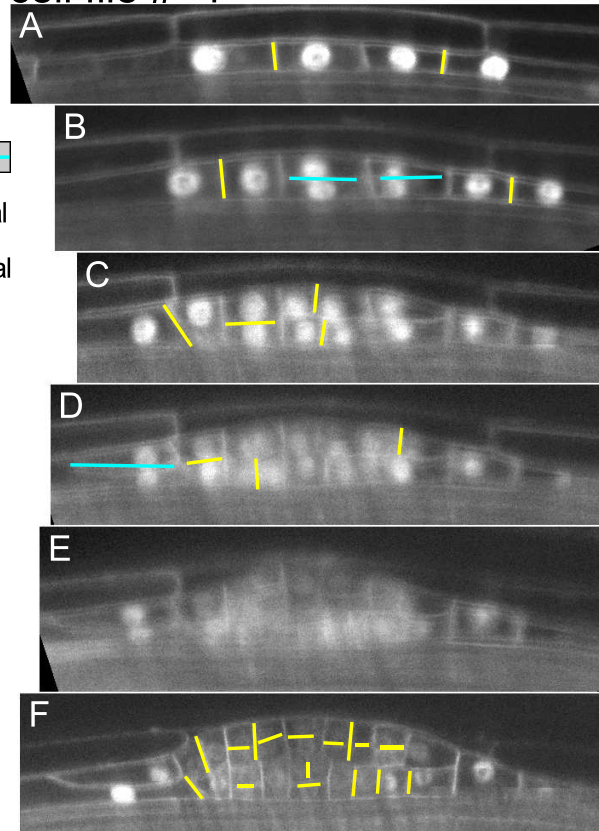
cell file # 0
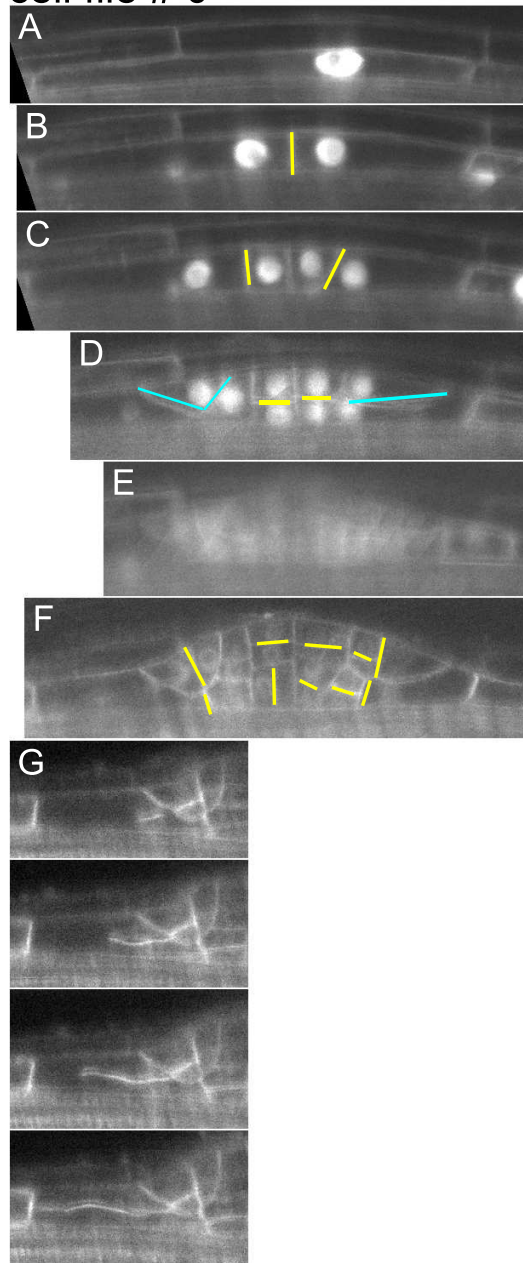
cell file # 1
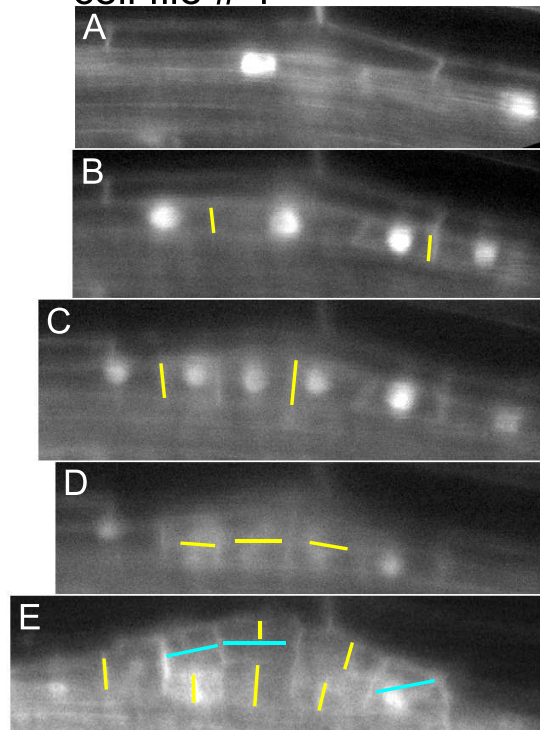
Figure 3.56: Symmetric and asymmetric divisions in dataset #130508. Single sections along indicated cell files (overview upper left). The sections are shown at several time points (A-G). Cell divisions were assigned into two classes depending on the size of the cell wall relative to the cell dimensions. Yellow - transversal (shortest area wall), blue - longitudinal (long cell wall).

3.2.12 Aurora double mutant, *aur1-2 aur2-2*

The α-Aurora kinases play a crucial role in the positioning of the cell plate during asymmetric cell divisions (Van Damme et al., 2011). In the *aur1-2 aur2-2* double mutant new cell walls of asymmetric cell divisions appear unstructured and folded. The shape analysis of this mutant described in chapter 3.2.2 (page 79) showed an impaired morphology and the continuous radialization (length/width ratio) observed in the wild type was replaced by an irregular decrease in the *aur1-2 aur2-2* mutant. In order to follow the cell division pattern during the impaired primordium growth a transgenic plant expressing PIN1::PIN1-GFP and UBQ10::H2B-RFP was recorded (Fig. 3.57). Furthermore, the cell nuclei lineage analysis pipeline was successfully applied.
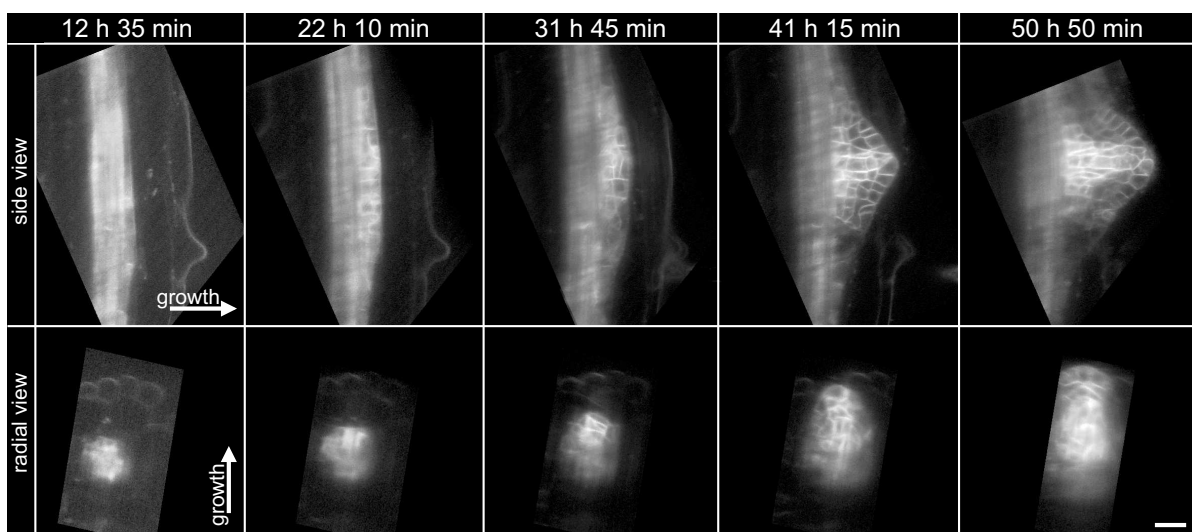
Figure 3.57: Time lapse recording of the *aur1-2 aur2-2* double mutant, dataset #131203. Five time points of a longitudinal section (side view) and a transverse section (radial view). Time is relative to the point of gravity-stimulation. The transgenic Arabidopsis expresses PIN1::PIN1-GFP. Images were collected with the $40\times/0.75$ objective lens in the detection path and the $5\times/0.16$ objective lens in the illumination path and camera binning 2×2. Scale bar: $20\,\mu m$. Detailed recording metadata on page 168. **Supplemental Movie-3.57**.

Especially in early stages cell walls appear to be defective (Fig. 3.58), e.g. two nuclei that derived from different founder cells merged because of a defective cell wall , or one cell tried to separate the chromosomes but failed. Another example is a cell that divided without building a cell wall, i.e. the daughters remained in the mother cell (binucleated cells). In the next round of division both nuclei divided anticlinal including a cell wall, thus the middle nuclei shared the same cell. A last example is depicted in Fig. 3.58. This founderdivided without building a cell wall (Fig. 3.58 A-C). The daughters both divided

periclinal and their cell plates grew towards each other and connected in the center (Fig. 3.58 D-F). As a consequence, each of the two cells contains two nuclei. Further cell divisions appear more or less arbitrarily (Fig. 3.58 G).

Although the cell divisions in the early stages are defective the primordium grew, and in later stages more cell divisions appear normal. The doubling time of $10\,h\,50\,min$ was lower compared to the wild type of 7-10 h (Fig. 3.59 C). A much higher number of cell layers were created compared to the wild type datasets (Fig. 3.59 D, E) and the history of periclinal divisions in the center showed no obvious pattern as in the wild type datasets (Fig. 3.59 B). Not all cells could be tracked because at least one cell file had no fluorescence signal in the nucleus channel. It was impossible to use the membrane channel for cell tracking because a) the first 220 time steps were recorded with a low laser intensity and therefore the fluorescence signal was too weak, and b) on the backside of the primordium the impaired cell walls were not detectable. Nevertheless, from the membrane channel one could see that only a handful of cells were missing and the dataset was used to analyze and compare it with the wild type datasets.
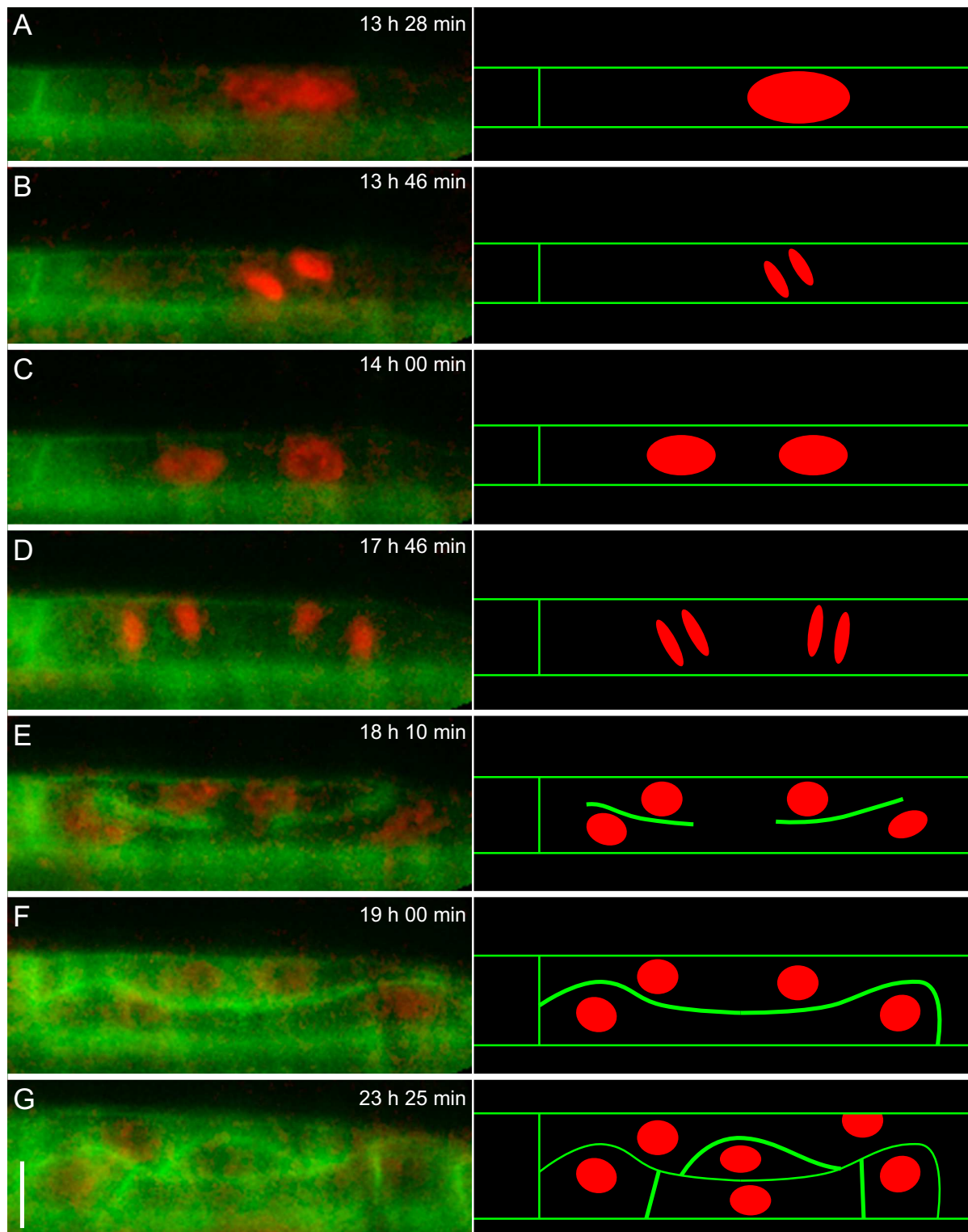
Figure 3.58: Altered cell divisions in the _aur1-2 aur2-2_ double mutant. Single slice of the master cell file in dataset #131203 at indicated time points. Raw data on the left and a sketch of the plasmamembrane and nuclei on the right. (A-C) The cell divided without building a cell wall. (D-F) Both daughter cells divided periclinal and their cell walls connected in the center creating two binucleated cells. (G) The next cell divisions appear more or less arbitrarily. Scale bar: $20\,\mu m$. **Supplemental Movie-3.58**.
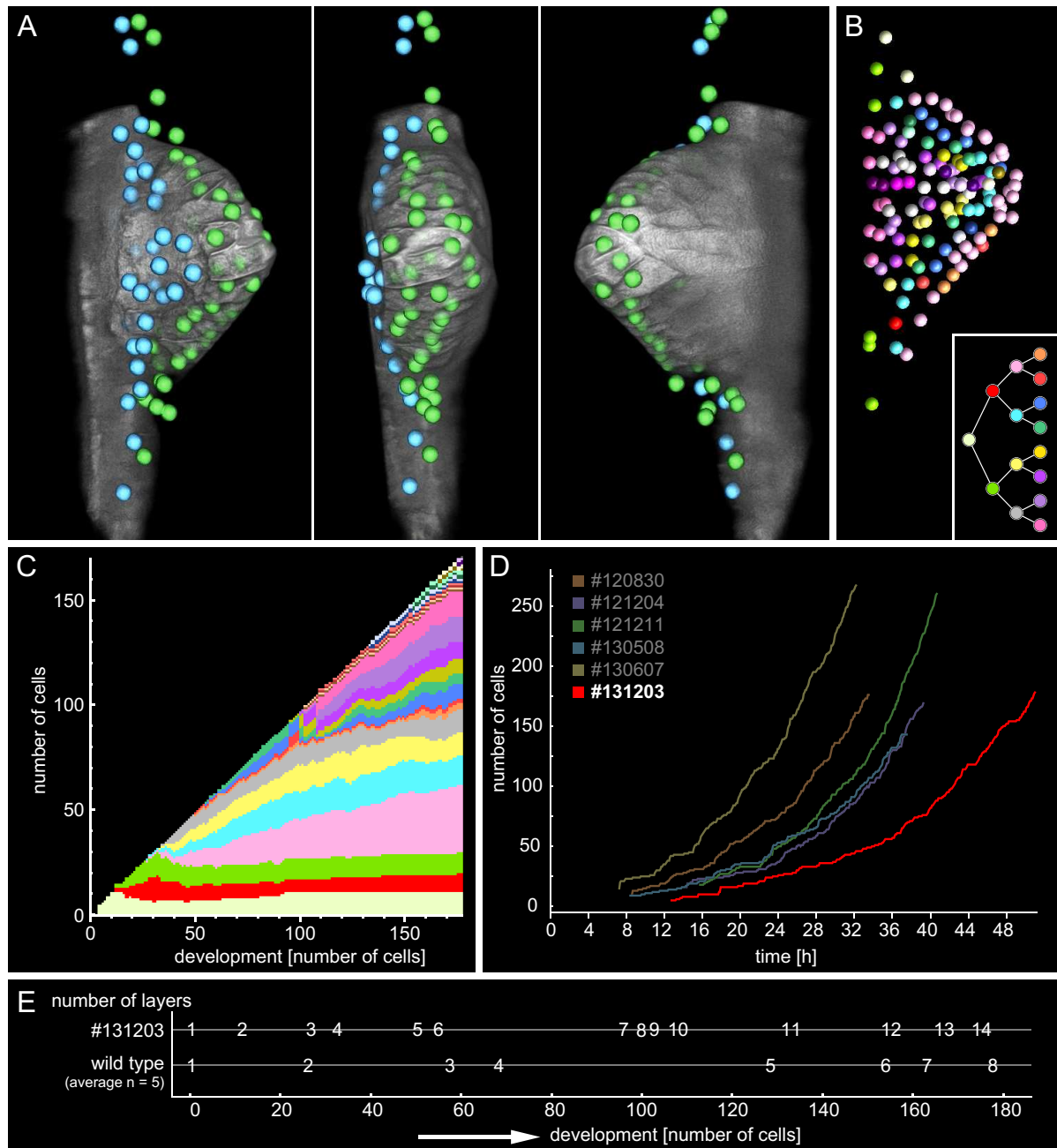
Figure 3.59: **Various properties of the aurora mutant**. (A) 3D overlay of the objects with the membrane channel (PIN1::PIN1-GFP) in the last time point of dataset #131203. Objects with the same color are located in the same cell file. (B) Nuclei position in the last time point of the time lapse in the side view. Same color means the same history of periclinal divisions. (C) Number of cells in each layer as a function of time. Layers are color coded according to the lineage tree legend in B. (D) The growth curve of the mutant (red) compared to the five wildtype growth curves (shaded). Time is relative to the time point of gravity-stimulation. (E) Time point of first layer occurrence in the mutant compared to the average of the wild type datasets. **Supplemental Movie-3.59.1** and **Supplemental Movie-3.59.2**.

4 Discussion

The aim of this work was to establish a non-invasive imaging method that allows the observation of plant growth over long periods of time with high spatial and temporal resolution. Several sample preparation methods were developed that allow for various applications. The process of root growth over a time period of up to $120\,h$ was successfully recorded without any obvious signs of damage to the plant. This is mainly by means of the special sample mounting, the growth conditions and the low photo-toxic effects of the microscope technique.

4.1 Plant imaging in the mDSLM

4.1.1 Growth conditions

The growth conditions, such as light quality, temperature, humidity or the availability of nutrients, can be controlled in the microscope setup during the experiment. Furthermore, the sample preparation method maintains the plant in its position as it grew in the plant incubator so that mechanical stresses due to transfer and rearrangement of the plant prior imaging was reduced to a minimum. This was confirmed by growth rates similar to those reported in literature (see chapter 3.1.1 on page 52) and quality controls that showed that the plant continued growing after the recording process (Fig. 3.2).

4.1.2 The monolithic Digital Scanned Light-Sheet Microscope

In contrast to conventional epi-fluorescent microscopy, Light Sheet-based Fluorescence Microscopy (LSFM) illuminates only a thin volume overlapping with the focal plane of the detection objective lens which is arranged perpendicular to the illumination. As a result, the microscope has a true optical sectioning capability and a reduced photo-toxicity and photo-bleaching property. The use of modern cameras allow for fast recording speed. To conclude, LSFM is ideal for long term observation of a large three-dimensional volume. In long term observations the stability of a system is very important, especially to

113

keep the plant in the 100-200 μm small field of view. The sample preparation is crucial, but also the microscope, the alignment of the two foci, the position of the stage, etc was extremely stable and allows to maintain the field of view for at least one week.

Another challenge was to maintain the balance between keeping the plant healthy and having a good enough resolution spatial as well as in time. Moreover, the photosynthetic activity of the plant is essential and this period should be as long as possible. Although multiple angle acquisition or structured illumination are great features of the microscope they were not used for long term observations because those applications stretch the time it takes to record a single time point. This in turn reduces the time period of leaves' illumination. The viability of the plant was dramatically reduced when a higher laser intensity was used which could be seen by a stop of growth. Because of the potential photo-toxic effects, the first recordings of the lateral root formation process were captured every $15\,min$. At that time, the spatio-temporal resolution was too low for a reasonable nucleus tracking, but allowed for global shape analysis. Later, experiments were performed with a $40\times$ instead of a $20\times$ and the time interval was reduced to $5\,min$. The use of camera binning heavily increased the contrast which allowed to decrease the laser intensity. The camera binning also increases the read-out speed which results in a higher frame rate. Furthermore, the exposure time was kept short (20-50 ms) and channels were recorded successively which altogether allowed to record a single time point in $40\,s$ (2 channel, 233 z-planes). This allowed to illuminate the leaves for $4\,min\,20\,s$ which further improved the physiological state of the plant. The trade-off between a high enough spatio-temporal resolution and keeping the plant healthy in the microscope remained a challenge. All other microscopic techniques expose the sample with more energy and are unable to reproduce observations obtained by LSFM. In conclusion, the none-phototoxic imaging by means of LSFM and the plant growth conditions in the mDSLM allowed for unprecedented observations of plant developmental processes.

4.1.3 Light conditions and growth

The viability of plants largely depends on the amount of light they receive. In contrast, fluorescence microscopy requires darkness to collect the relatively low emission light of fluorophores. The illumination system in the mDSLM allows both, the plant leaves are illuminated in between each recording. This artificial interval illumination seemed to not impair the phenotype of the root system, as the number of lateral roots was the same in continuous illumination conditions.

4.1.4 Roots usually grow in dark soil

Shading the root system revealed a dramatic effect on the architecture of the root system. Lateral roots in darkness grow at a constant angle relative to the vector of gravity, whereas lateral roots in light condition grow constantly down. How both, light and gravity synergistically contribute to plant growth is not completely understood although this phenomenon has been described already in the 19th century (for a review read Kutschera and Briggs (2012)). One of the photoreceptors in Arabidopsis is the blue light receptor PHOTOTROPIN-1 (phot1) which is expressed in the elongation zone of roots (Briggs and Christie, 2002; Sakamoto and Briggs, 2002; Wan et al., 2008). Therefore, the presence of phot1 could be connected to a molecular pathway of gravitropism and in the control of local elongation and differential growth. A light-induced gravitropism was reported to be regulated via a calcium signaling (Feldman and Briggs, 1987; Lu and Feldman, 1997), and recent studies showed that the redistribution of the auxin efflux carrier PIN is involved in the negative phototropic response in Arabidopsis (Wan et al., 2012; Zhang et al., 2013). In the latter studies dark-grown seedlings were stimulated with blue-light intensities of $2\,\mu mol/m^2/s$ to stimulate a phototropic response. Although the laser intensity of $0.2\,mW$ in the mDSLM is relatively low this energy is focused on a small area and thus, without any doubt, sufficient to activate blue light receptors. Therefore, it is impossible to study processes without inducing a phototropic response. Nevertheless, light-sheet microscopy exposes the sample with considerably less light compared to other fluorescence microscopes and the shading of the root system reduces the amount of light to a minimum.

4.1.5 Gravitropism

The plant grows in an upright position which allows to study gravitropism of roots. The establishment of the gravitropic set-point angle (GSA) at which lateral roots continuously grow is independent from any phototropic responses, since dark grown lateral roots grow at a constant GSA. The analysis of the mDSLM recordings show that young outgrowing lateral roots define the GSA by differential cell growth during the establishment of the elongation zone.

4.1.6 Diurnal rhythm

The illumination system can be further adjusted for any conceivable day-night rhythms. In the mDSLM setup, the growth rate of matured lateral roots was higher at daytime

compared to night time. Besides the higher growth rate an increased fluorescence intensity of the overexpressed membrane protein (35S::LTi6-GFP) was observed during the day compared to the night, which could reflect a higher activity of the plant. This observation was confirmed by a statistical analysis in the plant incubator. The potential controversy to the opposite observation of Yazdanbakhsh and Fisahn (2009) that roots grow more at night was solved. The increased growth at day time could be explained by the fact that the availability of sugar is higher due to the photosynthetic activity of the chloroplasts. At night, the availability of sugar depends on the active (energy consuming) release of sugar from starch granular. When sugar was added to the medium, the ratio of day/night growth rates did not differ from the ratio without sugar, which means that the diurnal differences of root growth are influenced by other parameters than only the availability of sugar. Despite all that, early stages of lateral root development, prior to emergence, showed no link between daytime and growth.

4.1.7 Aerial parts of the plant

The experiments of aerial parts of the plants show that it is indeed possible to study the shoot apical meristem or subcellular structures in stomata in the epidermis of the cotyledons. However, one should note, that this tissue is photosynthetically active and requires a gas exchange. Since the sample is maintained under water during the imaging process long term experiments of these tissues cannot be recommended. In contrast, the deepwater rice *Oryza sativa* L. ssp. *indica* is flooded by water under natural conditions. A reduced gas diffusion results in systemic adaptations (Steffens and Sauter, 2005). Besides genetically modifications, the accumulation of the gaseous hormone ethylene enhances stem cell growth which helps the plant to escape from the water (Hattori et al., 2009). Furthermore, the adventitious lateral roots get activated and overlaying epidermis cells become apoptotic (Steffens et al., 2012). The dynamic process of adventitious root emergence was captured. It is very likely that the strong colored cells are apoptotic epidermal cells that form a breaking point and facilitate the emergence of the growing lateral root.

4.1.8 Dynamics of subcellular compartments

Short term experiments are less problematic and can be performed to study e.g. the dynamics of chloroplasts. In general, the analysis of the endosomal compartments movements or the rapidly changing structures of the cytoskeleton has shown that the mi-

croscope setup is very suitable to capture intracellular dynamic processes with a high spatio-temporal resolution.

Furthermore, the microscope allowed statistical studies of endosomal compartments in a large field of view. The large volume of $416/351/252\,\mu m$ (x/y/z) was captured with a resolution of $0.1625\,\mu m/pixel$ in lateral (x-y) and $6.5\,\mu m$ in axial (z) direction every $2\,min$ over a period of $10\,h$, producing 1.15 terabytes of data. This combination of large field of view with high spatio-temporal resolution is unobtainable for most of current available fluorescence microscopes. From this single time lapse recording dozens of growing cell plates and growing root hairs could be analyzed with great details. GFP-RabA1d is localized at the growing cell plates during cytokinesis, which suggests a role in delivery of cargoes and membranes for cell plate formation. The growth rates of cell plate formation were measured. The observations allowed to distinguish between an average growth rate of the entire process and a much faster growth rate during the steady state growth of the cell plate. Eventually, it takes much longer to connect the cell plate to the mother cell walls and finish the process. Anyway, in the same recording, once the root grew further out of the field of view, root hairs emerged and their growth could be analyzed. The measurements revealed a cross-correlation of the root hair growth rates with the fluorescence intensity of the 35S::GFP-RabA1d reporter during an oscillating tip growth. Such an oscillation of the root hair growth was reported earlier and was correlated with variations in the Ca^{2+} concentration gradient in the tip (Monshausen et al., 2008). Ca^{2+} modifies the cytoskeleton and vesicle traffic which supports the hypothesis that the localization of the RabA1d-labeled endosomes might be associated with the root hair growth process.

In conclusion, with LSFM, studies of the intracellular distribution of a specific protein in combination with the overview on the development of the entire organ were possible. This gives rise to new possibilities in the field of developmental biology.

4.2 Lateral root development

In plants, the formation process of a new organ with a well-defined function and shape, especially the dynamic of the growing primordia is largely unknown. The focus on the lateral root formation process is a paradigm because: 1) the process illustrates the differentiation of cells into various types of tissues including the de novo synthesis of a meristem, 2) the process illustrates a switch between bilateral and radial organ symmetry, 3) the process illustrates the dynamic interactions between the lateral root primordium

and the overlaying tissues during emergence. Furthermore the process is relatively easy to study because a) lateral roots are continuously formed, b) the formation can be induced and c) the number of contributing cells is manageable. Nevertheless, non-invasive imaging technique and the physiological growth conditions during the experiment are requirements for a successful observation.

The formation of lateral roots was recorded from the first division until beyond the emergence from the primary root. Images of nuclei and plasma membranes every $5\,min$ for a maximum time period of $64\,h$ allow for detailed studies of the process. Shape analysis of single cells during the initial steps of lateral root formation revealed that the pericycle swells prior to the first division (Fig. 3.26 on page 79). The overlaying endodermis becomes thinner and obviously disappears while the primordium grows. In contrast, the cortex and epidermis maintain their volume but are being pushed apart during the emerging process. An immediate rupture of the cell adhesion was observed within minutes, which might occur within seconds (Fig. 3.27 on page 80). According to this, it seems that the primordium exerts a relatively high pressure onto the overlaying tissue and once released cells expand relatively quick. Shape analysis of the primordium during the formation process showed that the primordium's shape undergoes a continuous progression from ellipsoid to round (Fig. 3.28 on page 81). This progression was impaired in the aurora mutant (Fig. 3.30 on page 82), which revealed that the overall shape is defined by a succession of controlled divisions as well as mechanical properties of the overlaying tissue.

The manual tracking of all involved cells allowed for quantitative analysis of lateral root formation in terms of the spatial and temporal patterns of cell division, cellular contribution, lineage tracing and primordium growth parameters. An automatic segmentation was purposely avoided, because 1) the number of cell nuclei is assessable, 2) the cells are below several layers of cells inside the primary root, thus, the signal to noise ratio of the fluorescence signal of cells located deep inside the primary root is heavily degraded, 3) the fluorescence intensity of the proliferating cells is weak compared to the intensity of the surrounding but not obviously involved cells, and 4) the expression level is highly variable and depends on several parameters such as the developmental stage of the primordium, the overall condition of the plant, day time etc. As a conclusion, the variability of the fluorescence signal does not allow for a proper automatic segmentation and tracking of cell nuclei. And thereby, the limitations usually associated with automated implementations were avoided.

4.2.1 Founder cell contribution and the lateral root center position

A number of 5-11 founder cells located in 5-8 cell files are involved in the process of lateral root formation. Depending on the position of the primordium future center the cell division rates differ. Thus, the contribution of founder cells is variable (Fig. 4.1). Lateral root formation is influenced by the availability of nutrients, water and light. Controlled laboratory conditions showed that lateral root formation also depends on the current bending of the primary root, which alters the flow of hormones (Ditengou et al., 2008), or the timing of genetically controlled factors (Norman et al., 2014). The position of lateral root founder cells is predetermined by the position of the xylem pole in the underlying vasculature (Péret et al., 2009). However, the position along the main root is not fixed. Founder cells are arbitrarily located along the main root, but the relative local position of a founder cell with respect to the future center specifies how much a particular founder cell will contribute to the primordium. In fact, the data show that the position of the future center of the primordium cannot be predicted, neither by the position of pericycle cells nor the position of the overlaying endodermis cells, which is actively accommodating the initiation and growth of the primordium (Vermeer et al., 2014). It is probably the position of the root bending in relation to the topology of endodermis and pericycle cells that results in local mechanical and biochemical differences, which in turn promote particular cells to proliferate more than others and thereby develop a future center.
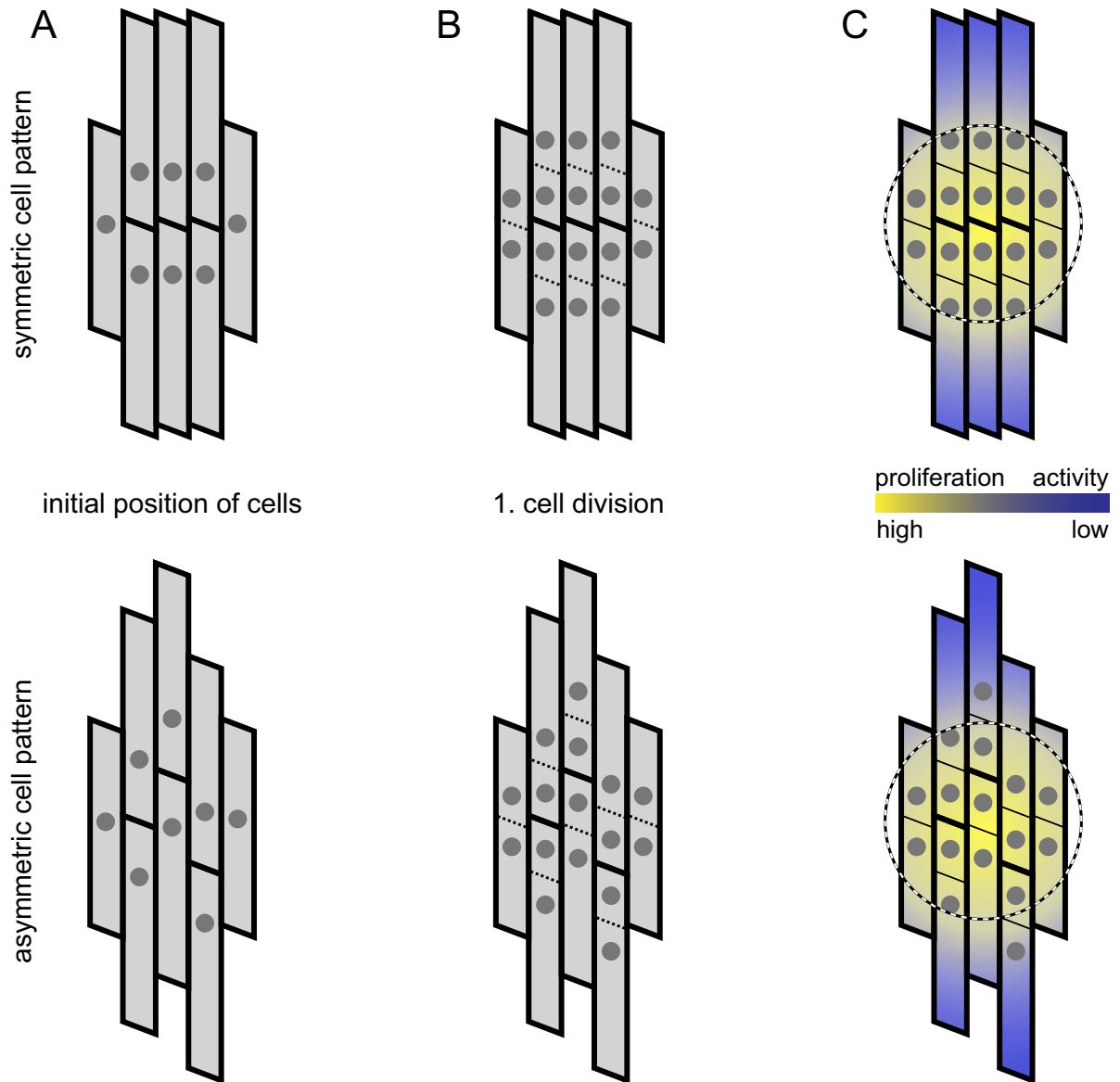
Figure 4.1: Proliferation activity relative to the primordiums future center. The cellular contribution of founder cells depends on the local position along the primary root relative to the primordium center. The position of founder cells in an idealized, symmetric arrangement (upper panel) in comparison to a more realistic, asymmetric arrangement (lower panel). (A) Initial position of founder cells. (B) The first division generates a central region with smaller cells. (C) Cells proliferate and build a primordium. The dashed circle indicates the subsequent center of the lateral root. Cells in the yellow area will contribute more cells than cells in the blue areas.

4.2.2 Cell files

Cells in the pericycle cell layer adjacent to the xylem pole can get activated and divide continuously to form a lateral root (De Smet, 2012). In the initiation steps of lateral root formation, the master cell file swelled and divided at first and at a developmental stage of 142 cells the master cell file has the highest point of the primordium. While the primordium grows in height (periclinal divisions), a radial component increases the thickness in upper layers of the cell files (radial divisions). A radialization of the cell files occurs (Fig. 4.3).

The overlay of the nuclei objects with the membrane channel allowed to follow the further development of the cell files during the emerging process, beyond the nuclei tracking. These results showed that cells at the base of the primordium, close to the primary root, elongate and push the lateral root out of the main root. At some point the new lateral root meristem originates and will provide, in far future, all cells to the growing lateral root. Considering the fact that a root apical meristem is located in the center of a lateral root tip and the center develops from the master cell file this would imply that the master cell file would slowly take over and contribute all cells to the matured lateral root (Fig. 4.2). In conclusion, the radial view visualization allows to follow the development of all contributing cell files during the formation process. This visualization has never been able before and gives an entirely new perspective in studying lateral root formation as it takes all cell files into account.
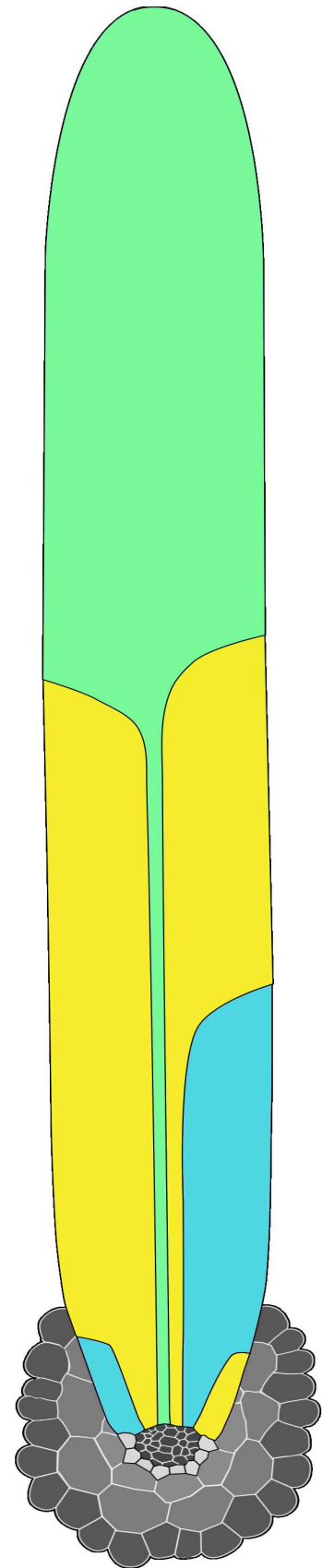
Figure 4.2: Speculative cell file contribution to a matured lateral root.
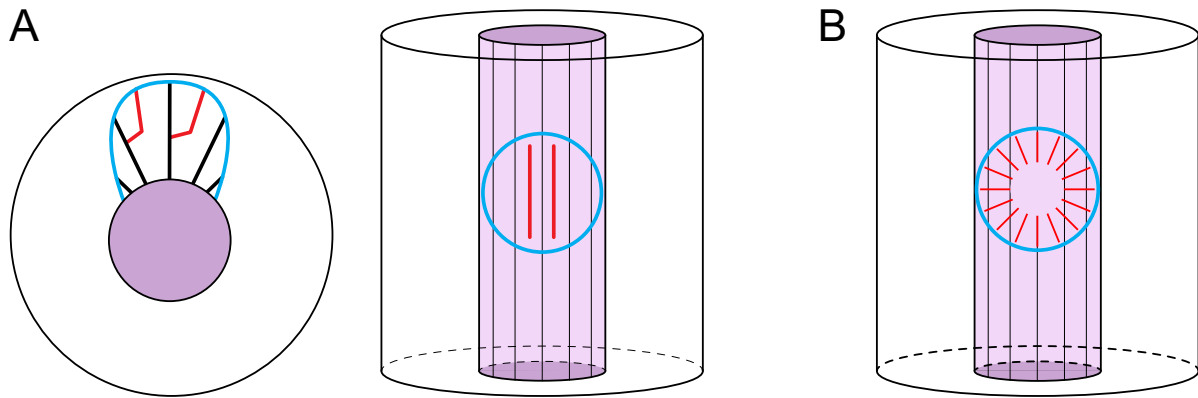
Figure 4.3: Radial division perform the transition from 2D to 3D. Cells are located in cell files. Cells within a cell file perform anticlinal and periclinal divisions, creating cell layer of smaller cells. At certain height of each cell file radial divisions occur that originate new cell files. These radial divisions initiate the radialization from the morphological point of view. (A) Radial view (left) and frontal view (right) of the lateral root primordium (blue outline), cell files are highlighted as black lines. Red lines indicate new cell files that derived from radial divisions. (B) Sketch of a radialized primordium. The red dashed lines indicate the cell files of the new lateral root.

4.2.3 Layer assignment

The Arabidopsis root is made up of concentric layers of tissue, the vasculature strand in the center of the root surrounded by one layer of pericycle-, cortex-, endodermis- and epidermis-cells (Dolan et al., 1993). All these layers derive from periclinal cell divisions in the lateral root primordium during the early steps of the formation process. The orientation of cell divisions was successfully analyzed by Jens Ferangau (Fangerau, 2014). The cell division classification worked very well because the angle measurements took the changing dome shape surface bending of the developing primordium into account. Only a few obviously wrong assigned cell divisions were manually corrected in *Mathematica*. According to the number of up to eight layers that were created one can speculate, that all types of tissue were established. This allows to reconstruct the lineage of a specific tissue layer. The history of periclinal divisions in the center region of the primordium is conserved throughout the data sets, i.e. cells within a particular cell layer derived from the same sequence of periclinal divisions. This history of periclinal division overlaps exactly with the division sequence pattern that was proposed by Malamy and Benfey (1997), e.g. after the first periclinal division the outer layer gives rise to the root cap, epidermis, cortex and endodermis, whereas the inner layer provides all other internal tissue (pericycle and the vasculature) (Malamy and Benfey, 1997). However, this is only the case for the core region of the primordium. At the margins of the primordia,

the data sets showed variations and the history of layer generation which reveals that there is no obvious division pattern at the single cell level. Malamy and Benfey (1997) divided the lateral root development into seven stages based on two dimensional images. The result confirms this sequence of layer generation. Furthermore, now all division patterns located in the three-dimensional primordium can be considered and quantified.

4.2.4 Cell division rules

The position of founder cells relative to the subsequent center is variable which causes differences in contribution of founder cells and cell files. The differences in layer generation at the margins of the primordia has to be encoded in the division patterns. The control of the direction of cell division is important. Cells usually grow because there is space and they divide because they reached a certain size. The results on the transversal versus longitudinal division showed that particularly the first two cell divisions seem to play an important role, because of a significantly higher number of longitudinal divisions in the second cell cycle compared to all subsequent cell cycles. At this stage (the second cell cycle) the boundaries of the primordium might get specified and therefore controlled cell divisions are required. With the further development, more cell division follow the shortest cell wall rule.

The cell identity depends mainly on their surrounding tissue (Scheres et al., 1994; van den Berg et al., 1997). Thus, a precise pattern of cell division orientation has to be discussed in the spatial context. The results revealed that lateral root formation does not show an apparent stereotyped pattern of cell division. This might be obvious because each lateral root primordium starts under certain preconditions (position and size of cells, main root bending, environmental conditions) but in all cases cells create a primordium that develops all types of tissue and organize the overall shape. Sudden changes during the cytokinesis events, e.g. the asymmetric division instead of a periclinal (Fig. 3.52 on page 103) lead to an instantaneous disorder but the cells can compensate that and integrate into their neighborhood in the further development. The first results on the *aur1-2 aur2-2* double mutant demonstrate this more clearly. Although structural changes of the primordium alter the cellular organization and shape of the primordium it develops to a viable lateral root. Specific markers for cell identity could reveal whether and when a tissue identity is adopted on a molecular level.

Outlook

The imaging pipeline allowed comprehensive studies of key aspects of lateral root formation by tracking individual cells and provides a data-base of cell lineage information for further investigations. The data sets are currently used by Jens Fangerau to establish a computational model understanding what cell division patterns obey the formation process.

A major bottleneck in this imaging setup is the capability to capture only a limited number of plants per week. This could be solved by a sample holder for several plants allowing for simultaneous culturing and imaging (Fig. 4.4). In order to optimize the post processing pipeline towards a high throughput approach, an (semi-)automatic cell nuclei segmentation and lineage tracking will be required. First applications performed by Alexis Maizel in Heidelberg using the open-source framework *iLastic* had promising results.
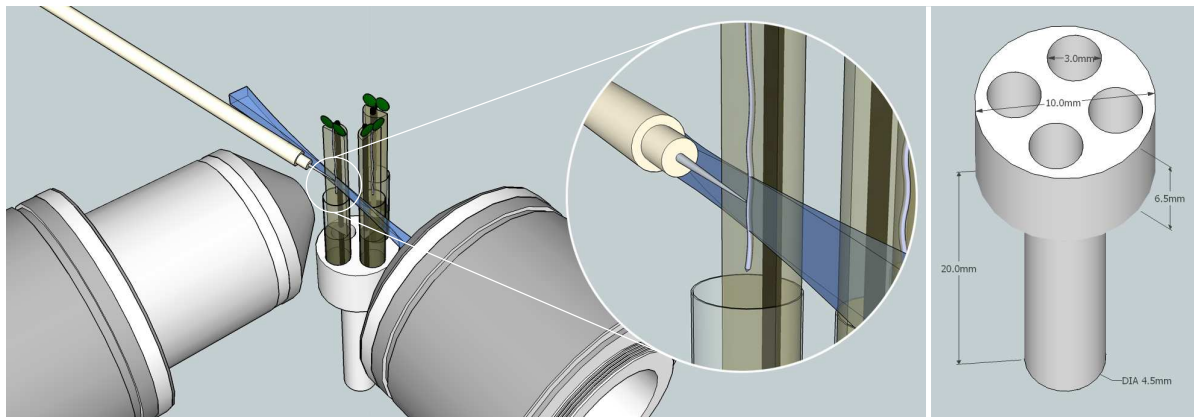
Figure 4.4: Design of a sample holder containing several plants in the mDSLM.

Imaging the root system architecture in a non-destructive way with a high spatial and temporal resolution will allow researchers to uncover fundamental mechanisms of plant development. Cells undergoing the transition from proliferation to differentiation have to orchestrate a variety of changes in cytoskeleton architecture, protein distribution and gene expression. The observation of multiple molecular compounds while cells differentiate will provide important insights into processes underlying the spatio-temporal regulation of development. Controlled growth conditions allow to study all kinds of stresses or tropisms and will give new insights in plant adaptations. The results on rice (*Oryza sativa*) showed that the system has the capacity for larger plants. Potential candidates for future studies are crops like maize (*Zea mays*) or barley (*Hordeum vulgare*).

Bibliography

Abel, S. and Theologis, A. (1996). Early genes and auxin action. *Plant Physiology*, 111(1):9–17.

Aloni, R., Langhans, M., Aloni, E., and Ullrich, C. I. (2004). Role of cytokinin in the regulation of root gravitropism. *Planta*, 220(1):177–182.

Asaoka, R., Uemura, T., Ito, J., Fujimoto, M., Ito, E., Ueda, T., and Nakano, A. (2013). Arabidopsis RABA1 GTPases are involved in transport between the trans-golgi network and the plasma membrane, and are required for salinity stress tolerance. *The Plant Journal*, 73(2):240–249.

Baluska, F., Salaj, J., Mathur, J., Braun, M., Jasper, F., Samaj, J., Chua, N. H., Barlow, P. W., and Volkmann, D. (2000). Root hair formation: F-actin-dependent tip growth is initiated by local assembly of profilin-supported f-actin meshworks accumulated within expansin-enriched bulges. *Developmental Biology*, 227(2):618–632.

Baskin, T. I. (2005). Anisotropic expansion of the plant cell wall. *Annual Review of Cell and Developmental Biology*, 21(1):203–222.

Beemster, G. T. and Baskin, T. I. (1998). Analysis of cell division and elongation underlying the developmental acceleration of root growth in arabidopsis thaliana. *Plant Physiology*, 116(4):1515 –1526.

Benjamins, R. and Scheres, B. (2008). Auxin: the looping star in plant development. *Annual Review of Plant Biology*, 59:443–465.

Benková, E., Michniewicz, M., Sauer, M., Teichmann, T., Seifertová, D., Jürgens, G., and Friml, J. (2003). Local, efflux-dependent auxin gradients as a common module for plant organ formation. *Cell*, 115(5):591–602.

Berson, T., Wangenheim, D. v., Takáč, T., Šamajová, O., Rosero, A., Ovečka, M., Komis, G., Stelzer, E. H., and Šamaj, J. (2014). Trans-golgi network localized small

GTPase RabA1d is involved in cell plate formation and oscillatory root hair growth. *BMC Plant Biology*, 14(1):252.

Besson, S. and Dumais, J. (2011). Universal rule for the symmetric division of plant cells. *Proceedings of the National Academy of Sciences*, 108(15):6294–6299.

Bibikova, T. N., Zhigilei, A., and Gilroy, S. (1997). Root hair growth in arabidopsis thaliana is directed by calcium and an endogenous polarity. *Planta*, 203(4):495–505.

Briggs, W. R. and Christie, J. M. (2002). Phototropins 1 and 2: versatile plant blue-light receptors. *Trends in Plant Science*, 7(5):204–210.

Calderón Villalobos, L. I. A., Lee, S., De Oliveira, C., Ivetac, A., Brandt, W., Armitage, L., Sheard, L. B., Tan, X., Parry, G., Mao, H., Zheng, N., Napier, R., Kepinski, S., and Estelle, M. (2012). A combinatorial TIR1/AFB–aux/IAA co-receptor system for differential sensing of auxin. *Nature Chemical Biology*, 8(5):477–485.

Carol, R. J. and Dolan, L. (2002). Building a hair: tip growth in \textbackslash-textbackslashtextitArabidopsis thaliana root hairs. *Philosophical Transactions of the Royal Society of London. Series B, Biological Sciences*, 357(1422):815–821.

Casimiro, I., Beeckman, T., Graham, N., Bhalerao, R., Zhang, H., Casero, P., Sandberg, G., and Bennett, M. J. (2003). Dissecting arabidopsis lateral root development. *Trends in Plant Science*, 8(4):165–171. 00428.

Casimiro, I., Marchant, A., Bhalerao, R. P., Beeckman, T., Dhooge, S., Swarup, R., Graham, N., Inze, D., Sandberg, G., Casero, P. J., and Bennett, M. (2001). Auxin transport promotes arabidopsis lateral root initiation. *Plant Cell*, 13(4):843–852.

Corson, F., Hamant, O., Bohn, S., Traas, J., Boudaoud, A., and Couder, Y. (2009). Turning a plant tissue into a living cell froth through isotropic growth. *Proceedings of the National Academy of Sciences*, 106(21):8453–8458.

Cosgrove, D. J. (2000). Loosening of plant cell walls by expansins. *Nature*, 407(6802):321–326.

Cosgrove, D. J. (2005). Growth of the plant cell wall. *Nature Reviews Molecular Cell Biology*, 6(11):850–861.

Costa, A., Candeo, A., Fieramonti, L., Valentini, G., and Bassi, A. (2013). Calcium dynamics in root cells of arabidopsis thaliana visualized with selective plane illumination microscopy. *PLoS ONE*, 8(10):e75646.

Curl, E. A., Truelove, B., and others (1986). *The rhizosphere.* Springer-Verlag.

Dastidar, M. G., Jouannet, V., and Maizel, A. (2012). Root branching: mechanisms, robustness, and plasticity. *Wiley Interdisciplinary Reviews: Developmental Biology*, 1(3):329–343.

De Rybel, B., Vassileva, V., Parizot, B., Demeulenaere, M., Grunewald, W., Audenaert, D., Van Campenhout, J., Overvoorde, P., Jansen, L., Vanneste, S., Möller, B., Wilson, M., Holman, T., Van Isterdael, G., Brunoud, G., Vuylsteke, M., Vernoux, T., De Veylder, L., Inzé, D., Weijers, D., Bennett, M. J., and Beeckman, T. (2010). A novel aux/IAA28 signaling cascade activates GATA23-dependent specification of lateral root founder cell identity. *Current Biology*, 20(19):1697–1706.

De Smet, I. (2012). Lateral root initiation: one step at a time. *New Phytologist*, 193(4):867–873.

De Smet, I. and Beeckman, T. (2011). Asymmetric cell division in land plants and algae: the driving force for differentiation. *Nature Reviews Molecular Cell Biology*, 12(3):177–188.

Dharmasiri, N., Dharmasiri, S., and Estelle, M. (2005a). The f-box protein TIR1 is an auxin receptor. *Nature*, 435(7041):441–445.

Dharmasiri, N., Dharmasiri, S., Weijers, D., Lechner, E., Yamada, M., Hobbie, L., Ehrismann, J. S., Jürgens, G., and Estelle, M. (2005b). Plant development is regulated by a family of auxin receptor f box proteins. *Developmental Cell*, 9(1):109–119.

Digby, J. and Firn, R. D. (1995). The gravitropic set-point angle (GSA): the identification of an important developmentally controlled variable governing plant architecture. *Plant, Cell & Environment*, 18(12):1434–1440.

Ditengou, F. A., Teale, W. D., Kochersperger, P., Flittner, K. A., Kneuper, I., van der Graaff, E., Nziengui, H., Pinosa, F., Li, X., Nitschke, R., Laux, T., and Palme, K. (2008). Mechanical induction of lateral root initiation in arabidopsis thaliana. *Proceedings of the National Academy of Sciences*, 105(48):18818 –18823.

Dolan, L., Janmaat, K., Willemsen, V., Linstead, P., Poethig, S., Roberts, K., and Scheres, B. (1993). Cellular organisation of the arabidopsis thaliana root. *Development*, 119(1):71–84.

Drew, M. C. (1975). Comparison of the effects of a localised supply of phosphate, nitrate, ammonium and potassium on the growth of the seminal root system, and the shoot, in barley. *New Phytologist*, 75(3):479–490. 00587.

Duan, L., Dietrich, D., Ng, C. H., Chan, P. M. Y., Bhalerao, R., Bennett, M. J., and Dinneny, J. R. (2013). Endodermal ABA signaling promotes lateral root quiescence during salt stress in arabidopsis seedlings. *The Plant Cell Online*, 25(1):324–341.

Dubrovsky, J. G., Gambetta, G. A., Hernández-Barrera, A., Shishkova, S., and González, I. (2006). Lateral root initiation in arabidopsis: Developmental window, spatial patterning, density and predictability. *Annals of Botany*, 97(5):903–915. 00082 PMID: 16390845.

Dubrovsky, J. G., Rost, T. L., Colón-Carmona, A., and Doerner, P. (2001). Early primordium morphogenesis during lateral root initiation in arabidopsis thaliana. *Planta*, 214(1):30–36.

Dubrovsky, J. G., Sauer, M., Napsucialy-Mendivil, S., Ivanchenko, M. G., Friml, J., Shishkova, S., Celenza, J., and Benková, E. (2008). Auxin acts as a local morphogenetic trigger to specify lateral root founder cells. *Proceedings of the National Academy of Sciences*, 105(25):8790 –8794.

Errera, L. (1888). Über zellformen und seifenblasen. *Bot. Zentralbl.*, (34):395–398.

Fangerau, J. (2014). *Visual Analytics of Similarities in Cell Developments of Model Organisms*. PhD thesis, Ruprecht-Karls-Universität Heidelberg.

Feldman, L. J. and Briggs, W. R. (1987). Light-regulated gravitropism in seedling roots of maize. *Plant Physiology*, 83(2):241–243.

Forde, B. and Lorenzo, H. (2001). The nutritional control of root development. *Plant and Soil*, 232(1-2):51–68.

Friml, J. (2003). Auxin transport — shaping the plant. *Current Opinion in Plant Biology*, 6(1):7–12.

Friml, J., Wiśniewska, J., Benková, E., Mendgen, K., and Palme, K. (2002). Lateral relocation of auxin efflux regulator PIN3 mediates tropism in arabidopsis. *Nature*, 415(6873):806–809.

Galway, M. E., Heckman, J. W., and Schiefelbein, J. W. (1997). Growth and ultrastructure of \textbackslashtextbackslashtextitArabidopsis root hairs: the rhd3 mutation alters vacuole enlargement and tip growth. *Planta*, 201(2):209–218.

Geitmann, A. and Ortega, J. K. E. (2009). Mechanics and modeling of plant cell growth. *Trends in Plant Science*, 14(9):467–478.

Geldner, N., V, D.-T., Hyman, D. L., Mayer, U., Stierhof, Y.-D., and Chory, J. (2009). Rapid, combinatorial analysis of membrane compartments in intact plants with a multicolor marker set. *The Plant Journal: For Cell and Molecular Biology*, 59(1):169–178.

Gruber, B. D., Giehl, R. F. H., Friedel, S., and Wirén, N. v. (2013). Plasticity of the arabidopsis root system under nutrient deficiencies. *Plant Physiology*, 163(1):161–179.

Guilfoyle, T. J. and Hagen, G. (2007). Auxin response factors. *Current Opinion in Plant Biology*, 10(5):453–460.

Hamant, O., Heisler, M. G., Jönsson, H., Krupinski, P., Uyttewaal, M., Bokov, P., Corson, F., Sahlin, P., Boudaoud, A., Meyerowitz, E. M., Couder, Y., and Traas, J. (2008). Developmental patterning by mechanical signals in arabidopsis. *Science*, 322(5908):1650–1655.

Hattori, Y., Nagai, K., Furukawa, S., Song, X.-J., Kawano, R., Sakakibara, H., Wu, J., Matsumoto, T., Yoshimura, A., Kitano, H., Matsuoka, M., Mori, H., and Ashikari, M. (2009). The ethylene response factors SNORKEL1 and SNORKEL2 allow rice to adapt to deep water. *Nature*, 460(7258):1026–1030.

Heisler, M. G., Hamant, O., Krupinski, P., Uyttewaal, M., Ohno, C., Jönsson, H., Traas, J., and Meyerowitz, E. M. (2010). Alignment between PIN1 polarity and microtubule orientation in the shoot apical meristem reveals a tight coupling between morphogenesis and auxin transport. *PLoS Biol*, 8(10):e1000516.

Heisler, M. G., Ohno, C., Das, P., Sieber, P., Reddy, G. V., Long, J. A., and Meyerowitz, E. M. (2005). Patterns of auxin transport and gene expression during primordium de-

velopment revealed by live imaging of the arabidopsis inflorescence meristem. *Current Biology*, 15(21):1899–1911.

Hepler, P. K. (2005). Calcium: A central regulator of plant growth and development. *Plant Cell*, 17(8):2142–2155.

Höckendorf, B., Thumberger, T., and Wittbrodt, J. (2012). Quantitative analysis of embryogenesis: A perspective for light sheet microscopy. *Developmental Cell*, 23(6):1111–1120.

Hodge, A. (2004). The plastic plant: root responses to heterogeneous supplies of nutrients. *New Phytologist*, 162(1):9–24. 00600.

Hodge, A., Berta, G., Doussan, C., Merchan, F., and Crespi, M. (2009). Plant root growth, architecture and function. *Plant and Soil*, 321(1-2):153–187.

Huisken, J., Swoger, J., Del Bene, F., Wittbrodt, J., and Stelzer, E. H. K. (2004). Optical sectioning deep inside live embryos by selective plane illumination microscopy. *Science*, 305(5686):1007–1009.

Kamiya, Y. (2010). Plant hormones: Versatile regulators of plant growth and development. *Annual Review of Plant Biology*, 61(1).

Keller, P. J., Schmidt, A. D., Santella, A., Khairy, K., Bao, Z., Wittbrodt, J., and Stelzer, E. H. K. (2010). Fast, high-contrast imaging of animal development with scanned light sheet-based structured-illumination microscopy. *Nat Meth*, 7(8):637–642.

Keller, P. J. and Stelzer, E. H. (2008). Quantitative in vivo imaging of entire embryos with digital scanned laser light sheet fluorescence microscopy. *Current Opinion in Neurobiology*, 18(6):624–632. 00059.

Kepinski, S. and Leyser, O. (2005). The arabidopsis f-box protein TIR1 is an auxin receptor. *Nature*, 435(7041):446–451.

Ketelaar, T., Faivre-Moskalenko, C., Esseling, J. J., de Ruijter, N. C. A., Grierson, C. S., Dogterom, M., and Emons, A. M. C. (2002). Positioning of nuclei in arabidopsis root hairs: An actin-regulated process of tip growth. *The Plant Cell Online*, 14(11):2941–2955.

Kim, C. and Apel, K. (2004). Substrate-dependent and organ-specific chloroplast protein import in planta. *The Plant Cell Online*, 16(1):88–98.

Kleine-Vehn, J. and Friml, J. (2008). Polar targeting and endocytic recycling in auxin-dependent plant development. *Annual Review of Cell and Developmental Biology*, 24(1):447–473.

Křeček, P., Skůpa, P., Libus, J., Naramoto, S., Tejos, R., Friml, J., and Zažímalová, E. (2009). The PIN-FORMED (PIN) protein family of auxin transporters. *Genome Biol*, 10(12):249.

Kumpf, R. P., Shi, C.-L., Larrieu, A., Stø, I. M., Butenko, M. A., Péret, B., Riiser, E. S., Bennett, M. J., and Aalen, R. B. (2013). Floral organ abscission peptide IDA and its HAE/HSL2 receptors control cell separation during lateral root emergence. *Proceedings of the National Academy of Sciences*, 110(13):5235–5240.

Kutschera, L. and Lichtenegger, E. (1992). In *Wurzelatlas mitteleuropäischer Grünlandpflanzen. Band 2: Pteridophyta und Dicotyledoneae; Teil 1: Morphologie, Anatomie, Ökologie, Verbreitung, Soziologie, Wirtschaft.* Gustav Fischer, Stuttgart.

Kutschera, U. and Briggs, W. R. (2012). Root phototropism: from dogma to the mechanism of blue light perception. *Planta*, 235(3):443–452.

Laskowski, M. (2013). Lateral root initiation is a probabilistic event whose frequency is set by fluctuating levels of auxin response. *Journal of Experimental Botany*, 64(9):2609–2617.

Laskowski, M., Grieneisen, V. A., Hofhuis, H., Hove, C. A. t., Hogeweg, P., Marée, A. F. M., and Scheres, B. (2008). Root system architecture from coupling cell shape to auxin transport. *PLoS Biol*, 6(12):e307.

Lavenus, J., Goh, T., Roberts, I., Guyomarc'h, S., Lucas, M., De Smet, I., Fukaki, H., Beeckman, T., Bennett, M., and Laplaze, L. (2013). Lateral root development in arabidopsis: fifty shades of auxin. *Trends in Plant Science*, 18(8):450–458.

Lee, H. W. and Kim, J. (2013). EXPANSINA17 up-regulated by LBD18/ASL20 promotes lateral root formation during the auxin response. *Plant and Cell Physiology*, 54(10):1600–1611.

López-Bucio, J., Cruz-Ramírez, A., and Herrera-Estrella, L. (2003). The role of nutrient availability in regulating root architecture. *Current Opinion in Plant Biology*, 6(3):280–287.

Lu, Y.-T. and Feldman, L. J. (1997). Light-regulated root gravitropism: a role for, and characterization of, a calcium/calmodulin-dependent protein kinase homolog. *Planta*, 203(1):S91–S97.

Lucas, M., Godin, C., Jay-Allemand, C., and Laplaze, L. (2008). Auxin fluxes in the root apex co-regulate gravitropism and lateral root initiation. *Journal of Experimental Botany*, 59(1):55–66.

Lucas, M., Kenobi, K., Wangenheim, D. v., Voβ, U., Swarup, K., Smet, I. D., Damme, D. V., Lawrence, T., Péret, B., Moscardi, E., Barbeau, D., Godin, C., Salt, D., Guyomarc'h, S., Stelzer, E. H. K., Maizel, A., Laplaze, L., and Bennett, M. J. (2013). Lateral root morphogenesis is dependent on the mechanical properties of the overlaying tissues. *Proceedings of the National Academy of Sciences*, 110(13):5229–5234.

Maizel, A., Wangenheim, D. v., Federici, F., Haseloff, J., and Stelzer, E. H. K. (2011). High-resolution live imaging of plant growth in near physiological bright conditions using light sheet fluorescence microscopy. *The Plant Journal*, 68(2):377–385.

Malamy, J. E. (2005). Intrinsic and environmental response pathways that regulate root system architecture. *Plant, Cell & Environment*, 28(1):67–77.

Malamy, J. E. and Benfey, P. N. (1997). Organization and cell differentiation in lateral roots of arabidopsis thaliana. *Development*, 124(1):33–44.

Marc, J., Granger, C. L., Brincat, J., Fisher, D. D., Kao, T.-h., McCubbin, A. G., and Cyr, R. J. (1998). A GFP-MAP4 reporter gene for visualizing cortical microtubule rearrangements in living epidermal cells. *The Plant Cell Online*, 10(11):1927 –1940.

Marhavý, P., Vanstraelen, M., De Rybel, B., Zhaojun, D., Bennett, M. J., Beeckman, T., and Benková, E. (2013). Auxin reflux between the endodermis and pericycle promotes lateral root initiation. *The EMBO Journal*, 32(1):149–158.

Miller, D. D., Ruijter, N. C. d., and Emons, A. M. C. (1997). From signal to form: aspects of the cytoskeleton-plasma membrane–cell wall continuuum in root hair tips. *J. Exp. Bot.*, 48(11):1881–1896. 00112.

Monshausen, G. B., Messerli, M. A., and Gilroy, S. (2008). Imaging of the yellow cameleon 3.6 indicator reveals that elevations in cytosolic ca2+ follow oscillating increases in growth in root hairs of arabidopsis. *Plant Physiology*, 147(4):1690–1698.

Moreno-Risueno, M. A., Van Norman, J. M., Moreno, A., Zhang, J., Ahnert, S. E., and Benfey, P. N. (2010). Oscillating gene expression determines competence for periodic arabidopsis root branching. *Science*, 329(5997):1306–1311.

Morita, M. T. (2010). Directional gravity sensing in gravitropism. *Annual Review of Plant Biology*, 61(1):705–720.

Mullen, J. L., Wolverton, C., and Hangarter, R. P. (2005). Apical control, gravitropic signaling, and the growth of lateral roots in arabidopsis. *Advances in Space Research*, 36(7):1211–1217.

Murashige, T. and Skoog, F. (1962). A revised medium for rapid growth and bio assays with tobacco tissue cultures. *Physiologia Plantarum*, 15(3):473–497.

Neil, M. A. A., Juskaitis, R., and Wilson, T. (1997). Method of obtaining optical sectioning by using structured light in a conventional microscope. *Optics Letters*, 22(24):1905–1907.

Neuteboom, L. W., Ng, J. M. Y., Kuyper, M., Clijdesdale, O. R., Hooykaas, P. J. J., and Zaal, B. J. v. d. (1999). Isolation and characterization of cDNA clones corresponding with mRNAs that accumulate during auxin-induced lateral root formation. *Plant Molecular Biology*, 39(2):273–287.

Norman, J. M. V., Zhang, J., Cazzonelli, C. I., Pogson, B. J., Harrison, P. J., Bugg, T. D. H., Chan, K. X., Thompson, A. J., and Benfey, P. N. (2014). Periodic root branching in arabidopsis requires synthesis of an uncharacterized carotenoid derivative. *Proceedings of the National Academy of Sciences*, page 201403016.

Nozue, K. and Maloof, J. N. (2006). Diurnal regulation of plant growth. *Plant, Cell & Environment*, 29(3):396–408.

Osmont, K. S., Sibout, R., and Hardtke, C. S. (2007). Hidden branches: Developments in root system architecture. *Annual Review of Plant Biology*, 58(1):93–113.

Ovečka, M., Berson, T., Beck, M., Derksen, J., Šamaj, J., Baluška, F., and Lichtscheidl, I. K. (2010). Structural sterols are involved in both the initiation and tip growth of root hairs in arabidopsis thaliana. *The Plant Cell Online*, 22(9):2999–3019.

Palanivelu, R. and Preuss, D. (2000). Pollen tube targeting and axon guidance: parallels in tip growth mechanisms. *Trends in Cell Biology*, 10(12):517–524.

Paque, S., Mouille, G., Grandont, L., Alabadí, D., Gaertner, C., Goyallon, A., Muller, P., Primard-Brisset, C., Sormani, R., Blázquez, M. A., and Perrot-Rechenmann, C. (2014). AUXIN BINDING PROTEIN1 links cell wall remodeling, auxin signaling, and cell expansion in arabidopsis. *The Plant Cell Online*, page tpc.113.120048.

Paredez, A. R., Somerville, C. R., and Ehrhardt, D. W. (2006). Visualization of cellulose synthase demonstrates functional association with microtubules. *Science*, 312(5779):1491–1495.

Parizot, B., Laplaze, L., Ricaud, L., Boucheron-Dubuisson, E., Bayle, V., Bonke, M., Smet, I. D., Poethig, S. R., Helariutta, Y., Haseloff, J., Chriqui, D., Beeckman, T., and Nussaume, L. (2008). Diarch symmetry of the vascular bundle in arabidopsis root encompasses the pericycle and is reflected in distich lateral root initiation. *Plant Physiology*, 146(1):140–148.

Péret, B., De Rybel, B., Casimiro, I., Benková, E., Swarup, R., Laplaze, L., Beeckman, T., and Bennett, M. J. (2009). Arabidopsis lateral root development: an emerging story. *Trends in Plant Science*, 14(7):399–408.

Péret, B., Li, G., Zhao, J., Band, L. R., Vo\textbackslashs s, U., Postaire, O., Luu, D.-T., Da Ines, O., Casimiro, I., Lucas, M., Wells, D. M., Lazzerini, L., Nacry, P., King, J. R., Jensen, O. E., Schäffner, A. R., Maurel, C., and Bennett, M. J. (2012). Auxin regulates aquaporin function to facilitate lateral root emergence. *Nature Cell Biology*, 14(10):991–998.

Péret, B., Middleton, A. M., French, A. P., Larrieu, A., Bishopp, A., Njo, M., Wells, D. M., Porco, S., Mellor, N., Band, L. R., Casimiro, I., Kleine-Vehn, J., Vanneste, S., Sairanen, I., Mallet, R., Sandberg, G., Ljung, K., Beeckman, T., Benkova, E., Friml, J., Kramer, E., King, J. R., De Smet, I., Pridmore, T., Owen, M., and Bennett, M. J. (2013). Sequential induction of auxin efflux and influx carriers regulates lateral root emergence. *Molecular Systems Biology*, 9(1).

Petricka, J. J., Van Norman, J. M., and Benfey, P. N. (2009). Symmetry breaking in plants: Molecular mechanisms regulating asymmetric cell divisions in arabidopsis. *Cold Spring Harbor Perspectives in Biology*, 1(5).

Pietzsch, T., Preibisch, S., Tomančák, P., and Saalfeld, S. (2012). ImgLib2—generic image processing in java. *Bioinformatics*, 28(22):3009–3011.

Rasmussen, C. G., Humphries, J. A., and Smith, L. G. (2011). Determination of symmetric and asymmetric division planes in plant cells. *Annual Review of Plant Biology*, 62(1):387–409.

Reddy, G. V., Heisler, M. G., Ehrhardt, D. W., and Meyerowitz, E. M. (2004). Real-time lineage analysis reveals oriented cell divisions associated with morphogenesis at the shoot apex of arabidopsis thaliana. *Development*, 131(17):4225–4237.

Richter, G. L., Monshausen, G. B., Krol, A., and Gilroy, S. (2009). Mechanical stimuli modulate lateral root organogenesis. *Plant Physiology*, 151(4):1855–1866. 00057 PMID: 19794120.

Robert, S., Kleine-Vehn, J., Barbez, E., Sauer, M., Paciorek, T., Baster, P., Vanneste, S., Zhang, J., Simon, S., Čovanová, M., Hayashi, K., Dhonukshe, P., Yang, Z., Bednarek, S. Y., Jones, A. M., Luschnig, C., Aniento, F., Zažímalová, E., and Friml, J. (2010). ABP1 mediates auxin inhibition of clathrin-dependent endocytosis in arabidopsis. *Cell*, 143(1):111–121.

Rosquete, M. R., Wangenheim, D. v., Marhavý, P., Barbez, E., Stelzer, E. H., Benková, E., Maizel, A., and Kleine-Vehn, J. (2013). An auxin transport mechanism restricts positive orthogravitropism in lateral roots. *Current Biology*, 23(9):817–822.

Rounds, C. M. and Bezanilla, M. (2013). Growth mechanisms in tip-growing plant cells. *Annual Review of Plant Biology*, 64(1):243–265.

Ryan, E., Steer, M., and Dolan, L. (2001). Cell biology and genetics of root hair formation in arabidopsis thaliana. *Protoplasma*, 215(1-4):140–149.

Sakamoto, K. and Briggs, W. R. (2002). Cellular and subcellular localization of phototropin 1. *The Plant Cell Online*, 14(8):1723–1735.

Šamajová, O., Takáč, T., Wangenheim, D. v., Stelzer, E., and Šamaj, J. (2012). Update on methods and techniques to study endocytosis in plants. In *Endocytosis in Plants*, pages 1–36. Springer Berlin Heidelberg.

Sappl, P. G. and Heisler, M. G. (2013). Live-imaging of plant development: latest approaches. *Current Opinion in Plant Biology*, 16(1):33–40. 00002.

Sauer, M. and Kleine-Vehn, J. (2011). AUXIN BINDING PROTEIN1: The outsider. *The Plant Cell Online*, 23(6):2033–2043.

Scheres, B., Wolkenfelt, H., Willemsen, V., Terlouw, M., Lawson, E., Dean, C., and Weisbeek, P. (1994). Embryonic origin of the arabidopsis primary root and root meristem initials. *Development*, 120(9):2475–2487.

Schnepf, E. (2003). *Cellular Polarity*. http://arjournals.annualreviews.org/doi/abs/ 10.1146/annurev.pp.37.060186.000323.

Sena, G., Frentz, Z., Birnbaum, K. D., and Leibler, S. (2011). Quantitation of cellular dynamics in growing arabidopsis roots with light sheet microscopy. *PLoS ONE*, 6(6):e21303.

Sena, G., Wang, X., Liu, H.-Y., Hofhuis, H., and Birnbaum, K. D. (2009). Organ regeneration does not require a functional stem cell niche in plants. *Nature*, 457(7233):1150–1153.

Shaw, S. L. and Ehrhardt, D. W. (2013). Smaller, faster, brighter: Advances in optical imaging of living plant cells. *Annual Review of Plant Biology*, 64(1):351–375.

Smet, I. D., Tetsumura, T., Rybel, B. D., Frey, N. F. d., Laplaze, L., Casimiro, I., Swarup, R., Naudts, M., Vanneste, S., Audenaert, D., Inzé, D., Bennett, M. J., and Beeckman, T. (2007). Auxin-dependent regulation of lateral root positioning in the basal meristem of arabidopsis. *Development*, 134(4):681–690. 00263 PMID: 17215297.

Sozzani, R., Busch, W., Spalding, E. P., and Benfey, P. N. (2014). Advanced imaging techniques for the study of plant growth and development. *Trends in Plant Science*, 19(5):304–310. 00001.

Steffens, B., Kovalev, A., Gorb, S. N., and Sauter, M. (2012). Emerging roots alter epidermal cell fate through mechanical and reactive oxygen species signaling. *The Plant Cell Online*, 24(8):3296–3306.

Steffens, B. and Sauter, M. (2005). Epidermal cell death in rice is regulated by ethylene, gibberellin, and abscisic acid. *Plant Physiology*, 139(2):713–721.

Strobl, F. and Stelzer, E. H. K. (2014). Non-invasive long-term fluorescence live imaging of tribolium castaneum embryos. *Development*, 141(11):2331–2338.

Swarup, K., Benková, E., Swarup, R., Casimiro, I., Péret, B., Yang, Y., Parry, G., Nielsen, E., De Smet, I., Vanneste, S., Levesque, M. P., Carrier, D., James, N., Calvo, V., Ljung, K., Kramer, E., Roberts, R., Graham, N., Marillonnet, S., Patel, K., Jones,

J. D. G., Taylor, C. G., Schachtman, D. P., May, S., Sandberg, G., Benfey, P., Friml, J., Kerr, I., Beeckman, T., Laplaze, L., and Bennett, M. J. (2008). The auxin influx carrier LAX3 promotes lateral root emergence. *Nature Cell Biology*, 10(8):946–954.

Swarup, R., Kramer, E. M., Perry, P., Knox, K., Leyser, H. M. O., Haseloff, J., Beemster, G. T. S., Bhalerao, R., and Bennett, M. J. (2005). Root gravitropism requires lateral root cap and epidermal cells for transport and response to a mobile auxin signal. *Nature Cell Biology*, 7(11):1057–1065.

Takahashi, K., Shimada, T., Kondo, M., Tamai, A., Mori, M., Nishimura, M., and Hara-Nishimura, I. (2010). Ectopic expression of an esterase, which is a candidate for the unidentified plant cutinase, causes cuticular defects in arabidopsis thaliana. *Plant and Cell Physiology*, 51(1):123–131.

Teale, W. D., Paponov, I. A., and Palme, K. (2006). Auxin in action: signalling, transport and the control of plant growth and development. *Nature Reviews Molecular Cell Biology*, 7(11):847–859.

Tromas, A., Paque, S., Stierlé, V., Quettier, A.-L., Muller, P., Lechner, E., Genschik, P., and Perrot-Rechenmann, C. (2013). Auxin-binding protein 1 is a negative regulator of the SCFTIR1/AFB pathway. *Nature Communications*, 4.

Uyttewaal, M., Traas, J., and Hamant, O. (2010). Integrating physical stress, growth, and development. *Current Opinion in Plant Biology*, 13(1):46–52.

Van Damme, D., De Rybel, B., Gudesblat, G., Demidov, D., Grunewald, W., De Smet, I., Houben, A., Beeckman, T., and Russinova, E. (2011). Arabidopsis α aurora kinases function in formative cell division plane orientation. *The Plant cell*, 23(11):4013–4024.

van den Berg, C., Willemsen, V., Hendriks, G., Weisbeek, P., and Scheres, B. (1997). Short-range control of cell differentiation in the arabidopsis root meristem. *Nature*, 390(6657):287–289.

Vanneste, S. and Friml, J. (2009). Auxin: A trigger for change in plant development. *Cell*, 136(6):1005–1016.

Vermeer, J. E. M., Wangenheim, D. v., Barberon, M., Lee, Y., Stelzer, E. H. K., Maizel, A., and Geldner, N. (2014). A spatial accommodation by neighboring cells is required for organ initiation in arabidopsis. *Science*, 343(6167):178–183. 00002 PMID: 24408432.

Verveer, P. J., Swoger, J., Pampaloni, F., Greger, K., Marcello, M., and Stelzer, E. H. K. (2007). High-resolution three-dimensional imaging of large specimens with light sheet-based microscopy. *Nature Methods*, 4(4):311–313.

Vieten, A., Sauer, M., Brewer, P. B., and Friml, J. (2007). Molecular and cellular aspects of auxin-transport-mediated development. *Trends in Plant Science*, 12(4):160–168.

Volkmann, D. and Sievers, A. (1979). Graviperception in multicellular organs. *Encyclopedia of plant physiology, NS*, 7:573–600.

Wan, Y., Jasik, J., Wang, L., Hao, H., Volkmann, D., Menzel, D., Mancuso, S., Baluška, F., and Lin, J. (2012). The signal transducer NPH3 integrates the phototropin1 photosensor with PIN2-based polar auxin transport in arabidopsis root phototropism. *The Plant Cell Online*, 24(2):551–565.

Wan, Y.-L., Eisinger, W., Ehrhardt, D., Kubitscheck, U., Baluska, F., and Briggs, W. (2008). The subcellular localization and blue-light-induced movement of phototropin 1-GFP in etiolated seedlings of arabidopsis thalianaw. *Molecular Plant*, 1(1):103–117.

Wang, B. and Qiu, Y.-L. (2006). Phylogenetic distribution and evolution of mycorrhizas in land plants. *Mycorrhiza*, 16(5):299–363.

Wang, R. and Estelle, M. (2014). Diversity and specificity: auxin perception and signaling through the TIR1/AFB pathway. *Current Opinion in Plant Biology*, 21:51–58.

Wangenheim, D. v. (2009). *Visualisierung dynamischer vesikulärer Kompartimente in Wurzelhaarzellen von Arabidopsis thaliana.* Diploma thesis, Rheinische Friedrich-Wilhelms-Universität Bonn.

Wangenheim, D. v., Daum, G., Lohmann, J. U., Stelzer, E. K., and Maizel, A. (2014). Live imaging of arabidopsis development. In *Arabidopsis Protocols*, pages 539–550. Springer.

Weiler, E. W. and Nover, L. (2008). *Allgemeine und molekulare Botanik.* Georg Thieme Verlag.

Wymer, C. L., Bibikova, T. N., and Gilroy, S. (1997). Cytoplasmic free calcium distributions during the development of root hairs of arabidopsis thaliana. *Plant Journal*, 12(2):427.

Xu, T., Dai, N., Chen, J., Nagawa, S., Cao, M., Li, H., Zhou, Z., Chen, X., Rycke, R. D., Rakusová, H., Wang, W., Jones, A. M., Friml, J., Patterson, S. E., Bleecker, A. B., and Yang, Z. (2014). Cell surface ABP1-TMK auxin-sensing complex activates ROP GTPase signaling. *Science*, 343(6174):1025–1028.

Xu, T., Wen, M., Nagawa, S., Fu, Y., Chen, J.-G., Wu, M.-J., Perrot-Rechenmann, C., Friml, J., Jones, A. M., and Yang, Z. (2010). Cell surface- and rho GTPase-based auxin signaling controls cellular interdigitation in arabidopsis. *Cell*, 143(1):99–110.

Yamagami, M., Haga, K., Napier, R. M., and Iino, M. (2004). Two distinct signaling pathways participate in auxin-induced swelling of pea epidermal protoplasts. *Plant Physiology*, 134(2):735–747.

Yang, Z. (1998). Signaling tip growth in plants. *Current Opinion in Plant Biology*, 1(6):525–530.

Yazdanbakhsh, N. and Fisahn, J. (2009). High throughput phenotyping of root growth dynamics, lateral root formation, root architecture and root hair development enabled by PlaRoM. *Funct. Plant Biol.*, 36(11):938–946.

Yoshida, S., Barbier de Reuille, P., Lane, B., Bassel, G. W., Prusinkiewicz, P., Smith, R. S., and Weijers, D. (2014). Genetic control of plant development by overriding a geometric division rule. *Developmental Cell*, 29(1):75–87.

Zažímalová, E., Murphy, A. S., Yang, H., Hoyerová, K., and Hošek, P. (2010). Auxin transporters—why so many? *Cold Spring Harbor Perspectives in Biology*, 2(3):a001552.

Zenser, N., Ellsmore, A., Leasure, C., and Callis, J. (2001). Auxin modulates the degradation rate of aux/IAA proteins. *Proceedings of the National Academy of Sciences*, 98(20):11795–11800.

Zhang, K.-X., Xu, H.-H., Yuan, T.-T., Zhang, L., and Lu, Y.-T. (2013). Blue-light-induced PIN3 polarization for root negative phototropic response in arabidopsis. *The Plant Journal*, 76(2):308–321.

Zonia, L. and Munnik, T. (2007). Life under pressure: hydrostatic pressure in cell growth and function. *Trends in Plant Science*, 12(3):90–97.

Supplementary Material

Figures and tables

Table 5.1: Key stages in lateral root development.

	time point of occurrence [$number of cells$ and $timepoint postgravity-stimulation$, h:min]						
event	#120830	#121204	#121211	#130508	#130607	average	StdDev
1. cell division	10 cells	11 cells	-	9 cells	15 cells	11 cells	2 cells
	8h 36min	ca 14h		9h 30min	7h 15min	10h 41min	3h 10min
total number	167 cells	160 cells	260 cells	143 cells	267 cells		
of cells	33h 30min	39h 15min	40h 40min	37h 30min	32h 10min		
142 cells	30h 50min	37h 40min	34h 45min	36h 55min	24h 50min		
2 layer	22 cells	25 cells	30 cells	16 cells	28 cells	24 cells	5 cells
3 layer	58 cells	51 cells	64 cells	50 cells	56 cells	56 cells	6 cells
1. radial division	36 cells	62 cells	106 cells	55 cells	97 cells	71 cells	39 cells
emergence	-	155 cells	208 cells	-	173 cells	179 cells	27 cells
	-	38h 55min	38h 20min	39h 40min	26h 35min	35h 52min	6h 13min
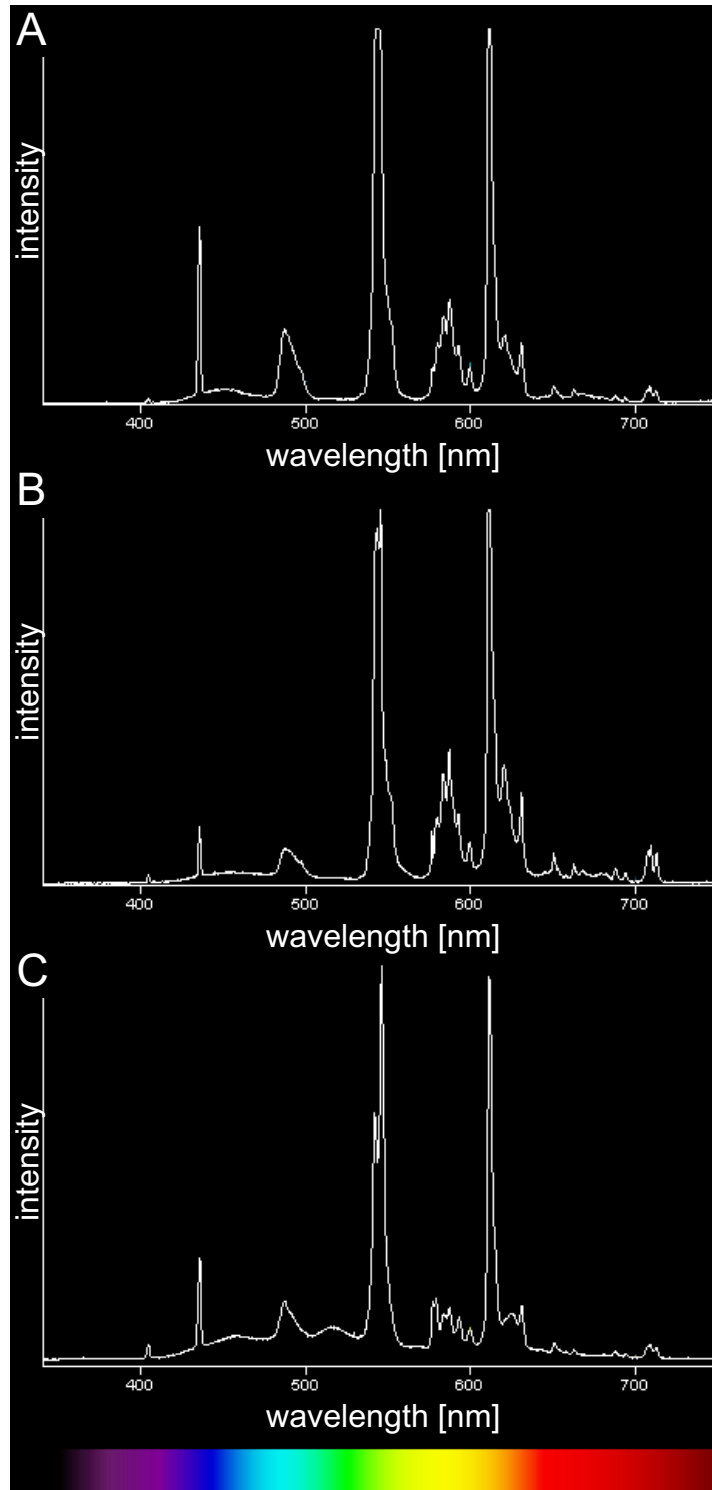
Figure 5.5: Spectral light quality of the illumination system in the mDSLM compared to the reference spectrum in the plant incubator. (A) Light spectrum measured in the plant incubator. (B) Light spectrum in the plant incubator but measured behind the glass fiber that is used in the mDSLM. (C) Light spectrum of the small fluorescence lamp in the mDSLM measured behind the glass fiber.
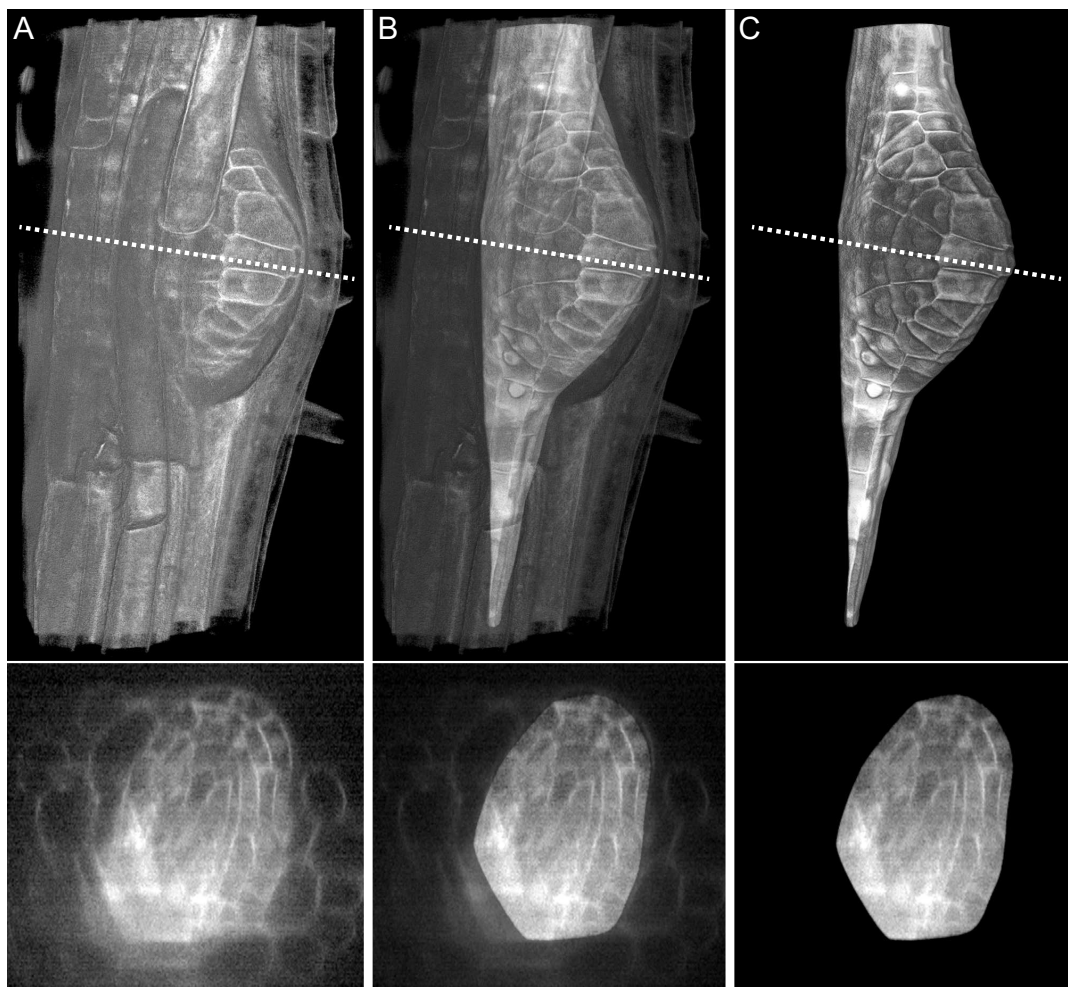
Figure 5.6: Retouche of the tissue overlaying the lateral root primordium. (A) The raw dataset #121211 in a 3D reconstruction (top image) and a single transverse section along the dashed line (bottom image). In *Adobe After Effects*, the transverse sections of the image stack was overlayed with a black mask to cover the cells that do not belong to the primordium. By animating the mask the overlaying cells were removed precisely along the longitudinal axis of the primary root. (B and C) The same images shown in A), but with the black mask opacity set to (B) 50 %, and (C) 100 %. **Supplemental Movie-5.6**.
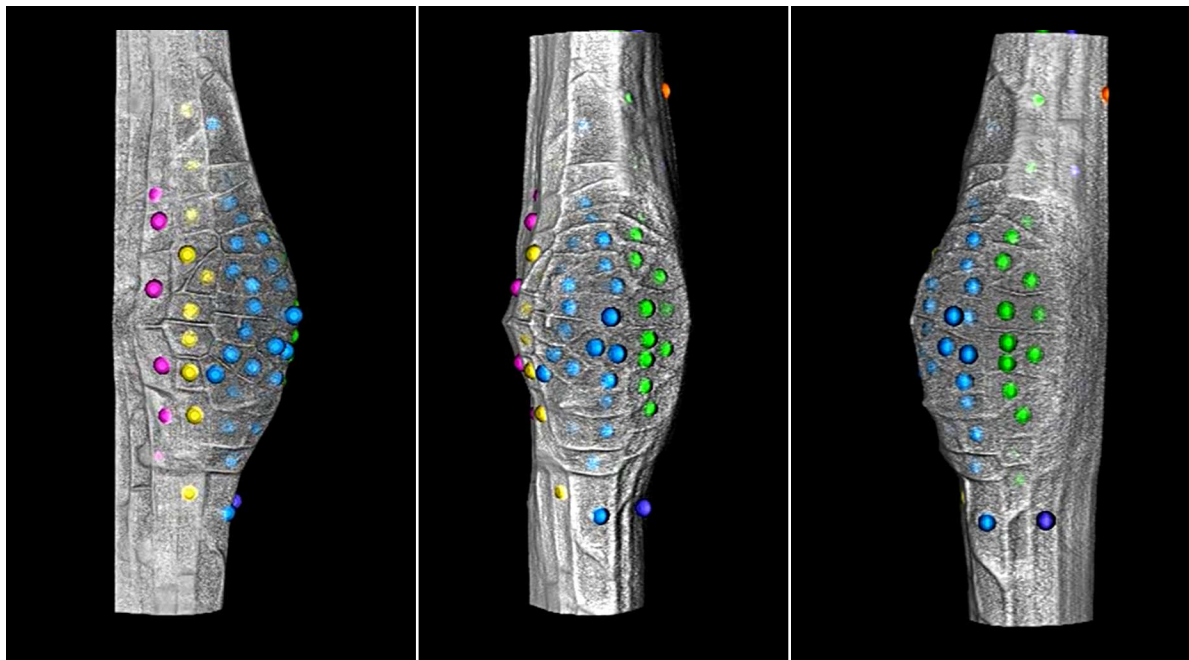
Figure 5.7: 3D overlay of the objects with the membrane channel in the last time point of dataset #120830. Front view (middle) and two angular views (left, right). Objects with the same color are located in the same cell file.
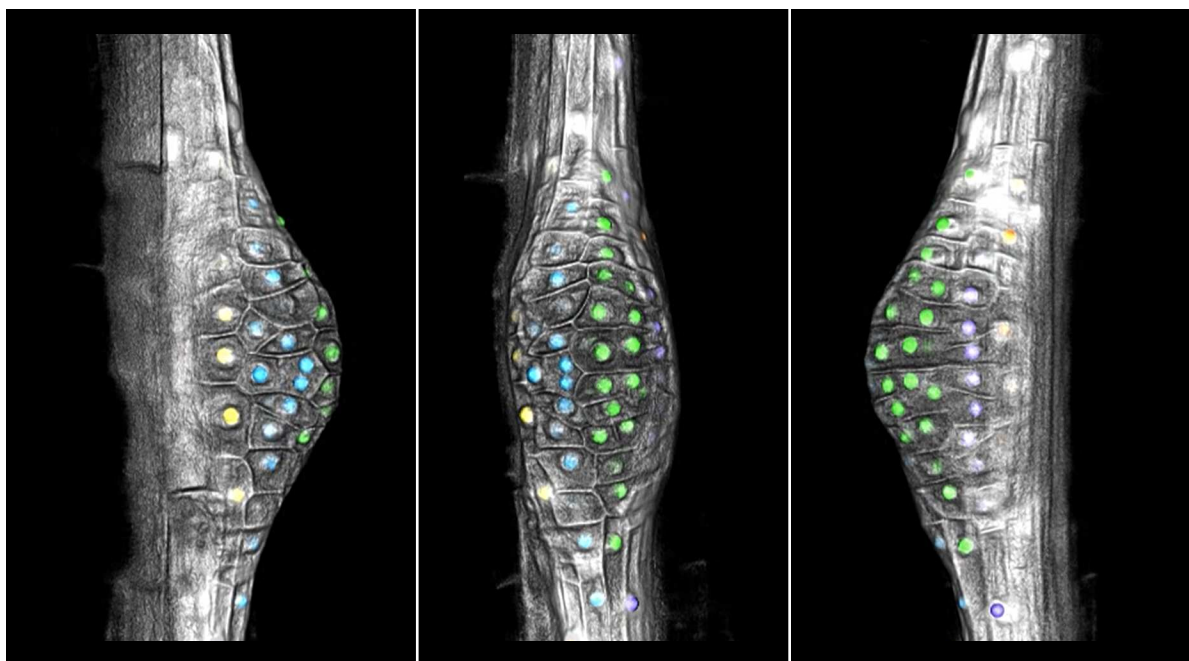
Figure 5.8: 3D overlay of the objects with the membrane channel in the last time point of dataset #121204. Front view (middle) and two angular views (left, right). Objects with the same color are located in the same cell file.
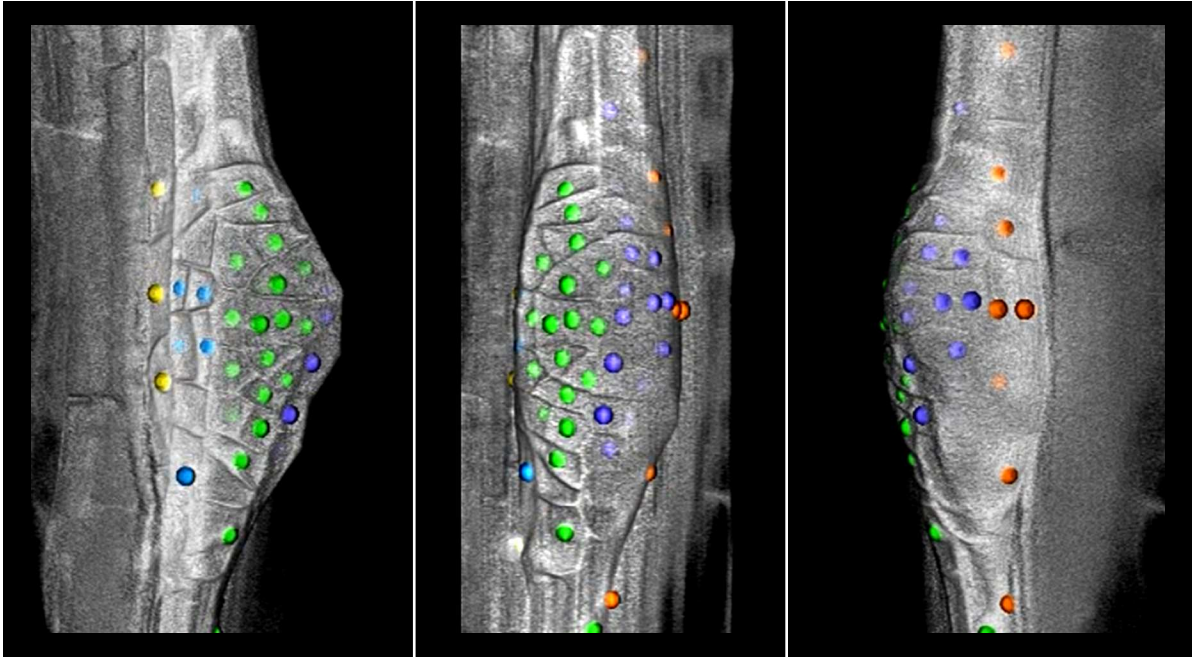
Figure 5.9: 3D overlay of the objects with the membrane channel in the last time point of dataset #130508. Front view (middle) and two angular views (left, right). Objects with the same color are located in the same cell file.
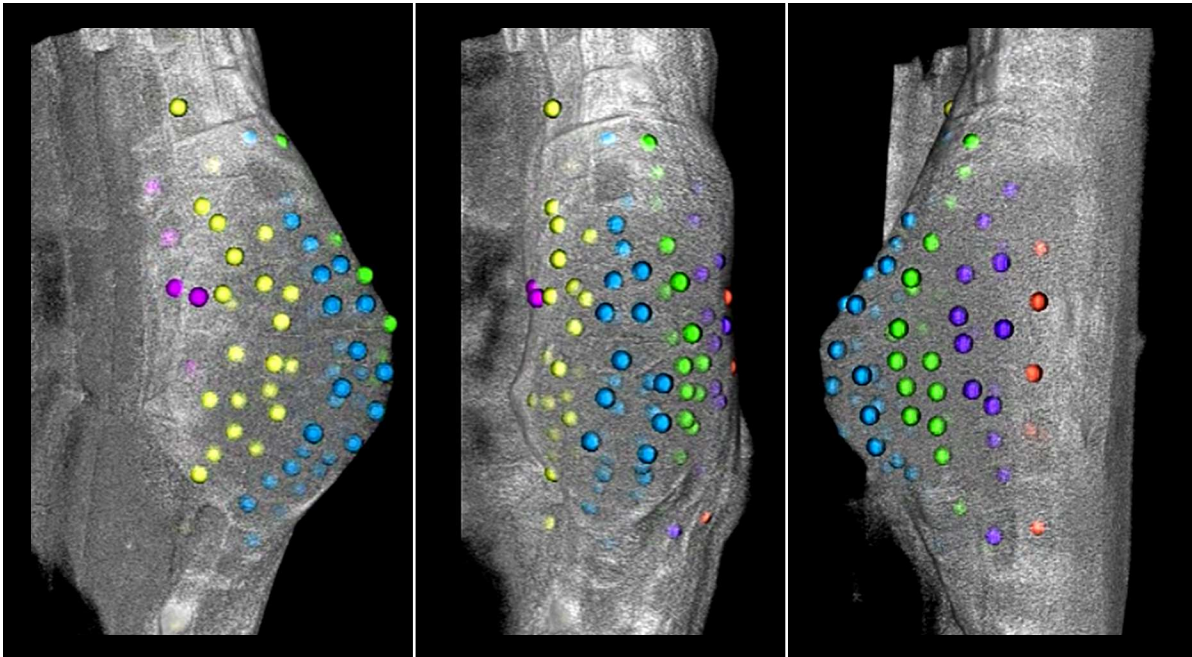
Figure 5.10: 3D overlay of the objects with the membrane channel in the last time point of dataset #130607. Front view (middle) and two angular views (left, right). Objects with the same color are located in the same cell file.
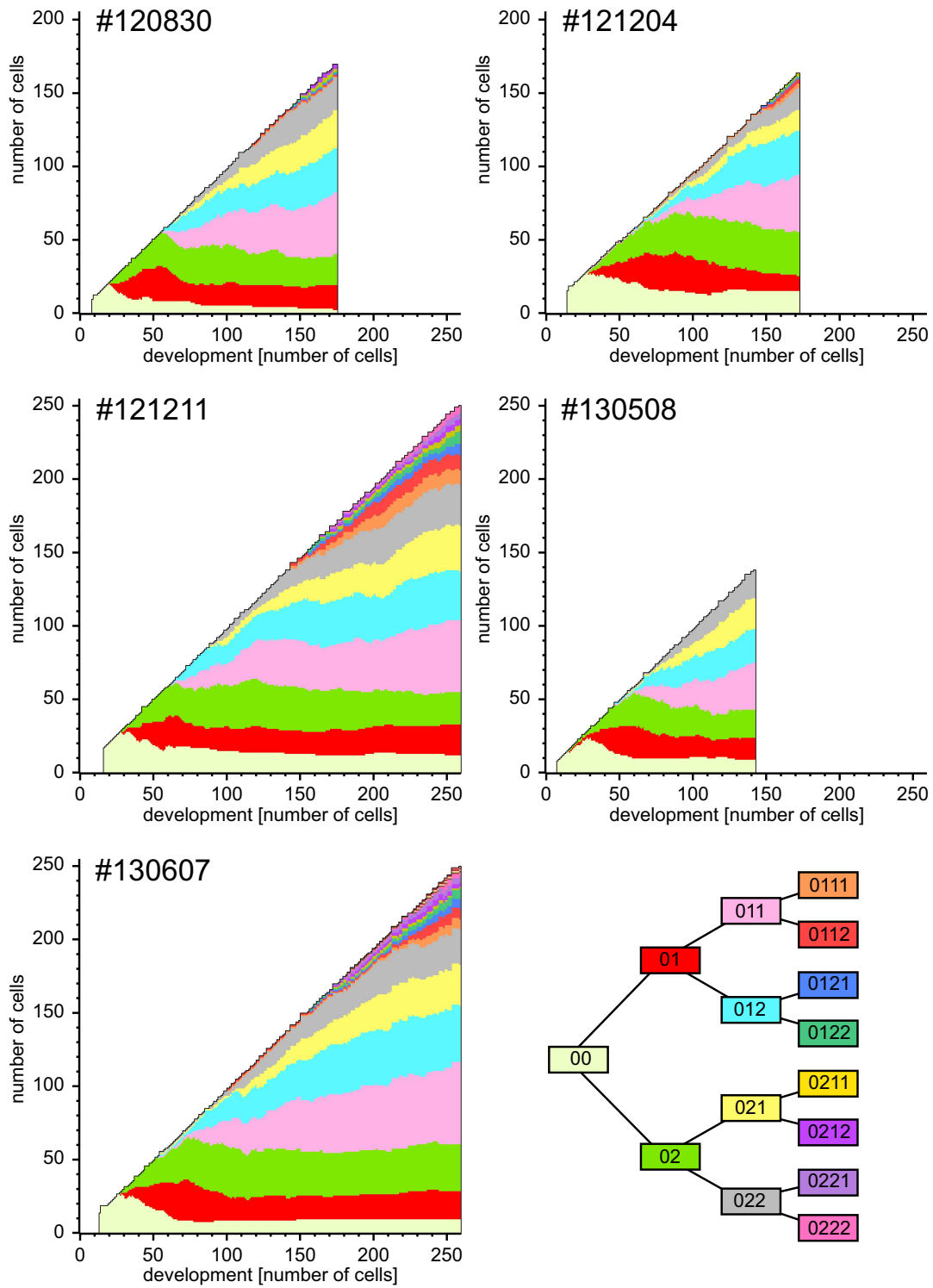
Figure 5.11: Number of cells in different layers. Number of cells in each layer as a function of time. Layers are color coded according to the lineage tree legend (bottom right).

Table 5.2: Number of transversal (shortest area wall, yellow) and longitudinal (long cell wall, blue) divisions.

#120830

cell file #	-2		-1		0		1		2		sum		
class of division													% longitudinal
1. cell cycle			1	0	3	0	2	0	2	0	8	0	**0.0**
2. cell cycle			1	1	2	2	2	2	0	3	5	8	**61.5**
3. cell cycle			2	2	7	1	5	3	6	0	20	6	**23.1**
4. cell cycle			5	1	10	2	10	3	5	2	30	8	**21.1**
sum			9	4	22	5	19	8	13	5	63	22	

#121204

| cell file #	-2		-1		0		1		2		sum		
class of division													% longitudinal
1. cell cycle	2	0	2	0	2	0	2	0			8	0	**0.0**
2. cell cycle	0	3	3	0	3	1	1	3			7	7	**50.0**
3. cell cycle	4	0	4	2	6	2	5	1			19	5	**20.8**
4. cell cycle	0	0	9	2	11	0	0	6			20	8	**28.6**
sum	6	3	18	4	22	3	8	10			54	20	

#130508

cell file #	-2		-1		0		1		2		sum		
class of division													% longitudinal
1. cell cycle			2	0	1	0	2	0			5	0	**0.0**
2. cell cycle			2	2	2	0	2	1			6	3	**33.3**
3. cell cycle			6	0	2	2	4	0			12	2	**14.3**
4. cell cycle			8	1	9	0	4	2			21	3	**12.5**
sum			18	3	14	2	12				44	8	
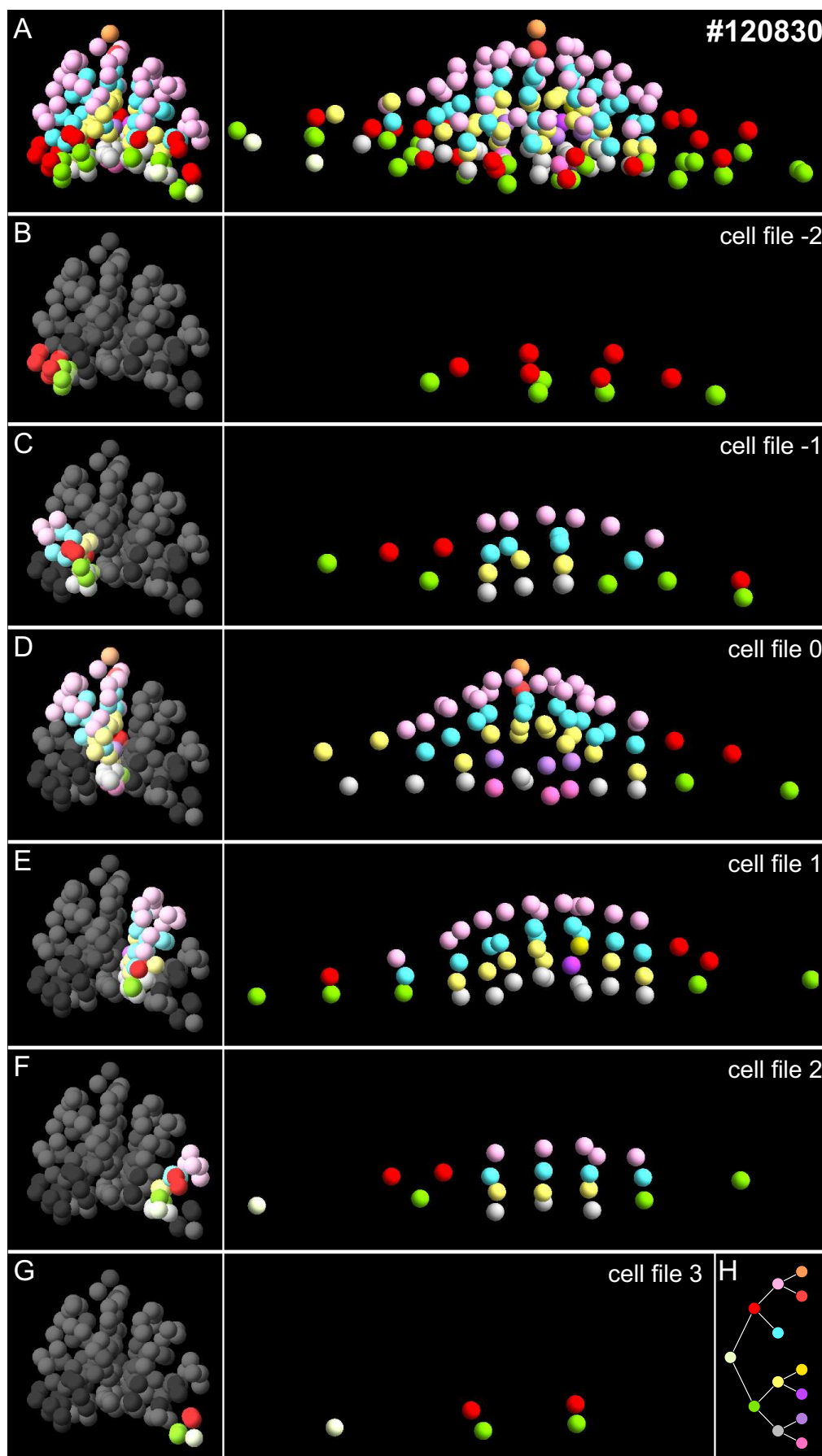
Figure 5.12: Layer assignment of the virtual lateral root #120830. The nuclei position in the last time point of the time lapse is shown in the radial view (left) and side view (right). (A) All nuclei objects. (B-G) Objects of a particular cell file. (H) Legend, colors indicate the history of periclinal divisions. **Supplemental Movie-5.12**.
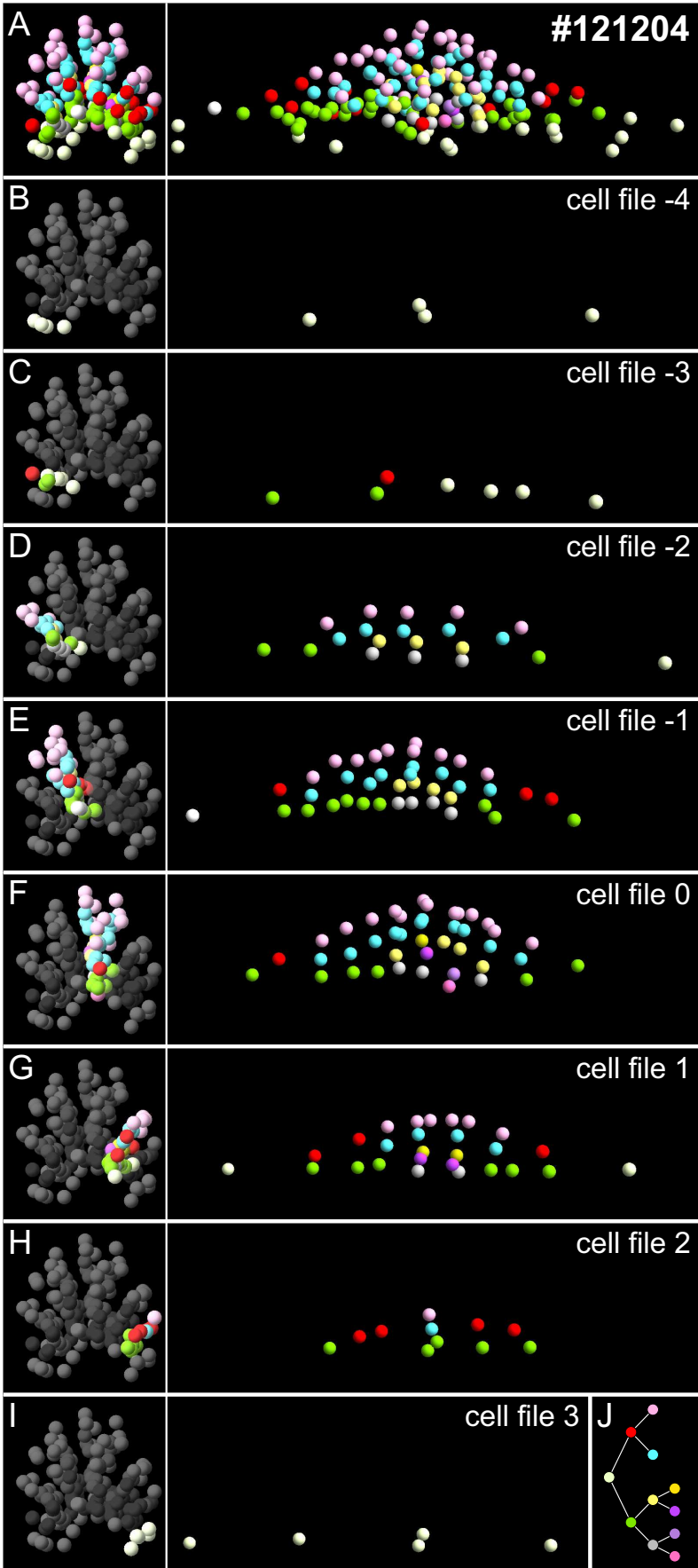
Figure 5.13: Layer assignment of the virtual lateral root #121204. The nuclei position in the last time point of the time lapse is shown in the radial view (left) and side view (right). (A) All nuclei objects. (B-I) Objects of a particular cell file. (J) Legend, colors indicate the history of periclinal divisions. **Supplemental Movie-5.13**.
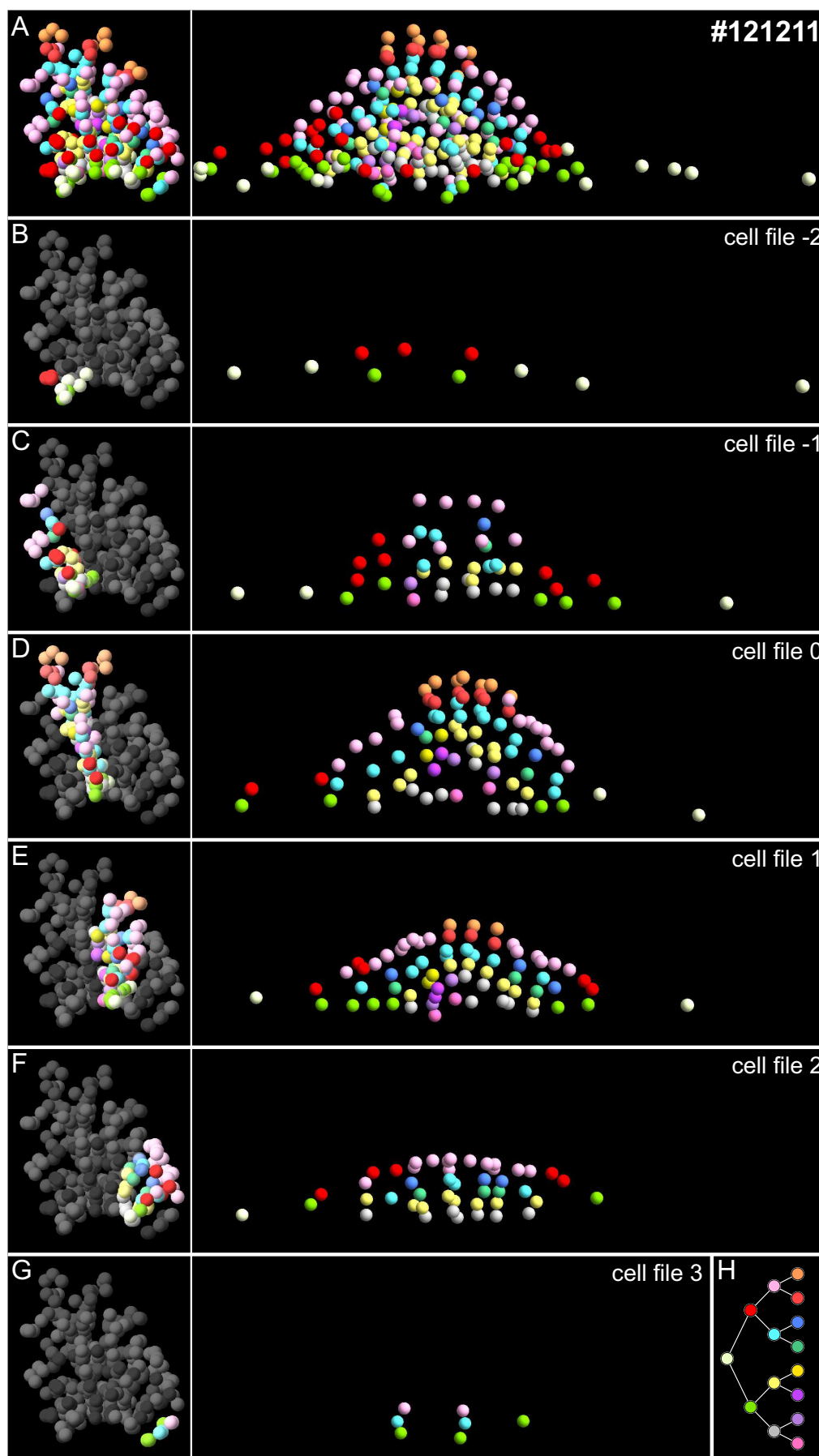
Figure 5.14: Layer assignment of the virtual lateral root #121211. The nuclei position in the last time point of the time lapse is shown in the radial view (left) and side view (right). (A) All nuclei objects. (B-G) Objects of a particular cell file. (H) Legend, colors indicate the history of periclinal divisions. **Supplemental Movie-5.14**.
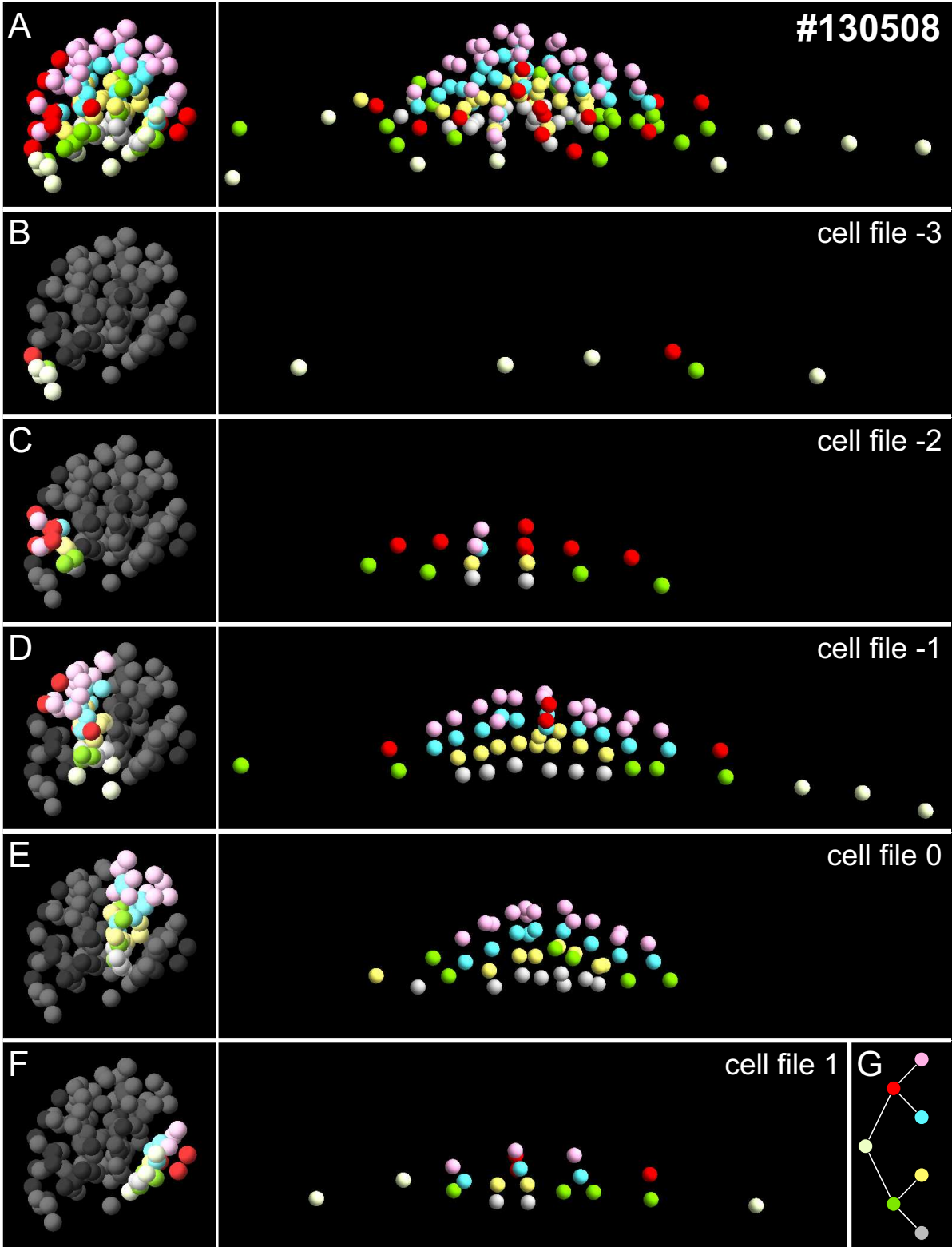
Figure 5.15: Layer assignment of the virtual lateral root #130508. The nuclei position in the last time point of the time lapse is shown in the radial view (left) and side view (right). (A) All nuclei objects. (B-F) Objects of a particular cell file. (G) Legend, colors indicate the history of periclinal divisions. **Supplemental Movie-5.15**.

mDSLM metadata
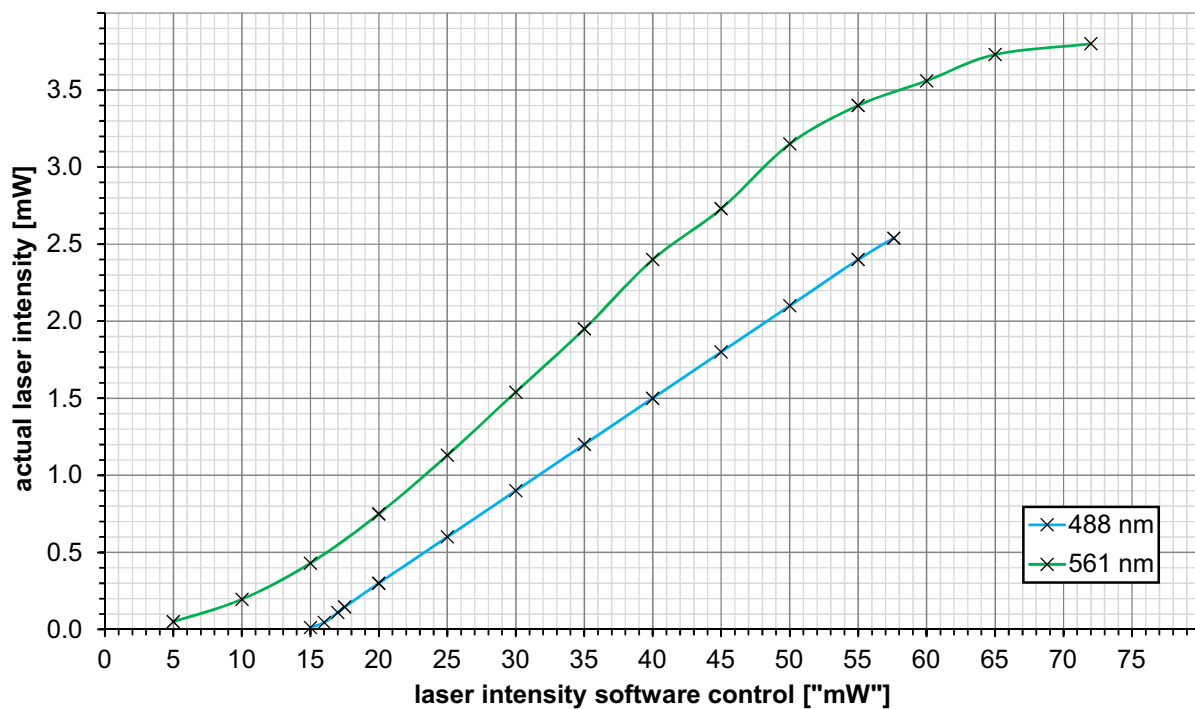
Figure 5.16: Laser intensities. The value for the laser intensity displayed in the software GUI does not reflect the actual laser intensity. The graphs can be used to calculate the real laser intensity on the sample (measured behind the illumination lens).

Shoot apical meristem - 110526

Metadata of the mDSLM recording in figure 3.23 on page 75

General Information

Date Time	5/26/2011 12:55
Machine Name	WS-STELZER-025
Software Version	0.3.5.0
File Name	110526.TIF

Acquisition Data

Timelapse	Preview Position
Enabled = False	x = 420
Start Time = 5/26/2011 12:55:22 PM	y = 12520
Interval = 00:00:30	z = 50
Total Duration = 00:01:00	angle = 420
Repeats = 2	

Specimens

Identifier	Position	Rotation	Stack	Channels
	x = 420	Enabled = False	Enabled = True	Channel 1
	y = 12520	Start Angle = 0	First Plane = -150	Enabled = True
	z = -50	End Angle = 0	Last Plane = 50	Wave Length = 488 nm
	angle = 50	Step Size = 1	Spacing = 0.645 µm	Laser Power = 1 mW
		Number Of Steps = 1	Depth = 200 µm	Filter = 525/50
			Number Of Planes = 311	Camera Integration Time = 100 ms
			Center = -50	
Specimen 1				

System Information

Detection Lens	Illumination Lens	Camera	Post Processing
Identifier = N-Achroplan	Identifier = Plan-Neofluar	Identifier = Andor Clara	Deconvolution
Magnification = 40 x	Magnification = 5	Binning	Deconvolution Type = None
Numerical Aperture = 0.75	Numerical Aperture = 0.16	Hardware Bin Enabled = False	Deconvolution Iterations = 3
Refractive Index = 1.33	Refractive Index = 1	Hardware Bin Factor = 2	Background
Working Distance = 2.1 mm	Working Distance = 18.5 mm	Software Bin Enabled = False	Bg Treatment = SubtractConst
		Format	
		Pixels = 1392 x 1040	
		Bits Per Pixel = 14	
		Pixel Pitch = 6.45 µm	
		Roi	
		Hard Roi Enabled = False	
		Soft Roi Enabled = False	
		Gain	
		Gain = 1	

Multiple angle acquisition - 110308

Metadata of the mDSLM recording in figure 2.14 on page 36

General Information

Date Time	3/8/2011 16:17
Machine Name	MDSLM-UI-02
Software Version	0.2.6.0
File Name	30.TIF

Acquisition Data

Timelapse	Preview Position
Enabled = False	x = 1200
Start Time = 08-Mar-11 4:17:28 PM	y = 10270
Interval = 00:00:01	z = -950
Total Duration = 00:01:00	angle = 1200
Repeats = 60	

Specimens

Identifier	Position	Rotation	Stack	Channels

	x = 1200
	y = 10270
	z = -950
	angle = 10
		Enabled = True
		Start Angle = 0
		End Angle = 150
		Step Size = 30
		Number Of Steps = 5
			Enabled = True
			First Plane = -1120
			Last Plane = -750
			Spacing = 1.29 µm
			Depth = 370 µm
			Number Of Planes = 287
			Center = -935
				Channel 1
				  Enabled = True
				  Wave Length = 488 nm
				  Laser Power = mW
				  Filter = 525/45
				  Camera Integration Time = 100 ms
				Channel 2
				  Enabled = True
				  Wave Length = 561 nm
				  Laser Power = mW
				  Filter = 607/70
				  Camera Integration Time = 100 ms

Specimen 1				

System Information

Detection Lens	Illumination Lens	Camera	Post Processing

Identifier = N-Achroplan
Magnification = 20 x
Numerical Aperture = 0.5
Refractive Index = 1.33
Working Distance = 2.6 mm
	Identifier = Epiplan-Neofluar
	Magnification = 2.5
	Numerical Aperture = 0.06
	Refractive Index = 1
	Working Distance = 15.1 mm
		Identifier =
		Binning
		  Hardware Bin Enabled = False
		  Hardware Bin Factor = 2
		  Software Bin Enabled = False
		Format
		  Pixels = 1392 x 1040
		  Bits Per Pixel = 14
		  Pixel Pitch = 6.45 µm
		Roi
		  Hard Roi Enabled = False
		  Soft Roi Enabled = False
		Gain
		  Gain = 1
			Deconvolution
			  Deconvolution Type = None
			  Deconvolution Iterations = 3
			Background
			  Bg Treatment = SubtractConst

Multiple specimen acquisition - 111122

Metadata of the mDSLM recording in figure 2.13 on page 35

General Information

Date Time	11/22/2011 15:46
Machine Name	WS-STELZER-025
Software Version	0.3.6.0
File Name	111122.TIF

Acquisition Data

Timelapse	Preview Position
Enabled = True Start Time = 11/22/2011 3:46:45 PM Interval = 00:07:30 Total Duration = 2.00:01:00 Repeats = 384	x = -950 y = 12300 z = 1151 angle = -950

Specimens

Identifier	Position	Rotation	Stack	Channels

Specimen1	x = -950
	y = 12300
	z = 1151
	angle = -100
		Enabled = False
		Start Angle = 0
		End Angle = 0
		Step Size = 1
		Number Of Steps = 1
			Enabled = True
			First Plane = 1051
			Last Plane = 1251
			Spacing = 1.29 µm
			Depth = 200 µm
			Number Of Planes = 156
			Center = 1151
				Channel 1
				  Enabled = False
				  Wave Length = 488 nm
				  Laser Power = 1.03 mW
				  Filter = 525/50
				  Camera Integration Time = 100 ms
				Channel 2
				  Enabled = True
				  Wave Length = 594 nm
				  Laser Power = 6 mW
				  Filter = 628/40
				  Camera Integration Time = 100 ms

Identifier	Position	Rotation	Stack	Channels

Specimen2	x = -780
	y = 13400
	z = 1450
	angle = -100
		Enabled = False
		Start Angle = 0
		End Angle = 0
		Step Size = 1
		Number Of Steps = 1
			Enabled = True
			First Plane = 1400
			Last Plane = 1500
			Spacing = 1.29 µm
			Depth = 100 µm
			Number Of Planes = 78
			Center = 1450
				Channel 1
				  Enabled = False
				  Wave Length = 488 nm
				  Laser Power = 1.03 mW
				  Filter = 525/50
				  Camera Integration Time = 100 ms
				Channel 2
				  Enabled = True
				  Wave Length = 594 nm
				  Laser Power = 6 mW
				  Filter = 628/40
				  Camera Integration Time = 100 ms

System Information

Detection Lens	Illumination Lens	Camera	Post Processing

Identifier = N-Achroplan
Magnification = 20 x
Numerical Aperture = 0.5
Refractive Index = 1.33
Working Distance = 2.6 mm
	Identifier = Plan-Apochromat
	Magnification = 5
	Numerical Aperture = 0.16
	Refractive Index = 1
	Working Distance = 12.1 mm
		Identifier = Andor Clara
		Binning
		  Hardware Bin Enabled = False
		  Hardware Bin Factor = 2
		  Software Bin Enabled = False
		Format
		  Pixels = 1392 x 1040
		  Bits Per Pixel = 14
		  Pixel Pitch = 6.45 µm
		Roi
		  Hard Roi Enabled = False
		  Soft Roi Enabled = False
		Gain
		  Gain = 1.5
			Deconvolution
			  Deconvolution Type = None
			  Deconvolution Iterations = 3
			Background
			  Bg Treatment = SubtractConst

Endosomes - 120119

Metadata of the mDSLM recording in figure 2.17 on page 39

General Information

Date Time	1/19/2012 16:42
Machine Name	WS-STELZER-025
Software Version	0.4.3.0
File Name	preview.TIF

Acquisition Data

Timelapse	Preview Position
Enabled = False	x = 691
Start Time = 1/19/2012 4:42:42 PM	y = 12320
Interval = 00:00:30	z = -1236.5
Total Duration = 00:01:00	angle = 691
Repeats = 2	

Specimens

Identifier	Position	Rotation	Stack	Channels
	x = 691	Enabled = False	Enabled = True	Channel 1
	y = 12320	Start Angle = 0	First Plane = -1346.5	Enabled = True
	z = -1291.5	End Angle = 0	Last Plane = -1236.5	Wave Length = 488 nm
	angle = -90	Step Size = 1	Spacing = 0.05 µm	Laser Power = 5.77 mW
		Number Of Steps = 1	Depth = 110 µm	Filter = 525/50
			Number Of Planes = 2201	Camera Integration Time = 50 ms
			Center = -1291.5	Channel 2
				Enabled = False
				Wave Length = 760 nm
				Laser Power = 0 mW
				Filter = Empty
				Camera Integration Time = 100 ms
Specimen1				

System Information

Detection Lens	Illumination Lens	Camera	Post Processing
Identifier = N-Achroplan	Identifier = Plan-Neofluar	Identifier = Andor Clara	Deconvolution
Magnification = 10 x	Magnification = 5	Binning	Deconvolution Type = None
Numerical Aperture = 0.3	Numerical Aperture = 0.16	Hardware Bin Enabled = True	Deconvolution Iterations = 3
Refractive Index = 1.33	Refractive Index = 1	Hardware Bin Factor = 2	Background
Working Distance = 2.6 mm	Working Distance = 18.5 mm	Software Bin Enabled = False	Bg Treatment = SubtractConst
		Format	
		Pixels = 1392 x 1040	
		Bits Per Pixel = 14	
		Pixel Pitch = 6.45 µm	
		Roi	
		Hard Roi Enabled = False	
		Soft Roi Enabled = False	
		Gain	
		Gain = 1	

Endosomes - 120322

Metadata of the mDSLM recording in figure 3.16 on page 68, and figure 3.20 on page 71

General Information

Date Time	3/22/2012 17:40
Machine Name	MDSLM04-WS
Software Version	4.9.0.0
File Name	120322.TIF

Acquisition Data

Timelapse	Preview Position
Enabled = True Start Time = 3/22/2012 5:40:16 PM Interval = 00:02:00 Total Duration = 10:01:00 Repeats = 300	x = -580 y = 12850 z = -920 angle = -580

Specimens

Identifier	Position	Rotation	Stack	Channels

	x = -580
	y = 12850
	z = -920
	angle = -40
		Enabled = False
		Start Angle = 0
		End Angle = 0
		Step Size = 1
		Number Of Steps = 1
			Enabled = True
			First Plane = -1045
			Last Plane = -795
			Spacing = 0.645 µm
			Depth = 250 µm
			Number Of Planes = 388
			Center = -920
				Channel 1
				  Enabled = True
				  Wave Length = 488 nm
				  Laser Power = 7.2 mW
				  Filter = 525/50
				  Camera Integration Time = 50 ms
				Channel 2
				  Enabled = False
				  Wave Length = 760 nm
				  Laser Power = 0 mW
				  Filter = 488LP
				  Camera Integration Time = 974 ms

Specimen1				

System Information

Detection Lens	Illumination Lens	Camera	Post Processing

Identifier = N-Achroplan
Magnification = 40 x
Numerical Aperture = 0.75
Refractive Index = 1.33
Working Distance = 2.1 mm
	Identifier = Plan-Neofluar
	Magnification = 5
	Numerical Aperture = 0.16
	Refractive Index = 1
	Working Distance = 18.5 mm
		Identifier = Andor Neo
		Binning
		  Hardware Bin Enabled = False
		  Hardware Bin Factor = 2
		  Software Bin Enabled = False
		Format
		  Pixels = 2560 x 2160
		  Bits Per Pixel = 12
		  Pixel Pitch = 6.5 µm
		Roi
		  Hard Roi Enabled = False
		  Soft Roi Enabled = False
		Gain
		  Gain = 1
			Deconvolution
			  Deconvolution Type = None
			  Deconvolution Iterations = 3
			Background
			  Bg Treatment = DoNothing

Actin - 131105

Metadata of the mDSLM recording in figure 3.11 on page 63

General Information

Date Time	11/5/2013 16:56
Machine Name	MDSLM03
Software Version	5.1.0.0
File Name	video_lateralhaar.TIF

Acquisition Data

Timelapse	Preview Position
Enabled = True	x = -90
Start Time = 11/5/2013 4:56:35 PM	y = 4387
Interval = 00:00:15	z = -298
Total Duration = 00:05:00	angle = -90
Repeats = 20	

Specimens

Identifier	Position	Rotation	Stack	Channels

	x = -90
	y = 4387
	z = -311
	angle = 30
		Enabled = False
		Start Angle = 0
		End Angle = 0
		Step Size = 1
		Number Of Steps = 1
			Enabled = True
			First Plane = -324
			Last Plane = -298
			Spacing = 0.645 µm
			Depth = 26 µm
			Number Of Planes = 41
			Center = -311
				Channel 1
				    Enabled = True
				    Wave Length = 488 nm
				    Laser Power = 7.86 mW
				    Filter = 525/45
				    Camera Integration Time = 20 ms
				Channel 2
				    Enabled = False
				    Wave Length = 760 nm
				    Laser Power = 0 mW
				    Filter = Empty
				    Camera Integration Time = 50 ms

Specimen1				

System Information

Detection Lens	Illumination Lens	Camera	Post Processing

Identifier = N-Achroplan
Magnification = 40 x
Numerical Aperture = 0.75
Refractive Index = 1.33
Working Distance = 2.1 mm
	Identifier = Plan-Neofluar
	Magnification = 5
	Numerical Aperture = 0.16
	Refractive Index = 1
	Working Distance = 18.5 mm
		Identifier = Andor Clara
		Binning
		    Hardware Bin Enabled = False
		    Hardware Bin Factor = 2
		    Software Bin Enabled = False
		Format
		    Pixels = 1392 x 1040
		    Bits Per Pixel = 14
		    Pixel Pitch = 6.45 µm
		Roi
		    Hard Roi Enabled = False
		    Soft Roi Enabled = False
		Gain
		    Gain = 1
			Deconvolution
			    Deconvolution Type = None
			    Deconvolution Iterations = 3
			Background
			    Bg Treatment = SubtractConst

Plastids - 131017

Metadata of the mDSLM recording in figure 3.13 on page 65

General Information

Date Time	10/17/2013 13:40
Machine Name	MDSLM04
Software Version	5.1.0.0
File Name	SSU131017.TIF

Acquisition Data

Timelapse	Preview Position
Enabled = True	x = -1245
Start Time = 10/17/2013 1:40:31 PM	y = 12715
Interval = 00:00:02	z = -1463
Total Duration = 00:05:00	angle = -1245
Repeats = 150	

Specimens

Identifier	Position	Rotation	Stack	Channels
	x = -1245	Enabled = False	Enabled = True	Channel 1
	y = 12715	Start Angle = 0	First Plane = -1473	Enabled = True
	z = -1468	End Angle = 0	Last Plane = -1463	Wave Length = 488 nm
	angle = -79	Step Size = 1	Spacing = 0.645 µm	Laser Power = 19.2 mW
		Number Of Steps = 1	Depth = 10 µm	Filter = 525/45
			Number Of Planes = 16	Camera Integration Time = 20 ms
Specimen1				

System Information

Detection Lens	Illumination Lens	Camera	Post Processing
Identifier = N-Achroplan	Identifier = Plan-Neofluar	Identifier = Andor Clara	Deconvolution
Magnification = 40 x	Magnification = 5	Binning	Deconvolution Type = None
Numerical Aperture = 0.75	Numerical Aperture = 0.16	Hardware Bin Enabled = True	Deconvolution Iterations = 3
Refractive Index = 1.33	Refractive Index = 1	Hardware Bin Factor = 2	Background
Working Distance = 2.1 mm	Working Distance = 18.5 mm	Software Bin Enabled = False	Bg Treatment = SubtractConst
		Format	
		Pixels = 1392 x 1040	
		Bits Per Pixel = 14	
		Pixel Pitch = 6.45 µm	
		Roi	
		Hard Roi Enabled = False	
		Soft Roi Enabled = False	
		Gain	
		Gain = 1	

Chloroplasts - 110519

Metadata of the mDSLM recording in figure 3.12 on page 64

General Information

Date Time	5/19/2011 13:22
Machine Name	WS-STELZER-025
Software Version	0.3.4.0
File Name	110519.TIF

Acquisition Data

Timelapse	Preview Position
Enabled = True	x = 877
Start Time = 5/19/2011 1:22:18 PM	y = 12330
Interval = 00:00:20	z = -313
Total Duration = 00:20:00	angle = 877
Repeats = 60	

Specimens

Identifier	Position	Rotation	Stack	Channels
	x = 877	Enabled = False	Enabled = True	Channel 1
	y = 12330	Start Angle = 0	First Plane = -353	Enabled = True
	z = -333	End Angle = 0	Last Plane = -313	Wave Length = 488 nm
	angle = 258	Step Size = 1	Spacing = 1 µm	Laser Power = 0.85 mW
		Number Of Steps = 1	Depth = 40 µm	Filter = 525/50
			Number Of Planes = 41	Camera Integration Time = 75 ms
			Center = -333	Channel 3
				Enabled = True
				Wave Length = 488 nm
				Laser Power = 0.85 mW
				Filter = 514 LP
Specimen 1				Camera Integration Time = 75 ms

System Information

Detection Lens	Illumination Lens	Camera	Post Processing
Identifier = Plan-Apochromat	Identifier = Plan-Neofluar	Identifier = Andor Clara	Deconvolution
Magnification = 63 x	Magnification = 5	Binning	Deconvolution Type = None
Numerical Aperture = 1	Numerical Aperture = 0.16	Hardware Bin Enabled = False	Deconvolution Iterations = 3
Refractive Index = 1.33	Refractive Index = 1	Hardware Bin Factor = 2	Background
Working Distance = 2.1 mm	Working Distance = 18.5 mm	Software Bin Enabled = False	Bg Treatment = SubtractConst
		Format	
		Pixels = 1392 x 1040	
		Bits Per Pixel = 14	
		Pixel Pitch = 6.45 µm	
		Roi	
		Hard Roi Enabled = False	
		Soft Roi Enabled = False	
		Gain	
		Gain = 1	

Lateral root outgrowth - 110614

Metadata of the mDSLM recording in figure 3.2 on page 53

General Information

Date Time	6/14/2011 15:44
Machine Name	WS-STELZER-025
Software Version	0.3.5.0
File Name	110614.TIF

Acquisition Data

Timelapse	Preview Position
Enabled = True Start Time = 6/14/2011 3:44:02 PM Interval = 00:15:00 Total Duration = 4.00:01:00 Repeats = 384	x = 570 y = 12120 z = -620 angle = 570

Specimens

Identifier	Position	Rotation	Stack	Channels

	x = 570
	y = 12120
	z = -620
	angle = -10
		Enabled = False
		Start Angle = 0
		End Angle = 0
		Step Size = 1
		Number Of Steps = 1
			Enabled = True
			First Plane = -770
			Last Plane = -470
			Spacing = 1.29 µm
			Depth = 300 µm
			Number Of Planes = 233
			Center = -620
				Channel 1
				  Enabled = True
				  Wave Length = 488 nm
				  Laser Power = 0.65 mW
				  Filter = 525/50
				  Camera Integration Time = 100 ms
				Channel 2
				  Enabled = True
				  Wave Length = 594 nm
				  Laser Power = 3 mW
				  Filter = 628/40
				  Camera Integration Time = 100 ms

Specimen 1				

System Information

Detection Lens	Illumination Lens	Camera	Post Processing

Identifier = N-Achroplan
Magnification = 20 x
Numerical Aperture = 0.5
Refractive Index = 1.33
Working Distance = 2.6 mm
	Identifier = Plan-Neofluar
	Magnification = 5
	Numerical Aperture = 0.16
	Refractive Index = 1
	Working Distance = 18.5 mm
		Identifier = Andor Clara
		Binning
		  Hardware Bin Enabled = False
		  Hardware Bin Factor = 2
		  Software Bin Enabled = False
		Format
		  Pixels = 1392 x 1040
		  Bits Per Pixel = 14
		  Pixel Pitch = 6.45 µm
		Roi
		  Hard Roi Enabled = False
		  Soft Roi Enabled = False
		Gain
		  Gain = 1.5
			Deconvolution
			  Deconvolution Type = None
			  Deconvolution Iterations = 3
			Background
			  Bg Treatment = SubtractConst

Lateral root formation - 120830

Metadata of the mDSLM recording in figure 2.16 on page 38, and figure 3.32 on page 85.

General Information

Date Time	8/30/2012 16:22
Machine Name	MDSLM04-WS
Software Version	5.1.0.0
File Name	120830.TIF

Acquisition Data

Timelapse	Preview Position
Enabled = True Start Time = 8/30/2012 4:22:44 PM Interval = 00:05:00 Total Duration = 4.01:01:00 Repeats = 1164	x = -620 y = 13830 z = -441 angle = -620

Specimens

Identifier	Position	Rotation	Stack	Channels

	x = -620
	y = 13830
	z = -435
	angle = -60
		Enabled = False
		Start Angle = 0
		End Angle = 0
		Step Size = 1
		Number Of Steps = 1
			Enabled = True
			First Plane = -510
			Last Plane = -360
			Spacing = 0.645 μm
			Depth = 150 μm
			Number Of Planes = 233
			Center = -435
				Channel 1
				  Enabled = True
				  Wave Length = 488 nm
				  Laser Power = 17.72 mW
				  Filter = 534/30
				  Camera Integration Time = 75 ms
				Channel 2
				  Enabled = True
				  Wave Length = 561 nm
				  Laser Power = 9.27 mW
				  Filter = 607/70
				  Camera Integration Time = 75 ms

Specimen1				

System Information

Detection Lens	Illumination Lens	Camera	Post Processing

Identifier = N-Achroplan
Magnification = 40 x
Numerical Aperture = 0.75
Refractive Index = 1.33
Working Distance = 2.1 mm
	Identifier = Plan-Neofluar
	Magnification = 5
	Numerical Aperture = 0.16
	Refractive Index = 1
	Working Distance = 18.5 mm
		Identifier = Andor Clara
		Binning
		  Hardware Bin Enabled = True
		  Hardware Bin Factor = 2
		  Software Bin Enabled = False
		Format
		  Pixels = 1392 x 1040
		  Bits Per Pixel = 14
		  Pixel Pitch = 6.45 μm
		Roi
		  Hard Roi Enabled = False
		  Soft Roi Enabled = False
		Gain
		  Gain = 1
			Deconvolution
			  Deconvolution Type = None
			  Deconvolution Iterations = 3
			Background
			  Bg Treatment = DoNothing

Lateral root formation - 121114

Metadata of the mDSLM recording in figure 3.26 on page 79

General Information

Date Time	11/14/2012 18:00
Machine Name	MDSLM04-WS
Software Version	5.1.0.0
File Name	121114.TIF

Acquisition Data

Timelapse	Preview Position
Enabled = True Start Time = 11/14/2012 6:00:08 PM Interval = 00:05:00 Total Duration = 2.00:00:00 Repeats = 576	x = -140 y = 13810 z = -343 angle = -140

Specimens

Identifier	Position	Rotation	Stack	Channels

	x = -140
	y = 13810
	z = -343
	angle = 30
		Enabled = False
		Start Angle = 0
		End Angle = 0
		Step Size = 1
		Number Of Steps = 1
			Enabled = True
			First Plane = -418
			Last Plane = -268
			Spacing = 0.645 µm
			Depth = 150 µm
			Number Of Planes = 233
			Center = -343
				Channel 1
				  Enabled = True
				  Wave Length = 488 nm
				  Laser Power = 18.4 mW
				  Filter = 525/50
				  Camera Integration Time = 100 ms
				Channel 2
				  Enabled = True
				  Wave Length = 561 nm
				  Laser Power = 10 mW
				  Filter = 607/70
				  Camera Integration Time = 100 ms

Specimen1				

System Information

Detection Lens	Illumination Lens	Camera	Post Processing

Identifier = N-Achroplan
Magnification = 40 x
Numerical Aperture = 0.75
Refractive Index = 1.33
Working Distance = 2.1 mm
	Identifier = Plan-Neofluar
	Magnification = 5
	Numerical Aperture = 0.16
	Refractive Index = 1
	Working Distance = 18.5 mm
		Identifier = Andor Clara
		Binning
		  Hardware Bin Enabled = True
		  Hardware Bin Factor = 2
		  Software Bin Enabled = False
		Format
		  Pixels = 1392 x 1040
		  Bits Per Pixel = 14
		  Pixel Pitch = 6.45 µm
		Roi
		  Hard Roi Enabled = False
		  Soft Roi Enabled = False
		Gain
		  Gain = 1
			Deconvolution
			  Deconvolution Type = None
			  Deconvolution Iterations = 3
			Background
			  Bg Treatment = SubtractConst

Lateral root formation - 121204

Metadata of the mDSLM recording in figure 3.33 on page 85

General Information

Date Time	12/4/2012 13:21
Machine Name	MDSLM04-WS
Software Version	5.1.0.0
File Name	121204.TIF

Acquisition Data

Timelapse	Preview Position
Enabled = True Start Time = 12/4/2012 1:21:14 PM Interval = 00:05:00 Total Duration = 2.00:01:00 Repeats = 576	x = -1080 y = 13870 z = -165 angle = -1080

Specimens

Identifier	Position	Rotation	Stack	Channels

Specimen1	x = -1080
	y = 13870
	z = -165
	angle = -90
		Enabled = False
		Start Angle = 0
		End Angle = 0
		Step Size = 1
		Number Of Steps = 1
			Enabled = True
			First Plane = -240
			Last Plane = -90
			Spacing = 0.645 μm
			Depth = 150 μm
			Number Of Planes = 233
			Center = -165
				Channel 1
				  Enabled = True
				  Wave Length = 488 nm
				  Laser Power = 18 mW
				  Filter = 525/50
				  Camera Integration Time = 40 ms
				Channel 2
				  Enabled = False
				  Wave Length = 561 nm
				  Laser Power = 9 mW
				  Filter = 607/70
				  Camera Integration Time = 40 ms

Identifier	Position	Rotation	Stack	Channels

561	x = -1080
	y = 13870
	z = -165
	angle = -90
		Enabled = False
		Start Angle = 0
		End Angle = 0
		Step Size = 1
		Number Of Steps = 1
			Enabled = True
			First Plane = -240
			Last Plane = -90
			Spacing = 0.645 μm
			Depth = 150 μm
			Number Of Planes = 233
			Center = -165
				Channel 1
				  Enabled = False
				  Wave Length = 488 nm
				  Laser Power = 18 mW
				  Filter = 525/50
				  Camera Integration Time = 40 ms
				Channel 2
				  Enabled = True
				  Wave Length = 561 nm
				  Laser Power = 12 mW
				  Filter = 607/70
				  Camera Integration Time = 40 ms

System Information

Detection Lens	Illumination Lens	Camera	Post Processing

Identifier = N-Achroplan
Magnification = 40 x
Numerical Aperture = 0.75
Refractive Index = 1.33
Working Distance = 2.1 mm
	Identifier = Plan-Neofluar
	Magnification = 5
	Numerical Aperture = 0.16
	Refractive Index = 1
	Working Distance = 18.5 mm
		Identifier = Andor Clara
		Binning
		  Hardware Bin Enabled = True
		  Hardware Bin Factor = 2
		  Software Bin Enabled = False
		Format
		  Pixels = 1392 x 1040
		  Bits Per Pixel = 14
		  Pixel Pitch = 6.45 μm
		Roi
		  Hard Roi Enabled = False
		  Soft Roi Enabled = False
		Gain
		  Gain = 1
			Deconvolution
			  Deconvolution Type = None
			  Deconvolution Iterations = 3
			Background
			  Bg Treatment = SubtractConst

Lateral root formation - 121211

Metadata of the mDSLM recording in figure 3.34 on page 86

General Information

Date Time	12/11/2012 14:45
Machine Name	MDSLM04-WS
Software Version	5.1.0.0
File Name	121211.TIF

Acquisition Data

Timelapse	Preview Position
Enabled = True	x = -90
Start Time = 12/11/2012 2:45:10 PM	y = 14370
Interval = 00:05:00	z = -539
Total Duration = 2.01:00:01	angle = -90
Repeats = 588	

Specimens

Identifier	Position	Rotation	Stack	Channels

	x = -90
	y = 14370
	z = -539
	angle = -30
		Enabled = False
		Start Angle = 0
		End Angle = 0
		Step Size = 1
		Number Of Steps = 1
			Enabled = True
			First Plane = -614
			Last Plane = -464
			Spacing = 0.645 µm
			Depth = 150 µm
			Number Of Planes = 233
			Center = -539
				Channel 1
				  Enabled = True
				  Wave Length = 488 nm
				  Laser Power = 17.02 mW
				  Filter = 525/50
				  Camera Integration Time = 40 ms
				Channel 2
				  Enabled = False
				  Wave Length = 561 nm
				  Laser Power = 8 mW
				  Filter = 607/70
				  Camera Integration Time = 40 ms

Specimen1				

Identifier	Position	Rotation	Stack	Channels

	x = -90
	y = 14370
	z = -539
	angle = -30
		Enabled = False
		Start Angle = 0
		End Angle = 0
		Step Size = 1
		Number Of Steps = 1
			Enabled = True
			First Plane = -614
			Last Plane = -464
			Spacing = 0.645 µm
			Depth = 150 µm
			Number Of Planes = 233
			Center = -539
				Channel 1
				  Enabled = False
				  Wave Length = 488 nm
				  Laser Power = 17.02 mW
				  Filter = 525/50
				  Camera Integration Time = 40 ms
				Channel 2
				  Enabled = True
				  Wave Length = 561 nm
				  Laser Power = 9 mW
				  Filter = 607/70
				  Camera Integration Time = 40 ms

Specimen2				

System Information

Detection Lens	Illumination Lens	Camera	Post Processing

Identifier = N-Achroplan
Magnification = 40 x
Numerical Aperture = 0.75
Refractive Index = 1.33
Working Distance = 2.1 mm
	Identifier = Plan-Neofluar
	Magnification = 5
	Numerical Aperture = 0.16
	Refractive Index = 1
	Working Distance = 18.5 mm
		Identifier = Andor Clara
		Binning
		  Hardware Bin Enabled = True
		  Hardware Bin Factor = 2
		  Software Bin Enabled = False
		Format
		  Pixels = 1392 x 1040
		  Bits Per Pixel = 14
		  Pixel Pitch = 6.45 µm
		Roi
		  Hard Roi Enabled = False
		  Soft Roi Enabled = False
		Gain
		  Gain = 1
			Deconvolution
			  Deconvolution Type = None
			  Deconvolution Iterations = 3
			Background
			  Bg Treatment = DoNothing

Lateral root formation - 130508

Metadata of the mDSLM recording in figure 3.35 on page 86

General Information

Date Time	5/8/2013 12:25
Machine Name	MDSLM04
Software Version	5.1.0.0
File Name	130508.TIF

Acquisition Data

Timelapse	Preview Position
Enabled = True Start Time = 5/8/2013 12:25:15 PM Interval = 00:05:00 Total Duration = 3.01:00:01 Repeats = 876	x = -340 y = 13770 z = -383 angle = -340

Specimens

Identifier	Position	Rotation	Stack	Channels

Specimen1	x = -340
	y = 13770
	z = -383
	angle = 25
		Enabled = False
		Start Angle = 0
		End Angle = 0
		Step Size = 1
		Number Of Steps = 1
			Enabled = True
			First Plane = -458
			Last Plane = -308
			Spacing = 0.645 μm
			Depth = 150 μm
			Number Of Planes = 233
			Center = -383
				Channel 1
				  Enabled = True
				  Wave Length = 488 nm
				  Laser Power = 22 mW
				  Filter = 534/30
				  Camera Integration Time = 30 ms
				Channel 2
				  Enabled = False
				  Wave Length = 561 nm
				  Laser Power = 9 mW
				  Filter = 607/70
				  Camera Integration Time = 30 ms

Identifier	Position	Rotation	Stack	Channels

Specimen2	x = -340
	y = 13770
	z = -383
	angle = 25
		Enabled = False
		Start Angle = 0
		End Angle = 0
		Step Size = 1
		Number Of Steps = 1
			Enabled = True
			First Plane = -458
			Last Plane = -308
			Spacing = 0.645 μm
			Depth = 150 μm
			Number Of Planes = 233
			Center = -383
				Channel 1
				  Enabled = False
				  Wave Length = 488 nm
				  Laser Power = 22 mW
				  Filter = 534/30
				  Camera Integration Time = 30 ms
				Channel 2
				  Enabled = True
				  Wave Length = 561 nm
				  Laser Power = 9 mW
				  Filter = 607/70
				  Camera Integration Time = 30 ms

System Information

Detection Lens	Illumination Lens	Camera	Post Processing

Identifier = N-Achroplan
Magnification = 40 x
Numerical Aperture = 0.75
Refractive Index = 1.33
Working Distance = 2.1 mm
	Identifier = Plan-Neofluar
	Magnification = 5
	Numerical Aperture = 0.16
	Refractive Index = 1
	Working Distance = 18.5 mm
		Identifier = Andor Clara
		Binning
		  Hardware Bin Enabled = True
		  Hardware Bin Factor = 2
		  Software Bin Enabled = False
		Format
		  Pixels = 1392 x 1040
		  Bits Per Pixel = 14
		  Pixel Pitch = 6.45 μm
		Roi
		  Hard Roi Enabled = False
		  Soft Roi Enabled = False
		Gain
		  Gain = 1
			Deconvolution
			  Deconvolution Type = None
			  Deconvolution Iterations = 3
			Background
			  Bg Treatment = DoNothing

Lateral root formation - 130607

Metadata of the mDSLM recording in figure 3.36 on page 87

General Information

Date Time	6/7/2013 14:57
Machine Name	MDSLM04
Software Version	5.1.0.0
File Name	130607.TIF

Acquisition Data

Timelapse	Preview Position
Enabled = True	x = -30
Start Time = 6/7/2013 2:57:50 PM	y = 13990
Interval = 00:05:00	z = -570
Total Duration = 4.01:01:00	angle = -30
Repeats = 1164	

Specimens

Identifier	Position	Rotation	Stack	Channels

	x = -30
	y = 13990
	z = -570
	angle = 0
		Enabled = False
		Start Angle = 0
		End Angle = 0
		Step Size = 1
		Number Of Steps = 1
			Enabled = True
			First Plane = -645
			Last Plane = -495
			Spacing = 0.645 µm
			Depth = 150 µm
			Number Of Planes = 233
			Center = -570
				Channel 1
				  Enabled = True
				  Wave Length = 488 nm
				  Laser Power = 22 mW
				  Filter = 525/50
				  Camera Integration Time = 30 ms
				Channel 2
				  Enabled = False
				  Wave Length = 561 nm
				  Laser Power = 15 mW
				  Filter = 607/70
				  Camera Integration Time = 30 ms

Specimen1				
Identifier	Position	Rotation	Stack	Channels

	x = -30
	y = 13990
	z = -570
	angle = 0
		Enabled = False
		Start Angle = 0
		End Angle = 0
		Step Size = 1
		Number Of Steps = 1
			Enabled = True
			First Plane = -645
			Last Plane = -495
			Spacing = 0.645 µm
			Depth = 150 µm
			Number Of Planes = 233
			Center = -570
				Channel 1
				  Enabled = False
				  Wave Length = 488 nm
				  Laser Power = 22 mW
				  Filter = 525/50
				  Camera Integration Time = 30 ms
				Channel 2
				  Enabled = True
				  Wave Length = 561 nm
				  Laser Power = 15 mW
				  Filter = 607/70
				  Camera Integration Time = 30 ms

Specimen2				

System Information

Detection Lens	Illumination Lens	Camera	Post Processing

Identifier = N-Achroplan
Magnification = 40 x
Numerical Aperture = 0.75
Refractive Index = 1.33
Working Distance = 2.1 mm
	Identifier = Plan-Neofluar
	Magnification = 5
	Numerical Aperture = 0.16
	Refractive Index = 1
	Working Distance = 18.5 mm
		Identifier = Andor Clara
		Binning
		  Hardware Bin Enabled = True
		  Hardware Bin Factor = 2
		  Software Bin Enabled = False
		Format
		  Pixels = 1392 x 1040
		  Bits Per Pixel = 14
		  Pixel Pitch = 6.45 µm
		Roi
		  Hard Roi Enabled = False
		  Soft Roi Enabled = False
		Gain
		  Gain = 1
			Deconvolution
			  Deconvolution Type = None
			  Deconvolution Iterations = 3
			Background
			  Bg Treatment = DoNothing

Lateral root formation - 131203

Metadata of the mDSLM recording in figure 3.57 on page 108

General Information

Date Time	12/3/2013 12:36
Machine Name	MDSLM04
Software Version	5.1.0.0
File Name	131203.TIF

Acquisition Data

Timelapse	Preview Position
Enabled = True	x = -320
Start Time = 12/3/2013 12:36:50 PM	y = 12820
Interval = 00:05:00	z = -180
Total Duration = 3.00:01:00	angle = -320
Repeats = 864	

Specimens

Identifier	Position	Rotation	Stack	Channels
	x = -320 y = 12820 z = -180 angle = 30	Enabled = False Start Angle = 0 End Angle = 0 Step Size = 1 Number Of Steps = 1	Enabled = True First Plane = -255 Last Plane = -105 Spacing = 0.645 µm Depth = 150 µm Number Of Planes = 233 Center = -180	Channel 1 Enabled = True Wave Length = 488 nm Laser Power = 18.4 mW Filter = 525/45 Camera Integration Time = 40 ms Channel 2 Enabled = False Wave Length = 561 nm Laser Power = 6 mW Filter = 607/70 Camera Integration Time = 40 ms
Specimen1				
Identifier	Position	Rotation	Stack	Channels
	x = -320 y = 12820 z = -180 angle = 30	Enabled = False Start Angle = 0 End Angle = 0 Step Size = 1 Number Of Steps = 1	Enabled = True First Plane = -255 Last Plane = -105 Spacing = 0.645 µm Depth = 150 µm Number Of Planes = 233 Center = -180	Channel 1 Enabled = False Wave Length = 488 nm Laser Power = 18.4 mW Filter = 525/45 Camera Integration Time = 40 ms Channel 2 Enabled = True Wave Length = 561 nm Laser Power = 6 mW Filter = 607/70 Camera Integration Time = 40 ms
Specimen2				

System Information

Detection Lens	Illumination Lens	Camera	Post Processing
Identifier = N-Achroplan Magnification = 40 x Numerical Aperture = 0.75 Refractive Index = 1.33 Working Distance = 2.1 mm	Identifier = Plan-Neofluar Magnification = 5 Numerical Aperture = 0.16 Refractive Index = 1 Working Distance = 18.5 mm	Identifier = Andor Clara Binning Hardware Bin Enabled = True Hardware Bin Factor = 2 Software Bin Enabled = False Format Pixels = 1392 x 1040 Bits Per Pixel = 14 Pixel Pitch = 6.45 µm Roi Hard Roi Enabled = False Soft Roi Enabled = False Gain Gain = 1	Deconvolution Deconvolution Type = None Deconvolution Iterations = 3 Background Bg Treatment = DoNothing

Gravitropic set-point angle formation - 110411

Metadata of the mDSLM recording in figure 3.7 on page 60

General Information

Date Time	4/11/2011 19:15
Machine Name	WS-STELZER-025
Software Version	0.3.1.0
File Name	110411.TIF

Acquisition Data

Timelapse	Preview Position
Enabled = True	x = 50
Start Time = 4/11/2011 7:15:12 PM	y = 12300
Interval = 00:15:00	z = 500
Total Duration = 4.00:01:00	angle = 50
Repeats = 384	

Specimens

Identifier	Position	Rotation	Stack	Channels
	x = 50	Enabled = False	Enabled = True	Channel 1
	y = 12400	Start Angle = 0	First Plane = 400	Enabled = True
	z = 500	End Angle = 0	Last Plane = 700	Wave Length = 488 nm
	angle = 120	Step Size = 1	Spacing = 1.29 µm	Laser Power = mW
		Number Of Steps = 1	Depth = 300 µm	Filter = 525/50
			Number Of Planes = 233	Camera Integration Time = 50 ms
			Center = 550	Channel 2
				Enabled = True
				Wave Length = 594 nm
				Laser Power = mW
				Filter = 628/40
Specimen 1				Camera Integration Time = 50 ms

System Information

Detection Lens	Illumination Lens	Camera	Post Processing
Identifier = N-Achroplan	Identifier = Plan-Neofluar	Identifier =	Deconvolution
Magnification = 20 x	Magnification = 5	Binning	Deconvolution Type = None
Numerical Aperture = 0.5	Numerical Aperture = 0.16	Hardware Bin Enabled = False	Deconvolution Iterations = 3
Refractive Index = 1.33	Refractive Index = 1	Hardware Bin Factor = 2	Background
Working Distance = 2.6 mm	Working Distance = 18.5 mm	Software Bin Enabled = False	Bg Treatment = SubtractConst
		Format	
		Pixels = 1392 x 1040	
		Bits Per Pixel = 14	
		Pixel Pitch = 6.45 µm	
		Roi	
		Hard Roi Enabled = False	
		Soft Roi Enabled = False	
		Gain	
		Gain = 1	

Gravitropic set-point angle formation - 120924

Metadata of the mDSLM recording in figure 3.8 on page 61

General Information

Date Time	9/24/2012 15:05
Machine Name	MDSLM04-WS
Software Version	5.1.0.0
File Name	20x_120924.TIF

Acquisition Data

Timelapse	Preview Position
Enabled = True	x = 610
Start Time = 9/24/2012 3:04:59 PM	y = 12670
Interval = 00:10:00	z = -570
Total Duration = 2.01:01:00	angle = 610
Repeats = 294	

Specimens

Identifier	Position	Rotation	Stack	Channels
	x = 610	Enabled = False	Enabled = True	Channel 1
	y = 12670	Start Angle = 0	First Plane = -770	Enabled = True
	z = -670	End Angle = 0	Last Plane = -570	Wave Length = 561 nm
	angle = -40	Step Size = 1	Spacing = 1.29 µm	Laser Power = 9.55 mW
		Number Of Steps = 1	Depth = 200 µm	Filter = 607/70
			Number Of Planes = 156	Camera Integration Time = 75 ms
			Center = -670	Channel 2
				Enabled = False
				Wave Length = 760 nm
				Laser Power = 0 mW
				Filter = Empty
Specimen1				Camera Integration Time = 100 ms

System Information

Detection Lens	Illumination Lens	Camera	Post Processing
Identifier = N-Achroplan	Identifier = Epiplan-Neofluar	Identifier = Andor Clara	Deconvolution
Magnification = 20 x	Magnification = 2.5	Binning	Deconvolution Type = None
Numerical Aperture = 0.5	Numerical Aperture = 0.06	Hardware Bin Enabled = False	Deconvolution Iterations = 3
Refractive Index = 1.33	Refractive Index = 1	Hardware Bin Factor = 2	Background
Working Distance = 2.6 mm	Working Distance = 15.1 mm	Software Bin Enabled = False	Bg Treatment = SubtractConst
		Format	
		Pixels = 1392 x 1040	
		Bits Per Pixel = 14	
		Pixel Pitch = 6.45 µm	
		Roi	
		Hard Roi Enabled = False	
		Soft Roi Enabled = False	
		Gain	
		Gain = 1	

Gravitropic set-point angle formation - 121116

Metadata of the mDSLM recording in figure 3.8 on page 61

General Information

Date Time	11/16/2012 15:55
Machine Name	MDSLM04-WS
Software Version	5.1.0.0
File Name	121116.TIF

Acquisition Data

Timelapse	Preview Position
Enabled = True Start Time = 11/16/2012 3:55:34 PM Interval = 00:10:00 Total Duration = 2.00:00:00 Repeats = 288	x = -600 y = 13470 z = 110 angle = -600

Specimens

Identifier	Position	Rotation	Stack	Channels

	x = -600
	y = 13470
	z = 110
	angle = -20
		Enabled = False
		Start Angle = 0
		End Angle = 0
		Step Size = 1
		Number Of Steps = 1
			Enabled = True
			First Plane = 10
			Last Plane = 210
			Spacing = 1.29 µm
			Depth = 200 µm
			Number Of Planes = 156
			Center = 110
				Channel 1
				  Enabled = False
				  Wave Length = 760 nm
				  Laser Power = 0 mW
				  Filter = Empty
				  Camera Integration Time = 100 ms
				Channel 2
				  Enabled = True
				  Wave Length = 561 nm
				  Laser Power = 10 mW
				  Filter = 607/70
				  Camera Integration Time = 50 ms
				Channel 3
				  Enabled = False
				  Wave Length = 760 nm
				  Laser Power = 0 mW
				  Filter = Empty
				  Camera Integration Time = 100 ms

Specimen1				

System Information

Detection Lens	Illumination Lens	Camera	Post Processing

Identifier=N-Achroplan
Magnification=20
NumericalAperture=0.5
RefractiveIndex=1.33
FreeWorkingDistance=2.6
	Identifier = Epiplan-Neofluar
	Magnification = 2.5
	Numerical Aperture = 0.06
	Refractive Index = 1
	Working Distance = 15.1 mm
		Identifier = Andor Clara
		Binning
		  Hardware Bin Enabled = True
		  Hardware Bin Factor = 2
		  Software Bin Enabled = False
		Format
		  Pixels = 1392 x 1040
		  Bits Per Pixel = 14
		  Pixel Pitch = 6.45 µm
		Roi
		  Hard Roi Enabled = False
		  Soft Roi Enabled = False
		Gain
		  Gain = 1
			Deconvolution
			  Deconvolution Type = None
			  Deconvolution Iterations = 3
			Background
			  Bg Treatment = SubtractConst

Lateral shape Analysis - 111017

Metadata of the mDSLM recording in figure 3.29 on page 82

General Information

Date Time	10/17/2011 11:12
Machine Name	WS-STELZER-025
Software Version	0.3.5.5
File Name	111017.TIF

Acquisition Data

Timelapse	Preview Position
Enabled = True Start Time = 10/17/2011 11:12:18 AM Interval = 00:30:00 Total Duration = 3.00:01:00 Repeats = 144	x = 800 y = 14000 z = 75 angle = 800

Specimens

Identifier	Position	Rotation	Stack	Channels

	x = 800
	y = 14000
	z = 75
	angle = 10
		Enabled = False
		Start Angle = 0
		End Angle = 0
		Step Size = 1
		Number Of Steps = 1
			Enabled = True
			First Plane = -50
			Last Plane = 200
			Spacing = 1.29 µm
			Depth = 250 µm
			Number Of Planes = 194
			Center = 75
				Channel 1
				  Enabled = True
				  Wave Length = 488 nm
				  Laser Power = 0.75 mW
				  Filter = 525/50
				  Camera Integration Time = 100 ms
				Channel 2
				  Enabled = True
				  Wave Length = 594 nm
				  Laser Power = 5 mW
				  Filter = 628/40

Specimen 1				Camera Integration Time = 100 ms
Identifier	**Position**	**Rotation**	**Stack**	**Channels**

	x = 890
	y = 13240
	z = 110
	angle = 10
		Enabled = False
		Start Angle = 0
		End Angle = 0
		Step Size = 1
		Number Of Steps = 1
			Enabled = False
			First Plane = -10
			Last Plane = 240
			Spacing = 1.29 µm
			Depth = 250 µm
			Number Of Planes = 194
			Center = 115
				Channel 1
				  Enabled = True
				  Wave Length = 488 nm
				  Laser Power = 0.75 mW
				  Filter = 525/50
				  Camera Integration Time = 100 ms
				Channel 2
				  Enabled = True
				  Wave Length = 594 nm
				  Laser Power = 5 mW
				  Filter = 628/40

2				Camera Integration Time = 100 ms

System Information

Detection Lens	Illumination Lens	Camera	Post Processing

Identifier = N-Achroplan
Magnification = 20 x
Numerical Aperture = 0.5
Refractive Index = 1.33
Working Distance = 2.6 mm
	Identifier = Plan-Neofluar
	Magnification = 5
	Numerical Aperture = 0.16
	Refractive Index = 1
	Working Distance = 18.5 mm
		Identifier = Andor Clara
		Binning
		  Hardware Bin Enabled = False
		  Hardware Bin Factor = 2
		  Software Bin Enabled = False
		Format
		  Pixels = 1392 x 1040
		  Bits Per Pixel = 14
		  Pixel Pitch = 6.45 µm
		Roi
		  Hard Roi Enabled = False
		  Soft Roi Enabled = False
		Gain
		  Gain = 1.5
			Deconvolution
			  Deconvolution Type = None
			  Deconvolution Iterations = 3
			Background
			  Bg Treatment = SubtractConst

Lateral shape Analysis - 111114

Metadata of the mDSLM recording in figure 2.15 on page 36 and figure 3.28 on page 81

General Information

Date Time	11/14/2011 11:23
Machine Name	WS-STELZER-025
Software Version	0.3.6.0
File Name	111114.TIF

Acquisition Data

Timelapse	Preview Position
Enabled = True Start Time = 11/14/2011 11:23:00 AM Interval = 00:15:00 Total Duration = 5.00:10:00 Repeats = 480	x = 970 y = 12620 z = -60 angle = 970

Specimens

Identifier	Position	Rotation	Stack	Channels

Specimen1	x = 170
	y = 12620
	z = -560
	angle = 30
		Enabled = False
		Start Angle = 0
		End Angle = 0
		Step Size = 1
		Number Of Steps = 1
			Enabled = True
			First Plane = -710
			Last Plane = -410
			Spacing = 1.29 µm
			Depth = 300 µm
			Number Of Planes = 233
			Center = -560
				Channel 1
				  Enabled = True
				  Wave Length = 488 nm
				  Laser Power = 0.7 mW
				  Filter = 525/50
				  Camera Integration Time = 100 ms
				Channel 2
				  Enabled = True
				  Wave Length = 594 nm
				  Laser Power = 5 mW
				  Filter = 628/40
				  Camera Integration Time = 100 ms

Identifier	Position	Rotation	Stack	Channels

	x = 970
	y = 12620
	z = -60
	angle = 75
		Enabled = False
		Start Angle = 0
		End Angle = 0
		Step Size = 1
		Number Of Steps = 1
			Enabled = True
			First Plane = -210
			Last Plane = 90
			Spacing = 1.29 µm
			Depth = 300 µm
			Number Of Planes = 233
			Center = -60
				Channel 1
				  Enabled = True
				  Wave Length = 488 nm
				  Laser Power = 0.7 mW
				  Filter = 525/50
				  Camera Integration Time = 100 ms
				Channel 2
				  Enabled = True
				  Wave Length = 594 nm
				  Laser Power = 5 mW
				  Filter = 628/40
				  Camera Integration Time = 100 ms

System Information

Detection Lens	Illumination Lens	Camera	Post Processing

Identifier = N-Achroplan
Magnification = 20 x
Numerical Aperture = 0.5
Refractive Index = 1.33
Working Distance = 2.6 mm
	Identifier = Plan-Neofluar
	Magnification = 5
	Numerical Aperture = 0.16
	Refractive Index = 1
	Working Distance = 18.5 mm
		Identifier = Andor Clara
		Binning
		  Hardware Bin Enabled = False
		  Hardware Bin Factor = 2
		  Software Bin Enabled = False
		Format
		  Pixels = 1392 x 1040
		  Bits Per Pixel = 14
		  Pixel Pitch = 6.45 µm
		Roi
		  Hard Roi Enabled = False
		  Soft Roi Enabled = False
		Gain
		  Gain = 1.5
			Deconvolution
			  Deconvolution Type = None
			  Deconvolution Iterations = 3
			Background
			  Bg Treatment = SubtractConst

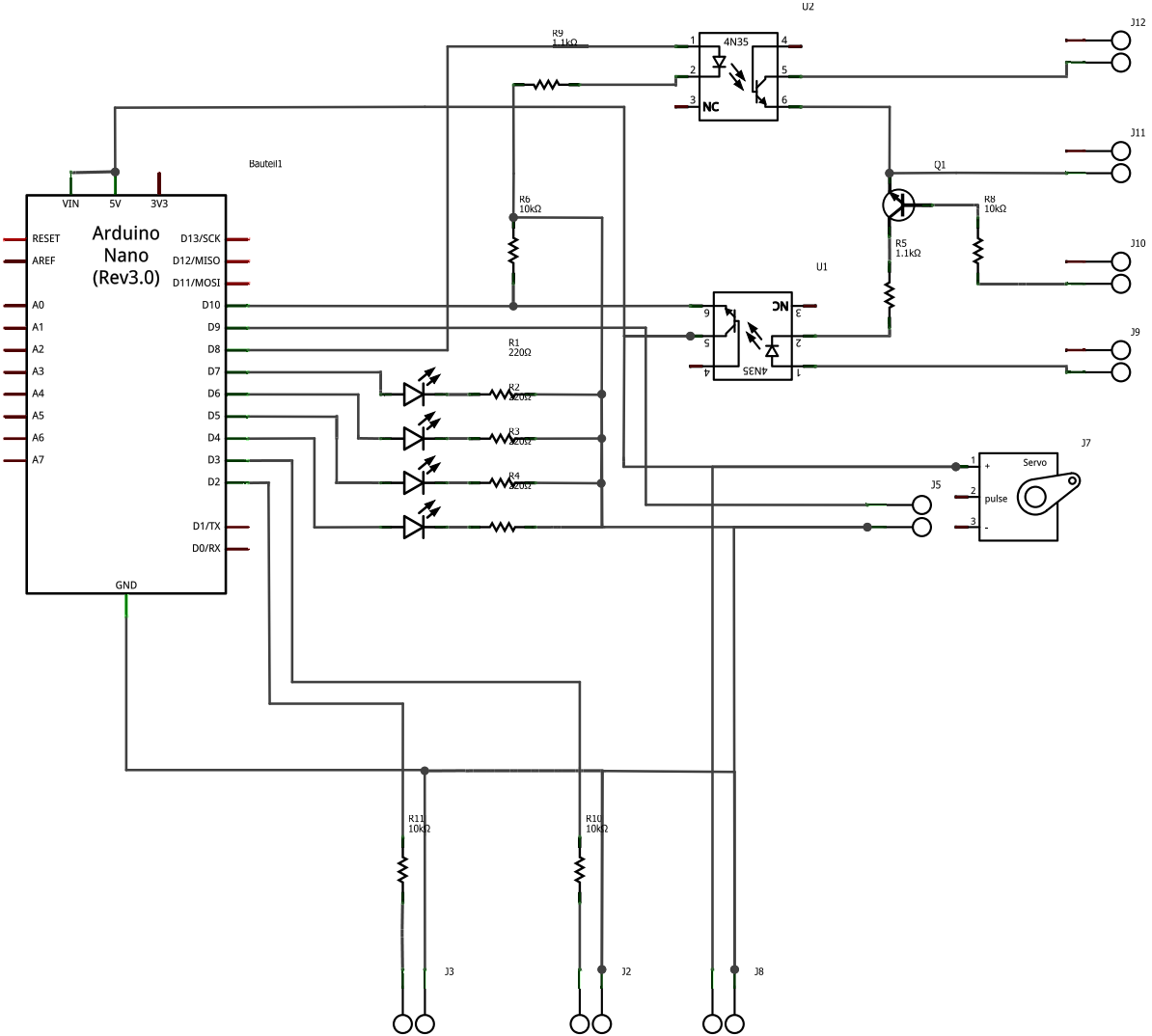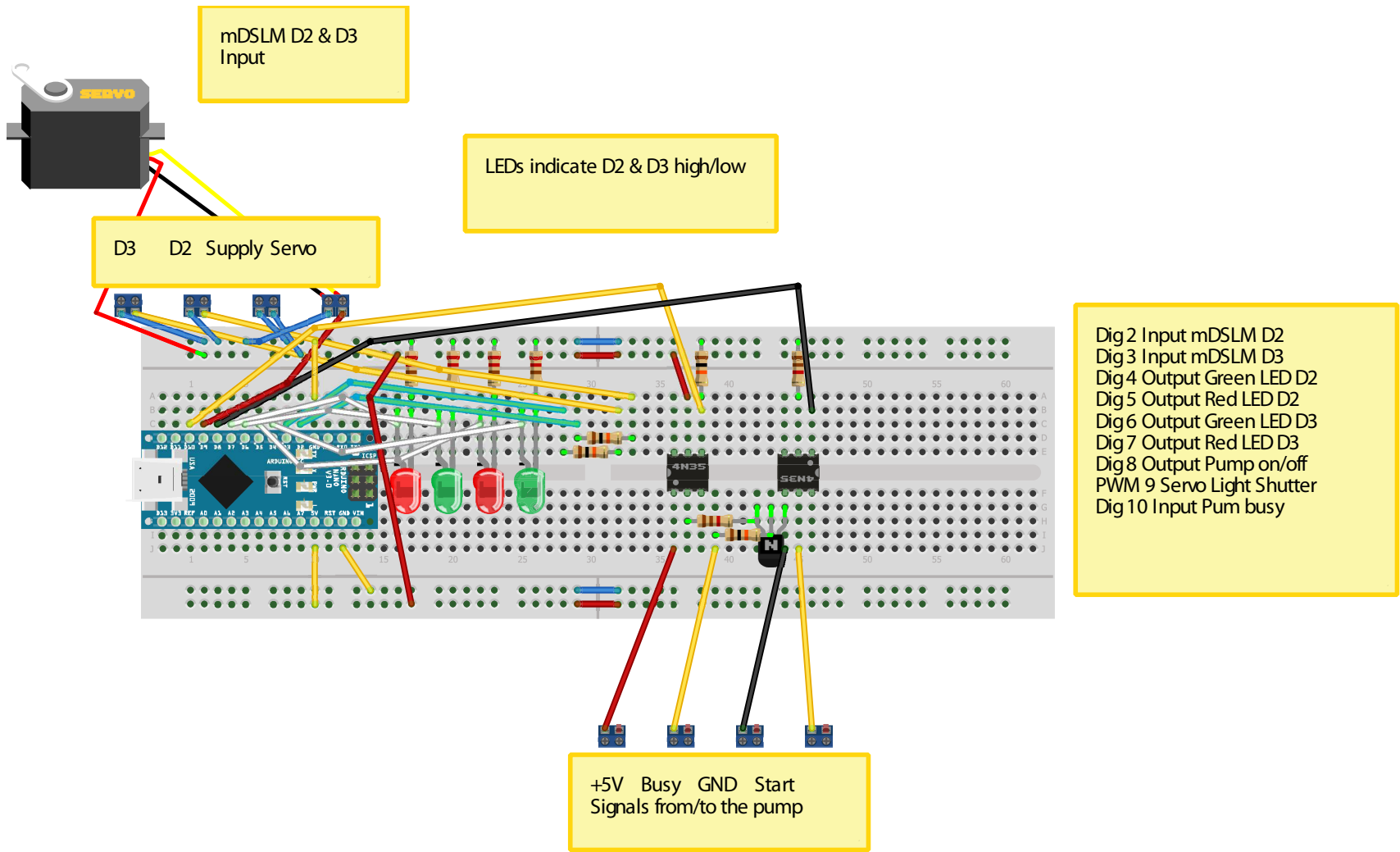# Lateral shape Analysis - 111115

Metadata of the mDSLM recording in figure 3.28 on page 81

General Information

Date Time	11/15/2011 18:20
Machine Name	WS-STELZER-025
Software Version	0.3.6.0
File Name	111115.TIF

Acquisition Data

Timelapse	Preview Position
Enabled = True	x = 240
Start Time = 11/15/2011 6:20:35 PM	y = 12540
Interval = 00:15:00	z = 624
Total Duration = 3.00:01:00	angle = 240
Repeats = 288	

Specimens

Identifier	Position	Rotation	Stack	Channels
	x = 240	Enabled = False	Enabled = True	Channel 1
	y = 12540	Start Angle = 0	First Plane = 524	Enabled = True
	z = 624	End Angle = 0	Last Plane = 724	Wave Length = 488 nm
	angle = 80	Step Size = 1	Spacing = 1.29 µm	Laser Power = 0.8 mW
		Number Of Steps = 1	Depth = 200 µm	Filter = 525/50
			Number Of Planes = 156	Camera Integration Time = 100 ms
			Center = 624	Channel 2
				Enabled = True
				Wave Length = 594 nm
				Laser Power = 10 mW
				Filter = 628/40
Specimen1				Camera Integration Time = 100 ms
Identifier	Position	Rotation	Stack	Channels
	x = 130	Enabled = False	Enabled = True	same as Specimen1
	y = 12540	Start Angle = 0	First Plane = 317	
	z = 417	End Angle = 0	Last Plane = 517	
	angle = 35	Step Size = 1	Spacing = 1.29 µm	
		Number Of Steps = 1	Depth = 200 µm	
			Number Of Planes = 156	
Specimen2			Center = 417	
Identifier	Position	Rotation	Stack	Channels
	x = -130	Enabled = False	Enabled = True	same as Specimen1
	y = 12540	Start Angle = 0	First Plane = 277	
	z = 377	End Angle = 0	Last Plane = 477	
	angle = -10	Step Size = 1	Spacing = 1.29 µm	
		Number Of Steps = 1	Depth = 200 µm	
			Number Of Planes = 156	
Specimen3			Center = 377	

System Information

Detection Lens	Illumination Lens	Camera	Post Processing
Identifier = N-Achroplan	Identifier = Plan-Neofluar	Identifier = Andor Clara	Deconvolution
Magnification = 20 x	Magnification = 5	Binning	Deconvolution Type = None
Numerical Aperture = 0.5	Numerical Aperture = 0.16	Hardware Bin Enabled = False	Deconvolution Iterations = 3
Refractive Index = 1.33	Refractive Index = 1	Hardware Bin Factor = 2	Background
Working Distance = 2.6 mm	Working Distance = 18.5 mm	Software Bin Enabled = False	Bg Treatment = SubtractConst
		Format	
		Pixels = 1392 x 1040	
		Bits Per Pixel = 14	
		Pixel Pitch = 6.45 µm	
		Roi	
		Hard Roi Enabled = False	
		Soft Roi Enabled = False	
		Gain	
		Gain = 1.5	

Lateral shape Analysis - 111208

Metadata of the mDSLM recording in figure 3.27 on page 80

General Information

Date Time	12/8/2011 16:56
Machine Name	WS-STELZER-025
Software Version	0.3.6.0
File Name	111208.TIF

Acquisition Data

Timelapse	Preview Position
Enabled = True Start Time = 12/8/2011 4:56:44 PM Interval = 00:07:30 Total Duration = 2.00:01:00 Repeats = 384	x = 340 y = 11250 z = -300 angle = 340

Specimens

Identifier	Position	Rotation	Stack	Channels

	x = 340
	y = 11250
	z = -400
	angle = 0
		Enabled = False
		Start Angle = 0
		End Angle = 0
		Step Size = 1
		Number Of Steps = 1
			Enabled = True
			First Plane = -500
			Last Plane = -300
			Spacing = 0.645 µm
			Depth = 200 µm
			Number Of Planes = 311
			Center = -400
				Channel 1
				  Enabled = False
				  Wave Length = 488 nm
				  Laser Power = 2.38 mW
				  Filter = 525/50
				  Camera Integration Time = 100 ms
				Channel 2
				  Enabled = True
				  Wave Length = 594 nm
				  Laser Power = 7 mW
				  Filter = 628/40
				  Camera Integration Time = 50 ms

Specimen1				

System Information

Detection Lens	Illumination Lens	Camera	Post Processing

Identifier = N-Achroplan
Magnification = 40 x
Numerical Aperture = 0.75
Refractive Index = 1.33
Working Distance = 2.1 mm
	Identifier = Plan-Neofluar
	Magnification = 5
	Numerical Aperture = 0.16
	Refractive Index = 1
	Working Distance = 18.5 mm
		Identifier = Andor Clara
		Binning
		  Hardware Bin Enabled = False
		  Hardware Bin Factor = 2
		  Software Bin Enabled = False
		Format
		  Pixels = 1392 x 1040
		  Bits Per Pixel = 14
		  Pixel Pitch = 6.45 µm
		Roi
		  Hard Roi Enabled = False
		  Soft Roi Enabled = False
		Gain
		  Gain = 1
			Deconvolution
			  Deconvolution Type = None
			  Deconvolution Iterations = 3
			Background
			  Bg Treatment = SubtractConst

PIN1 wild type - 120413

Metadata of the mDSLM recording and diagram 3.30 on page 82

General Information

Date Time	4/13/2012 16:56
Machine Name	MDSLM05-WS
Software Version	4.9.0.0
File Name	120413.TIF

Acquisition Data

Timelapse	Preview Position
Enabled = True	x = 20
Start Time = 4/13/2012 4:56:47 PM	y = 12030
Interval = 00:07:30	z = -520
Total Duration = 3.03:00:01	angle = 20
Repeats = 600	

Specimens

Identifier	Position	Rotation	Stack	Channels
	x = 20	Enabled = False	Enabled = True	Channel 1
	y = 12030	Start Angle = 0	First Plane = -770	Enabled = True
	z = -645	End Angle = 0	Last Plane = -520	Wave Length = 488 nm
	angle = -70	Step Size = 1	Spacing = 0.645 µm	Laser Power = 2.4 mW
		Number Of Steps = 1	Depth = 250 µm	Filter = 525/50
			Number Of Planes = 388	Camera Integration Time = 100 ms
			Center = -645	Channel 2
				Enabled = False
				Wave Length = 760 nm
				Laser Power = 0 mW
				Filter = 488LP
Specimen1				Camera Integration Time = 100 ms

System Information

Detection Lens	Illumination Lens	Camera	Post Processing
Identifier = N-Achroplan	Identifier = Plan-Neofluar	Identifier = Andor Clara	Deconvolution
Magnification = 40 x	Magnification = 5	Binning	Deconvolution Type = None
Numerical Aperture = 0.75	Numerical Aperture = 0.16	Hardware Bin Enabled = True	Deconvolution Iterations = 3
Refractive Index = 1.33	Refractive Index = 1	Hardware Bin Factor = 2	Background
Working Distance = 2.1 mm	Working Distance = 18.5 mm	Software Bin Enabled = False	Bg Treatment = DoNothing
		Format	
		Pixels = 1392 x 1040	
		Bits Per Pixel = 14	
		Pixel Pitch = 6.45 µm	
		Roi	
		Hard Roi Enabled = False	
		Soft Roi Enabled = False	
		Gain	
		Gain = 1	

PIN1 aur1-2;2-2 - 120319

Metadata of the mDSLM recording in figure 3.30 on page 82

General Information

Date Time	3/19/2012 14:58
Machine Name	MDSLM05-WS
Software Version	4.8.2.0
File Name	120319.TIF

Acquisition Data

Timelapse	Preview Position
Enabled = True Start Time = 3/19/2012 2:58:34 PM Interval = 00:07:30 Total Duration = 2.00:01:00 Repeats = 384	x = -340 y = 12290 z = 613 angle = -340

Specimens

Identifier	Position	Rotation	Stack	Channels

Specimen1	x = -340
	y = 12290
	z = 622
	angle = 40
		Enabled = False
		Start Angle = 0
		End Angle = 0
		Step Size = 1
		Number Of Steps = 1
			Enabled = True
			First Plane = 547
			Last Plane = 697
			Spacing = 0.645 µm
			Depth = 150 µm
			Number Of Planes = 233
			Center = 622
				Channel 1
				  Enabled = True
				  Wave Length = 488 nm
				  Laser Power = 2.33 mW
				  Filter = 525/50
				  Camera Integration Time = 50 ms

System Information

Detection Lens	Illumination Lens	Camera	Post Processing

Identifier = N-Achroplan
Magnification = 40 x
Numerical Aperture = 0.75
Refractive Index = 1.33
Working Distance = 2.1 mm
	Identifier = Plan-Neofluar
	Magnification = 5
	Numerical Aperture = 0.16
	Refractive Index = 1
	Working Distance = 18.5 mm
		Identifier = Andor Clara
		Binning
		  Hardware Bin Enabled = True
		  Hardware Bin Factor = 2
		  Software Bin Enabled = False
		Format
		  Pixels = 1392 x 1040
		  Bits Per Pixel = 14
		  Pixel Pitch = 6.45 µm
		Roi
		  Hard Roi Enabled = False
		  Soft Roi Enabled = False
		Gain
		  Gain = 1
			Deconvolution
			  Deconvolution Type = None
			  Deconvolution Iterations = 3
			Background
			  Bg Treatment = DoNothing

Adventitious root emergence - 130424

Metadata of the mDSLM recording in figure 3.1.6 on page 76

General Information

Date Time	4/24/2013 8:50
Machine Name	MDSLM04
Software Version	5.1.0.0
File Name	130424.TIF

Acquisition Data

Timelapse	Preview Position
Enabled = True	x = 2000
Start Time = 4/24/2013 8:50:20 AM	y = 12895
Interval = 00:15:00	z = -1800
Total Duration = 2.01:01:00	angle = 2000
Repeats = 196	

Specimens

Identifier	Position	Rotation	Stack	Channels
	x = 1945	Enabled = False	Enabled = True	Channel 1
	y = 13070	Start Angle = 0	First Plane = -2000	Enabled = True
	z = -1762.5	End Angle = 0	Last Plane = -1525	Wave Length = 561 nm
	angle = -100	Step Size = 1	Spacing = 2.58 μm	Laser Power = 10 mW
		Number Of Steps = 1	Depth = 475 μm	Filter = 607/70
			Number Of Planes = 185	Camera Integration Time = 50 ms
			Center = -1762.5	
Specimen1				

Identifier	Position	Rotation	Stack	Channels
	x = 2000	Enabled = False	Enabled = True	Channel 1
	y = 13070	Start Angle = 0	First Plane = -2000	Enabled = True
	z = -1737.5	End Angle = 0	Last Plane = -1475	Wave Length = 561 nm
	angle = -185	Step Size = 1	Spacing = 2.58 μm	Laser Power = 10 mW
		Number Of Steps = 1	Depth = 525 μm	Filter = 607/70
			Number Of Planes = 204	Camera Integration Time = 50 ms
			Center = -1737.5	
Specimen2				

Identifier	Position	Rotation	Stack	Channels
	x = 2000	Enabled = False	Enabled = True	Channel 1
	y = 12895	Start Angle = 0	First Plane = -2000	Enabled = True
	z = -1800	End Angle = 0	Last Plane = -1600	Wave Length = 561 nm
	angle = -63	Step Size = 1	Spacing = 2.58 μm	Laser Power = 10 mW
		Number Of Steps = 1	Depth = 400 μm	Filter = 607/70
			Number Of Planes = 156	Camera Integration Time = 50 ms
			Center = -1800	
Specimen3				

System Information

Detection Lens	Illumination Lens	Camera	Post Processing
Identifier = N-Achroplan	Identifier = Epiplan-Neofluar	Identifier = Andor Clara	Deconvolution
Magnification = 10 x	Magnification = 2.5	Binning	Deconvolution Type = None
Numerical Aperture = 0.3	Numerical Aperture = 0.06	Hardware Bin Enabled = False	Deconvolution Iterations = 3
Refractive Index = 1.33	Refractive Index = 1	Hardware Bin Factor = 2	Background
Working Distance = 2.6 mm	Working Distance = 15.1 mm	Software Bin Enabled = False	Bg Treatment = SubtractConst
		Format	
		Pixels = 1392 x 1040	
		Bits Per Pixel = 14	
		Pixel Pitch = 6.45 μm	
		Roi	
		Hard Roi Enabled = False	
		Soft Roi Enabled = False	
		Gain	
		Gain = 1	

Arduino plant illumination control

Figure 5.17: Arduino plant illumination schematic circuit diagram.

mDSLM D2 & D3
Input

LEDs indicate D2 & D3 high/low

D3   D2   Supply Servo

Dig 2 Input mDSLM D2
Dig 3 Input mDSLM D3
Dig 4 Output Green LED D2
Dig 5 Output Red LED D2
Dig 6 Output Green LED D3
Dig 7 Output Red LED D3
Dig 8 Output Pump on/off
PWM 9 Servo Light Shutter
Dig 10 Input Pum busy

+5V   Busy GND   Start
Signals from/to the pump

Figure 5.18: Arduino plant illumination plugin chart.

Made with Fritzing.org

```
/*
  DSLMPumpLightControl

 Responds to the output of the digital mDSLM signals D2 & D3
 Switches light on/off by moving a metal plate attached to a servo motor
 Reads the busy flag of a peristaltic pump and toggles the pump on/off if necessary
 Current status is indicated by green/red LED pairs

Designed for Arduino Mega 2560

 Sven Plath / Ernst H.K. Stelzer, GU Ffm, July 2013
 */

#include <Servo.h>
Servo myservo;      // create servo object to control a servo

int iPOS1 = 20;        // variable to store the servo position #1 (shutter open)
int iPOS2 = 160;     // variable to store the servo position #2 (shutter closed)

int iIN2 = 48;  // Pin for Input2
int iIN3 = 49;  // Pin for Input3
int iLED1 = 50;  // Pin for LED1 (pump on)
int iLED2 = 51;  // Pin for LED2 (pump off)
int iLED3 = 52;  // Pin for LED3 (shutter open)
int iLED4 = 53;  // Pin for LED4 (shutter closed)
int iPUMP = 46;  // Pin for PUMP
int iSERVO1 = 47;  // Pin for SERVO1
int iIN4 = 45;  // Pin for busy-flag of the pump

boolean bD2 = 0;       // mDSLM D2 input
boolean bD3 = 0;       // mDSLM D3 input
boolean bPbusy = 0;

void setup()
{
  // initialize digital pins as input and output.

  pinMode(iIN2, INPUT_PULLUP);   // mDSLM D2
  pinMode(iIN3, INPUT_PULLUP);   // mDSLM D3
  pinMode(iLED1, OUTPUT);  // green LED D2
  pinMode(iLED2, OUTPUT);  // red LED D2
  pinMode(iLED3, OUTPUT);  // green LED D3
  pinMode(iLED4, OUTPUT);  // red LED D3
  pinMode(iPUMP, OUTPUT);  // pump on/off
  pinMode(iIN4, INPUT);  // busy flag of the pump, high -> pump is active

  myservo.attach(iSERVO1);    // attaches pin iSERVO1 to the servo object
}

void loop()
{
  bD2 = digitalRead(iIN2);   // get mDSLM D2
  bD3 = digitalRead(iIN3);   // get mDSLM D3
```

```
  bPbusy = digitalRead(iIN4);  // get pump busy flag


  if ((bD2 == HIGH) and (bD3 == HIGH) and (bPbusy == LOW))  // // did the RTC switch the pump on while
  the shutter is open and the pump is off?
  {
    digitalWrite(iPUMP, HIGH);  // then toogle the pump to on
    delay(100);
    digitalWrite(iPUMP, LOW);
    delay(100);  // Wait till pump is really toggled on
  }
  else if((bD2 == LOW) and (bD3 == HIGH) and (bPbusy == HIGH))  // did the RTC switch the pump off while
  the shutter is open and the pump is on?
  {
    delay(100);
    if((bD2 == LOW) and (bD3 == HIGH) and (bPbusy == HIGH))  // is it still the same state?
    {
      digitalWrite(iPUMP, HIGH);  // then toogle the pump to off
      delay(100);
      digitalWrite(iPUMP, LOW);
      delay(100);  // Wait till pump is really toggled off
    }
  }


  if (bPbusy == HIGH)  // is the pump running?
  {
    digitalWrite(iLED1, HIGH);    // set green LED on
    digitalWrite(iLED2, LOW);     // set red LED off
  }
  else
  {
    digitalWrite(iLED1, LOW);     // set green LED off
    digitalWrite(iLED2, HIGH);    // set red LED on
  }


  if (bD3 == HIGH)  // did the RTC close the shutter?
  {
    digitalWrite(iLED3, HIGH);    // set green LED on
    digitalWrite(iLED4, LOW);     // set red LED off
    myservo.write(iPOS1);     // tell servo to go to position pos1
  }
  else
  {
    digitalWrite(iLED3, LOW);     // set green LED off
    digitalWrite(iLED4, HIGH);    // set red LED on
    myservo.write(iPOS2);     // tell servo to go to position pos2
  }
}
```

Abbreviations

abbreviation	written in full
CCD	charge-coupled device
CMOS	complementary metal-oxide-semiconductor
LSFM	Light Sheet-based Fluorescence Microscopy
fps	frames per second
mDSLM	monolithic Digital Scanned Light Sheet Microscope
CUDA	Compute Unified Device Architecture
PPB	preprophase band
RAM	root apical meristem
SAM	shoot apical meristem

promotors

abbreviation	written in full
35S	35S RNA, from the Cauliflower mosaic virus
GATA23	zinc-finger transcription factor
UBQ10	promotor Ubiquitin10

proteins

abbreviation	written in full
GFP	green fluorescent protein
H2B	histone 2B
LTi6	low-temperature induced
MAP4	microtubules associated protein
PIN	Pin-formed
PIP2;4	plasmamembrane intrinsic protein
Rab	Ras-related in brain
RFP	red fluorescent protein
SSU	small subunit of ribulose-1,5-bisphosphate carboxylase
YFP	yellow fluorescent protein

List of Figures

List of Tables

List of Movies

Acknowledgement

Curriculum Vitae

Name	Daniel von Wangenheim
Date of birth	9. January 1981
Place of birth	Frankfurt am Main

Research Experience

11/2014	PhD-thesis submission, Goethe Universität Frankfurt am Main, Germany. Thesis: *Long-term observations of Arabidopsis root system under close to natural conditions using Light Sheet-based Fluorescence Microscopy*
04/2010 - 11/2014	PhD Student, Goethe Universität Frankfurt am Main, Germany. Mentor: Prof. Ernst H. K. Stelzer
11/2009	Diploma Thesis, Rheinische Friedrich Wilhelm Universität Bonn, Germany. Mentor: Prof. Jozef Šamaj, Thesis: *Visualization of dynamic vesicular compartments in root hairs of Arabidopsis thaliana*
10/2002 - 11/2009	Studies in Biology, Goethe Universität Frankfurt am Main (Intermediate Diploma), Rheinische Friedrich Wilhelm Universität Bonn (Diploma)

Publications

All publications can be found on http://www.researcherid.com/rid/N-9054-2014

Articles

Berson, T.*, von Wangenheim, D. v.*, Takáč, T., Šamajová, O., Rosero, A., Ovečka, M., Komis, G., Stelzer, E. H. K., Šamaj, J. (2014). Trans-Golgi network localized small GTPase RabA1d is involved in cell plate formation and oscillatory root hair growth. BMC Plant Biology, 14:252

Vermeer, J. E. M., Wangenheim, D. v., Barberon, M., Lee, Y., Stelzer, E. H. K., Maizel, A., and Geldner, N. (2014). A spatial accommodation by neighboring cells is required for organ initiation in *Arabidopsis*. Science, 343(6167):178–183. PMID: 24408432.

Lucas, M., Kenobi, K., Wangenheim, D. v., Voβ, U., Swarup, K., Smet, I. D., Damme, D. V., Lawrence, T., Péret, B., Moscardi, E., Barbeau, D., Godin, C., Salt, D., Guyomarc'h, S., Stelzer, E. H. K., Maizel, A., Laplaze, L., and Bennett, M. J. (2013). Lateral root morphogenesis is dependent on the mechanical properties of the overlaying tissues. Proceedings of the National Academy of Sciences, 110(13):5229–5234. PMID: 23479644.

Rosquete, M. R., Wangenheim, D. v., Marhavý, P., Barbez, E., Stelzer, E. H. K., Benková, E., Maizel, A., and Kleine-Vehn, J. (2013). An auxin transport mechanism restricts positive orthogravitropism in lateral roots. Current Biology, 23(9):817–822.

Maizel, A.*, Wangenheim, D. v.*, Federici, F., Haseloff, J., and Stelzer, E. H. K. (2011). High-resolution live imaging of plant growth in near physiological bright conditions using light sheet fluorescence microscopy. The Plant Journal, 68(2):377–385.

*These authors contributed equally to the work.

Book Chapter

Wangenheim, D. v., Daum, G., Lohmann, J. U., Stelzer, E. H. K., and Maizel, A. (2014). Live imaging of arabidopsis development. In Arabidopsis Protocols, page 539–550. Springer.

Šamajová, O., Takáč, T., Wangenheim, D. v., Stelzer, E. H. K., Šamaj, J., (2012). Update on methods and techniques to study endocytosis in plants. In *Endocytosis in Plants*, pages 1–36. Springer Berlin Heidelberg.

Conference Abstracts

Oral presentations (presenting author underlined)

Wangenheim, D. v., Maizel, A., Schmitz, A., Chang, B.-J., Stelzer, E. H. K.. *Imaging lateral root organ emergence deep inside the main root with Light Sheet Fluorescence Microscopy.* Focus on Microscopy 2014, April 13 – 16, 2014, Sydney, Australia

Wangenheim, D. v., Maizel, A., Schmitz, A., Stelzer, E. H. K.. *Imaging lateral root organ emergence deep inside the main root with Light Sheet Fluorescence Microscopy.* 5th Annual Light-Sheet Microscopy Workshop, September 15 – 17, 2013, Thornwood, New York, USA

Wangenheim, D. v., Maizel, A., Stelzer, E. H. K.. *Light Sheet-based Fluorescence Microscopy (LSFM) allows long term imaging of Arabidopsis root growth in close-to-natural growth conditions.* Focus on Microscopy 2013, March 24 – 27, 2013, Maastricht, Netherlands

Wangenheim, D. v., Maizel, A., Stelzer, E. H. K.. *Long term imaging of Arabidopsis root growth in close-to-natural growth conditions using Light Sheet-based Fluorescence Microscopy.* 4th International Light-Sheet Microscopy Workshop, September 19 – 21, 2012, Frankfurt, Germany

Wangenheim, D. v., Maizel, A., Stelzer, E. H. K.. *Light Sheet-based Fluorescence Microscopy (LSFM) allows long term imaging of Arabidopsis root growth in close-to-natural growth conditions.* Focus on Microscopy 2012, April 1 – 4, 2012, Singapore, Singapore

Wangenheim, D. v., Maizel, A., Stelzer, E. H. K.. *Long term imaging of Arabidopsis thaliana root growth in close-to-natural growth conditions using Digital Scanned Light Sheet Microscopy (DSLM).* 3rd Light-Sheet Microscopy Workshop, October 13 – 14, 2011, Toulouse, France

Wangenheim, D. v., Stelzer, E. H. K.. *Light Sheet Based Fluorescence Microscopy (LSFM) allows long-time observations of Arabidopsis root growth.* Focus on Microscopy 2011, April 17 – 20, 2011, Konstanz, Germany

Wangenheim, D. v., Stelzer, E. H. K.. *Observing plant cell growth with EMBL's monolithic DSLM.* 2nd Light-Sheet Microscopy Workshop, September 2 – 4, 2010, Dublin, Ireland

Poster presentations

Wangenheim, D. v., Maizel, A., Stelzer, E. H. K.. *Light Sheet-based Fluorescence Microscopy (LSFM) allows long term imaging of Arabidopsis root growth at the organ, cellular and sub-cellular level in close-to-natural growth conditions.* 2nd Symposium of the International Plant Phenotyping Network, September 5 – 7, 2011, Jülich, Germany